Covalent organic frameworks for solar fuels production

Xiaoyan Wang

Department of Chemistry and Materials Innovation Factory,
University of Liverpool

Thesis submitted in accordance with the requirements of the University of Liverpool for the degree of Doctor of Philosophy

June 2020

Supervisor: Prof. Andrew I. Cooper

Abstract

Photocatalytic fuels production has the potential to produce clean energy for the future. Inorganic semiconductors such as TiO_2, CdS and WO_3 have been developed for photocatalytic hydrogen evolution and CO_2 reduction. To be scalable and practical, photocatalysts should be made of nontoxic and earth-abundant elements. Organic semiconductors have been studied intensively since carbon nitride has been developed for photocatalytic water splitting in 2009. Covalent organic frameworks (COFs) are a class of crystalline and porous materials made of molecular building blocks. The highly ordered feature of COFs allows for precisely tuning of COFs properties, such as band gap, porosity and hydrophobicity. More importantly, there is potential to construct atomistic structure–property relationships for materials where the 3D architecture is well defined. This work focuses on addressing some of the challenges faced in COF catalysts for solar fuels production. There are two themes: one concerns the targeted synthesis of highly active COF photocatalysts for photocatalytic hydrogen evolution and CO_2 reduction, and the other one deals with structure–property–activity relationships in COF catalysts for photocatalytic hydrogen production and CO_2 reduction.

In order to make highly active COF photocatalysts for hydrogen evolution, a dibenzo[*b,d*]thiophene sulfone moiety was introduced into frameworks. The resulting sulfone-based **FS-COF** shows excellent activity for photocatalytic hydrogen production. To further enhance the activity, the possibility to make dye-sensitized COF composites was explored. The processability of COF photocatalysts was also studied. The hydrogen production activity was found to be related to many properties of COF catalysts such as crystallinity, light absorption, wettability, and surface area. Furthermore, the interplay between these factors and their trade-off for hydrogen evolution activity was investigated by exploring the activity of a series fluorinated, isostructural COF catalysts.

Inspired by homogeneous photocatalytic CO_2 reduction systems, a post-synthetic modification strategy was applied to introduce molecular catalysts into COFs, in which iminopyridine moiety served as metal coordination site to anchor molecular catalysts. A partially-fluorinated, cobalt-loaded covalent organic framework nanosheet (CON) shows a performance comparable with the state-of-the-art heterogeneous catalysts under similar conditions. CONs outperformed their bulk counterparts, suggesting a general strategy to enhance the photocatalytic activities of two-dimensional COF catalysts.

Acknowledgement

I am so fortunate to have support, resource and love from numerous mentors, colleagues, friends, and my family. Although, it is impossible to list everyone who has helped me over the years, the people mentioned will have my greatest respect and gratitude.

First and foremost, I would like to express my sincerest gratitude to my Ph.D. supervisor Prof. Andy Cooper for the opportunity to study in his lab and to work on this fascinating Ph.D. project. His foreword-thinking scientific visions laid the essential foundation for this thesis. I really appreciate for his generous support and inspirational guidance. I have benefited immensely from his expertise, insights and enthusiasm. Without his support and encouragement, I would not have gone this far.

I would like to gratefully thank Dr. Linjiang Chen who always has his door open for me. I am deeply grateful for our discussions and his valuable suggestions. I have learnt a lot of knowledge about computational chemistry from him. A big thanks also goes to Dr. Reiner Sebastian Sprick for co-supervising my Ph.D. research and for his help and guidance.

My sincere gratitude also goes to people who have made contributions to this work. In no particular order, I am immensely grateful to Dr. Sam Chong, Dr. Marc Little, Rob Clowes, Dr. Yong Yan, Dr. Matthew Bilton, Dr. Fiona McBride, Dr. Xiaofeng Wu, Zhiwei Fu, Yang Bai, Lunjie Liu, Xue Wang and Chengxi Zhao (University of Liverpool); to Prof. Yongzhen Wu and Prof. Wei-Hong Zhu (East China University of Science and Technology); to Dr. Martijn A. Zwijnenburg (University College London); and to Prof. Lirong Zheng (Chinese Academy of Science). I have benefited immensely from all these collaborations, through which I acquired and enhanced my knowledge, technical skills and experiences. I had a fantastic journey over the years and enjoyed the companionship of friends and colleagues in the Cooper group; a big thanks goes to all present and past members in Cooper group, particularly Ming, Christian, Duncan, Zhongfu, Aiting, Ai, Hui, Peng, Cath, Ben and Michael.

Finally, I want to thank and dedicate this thesis to my parents. I hope that you will be proud of me. Thank you for your unwavering support and endless love. I wouldn't have been able to finish these studies without your encouragement and support. My final acknowledgement goes

to Xinni Long who has already become part of my life. I am grateful that I can share my happiness and sorrow with you during this special journey.

List of publications

1. **X. Wang**, L. Chen, S. Y. Chong, M. A. Little, Y. Wu, W. Zhu, R. Clowes, Y. Yan, M. A. Zwijnenburg, R. S. Sprick, A. I. Cooper. Sulfone-containing covalent organic frameworks for photocatalytic hydrogen evolution from water. *Nat. Chem.*, **10**, 1180.

2. Z. Fu, **X. Wang**, A. Gardner, X. Wang, S. Y. Chong, G. Neri, A. J. Cowan, L. Liu, X. Li, A. Vogel, R. Clowes, M. Bilton, L. Chen, R. S. Sprick, A. I. Cooper, A stable covalent organic framework for photocatalytic carbon dioxide reduction. *Chem. Sci.* 2020, **11**, 543–550.

3. C. Aitchison, C. Kane, D. McMahon, P. Spackman, A. Pulido, **X. Wang**, L. Wilbraham, L. Chen, R. Clowes, M. A. Zwijnenburg, R. S. Sprick, M. A. Little, G. M Day, A. I Cooper, Photocatalytic proton reduction by a computationally identified, molecular hydrogen-bonded framework. *J. Mater. Chem. A*., 2020, **8**, 7158-7170.

4. B. Burger, P. Maffettone, V. Gusev, C. Aitchison, Y. Bai, **X. Wang**, X. Li, B. Alston, B. Li, R. Clowes, N. Rankin, B. Harris, R. S. Sprick and A. I. Cooper, A mobile robotic chemist. *Nature*, 2020, **583**, 237–241.

5. **X. Wang**, Z. Fu, L. Zheng, C. Zhao, X. Wang, S. Y. Chong, F. McBride, R. Raval, M. Bilton, L. Liu, X. Wu, L. Chen, R. S. Sprick, and A. I. Cooper, Covalent organic framework nanosheets embedding single cobalt sites for photocatalytic reduction of carbon dioxide. *Chem. Mater.*, ***Accepted***.

6. **X. Wang**, Z. Fu, X. Wang, L. Liu, Y. Bai, S. Y. Chong, R. S. Sprick, L. Chen, A. I. Cooper. Surface engineering covalent organic frameworks for photocatalytic hydrogen evolution from water. ***In preparation***.

List of Abbreviations

COF	Covalent Organic Framework
CMP	Conjugated Microporous Polymer
CTF	Covalent Triazine Framework
MOF	Metal Organic Framework
PXRD	Powder X-ray Diffraction
BET	Brunauer Emmett Teller
FTIR	Fourier Transform Infrared Spectroscopy
TGA	Thermogravimetric Analysis
SEM	Scanning Electron Microscope
TEM	Transmission Electron Microscope
EA	Electron Affinity
IP	Ionization Potential
VBM	Valence Band Maximum
CBM	Conduction Band Minimum
HER	Hydrogen Evolution Reaction
TEOA	Triethanolamine
TEA	Triethylamine
P1	Poly(*p*-phenylene)s
P7	Dibenzo[*b,d*]thiophene sulfone-*co*-phenylene polymer
P10	Dibenzo[*b,d*]thiophene sulfone homopolymer

Contents

Chapter 1

Introduction

1.1 Solar fuels

Global energy consumption has rapidly increased over the past 10 years, reaching.13864.9 million tonnes oil equivalent in 2018.[1] The current reliance on fossil fuels, such as petroleum and coal, has raised concern of environmental problems (*e.g.*, global warming, and air pollution) and energy sustainability. Thus, there has never been such an urgency to explore alternative clean, renewable energy supplies. The sun delivers abundant, inexpensive, and environmentally clean energy to earth surface, which makes solar energy could be one of the promising candidates to replace our reliance on fossil fuels. Tremendous efforts have been made towards to utilize solar energy with different strategies, such as photovoltaics and photoelectrochemical cells.[2–4] Compared to photovoltaics, solar fuels are more convenient for storage and transport, which also possess higher energy density. Particularly, photocatalytic water splitting and CO_2 reduction is ideal for harvesting solar energy and converting to chemical fuels.[5,6]

Plants convert solar energy into chemical energy via a thermodynamically uphill reaction known as photosynthesis, where carbohydrates are synthesized from carbon dioxide and water. Inspired by these reactions, scientists have developed the strategy to directly convert of sunlight into chemical energy by using inorganic and organic materials and devices, known as artificial photosynthesis.[7,8] However, the thermodynamically uphill chemical reaction for artificial photosynthesis is fundamental barriers. For example, for water splitting reaction, the thermodynamic potential needed to drive the reaction has to be greater than 1.23 eV.[9] Fujishima and Honda first reported the photocatalytic water splitting in a photo-electrochemical cell (PEC) in 1972.[10] There are four steps in this process: light absorption by photosensitizers and generation of excited charge carriers (electrons and holes) and migration of excited charge carriers to catalytic centre, and utilization of photoexcited charge carriers to drive reduction and oxidation half reactions at catalytic centre.[11]

Since that, many approaches had been developed to overcome the thermodynamic and kinetic barriers for these thermodynamically uphill reactions. For instance, by mimicking natural photosynthesis processes, a dual photocatalysts system has been developed that utilize the solar light from different wavelength, so called as "Z-scheme".[12–14] However, it is still far from making this artificial photosynthesis technic to be practical. We are in need of new materials

with proper band structures and fundamental understanding of relation between materials properties and photocatalytic activity.

1.1.1 H_2 production

Hydrogen energy is a clean energy carrier but its terrestrial abundance is very low – it has to be synthesized artificially. There are around 5×10^{11} N/m^3 of hydrogen produced every year.[15] Thermal processes, such as steam reforming and biomass gasification, are the most widely used process for production of hydrogen. Steam reforming reaction produce hydrogen and carbon monoxide by using fuel and steam as the reactants. Although steam reforming shows high efficiency (>80%) and low cost, it still produces large amounts of CO_2 emission and suffer the catalyst deactivation.[16] Hydrogen also can be produced by biomass gasification. This process has considered to be an alternative large-scale hydrogen production method for steam reforming, because it is environmentally friendly and economically viable.[16] However, the amount of available fast-growing biomass means that this process cannot meet the total demand for hydrogen.

Electrolysis of water is an entirely clean hydrogen production process. This process involves two half reaction: hydrogen evolution reaction (HER) on the cathode and oxygen evolution reaction (OER) on the anode. The standard equilibrium electrode potential of this reaction at 25 ^oC and 1 atm is 1.23 V. Compared to the reforming process, electrolysis water process exhibits high production cost and relatively low efficiency. Water thermolysis process is one step water dissociation method. However, this process normally requires high temperatures (<2500 ^oC) that make it impractical.[17]

Photocatalytic water splitting is an emerging process to produce hydrogen. There are two half-equations for the overall water splitting. The mechanism basically involves several main steps, (i) absorption of photons with energies exceeding the semiconductor bandgap, leading to generate of excitons in the semiconductor; (ii) charge separation followed by migration of these photogenerated carriers to the surface; (iii) hydrogen and oxygen evolution reactions happened between the carriers with H_2O; electrons and holes may also recombine with each other without participating in any chemical reactions (Figure 1-1).[18] The past few years have witnessed increasing development of photo-induced water splitting research,[19,20] the making of photocatalytic active materials for water splitting is far from easy. Several criteria must be met

by semiconductors to qualify as potential catalysts: they first have to absorb light efficiently to form photo-excited states, but also the generated photo-excited states have to be long-lived, effectively separated, and able to migrate to the catalyst surface. Then, the band-gap energy of semiconductors should be at least 1.23 eV (potential of water splitting reaction) to drive the water splitting reaction.[18]

Since photocatalytic water splitting reaction is a thermodynamically uphill chemical reaction, photocatalysts often require additional 'sacrificial' agents with a larger thermodynamic driving force than water to accept a light-generated charge carrier. This can facilitate water splitting reaction, because photoexcited holes or electrons can be consumed by the sacrificial agents, which prevent recombination of photoexcited electrons and holes. L-Ascorbic acid (H_2A) and related ascorbate ions are famous sacrificial agents. H_2A will be used in the photocatalytic hydrogen evolution cases in this thesis. In general, H_2A will quench holes from excitonic state of the photocatalyst which allow the excited electron to participate in the proton reduction half-reaction. On the other hand, H_2A degrades to form A and A^{2-}. H_2A had been proved to be efficient quencher for $[Ru(bpy)_3]^{2+}$ photosensitizer, because it is irreversible transformation from H_2A into A and A^{2-}.[21] Moreover, co-catalysts are often loaded onto photocatalysts to serve as electron sinks and also active sites for proton reductions thus facilitating hydrogen and oxygen evolution reaction.

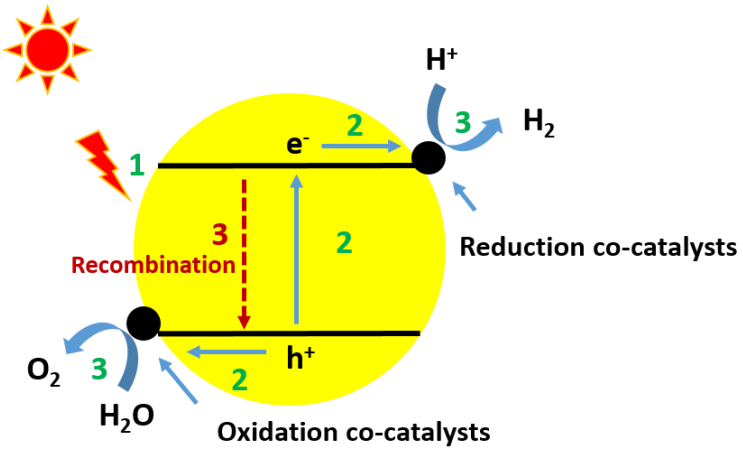

Figure 1-1. Schematic illustration of photocatalytic water splitting mechanism.[18]

1.1.2 CO_2 reduction

The growing consumption of fossil fuels has caused increasing of the concentration of the greenhouse gases (CO_2) in the atmosphere and a global energy crisis. Thus, the development

of renewable and clean energy technologies has been an urgent task for human society. Electrochemical reduction of CO_2 is potential strategy to recycle of CO_2 as an energy carrier, which store the electricity energy in a high density and convenient way. However, the high over potentials for CO_2 reduction makes energy efficiency is relatively low.[22] The recent development of artificial photosynthesis is promising strategy to simultaneously produce environmentally friendly solar fuels and decrease CO_2 concentration in the atmosphere.[23,24] Similarly like natural photosynthesis, artificial photosynthesis allows to reduce CO_2 into chemical fuels such as CO, CH_4, HCOOH, and CH_3OH.[25] The general mechanism for photocatalytic CO_2 reduction reaction using semiconductor photocatalysts as the catalyst include four steps: (i) CO_2 absorption; (ii) electron-hole generation by absorbing light; (iii) electron-hole separation and migration of these carriers to the photocatalysts surface; (iv) CO_2 reduction (Figure 1-2).[26] However, the order for these reactions is unclear. CO_2 reduction activity can be improved by optimization of CO_2 adsorption and light absorption, charge separation, and their synergistic effects.

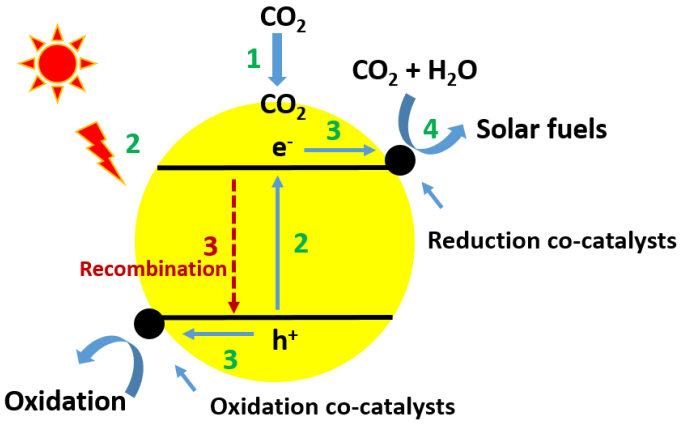

Figure 1-2. Schematic illustration of photocatalytic CO_2 reduction mechanism.[26]

Since CO_2 is highly stable molecule, thus the electron with sufficient reduction potential can only do CO_2 reduction reaction. Different of CO_2 reduction reactions show the different standard redox potentials (Reaction 1.1-1.5). The reduction products will be determined by specific reaction pathway and rates and number of multi-electron transfer between photogenerated carriers and species in the reaction system.[25] Similarly to photocatalytic water splitting, co-catalyst also be introduced to accumulate electrons on the surface of semiconductors to achieve multi-electron transfer. For photocatalytic CO_2 reduction system, H_2O is generally used as the hydrogen source and electron donor. However, proton from H_2O

also can be reduced to produce H_2. Thus, H_2O is also a competing reagent for CO_2 reduction. In addition, proton reduction is thermodynamically and kinetically more favourable than CO_2 reduction, because of more negative reduction potential and more complicated reaction mechanisms for photocatalytic CO_2 reduction. Thus, an ideal photocatalysts should spatially separate electrons and proton to avoid H_2 evolution. Sacrificial agents also used in photocatalytic CO_2 reduction to consume photoexcited holes from excited photocatalysts. Triethanolamine (TEOA) will be used in this thesis for photocatalytic CO_2 reduction.

$CO_2 + 2\,H^+ + 2\,e^- \longrightarrow HCOOH$	$E^0 = -0.61$ V vs NHE at PH = 7	1.1
$CO_2 + 2\,H^+ + 2\,e^- \longrightarrow CO + H_2O$	$E^0 = -0.53$ V vs NHE at PH = 7	1.2
$CO_2 + 4\,H^+ + 4\,e^- \longrightarrow HCHO + H_2O$	$E^0 = -0.48$ V vs NHE at PH = 7	1.3
$CO_2 + 6\,H^+ + 6\,e^- \longrightarrow CH_3OH + H_2O$	$E^0 = -0.38$ V vs NHE at PH = 7	1.4
$CO_2 + 8\,H^+ + 8\,e^- \longrightarrow CH_4 + 2\,H_2O$	$E^0 = -0.24$ V vs NHE at PH = 7	1.5

1.2 Organic photocatalysts

1.2.1 Organic photocatalysts for hydrogen evolution form water splitting

Since TiO_2 was first developed as a water splitting photocatalyst,[10] inorganic materials have been extensively studied for photocatalytic water splitting. [20,27] However, it is challenging to tune the property (*e.g.*, band gap) of inorganic materials.[28] Compared to the inorganic materials, organic materials have properties that are (arguably) more easily controlled by synthesis. In 1985, Poly(*p*-phenylene) was first reported as the organic photocatalysts for hydrogen evolution in the presence of sacrificial electron donors.[29] The quantum yield was < 0.04 under irradiation at $\lambda > 290$ nm. A visible light active polymeric carbon nitride (CNxHy) have been made as photocatalysts for hydrogen evolution reaction and oxygen evolution reaction, with quantum efficiency of approximately 0.1% at irradiation of 420–460 nm.[30]

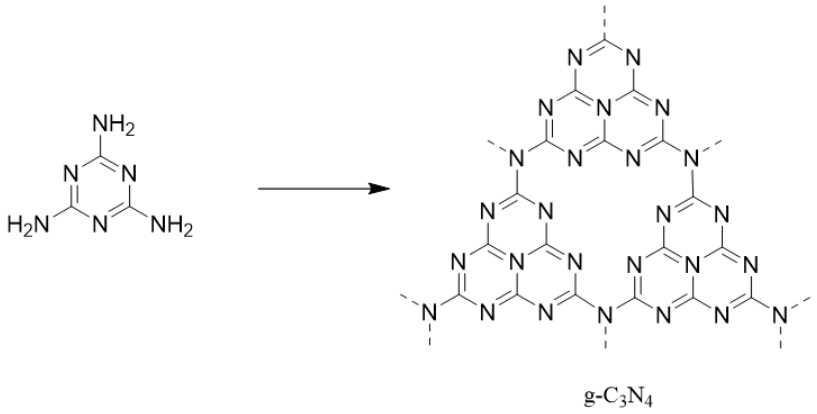

Figure 1-3. Synthesis of graphitic carbon nitride.[30]

Porous conjugated microporous polymers (CMP) and covalent triazine-based frameworks (CTF) also have been used as sacrificial hydrogen evolution photocatalysts.[31,32] Pyrene-based CMPs have been synthesized for photocatalytic hydrogen evolution, reaching rate of 17.4 ± 0.9 μmol h^{-1} under visible light irradiation.[30] Fluorene based linear conjugated polymers were developed as a series of very active hydrogen evolution photocatalysts.[33,34] For example, sulfonated co-polymer P10 shows hydrogen evolution rate of 81.5 ± 4.1 μmol h^{-1} under visible light irradiation.[33] By introducing the co-catalysts, carbon nitride hybrid materials can facilitate overall water splitting reactions.[35] CMPs have also been reported for overall water splitting.[36] Although, the semiconductor properties such as band gap can be tuned for organic photocatalyst, most of organic materials are amorphous, which will limit the transport of photogenerated carries. Generally, it is challenging to define the atomic three-dimension structure for these organic materials. Therefore, it is highly desirable to developed crystalline organic materials for photocatalytic water splitting.

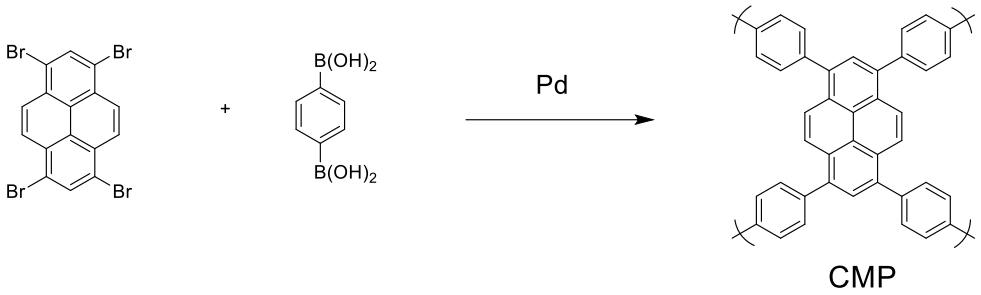

Figure 1-4. Synthesis of conjugated microporous polymers photocatalysts.[36]

1.2.2 Organic photocatalysts for CO_2 reduction

Development of homogeneous metal based molecular catalysts for photocatalytic CO_2 reduction can be traced back to 1980s. In these systems, photosensitizers (*e.g.*, $[Ru(bpy)_3]^{2+}$), catalysts (*e.g.*, Co(2,2'-bipyridine)$_3^{2+}$) and electron donors (*e.g.*, TEA) are commonly used. $Re(bpy)(CO)_3Cl$ is one of most important catalysts for CO_2 reduction, which shows an excellent selectivity for the reduction of CO_2 to CO. This catalyst can work without photosensitizers, because its excited state has sufficient long lifetimes and ability to react with electron donors. Tetraaza-macrocycle Co and Ni complexes have also been developed for photocatalytic CO_2 reduction. The properties of these complex catalysts (*e.g.*, steric hindrance and redox potential) can be fine-tuned by ligation with different macrocycle ligands, resulting different catalytic efficiency and selectivity.

C_3N_4 and its derivatives have been widely used for photocatalytic CO_2 reduction. For example, Pt co-catalyst was employed into C_3N_4 to overcome the recombination of photogenerated electrons and holes. Pt affected the selectivity of products.[37] Heterostructures was employed to enhance the conversion of CO_2. Zou and co-workers reported a g-C_3N_4/$NaNbO_3$ heterojunction photocatalysts for CO_2 reduction. The composite shows higher activity than g-C_3N_4 and $NaNbO_3$ alone, because of improved separation of photogenerated electron–hole pairs for heterojunctions.[38] Functional CMPs also used for photocatalytic CO_2 reduction.[39,40] For instance, Eosin Y-functionalized CMPs exhibits high CO production rate and selectivity.[39] To achieve high CO_2 conversion rate and selectivity is very challenging, because of complicated mechanism and proton reduction competition. Thus, crystalline organic materials are promising for CO_2 reduction, because their well-defined structure allows for controlling the catalysts properties precisely.

1.3 Introduction of covalent organic frameworks

Porous materials have attracted a great deal of interest due to their unique properties (*e.g.*, highly crystalline and porous) and versatile applications, such as separation, adsorption, purification, catalysis and energy storage. The commercialized zeolites and activated carbons have been developed to act as good catalysts and adsorbents. However, porous materials are not only of interest in adsorption and catalysis, but also interest in energy storage, light

harvesting and molecular sensing. Thus, new porous materials with electronic and photochemical properties are desired.

Dynamic covalent chemistry is a process in which molecular components can freely exchange to achieve thermodynamic minimum of the system.[41] Dynamic covalent chemistry with reversible covalent bond formation is the key to form a crystalline organic framework. These reversible reactions allow for error correction and rearrangement of the frameworks by broken and reformation of bounds within the extended structure. By carefully thermodynamic control over the reactions enable COFs self-healing to form the crystalline structure. This is a general synthetic principle for all COFs.

Covalent organic frameworks (COFs) were reported by Yaghi in 2005 (Figure 1-5),[42] which are one of the representatives for new porous materials. COFs are crystalline polymers built from organic linkers via reversible covalent bond formation.[43] COF-1 shows high crystallinity with large surface area of 711 m^2 g^{-1}. The geometry and pore size of the COFs can be facilely tuned by different building blocks, which enables to control of fine-tuning physical and chemical properties for the materials. The well-defined large porous surface will be beneficial to the catalysis, separation and sensing, because the porous structure facilitates mass transfer. Moreover, the π-interactions of the stacked organic unites and the crystalline nature make COFs interesting candidates for electrochemical and optoelectronics energy storage applications.

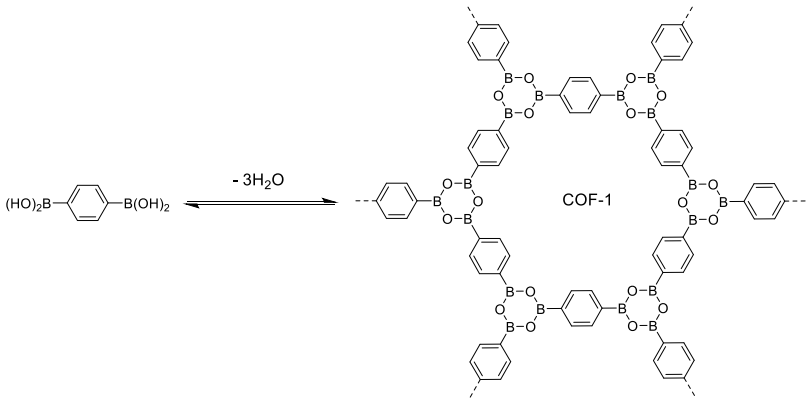

Figure 1-5. Synthesis of COF-1 and its structural representation.[42]

1.4 Design and synthesis of covalent organic frameworks

1.4.1 Linkage of COFs

As discussed above, a reversible reaction is critical to formation of COFs. The crystallinity of COFs was determined by the reversibility of the synthetic reaction. The first COF made by the self-condensation of boronic acids to form boroxines rings as linkage between the building blocks (Figure 1-5).[42] Since then, a variety of the different linkages have developed for the synthesis of COFs (Figure 1-6).

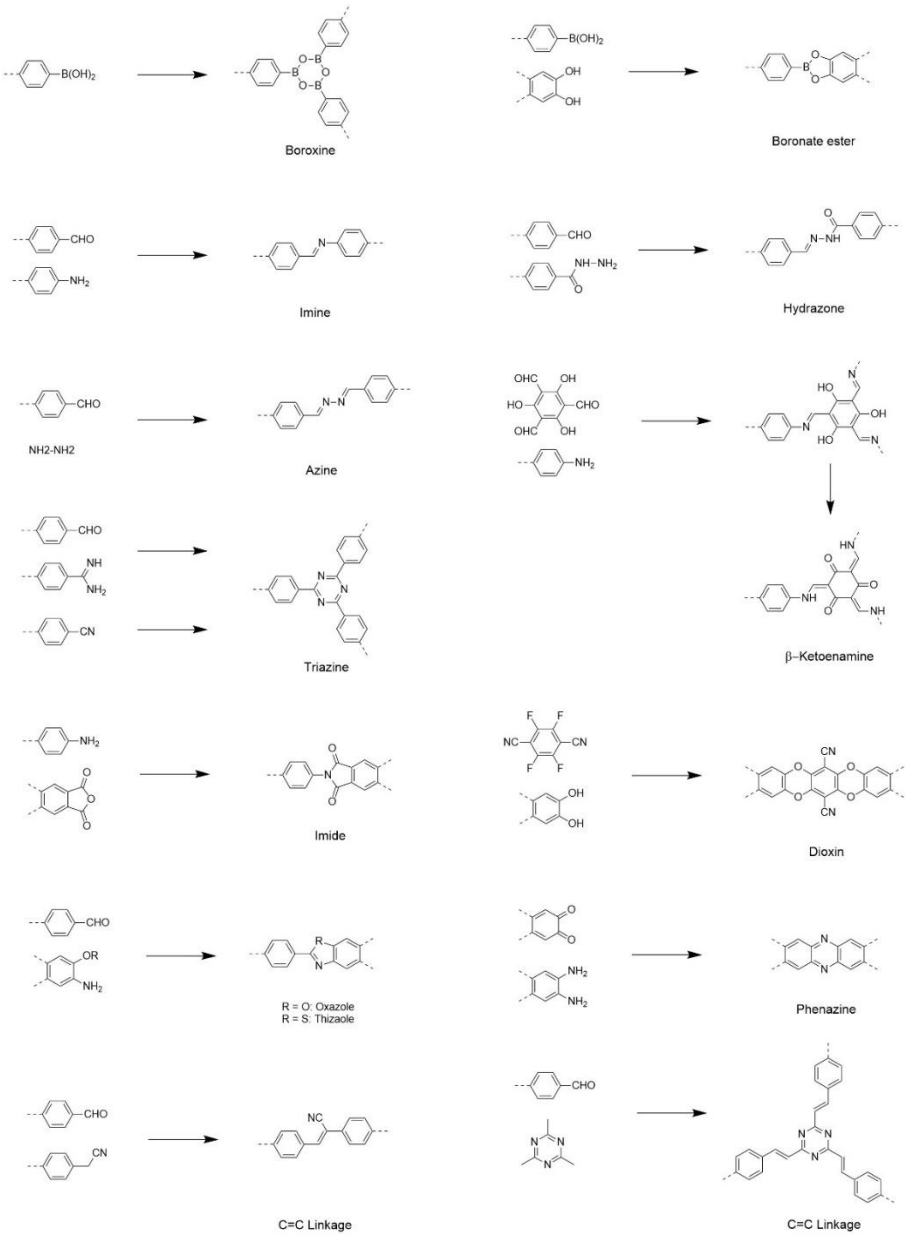

Figure 1-6. Synthetic reactions for the formation of COF.

1.4.1.1 Boroxines and Boronic Esters

The first COF introduced by Yaghi and co-workers in 2005 which is based on the self-condensation of 1,4-benzenediboronic acid. The self-condensation of boronic acids form a 1.5 nm pore network with six-membered boroxine linkages. They also reported the condensation of diboronic acid (BDBA) and hexahydroxy triphenylene (HHTP) to synthesize boronic esters crystalline frameworks (Figure 1-7).[42]

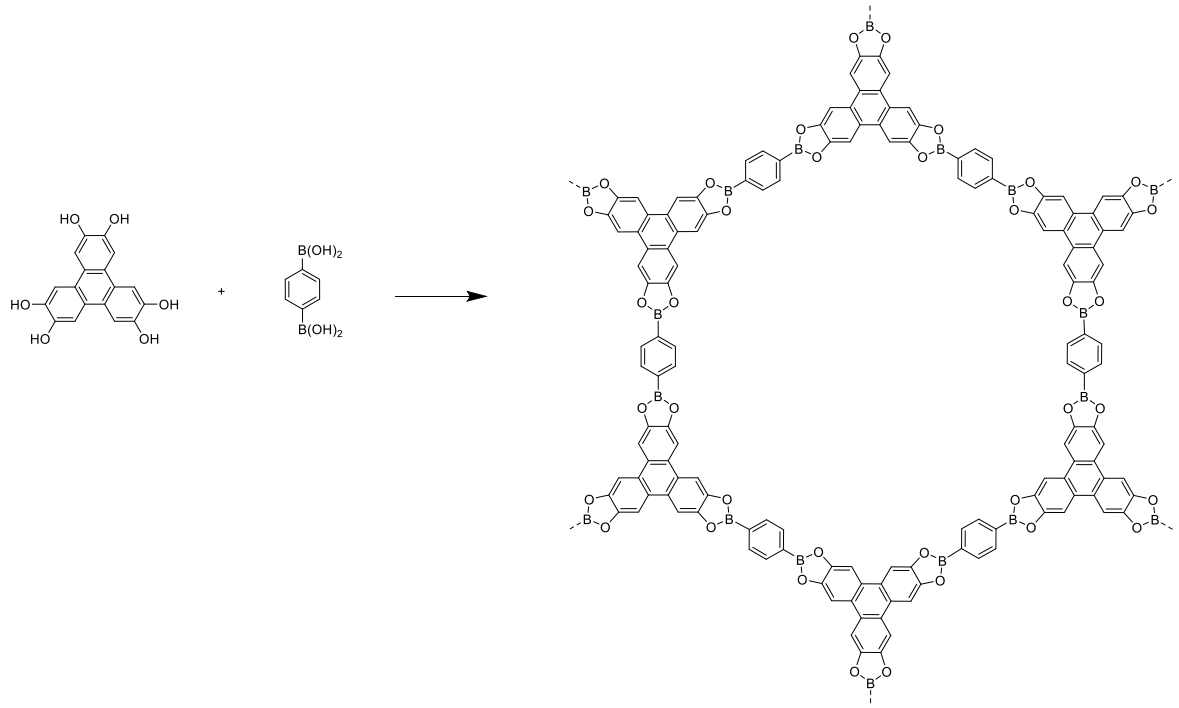

Figure 1-7. Synthesis of boronic esters COF-5.[42]

Yaghi and co-workers also introduced 3D linked organic frameworks. By self-condensation of tetrahedral boronic acid tetra(4-dihydroxyborylphenyl) methane (TBPM) and tetra(4-dihydroxyborylphenyl)silane (TBPS) or co-condensation with HHTP, they formed 3D COFs (COF-102, COF-103, COF-105 and COF-108) (Figure 1-9). The 3D COFs have very high surface areas of 3472 $m^2 g^{-1}$ and 4210 $m^2 g^{-1}$ for COF-102 and COF-103, respectively.[44]

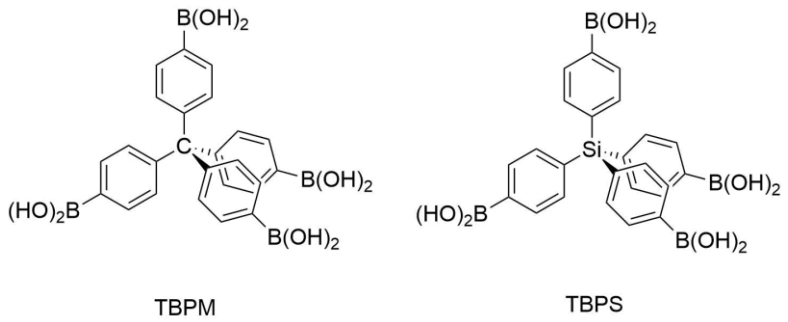

Figure 1-8. Tetrahedral building blocks for the synthesis of 3D COFs.

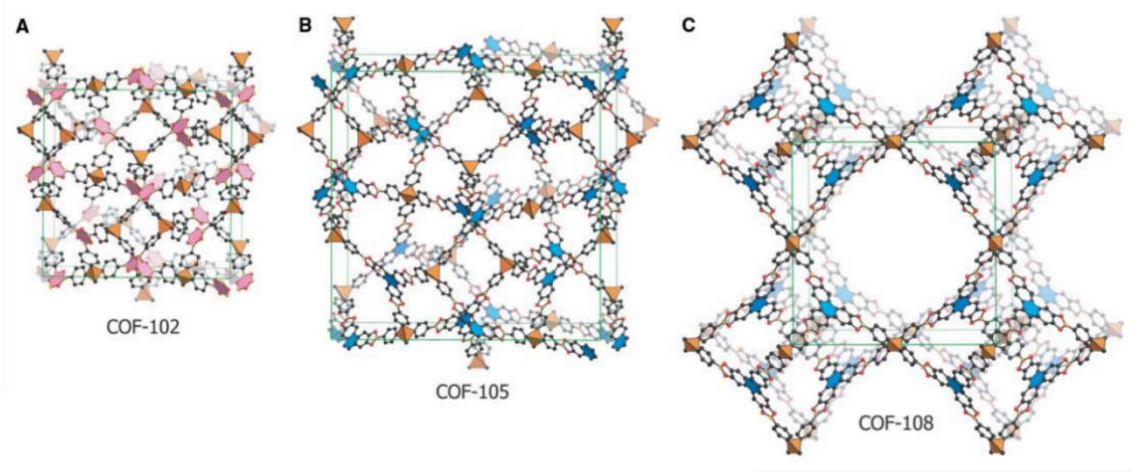

Figure 1-9. Model of crystalline 3D COFs. (**A**) COF-102, (**B**) COF-105 and (**C**) COF-108. Grey, orange, and red spheres represent carbon, boron, and oxygen atoms, respectively.[44]

Jiang *et al* have expanded the idea of linking different organic building blocks to form the multiple-component COFs. They reported a general strategy to made tetragonal and hexagonal multiple-component COFs by using one knot and two or three linkers at same time. The multiple-component system enhances the structural diversity and complexity for COFs materials.[45] Although boroxines and boronic esters chemistry shows good reversibility and caused a very crystalline frameworks formed, the poor hydrolytic stability of these linkages makes these materials unsuitable for many applications. These linkages also break the extended conjugation in these materials.

1.4.1.2 Imine

Imine linked COF was made by Schiff base condensation of aldehydes and amines. Imine bond is much stable than boroxines and boronic esters, which made imine COFs are more applicable

in wide ranges of applications. Moreover, unlike boroxines and boronic esters linkages, the imine linkages can link the aromatic building blocks to allow conjugation over whole 2D COF layers. This has made imine coupling the most common synthesis strategy to form COFs to date. Yaghi and co-workers reported the first imine COF in 2009 (Figure 1-10).[46] The tetrahedral 3D COF with 5-fold interpenetration was made by co-condensation of tetra-(4-anilyl) methane and terephthalaldehyde.[46]

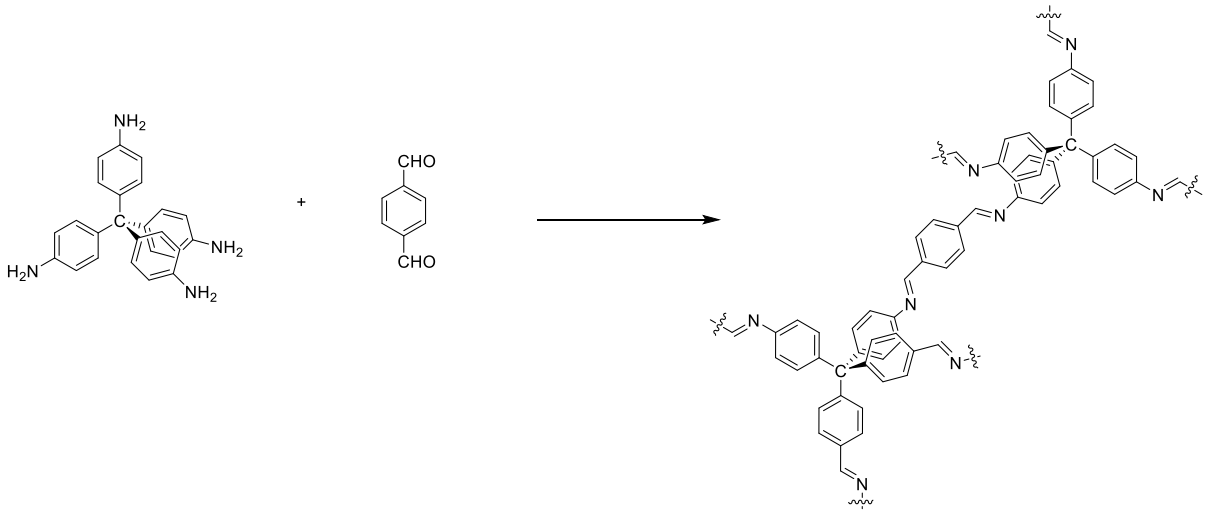

Figure 1-10. Synthesis of 3D imine linked COF.[46]

The first 2D imine linked COF was explored by Wang and co-workers in 2011. They condense 1,3,5-triformylbenzene and 1,4-phenylenediamine to create a 2D COF with hexagonal channels. This new COF-LZU1 is robust and stable showing great potential for heterogonous catalysis.[47] After ligation with Pd, a Pd-containing COF, Pd/COF-LZU1, was successfully synthesized. This Pd/COF-LZU1 shows excellent yields (96-98%) for Suzuki-Miyaura coupling reaction, and the catalyst was applicable for broad scope of the reactants. In 2014, Zhao *et al.* reported a star-shaped dual pore COF with the hexagonal 26.9 Å diameter mesopores and 7.1 Å diameter triangular microporous pores, by using 4,4′,4″,4‴-(ethene-1,1,2,2-tetrayl)-tetraaniline and terephthalaldehyde as monomer.[48] By mixing of linear linkers with different lengths, Zhao and co-workers synthesized a 2D imine COF with three different pore sizes, which has one hexagonal pore and two different triangular pores.[49]

It is challenging to produce single crystal COFs because of the limited reversibility of the COF-forming reactions. Very recently, a general method to grow large single crystals of 3D imine-based COFs was developed.[50] Aniline is a monofunctional molecule, which was serve as a

competitive modulator and nucleation inhibitor for multifunctional amine-based building units. By using aniline in synthetic system, the reversibility of imine bond formation will be increased, thus resulting highly crystalline COFs. Some unresolved questions related to COFs structure and guest molecules, such as degree of interpenetration and arrangement of water guests, were resolved in this study.[50]

1.4.1.3 Ketoenamine

Improving the stability of COFs is a very important issue for COFs applications. In 2012, Banerjee and co-workers reported a chemically stable COF with *β*-ketoenamine linkage. They use 1,3,5-triformylphloroglucinol as aldehyde monomer and *p*-phenylenediamine as amine monomer for COF synthesis. An enol-imine COF was first formed, and then an irreversible enol-keto tautomerization was underwent to form a *β*-ketoenamine-linked COF (Figure 1-11). The resulting ketoenamine-linked COF shows good stability in acid (9 N HCl) and boiling water for 7 days.[51] These *β*-ketoenamine COFs can be exfoliated to nanosheets by simply grinding in the mortar.[52] They also reported a room-temperature solvent-free mechanochemical grinding method to synthesize *β*-ketoenamine COFs.[53] However, the mechanochemically synthesized COFs showed moderate crystallinity and lower surface compared to their solvothermally synthesized analogues.

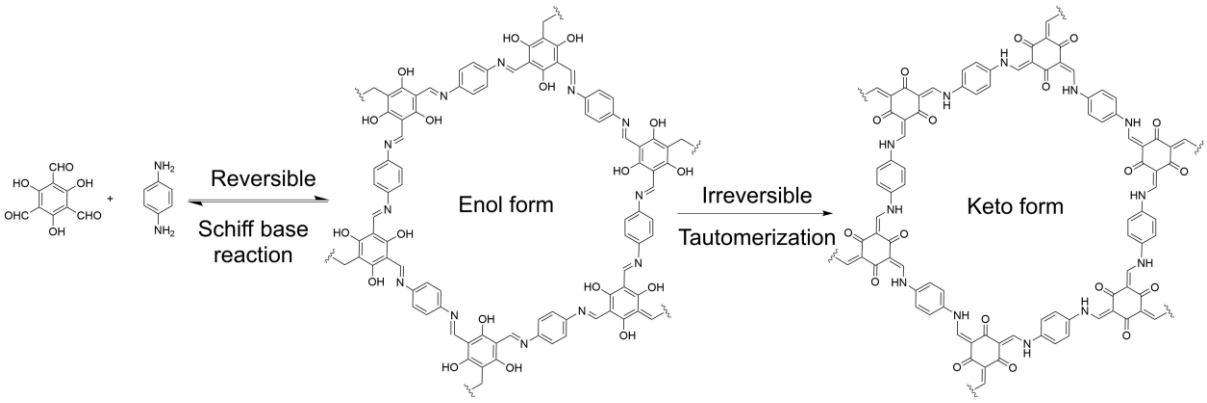

Figure 1-11. Synthesis of ketoenamines COFs TpPa-1 by the condensation of 1,3,5-triformylphloroglucinol with *p*-phenylenediamine.[51]

In 2017, Banerjee *et al.* introduced a series of self-standing, porous and *β*-ketoenamine-linked COF membranes.[54] They use co-reagents *p*-toluene sulfonic acid in the reaction which not only play the role of binding the precursors but also the catalyst for the Schiff base reaction. The

resultant COF membranes exhibit high crystallinity and porosity, and also can maintain its structure in water, organic solvents and mineral acid (3 N HCl). These free-standing membranes show great potential for separation applications, such as recovery of valuable pharmaceutical ingredients from organic solvents and wastewater treatment.

1.4.1.4 Imide

Yan *et al.* reported a series of large pore crystalline polyimide COFs by using reversible imidization reaction[55] (Figure 1-12). These polyimide COFs show remarkable thermal stability. The reported PI-COF-3 exhibit very large Brunauer-Emmett-Teller (BET) surface area up to 2346 $m^2 g^{-1}$. After loaded with dye molecules, the dye-doped COF shows special temperature-dependent luminescent properties, indicating this composite material is the promising candidate for the temperature-sensing devices.

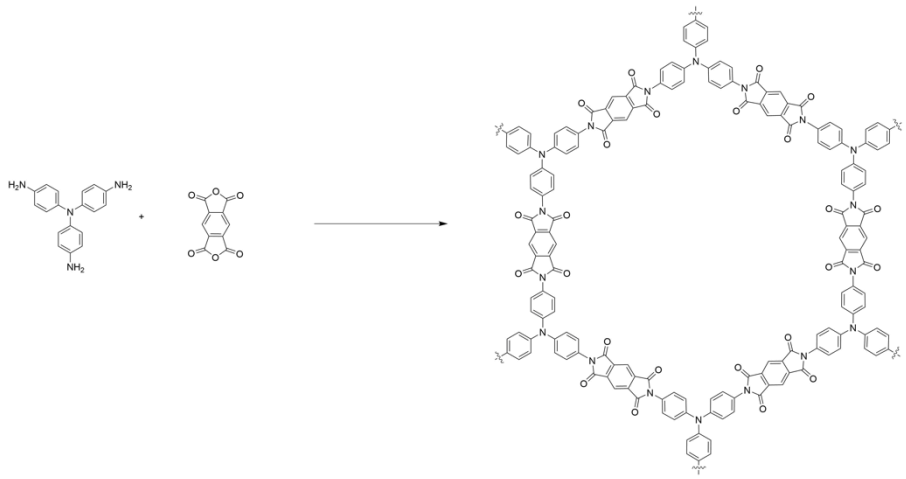

Figure 1-12. Synthesis of polyimide PI-COF-1.[55]

1.4.1.5 Olefin

In 2017, Jiang and co-workers made a series of extended conjugated 2D COFs which built all from sp^2 carbons by condensation of tetrakis(4-formylphenyl)pyrene and 1,4-phenylenediacetonitrile (Figure 1-13). The crystalline 2D COFs were connected by the C=C linkages to form the extended conjugations along both x and y directions.[56] Very recently, Yaghi *et al*. introduced the first unsubstituted olefin linked COF by Aldol condensation of 2,4,6-trimethyl-1,3,5-triazine and 4 4'-biphenyl carboxaldehyde. This olefin linked COF has surface area of 1715 $m^2 g^{-1}$ and retains its crystallinity under strong acid and base conditions.[57]

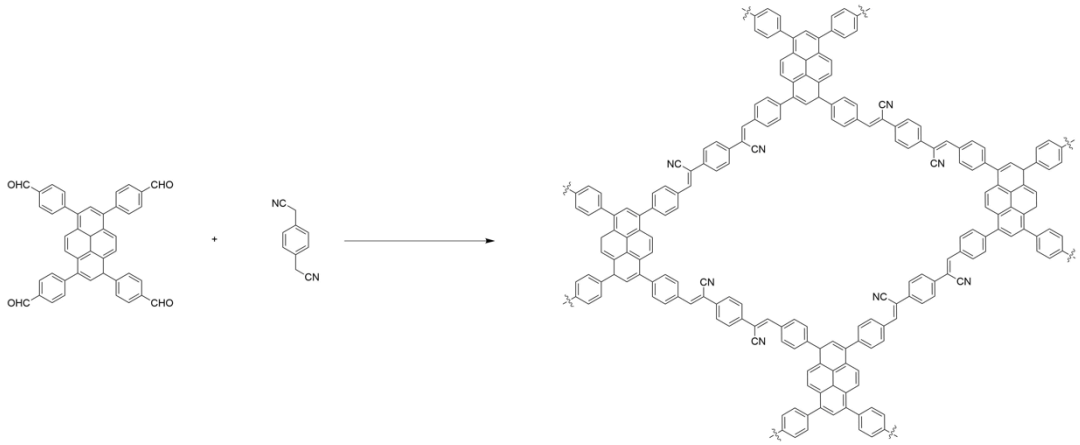

Figure 1-13. Synthesis of olefin linked sp^2c-COF.[56]

1.4.1.6 Other linkages

Besides the reactions described above, there are also some other coupling reactions were used to build COFs. Jiang and co-workers reported a 2D azine linked COF by condensation of hydrazine with 1,3,6,8- tetrakis(4-formylphenyl)pyrene.[58] This pyrene based azine COF was highly sensitive for the detection of 2,4,6-trinitrophenol explosive. Lotsch *et al.* made a COF linked by hydrozone linkage.[59] This COF can utilize visible light to produce hydrogen from water. Although, most of covalent triazine frameworks (CTF) reported so far are amorphous, Tan and co-workers reported a new strategy to get highly crystalline CTF by controlling the feed rate of monomers.[60] The crystalline 1,4-dioxin linked COFs were reported by Yaghi group in 2018.[61] They use 2,3,6,7,10,11-hexahydroxytriphenylene and linear tetrafluorophthalonitrile or 2,3,5,6-tetrafluoro-4-pyridinecarbonitrile as monomer to build the hexagonal pore 2D dioxin COFs. These COFs exhibit high chemical stability in both acid and base, because irreversible steps have been involved in the reactions.

1.4.1.7 Two steps bond formation

Yaghi and co-workers reported a two-step chemical conversion strategy to form a polyamide COF.[62] An imine COF was first made, and then the imine linkages have been transformed into amide linkages by introducing oxidation agent. The polyamide COFs retain the porosity and crystallinity over their imine COF precursors. Besides, imine COFs can also be converted to thiazole COF by post-synthetic modification strategies (Figure 1-14). The resulting thiazole linked COF shows significant enhancement of chemical and electron beam stability, which

allows to investigate of the detailed real framework structure.[63] Aza-Diels-Alder cycloaddition reaction was also used to fix reversible imine linkage.[64] Comparing to the imine COF, the as formed quinolone linked COFs retain and crystallinity and porosity, and also exhibits excellent chemical stability.

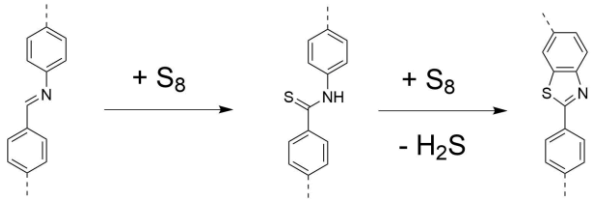

Figure 1-14. Schematic of conversion of imine linkage to thiazole linkage.[63]

1.4.2 Topology

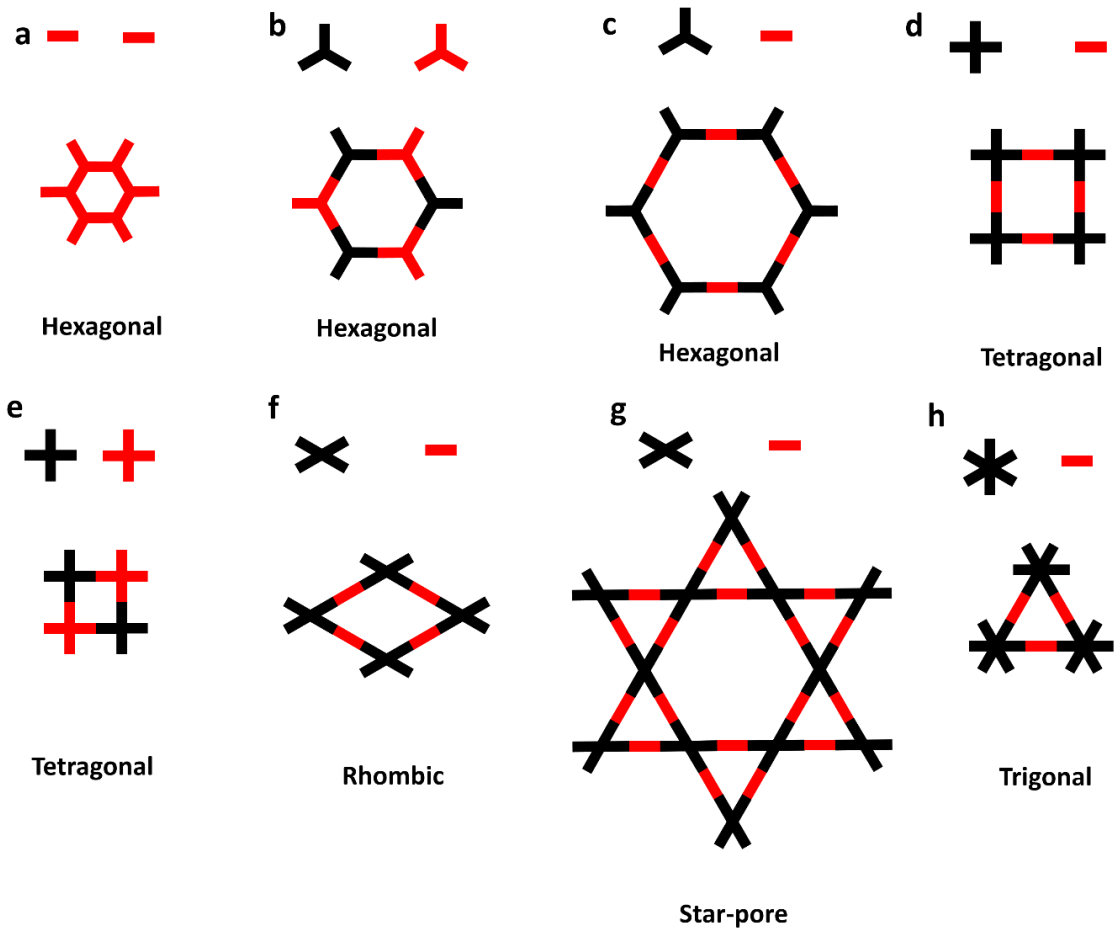

Figure 1-15. Topology diagrams for common linker and the resulting 2D COFs.

The geometry of the COF is determined by the topological connection of monomers. For co-condensation system, at least one of monomers should have more than two reactive groups. Similarly, for self-condensation system, the monomer should have two or three reactive sites. For example, hexagonal pore COFs can made by co-condensation of trigonal planar linkers and linear linkers or two different trigonal planar linkers (Figure 1-15b, c). These 2D COFs process 1D-channels which come from stacking of extended 2D layers. The common 2D geometries realized for COFs are shown in Figure 1-15.

3D-COFs were made by using monomers with three dimensions connectivity. As shown in Figure 1-16, 3D COF can be made into different geometries, including *dia, bor, ctn, srs and pts.* In 2007, Yaghi and co-workers reported the first 3D COFs with *ctn* or *bor* nets derived from the [Td + C3] diagram (Figure 1-16).[44] The *dia* network can be synthesized from [Td + Td] or [Td + C2] diagrams.[46] Wang *et al.* reported a pyrene based COF with two-fold interpenetrated pts topology generated by [Td + C4] diagram.[65] Interpenetrated structures can be commonly observed in 3D-COFs. However, it is still unclear that how many folds can be formed for specific COF.

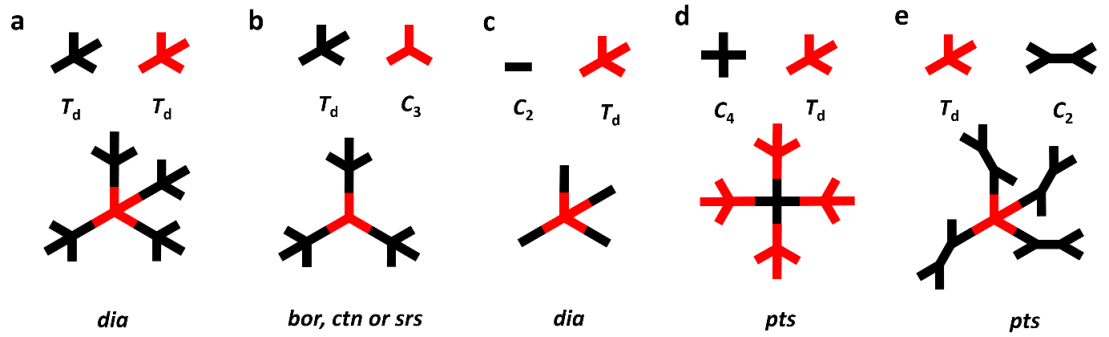

Figure 1-16. Topology diagrams for common linker and the resulting 3D COFs.

1.4.3 COF characterization

1.4.3.1 X-Ray Diffraction

X-rays were first observed by Röntgen in 1895. Braggs determined the constructive interference between the X-ray waves. Since then, X-ray diffraction (XRD) has been developed to be a powerful technique to reveal information about structure of crystalline materials. As

shown in Figure 1-17, the lattices of materials must be periodic and path difference an integral number of wavelengths. This principle is described as Bragg´s Law:

$$2d \sin\theta = n \lambda \qquad 1.6$$

Where d is the spacing of the crystal lattice, θ is the angle of incident X-rays, n is an integer and λ is the wavelength of X-rays.

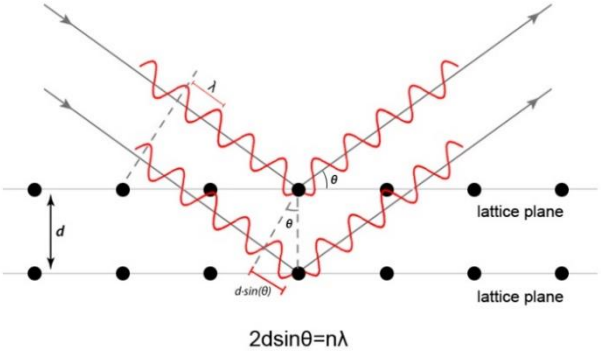

Figure 1-17. Schematic illustration of the Bragg relation, X-rays diffracted at a lattice plane.

The crystallinity of COFs is normally determined by powder X-ray diffraction (PXRD). PXRD pattern was used to determine the crystal structure of COFs by comparison of experimental PXRD results with calculated PXRD patterns from predicted COF models.

1.4.3.2 N_2 adsorption

N_2 adsorption experiments were carried out to characterize the porosity of materials. N_2 adsorption can be attributed to the weak interaction between materials and N_2 molecules, which was classified as physisorption. Normally, the amount of nitrogen adsorption is measured under different pressures P/P_0 with constant temperature of 77 K, where P is the absolute pressure and P_0 is the nitrogen saturation vapour pressure. The obtained isotherms can be classified to six different types by IUPAC (Figure 1-18). These different isotherms can be attributed to different pore structure and interactions between nitrogen molecules and adsorbent.

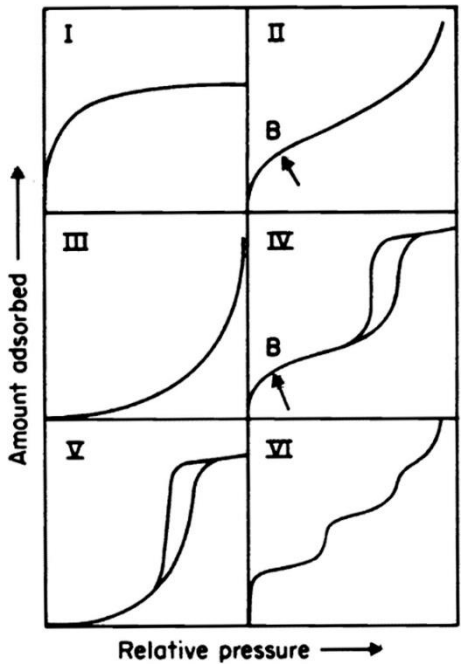

Figure 1-18. Different types of physisorption isotherms.[66]

Type I isotherms are given by microporous materials, showing steep increase of adsorption at relatively low pressures and reaching saturation of adsorption after pore filling.

Type II isotherms are normally obtained from macroporous or non-porous materials. Unrestricted multilayer adsorption taken place after monolayer adsorption finished. As shown in Figure 1-18, point B indicates the completion of monolayer adsorption and beginning of multilayer adsorption.

Type III isotherms are not common. They only occurred when adsorbent and adsorbate show weak interactions between each other.

Type IV isotherms are associated with mesoporous materials. The hysteresis loop can be attributed to capillary condensation in mesopores. This is a commonly observed isotherm type for COFs.

Type V isotherms are similar to type III which adsorbent shows weak interaction with adsorbate. However, the hysteresis loop can be found from this type of isotherm.

Type VI isotherms shows stepwise multilayer adsorption, which can be observed in non-porous materials.

Brunauer-Emmett-Teller (BET) theory is the most commonly method used to determine the surface areas of materials. This theory covers both monolayer adsorption and multilayer adsorption. BET equation can be expressed in a linear form at low pressure ($P/P_0 < 0.3$).

$$\frac{P}{(P_O - P)n} = \frac{1}{n_m C} + \frac{(C-1)}{n_m C}\frac{P}{P_O} \qquad 1.7$$

Where P is the equilibrium pressure, P_0 is the saturation pressure, n is the amount adsorbed at the relative pressure P/P_0 and n_m is the monolayer adsorbed gas quantity.

The BET surface areas are calculated based on the adsorbed gas quantity n_m (mol g^{-1}) from experiments. The equation can be expressed as:

$$A_s\,(BET) = n_m N_A a_m \qquad 1.8$$

Where A_s is the BET surface areas, N_A is Avogadro constant and a_m is cross-sectional area of the adsorbate molecule.

The porosity distribution can be calculated from sorption isotherms.

1.4.3.3 Transmission Electron Microscopy

Transmission electron microscopy (TEM) is a technique to observe the morphology and structure of materials with atomic length scale. When the electron hits the martial, some of electrons will transmitted through the sample without any energy loss. These electrons are used to image the material which will detect by a CCD camera. TEM are normally used to illustrate the morphology and structure of COFs.

1.5 Functional covalent organic frameworks for photocatalysis

Covent organic frameworks are crystalline, porous polymers in which organic building blocks are linked by the covalent bonds. The diversity of organic building blocks allows COFs properties, such as light absorption, porosity and charge transport can be precisely tuned for photocatalysis. The inherent porosity enables the rapid photogenerated charges diffusion and high interaction surface for co-catalysts and sacrificial compounds. Highly crystalline frameworks can increase the charge transport and decrease charge trapping to prevent their recombination. Extended π system facilitates the intralayer interactions and inter-layer electronic communications to enhance the charge mobility. COFs were linked by the robust covalent bounds, enabling strong resistant to the solvent, hydrolysis, acid and base environments. These merits make COFs materials are promising candidates for photocatalysis.

1.5.1 COFs for photocatalytic water splitting.

In 2014, Lotsch and co-workers reported a hydrazone linked COF by condensation of 1,3,5-tris(4-formyl-phenyl)triazine and 2,5-diethoxy-terephthalohydrazide.[59] This COF can produce hydrogen under visible light irradiation with addition of metallic platinum. H_2 evolution rate in 52 hours of this COF is 230 μmol h^{-1} g^{-1}, with ascorbic acid as the electron donor. The H_2 evolution activity rate could be enhanced to 1970 μmol h^{-1} g^{-1} using triethanolamine (TEOA) as sacrificial electron donor, however showing a quicker deactivation. This COF exhibits 3 times of hydrogen evolution rate than previous reported organic photocatalysts such as, carbon nitrides and crystalline poly(triazine imide). A series of azine-linked N_x-COFs with triphenylaryl nodes have been made for photocatalytic hydrogen evolution (Figure 1-19).[67] By increasing the number of nitrogen atoms in the central aryl ring, the as formed COFs show the decreasing of dihedral angles between the peripheral phenyl rings and the central aryl ring. These structural changes have huge influence on crystallinity, porosity and electronic properties. The increased planarity for the COFs will enhance the crystallinity and facile exciton migration. Although all the COFs exhibit similar visible optical band gaps of around 2.6−2.7 eV, the HER rate shows 4-fold enhancement with nitrogen atoms increase in the central aryl ring. N_3-COFs is the most active COF in these materials, showing HER rate of 1703 μmol h^{-1} g^{-1} with TEOA as sacrificial donor. In addition, the materials retained their crystallinity after photocatalysis.

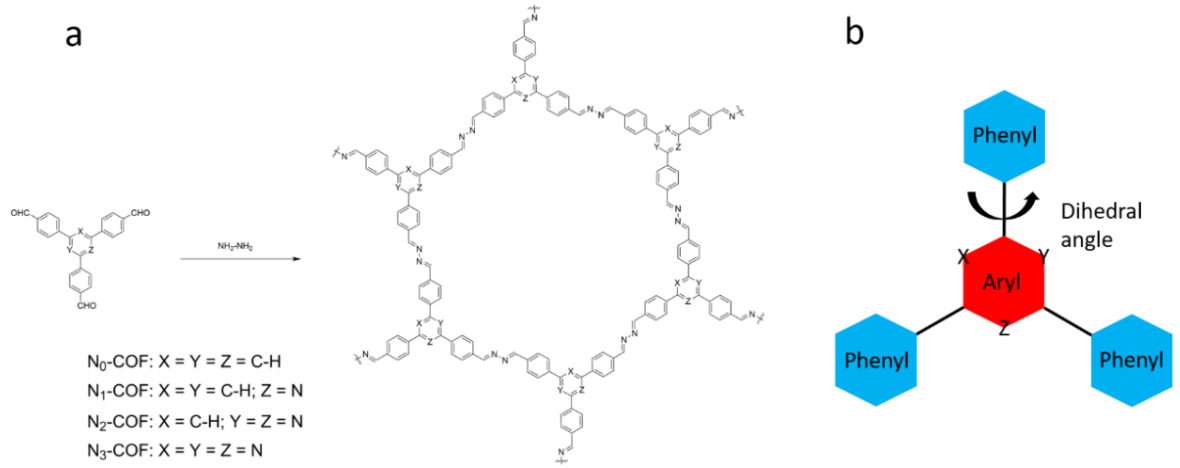

Figure 1-19. (a) Synthesis of Nx–COFs by condense of Nx–aldehydes and hydrazine. (b) Replacement of 'hydrogen atoms' by 'nitrogen atoms' at X, Y and Z will changes the angle between central aryl and peripheral phenyl rings.

Metallic Pt is the most used co-catalysts for HER, because of its low Fermi level and large work function. It served as a proton reduction site for H_2 formation. However, Pt is a rare and expensive element.[68] It is therefore desirable to discover of replacement co-catalysts for HER. Lotsch and co-workers have introduced a series of single site molecular cobaloxime co-catalysts for HER (Figure 1-20).[69] Using N_2-COF as photosensitizer, this heterogonous photocatalytic system shows HER rate of 782 μmol h^{-1} g^{-1} with an apparent quantum efficiency of 0.16% at 400 nm using TEOA as electron donor. More importantly, this system shows higher HER rate than similar system using same mole of metallic Pt when using same measurement conditions (4:1 acetonitrile/water). However, the metallic Pt system has higher HER rate in pure water, and good dispersion of Pt nanoparticles on COF surface. These results indicate that distribution of Pt is sensitive to reaction solvents, which is an important factor for HER. Furthermore, this research also provides the possibility to study the photocatalytic processes. However, molecular co-catalysts can only survive for about 8 hours, which poor stability is the bottleneck for this photocatalytic system.

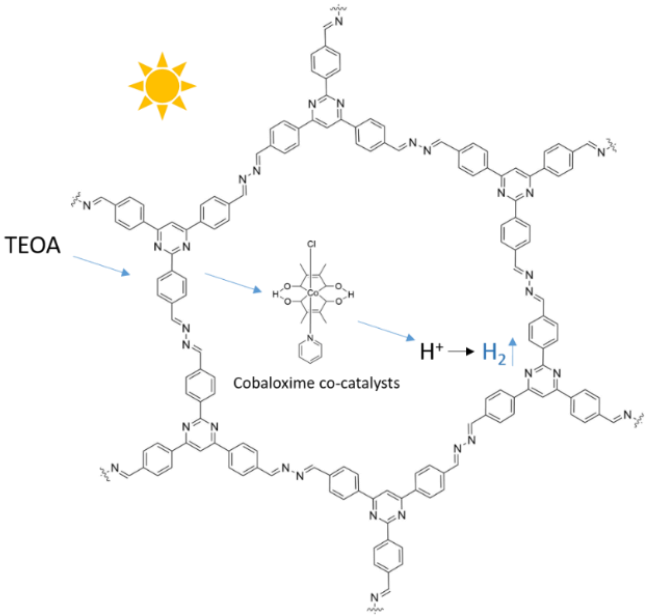

Figure 1-20. Photocatalytic H_2 evolution using N_2- COF as photosensitizer and Co-1 as co-catalyst.[69]

Compared with the boron-linked and imine linked COFs, the *β*-ketoenamine linked COFs show much better chemical stability, thus making these COFs more capable for photocatalysis. The diacetylene moiety is a highly conjugated structure, which shows high charge mobility. Therefore, the diacetylene based materials exhibits great attention in optoelectronics and photocatalysis.[70,71] In 2018, Thoams *et al.* reported a diacetylene COF linked by the *β*-ketoenamine linkages for photocatalytic HER. This COF was the first COF photocatalyst without introducing of any heteronuclear molecular functionalities.[72] The diacetylene functionalized COF shows higher HER rate than the acetylene functionalized COF, reaching 324 μmol h^{-1} g^{-1} under visible light with TEOA as electron donor. Covalent triazine-based frameworks (CTFs) have been received enormous attention, because of their high porosity, high chemical stability and rich nitrogen content.[73–75] However, most of present CTFs are amorphous or relatively low crystalline. Tan and co-workers have developed a strategy to make a series highly crystalline CTFs in mild condition.[76] The as-synthesized CTF-HUSTC1 shows very high HER rate of 5100 μmol h^{-1} g^{-1} under visible light irradiation, which is about 4 times higher than its amorphous analogue.

The recent development of the olefin linked COFs were very promising candidate for photocatalytic HER, because of their fully π-conjugated structure, high porosity and good chemical stability. The recent progress of pyrene based 2D sp^2 COFs for photocatalytic HER

shown the great potential for these COFs for photocatalysis application.[77] Comparing to imine and hydrazone linked COFs, the as-synthesized sp^2 COF shows extended π conjugation, inducing higher HER rate under same condition. In addition, these COFs enable a broad light absorption extended to 800 nm. Another example of sp^2 COF for photocatalytic HER was reported by Zhang and co-workers.[78] They introduce triazine units into 2D sp^2 COFs to increase the planarity of the framework further to boost the electron communications. The $C_{18}N_3$-COF exhibits high HER rate of 14.6 μmol h^{-1} (50 mg materials), which is 4 times higher than $C_{33}N_3$-COF. These results suggest that tuning of molecular knot has huge influence of photocatalytic activity.

1.5.2 COFs for photocatalytic CO_2 reduction.

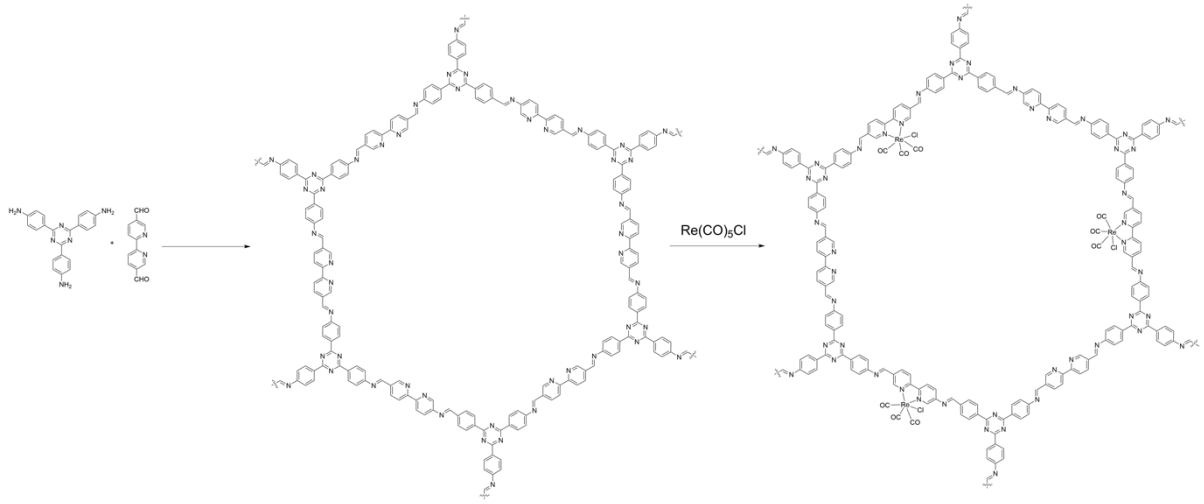

Figure 1-21. Synthesis of bipyridine COF and Re-COF.[79]

COFs are, in principle, ideal materials for CO_2 reduction because the high surface area and tuneable pore sizes can facilitate CO_2 adsorption, diffusion, and activation. In addition, COF with conjugated structure is ideal photosensitizer. Re complex is a series highly active molecular catalysts for photocatalytic CO_2 reduction.[80,81] Combined with COF and Re complex can possibly make stable and highly active hybrid CO_2 reduction catalysts. A COF functionalized with bipyridine moiety was used to anchor the Re complex to make a Re-COF photocatalyst (Figure 1-21).[79] Re-COF photocatalyst can reduce CO_2 to CO with a turnover number (TON) of 48 and a high selectivity (98%), which TON is 22 times higher than the Re homogeneous system. In this system, the Re moiety received the electron to form photoexcited COFs undergo an intramolecular charge transfer process. A similar example was reported by Zou and co-workers, they synthesized a *β*-ketoenamine linked COF bearing with single Ni sites for photocatalytic CO_2 reduction with TEOA as an electron donor.[82] Here, the bipyridine moiety also was used to fix the active metal site into the frameworks. The resulting Ni-TpBpy exhibits excellent CO_2 reduction activity, reaching a CO production rate of 4057 μmol g^{-1} of CO in 5 hours and with a 96% selectivity over H_2 production. Zinc also is an active metal site for CO_2 reduction. As discussed above, following the concept, Zinc has been introduce into COFs by using porphyrin as a 'coordination site'.[83] As formed TTCOF-Zn catalyst can evolve CO 12.33 μmol in 60 hours period with nearly 100% selectivity, using H_2O as an electron donor.

1.6 Project aims

Targeted synthesis of crystalline COF photocatalysts with functional building blocks allows for tuning of the key properties influencing their photocatalytic activities, such as light absorption, charge separation and migration, porosity, mass transport and binding affinity toward water and CO_2. For example, large pores and channels in COFs will benefit the diffusion of reactants and the dispersion of co-catalysts. COFs with a wide range of visible light absorption may be synthesized by incorporating different visible-light-active building blocks. Furthermore, wettable COFs can be obtained using hydrophilic building blocks. Similarly, for CO_2 reduction, the COF photocatalyst's affinity to CO_2 can be enhanced by integrating moieties that have strong interactions with CO_2. In addition, the possibility to engineer their pore sizes and shapes lends COFs great potential to act as a host for molecular co-catalysts, forming heterogeneous systems.

The aim of this project was to synthesize, characterize and investigate COF photocatalysts for hydrogen evolution from water and CO_2 reduction. Structure–activity relationships are probed and interpreted so that fundamental insights and design principles can be drawn to help guide future studies and developments of COF catalysts, as well as their derivatives, for photocatalytic water splitting and CO_2 reduction. The effects of the COF materials morphologies on their catalytic performances are also discussed.

By the start of this Ph.D. project, most of the reported organic photocatalysts had been amorphous polymers, and the literature of crystalline COF materials for photocatalysis was scarce. Sprick *et al.* reported that dibenzo[*b,d*]thiophene sulfone based conjugated linear polymers show excellent activity for photocatalytic hydrogen evolution.[33] In **Chapter 2**, the photoactive dibenzo[*b,d*]thiophene moiety will be introduced into crystalline COFs to investigate the influence of crystallinity, light absorption, wettability, and surface area on hydrogen evolution activity. Taking inspiration from the field of dye-sensitized solar cells, the effect of dye-sensitization on possible enhancement of photocatalytic activity will be studied. The processability of COF photocatalysts has also been investigated in this chapter.

In **Chapter 3**, a series of *β*-ketoenamine COFs, with fluorinated phenyl linkers varying in degrees of fluorination, will be synthesized and explored for photocatalytic hydrogen production. Following the discussions in **Chapter 2,** various factors affecting the COFs'

hydrogen evolution performances will be investigated here, highlighting the trade-off and interplay between those factors.

In **Chapter 4,** molecular catalysts, known for photocatalytic CO_2 reduction, are incorporated into two-dimensional porous covalent organic framework nanosheets (CONs) in order to construct heterogeneous photocatalytic CO_2 reduction systems. A partially-fluorinated CON embedding with single cobalt sites shows a performance comparable with the state-of-the-art heterogeneous catalysts in the literature under similar conditions. The CONs act as a semiconducting support, facilitating electron transfer between the dye and the cobalt centers. CONs outperformed their bulk counterparts in all cases, which suggest a general strategy to enhance the photocatalytic activities of two-dimensional COF catalysts. This research presents a promising strategy for incorporating atomically distributed catalytic metal centers into well-defined pore structures with desirable chemical environments.

1.7 References

1. *Ed. BP Stat. Rev. World Energy*.
2. B. O'Regan, M. Gratzel, *Nature*, 2001, **414**, 338–344.
3. B. Kippelen and J.-L. Brédas, *Energy Environ. Sci.*, 2009, **2**, 241–332.
4. D. Gust, T. A. Moore and A. L. Moore, *Acc. Chem. Res.*, 2009, **42**, 1890–1898.
5. W. J. Youngblood, S.-H. A. Lee, K. Maeda and T. E. Mallouk, *Acc. Chem. Res.*, 2009, **42**, 1966–1973.
6. J. Barber, *Chem. Soc. Rev.*, 2009, **38**, 185–196.
7. J. J. Concepcion, J. W. Jurss, M. K. Brennaman, P. G. Hoertz, A. O. T. Patrocinio, N. Y. Murakami Iha, J. L. Templeton and T. J. Meyer, *Acc. Chem. Res.*, 2009, **42**, 1954–1965.
8. S. Chen, T. Takata and K. Domen, *Nat. Rev. Mater.*, 2017, **2**, 17050.
9. P. Du and R. Eisenberg, *Energy Environ. Sci.*, 2012, **5**, 6012–6021.
10. A. Fushijima and K. Honda, *Nature*, 1972, **238**, 37–38.
11. T. Zhang and W. Lin, *Chem. Soc. Rev.*, 2014, **43**, 5982–5993.
12. Q. Wang, T. Hisatomi, Q. Jia, H. Tokudome, M. Zhong, C. Wang, Z. Pan, T. Takata, M. Nakabayashi, N. Shibata, Y. Li, I. D. Sharp, A. Kudo, T. Yamada and K. Domen, *Nat. Mater.*, 2016, **15**, 1–3.
13. L. Wang, X. Zheng, L. Chen, Y. Xiong and H. Xu, *Angew. Chem. Int. Ed.*, 2018, **57**, 3454–3458.
14. A. Iwase, Y. H. Ng, Y. Ishiguro, A. Kudo and R. Amal, *J. Am. Chem. Soc.*, 2011, **133**, 11054–11057.
15. B. C. R. Ewan and R. W. K. Allen, *Int. J. Hydrogen Energy*, 2005, **30**, 809–819.
16. T. da Silva Veras, T. S. Mozer, D. da Costa Rubim Messeder dos Santos and A. da Silva César, *Int. J. Hydrogen Energy*, 2017, **42**, 2018–2033.
17. P. Nikolaidis and A. Poullikkas, *Renew. Sustain. Energy Rev.*, 2017, **67**, 597–611.
18. A. A. Ismail and D. W. Bahnemann, *Sol. Energy Mater. Sol. Cells*, 2014, **128**, 85–101.
19. V. S. Vyas and B. V. Lotsch, *Nature*, 2015, **521**, 41–42.
20. Z. Wang, C. Li and K. Domen, *Chem. Soc. Rev.*, 2019, **48**, 2109–2125.
21. G. Neshvad and M. Z. Hoffman, *J. Phys. Chem.*, 1989, **93**, 2445–2452.
22. D. T. Whipple and P. J. A. Kenis, *J. Phys. Chem. Lett.*, 2010, **1**, 3451–3458.
23. E. V. Kondratenko, G. Mul, J. Baltrusaitis, G. O. Larrazábal and J. Pérez-Ramírez, *Energy Environ. Sci.*, 2013, **6**, 3112–3135.
24. A. Dhakshinamoorthy, S. Navalon, A. Corma and H. Garcia, *Energy Environ. Sci.*, 2012, **5**, 9217–9233.
25. L. Yuan and Y. J. Xu, *Appl. Surf. Sci.*, 2015, **342**, 154–167.
26. J. Low, B. Cheng and J. Yu, *Appl. Surf. Sci.*, 2017, **392**, 658–686.
27. T. Takata and K. Domen, *ACS Energy Lett.*, 2019, **4**, 542–549.
28. D. S. Su, J. Zhang, B. Frank, A. Thomas, X. Wang, J. Paraknowitsch and R. Schlögl, *ChemSusChem*, 2010, **3**, 169–180.
29. S. Yanagida, A. Kabumoto, K. Mizumoto, C. Pac and K. Yoshino, *J. Chem. Soc. Chem. Commun.*, 1985, 474.
30. X. Wang, K. Maeda, A. Thomas, K. Takanabe, G. Xin, J. M. Carlsson, K. Domen and M. Antonietti, *Nat. Mater.*, 2009, **8**, 76–80.
31. R. S. Sprick, J. X. Jiang, B. Bonillo, S. Ren, T. Ratvijitvech, P. Guiglion, M. A. Zwijnenburg, D. J. Adams and A. I. Cooper, *J. Am. Chem. Soc.*, 2015, **137**, 3265–3270.
32. J. Bi, W. Fang, L. Li, J. Wang, S. Liang, Y. He, M. Liu and L. Wu, *Macromol. Rapid Commun.*, 2015, **36**, 1799–1805.

33. R. S. Sprick, B. Bonillo, R. Clowes, P. Guiglion, N. J. Brownbill, B. J. Slater, F. Blanc, M. A. Zwijnenburg, D. J. Adams and A. I. Cooper, *Angew. Chem. Int. Ed.*, 2016, **55**, 1792–1796.
34. M. Sachs, R. S. Sprick, D. Pearce, S. A. J. Hillman, A. Monti, A. A. Y. Guilbert, N. J. Brownbill, S. Dimitrov, X. Shi, F. Blanc, M. A. Zwijnenburg, J. Nelson, J. R. Durrant and A. I. Cooper, *Nat. Commun.*, 2018, **9**, 1–11.
35. L. Lin, C. Wang, W. Ren, H. Ou, Y. Zhang and X. Wang, *Chem. Sci.*, 2017, **8**, 5506-5511.
36. L. Wang, Y. Wan, Y. Ding, S. Wu, Y. Zhang, X. Zhang, G. Zhang, Y. Xiong, X. Wu, J. Yang, H. Xu, *Adv. Mater.*, 2017, **29**, 1702428
37. J. Yu, K. Wang, W. Xiao and B. Cheng, *Phys. Chem. Chem. Phys.*, 2014, **16**, 11492–11501.
38. H. Shi, G. Chen, C. Zhang and Z. Zou, *ACS Catal.*, 2014, **4**, 3637–3643.
39. X. Yu, Z. Yang, B. Qiu, S. Guo, P. Yang, B. Yu, H. Zhang, Y. Zhao, X. Yang, B. Han and Z. Liu, *Angew. Chem. Int. Ed.*, 2019, **58**, 632–636.
40. C. Yang, W. Huang, L. C. da Silva, K. A. I. Zhang and X. Wang, *Chem. A Eur. J.*, 2018, **24**, 17454–17458.
41. Y. Jin, Q. Wang, P. Taynton and W. Zhang, *Acc. Chem. Res.*, 2014, **47**, 1575–1586.
42. N. W. Ockwig, A. P. Co, M. O. Keeffe, A. J. Matzger and O. M. Yaghi, *Science*, 2005, **310**, 1166–1171.
43. C. S. Diercks and O. M. Yaghi, *Science*, 2017, **355**, eaal1585.
44. H. M. El-Kaderi, J. R. Hunt, J. L. Mendoza-Cortés, A. P. Côté, R. E. Taylor, M. O'Keeffe and O. M. Yaghi, *Science*, 2007, **316**, 268–272.
45. N. Huang, L. Zhai, D. E. Coupry, M. A. Addicoat, K. Okushita, K. Nishimura, T. Heine and D. Jiang, *Nat. Commun.*, 2016, **7**, 1–12.
46. F. J. Uribe-Romo, J. R. Hunt, H. Furukawa, C. Klöck, M. O'Keeffe and O. M. Yaghi, *J. Am. Chem. Soc.*, 2009, **131**, 4570–4571.
47. S. Y. Ding, J. Gao, Q. Wang, Y. Zhang, W. G. Song, C. Y. Su and W. Wang, *J. Am. Chem. Soc.*, 2011, **133**, 19816–19822.
48. T. Y. Zhou, S. Q. Xu, Q. Wen, Z. F. Pang and X. Zhao, *J. Am. Chem. Soc.*, 2014, **136**, 15885–15888.
49. Z. F. Pang, S. Q. Xu, T. Y. Zhou, R. R. Liang, T. G. Zhan and X. Zhao, *J. Am. Chem. Soc.*, 2016, **138**, 4710–4713.
50. T. Ma, E. A. Kapustin, S. X. Yin, L. Liang, Z. Zhou, J. Niu, L. H. Li, Y. Wang, J. Su, J. Li, X. Wang, W. D. Wang, W. Wang, J. Sun and O. M. Yaghi, *Science*, 2018, **361**, 48–52.
51. S. Kandambeth, A. Mallick, B. Lukose, M. Mane, T. Heine, and R. Banerjee, *J. Am. Chem. Soc.*, 2012, **134**, 19524–19527.
52. S. Chandra, S. Kandambeth, B. P. Biswal, B. Lukose, S. M. Kunjir, M. Chaudhary, R. Babarao, T. Heine and R. Banerjee, *J. Am. Chem. Soc.*, 2013, **135**, 17853–17861.
53. B. Biswal, S. Chandra, S. Kandambeth, B. Lukose, T. Heine and R. Banerjee, *J. Am. Chem. Soc.*, 2013, **135**, 5328-5331.
54. S. Kandambeth, B. P. Biswal, H. D. Chaudhari, K. C. Rout, S. Kunjattu H., S. Mitra, S. Karak, A. Das, R. Mukherjee, U. K. Kharul and R. Banerjee, *Adv. Mater.*, 2017, **29**, 1–9.
55. Q. Fang, Z. Zhuang, S. Gu, R. B. Kaspar, J. Zheng, J. Wang, S. Qiu and Y. Yan, *Nat. Commun.*, 2014, **5**, 4503.
56. E. Jin, M. Asada, Q. Xu, S. Dalapati, M. A. Addicoat, M. A. Brady, H. Xu, T. Nakamura, T. Heine, Q. Chen and D. Jiang, *Science*, 2017, **357**, 673–676.
57. H. Lyu, C. S. Diercks, C. Zhu and O. M. Yaghi, *J. Am. Chem. Soc.*, 2019, **141**, 6848–

6852.
58. S. Dalapati, S. Jin, J. Gao, Y. Xu, A. Nagai and D. Jiang, *J. Am. Chem. Soc.*, 2013, **135**, 17310–17313.
59. L. Stegbauer, K. Schwinghammer and B. V. Lotsch, *Chem. Sci.*, 2014, **5**, 2789–2793.
60. M. Liu, K. Jiang, X. Ding, S. Wang, C. Zhang, J. Liu, Z. Zhan, G. Cheng, B. Li, H. Chen, S. Jin and B. Tan, *Adv. Mater.*, 2019, **31**, 1807865
61. B. Zhang, M. Wei, H. Mao, X. Pei, S. A. Alshmimri, J. A. Reimer and O. M. Yaghi, *J. Am. Chem. Soc.*, 2018, **140**, 12715–12719.
62. P. J. Waller, S. J. Lyle, T. M. Osborn Popp, C. S. Diercks, J. A. Reimer and O. M. Yaghi, *J. Am. Chem. Soc.*, 2016, **138**, 15519–15522.
63. F. Haase, E. Troschke, G. Savasci, T. Banerjee, V. Duppel, S. Dörfler, M. M. J. Grundei, A. M. Burow, C. Ochsenfeld, S. Kaskel and B. V Lotsch, *Nat. Commun.*, 2018, **9**, 2600.
64. X. Li, C. Zhang, S. Cai, X. Lei, V. Altoe, F. Hong, J. J. Urban, J. Ciston, E. M. Chan and Y. Liu, *Nat. Commun.*, 2018, **9**, 1–8.
65. G. Lin, H. Ding, D. Yuan, B. Wang and C. Wang, *J. Am. Chem. Soc.*, 2016, **138**, 3302–3305.
66. R. A. W. Sing, K.S.W., Everet, D. H., Haul, *Pure Appl. Chem.*, 1985, **57**, 603–619.
67. V. S. Vyas, F. Haase, L. Stegbauer, G. Savasci, F. Podjaski, C. Ochsenfeld and B. V Lotsch, *Nat. Commun.*, 2015, **6**, 8508.
68. J. Yang, D. Wang, H. Han and C. Li, *Acc. Chem. Res.*, 2013, **46**, 1900–1909.
69. T. Banerjee, F. Haase, G. Savasci, K. Gottschling, C. Ochsenfeld and B. V. Lotsch, *J. Am. Chem. Soc.*, 2017, **139**, 16228-16234.
70. S. Ghosh, N. A. Kouamé, L. Ramos, S. Remita, A. Dazzi, A. Deniset-Besseau, P. Beaunier, F. Goubard, P. H. Aubert and H. Remita, *Nat. Mater.*, 2015, **14**, 505–511.
71. M. Planells, A. Abate, D. J. Hollman, S. D. Stranks, V. Bharti, J. Gaur, D. Mohanty, S. Chand, H. J. Snaith and N. Robertson, *J. Mater. Chem. A*, 2013, **1**, 6949–6960.
72. P. Pachfule, A. Acharjya, J. Roeser, T. Langenhahn, M. Schwarze, R. Schomaecker, A. Thomas and J. Schmidt, *J. Am. Chem. Soc.*, 2018, **140**, 1423-1427
73. P. Kuhn, M. Antonietti and A. Thomas, *Angew. Chem. Int. Ed.*, 2008, **47**, 3450–3453.
74. K. Sakaushi and M. Antonietti, *Acc. Chem. Res.*, 2015, **48**, 1591–1600.
75. K. Wang, L. M. Yang, X. Wang, L. Guo, G. Cheng, C. Zhang, S. Jin, B. Tan and A. Cooper, *Angew. Chem. Int. Ed.*, 2017, **56**, 14149–14153.
76. M. Liu, Q. Huang, S. Wang, Z. Li, B. Li, S. Jin and B. Tan, *Angew. Chem. Int. Ed.*, 2018, **57**, 11968–11972.
77. E. Jin, Z. Lan, Q. Jiang, K. Geng, G. Li, X. Wang and D. Jiang, *Chem*, 2019, **5**, 1632–1647.
78. S. Wei, F. Zhang, W. Zhang, P. Qiang, K. Yu, X. Fu, D. Wu, S. Bi and F. Zhang, *J. Am. Chem. Soc.*, 2019, **141**, 14272–14279.
79. S. Yang, W. Hu, X. Zhang, P. He, B. Pattengale, C. Liu, M. Cendejas, I. Hermans, X. Zhang, J. Zhang and J. Huang, *J. Am. Chem. Soc.*, 2018, **140**, 14614–14618.
80. H. Hori, F. P. A. Johnson, K. Koike, O. Ishitani and T. Ibusuki, *J. Photochem. Photobiol. A Chem.*, 1996, **96**, 171–174.
81. A. Nakada, K. Koike, T. Nakashima, T. Morimoto and O. Ishitani, *Inorg. Chem.*, 2015, **54**, 1800–1807.
82. W. Zhong, R. Sa, L. Li, Y. He, L. Li, J. Bi, Z. Zhuang, Y. Yu and Z. Zou, *J. Am. Chem. Soc.*, 2019, **141**, 7615–7621.
83. M. Lu, J. Liu, Q. Li, M. Zhang, M. Liu, J.-L. Wang, D.-Q. Yuan and Y.-Q. Lan, *Angew. Chem. Int. Ed.*, 2019, **58**, 12392–12397.

Chapter 2

Sulfone-containing covalent organic frameworks for photocatalytic hydrogen evolution from water

2.1 Author contributions

All COF materials were synthesized by the thesis author. P7 and P10 were prepared by Dr Reiner Sebastian Sprick. Prof Yongzhen Wu and Prof Weihong Zhu synthesized the **WS5F** dye and characterized it. Modelling calculations was performed by Dr Linjiang Chen and Dr Martijn A. Zwijnenburg. Dr Samantha Y. Chong carried out PXRD analyses. Dr Marc A. Little carried out single-crystal X-ray structure analysis. Dr Reiner Sebastian Sprick measured the TCSPC experiments. Dr Yong Yan collected the water sorption isotherms. Rob Clowes performed the gas adsorption measurements. Dr Matthew Bilton captured the TEM images.

This chapter is based on the following publication: X. Wang, L. Chen, S. Y. Chong, M. A. Little, Y. Wu, W. Zhu, R. Clowes, Y. Yan, M. A. Zwijnenburg, R. S. Sprick, A. I. Cooper. *Nat. Chem.*, **10**, 1180.

2.2 Introduction

A previous work was published in our group that investigated highly active novel polymer photocatalysts for photocatalytic hydrogen evolution. This research indicated that the **P7** polymer based on dibenzo[*b*,*d*]thiophene sulfone units shows an hydrogen evolution rate of 1492 μmol g^{-1} h^{-1} under visible light (≥ 420 nm) using TEA as an electron donor.[1] The external quantum efficiency (EQE, incident photon to hydrogen conversion yield) of **P7** was 2.3% at 420 nm, which was much higher than platinized commercial pristine carbon nitride. Further research for the homopolymer of dibenzo[*b*,*d*]thiophene sulfone moiety (**P10**) exhibited a higher hydrogen evolution rate and quantum efficiency than **P7**, reaching of 3260 μmol g^{-1} h^{-1} under visible light (≥ 420 nm) with an EQE of 11.6% at 420 nm.[2] This research also indicated that sulfonated polymers with highly polar environment can accelerate the proton and charge transfer steps in the reaction, suggesting that sulfone moieties are promising candidates to make organic photocatalysts for photoinduced proton reduction. COFs are a class of porous and crystalline organic materials, which properties can be fine-tuned by using different moieties. With suitable building blocks, COFs have been proved to have high charge-carrier mobilities, which will benefit to photocatalytic activity.[3] Bearing this in mind, we introduced dibenzo[*b*,*d*]thiophene sulfone moieties into COFs to make photocatalysts.

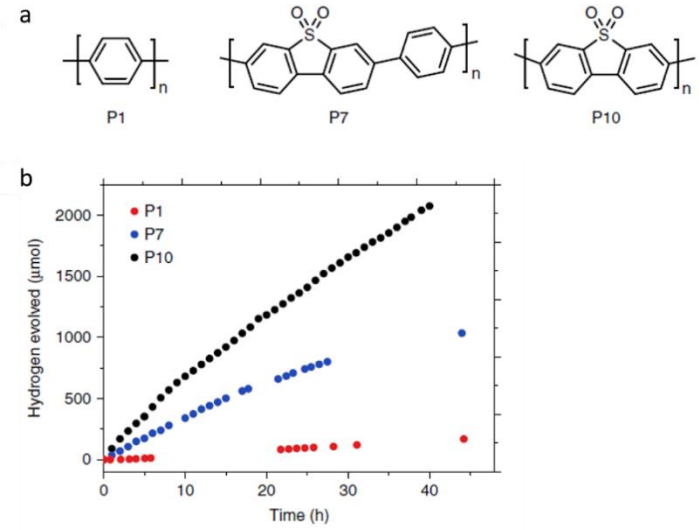

Figure. 2-1 (a) Chemical structures of polymer photocatalysts **P1**, **P7**, and **P10**. (b) Time course for photocatalytic hydrogen evolution under visible light illumination (λ > 420 nm) using **P1**, **P7** and **P10**.[2]

2.3 COFs design, synthesis and characterization

2.3.1 Influence of linkages and linkers

For sacrificial hydrogen evolution, electron donors are used in the reaction system, resulting normally acidic or basic catalytic environments. Thus, photocatalysts should be robust in acid and (or) base. As the pervious discussion, a class of COFs linked by *β*-ketoenamine linkage shows relevant good stability in acid and base.[4] Therefore, in this chapter, *β*-ketoenamine linked COFs were studied for photocatalytic hydrogen evolution. To make a *β*-ketoenamine linked COFs, 1,3,5-triformylphloroglucinol and an amine monomer was used. As shown in Figure 2-2, sulfonated COF (**S-COF**) was synthesized via a Schiff-base condensation reaction of 1,3,5-triformylphloroglucinol (**TFG**) with 3,7-diaminodibenzo[*b*,*d*]thiophene sulfone (**SA**).

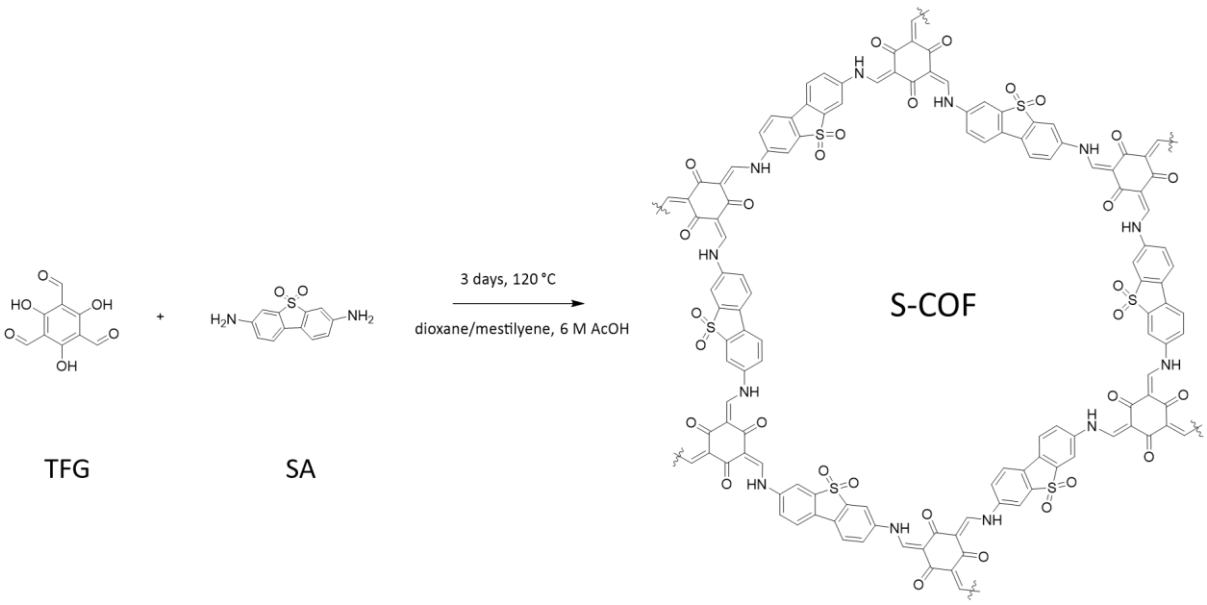

Figure 2-2. Scheme of the synthesis of **S-COF**.

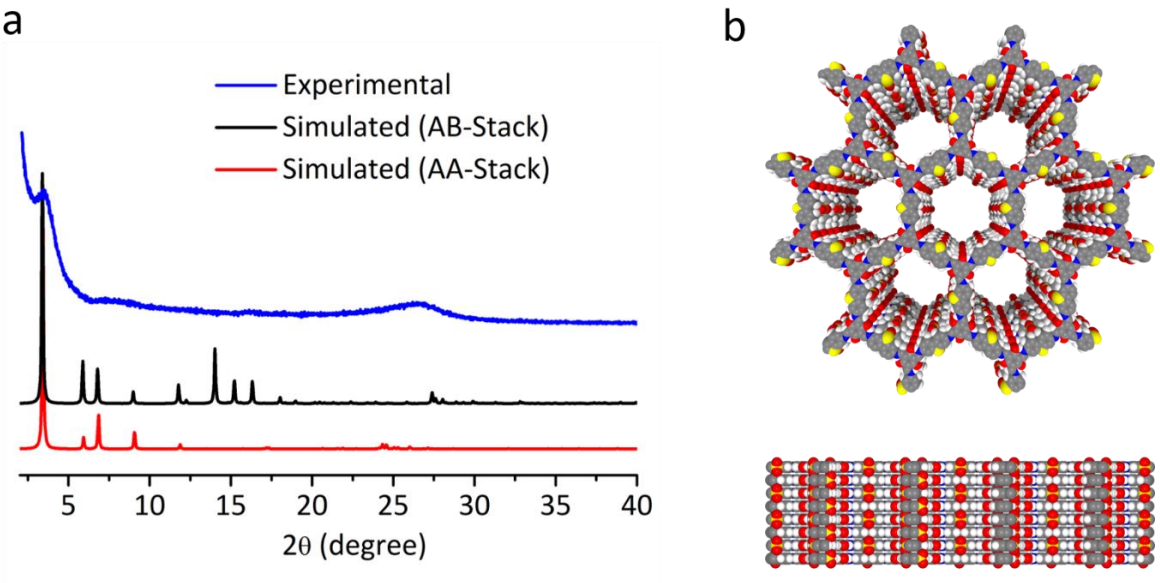

Figure 2-3. (a) Experimental powder X-ray diffraction pattern of **S-COF** (blue) and simulated PXRD pattern (red and black). (b) Structural models for **S-COF** with perfectly eclipsed AA stacking patterns, shown parallel to the pore channel along the crystallographic c axis (top) and parallel to the hexagonal layers (bottom). The pores of COF are lined with oxygen atoms. Grey, white, blue, red and yellow atoms represent carbon, hydrogen, nitrogen, oxygen and sulfur, respectively.

Based on powder X-ray diffraction (PXRD) data (Figure 2-3a), **S-COF** showed broad diffraction peaks at 3.84 and 26.36°, which is consistent with a primitive hexagonal structure with an in-plane lattice parameter of 27.44 Å and a π-stacking distance of ~3.7 Å. Furthermore, **S-COF** was proposed to have AA layer stackings (Figure 2-3b), rather than AB stacking. Although **S-COF** shows crystalline structure, the crystallinity of this material is relatively low. Highly crystalline sulfonated COF was expected to make. From single crystal structure of **SA**, the angle between the C–N bonds in the **SA** monomer is ~163° (Figure 2-4a). Because of this non-linear feature, which will induce large strain in the extend structure, resulting low crystalline **S-COF**. Moreover, since sulfone is not a planar moiety, which will cause large steric repulsion between the adjacent layers, resulting a less stacked conformation and lower crystalline framework. However, a fused and parallel sulfone moiety can stack the sulfone moiety with alternating sides of the stacking, which allowing for close stacking. A parallel, fused and extended amine monomer, 3,9-diamino-benzo[1,2-*b*:4,5-*b*']bis[1]benzothiophene-5,5,11,11-tetraoxide (**FSA**), has been made to synthesize more crystalline COF (Figure 2-4b).

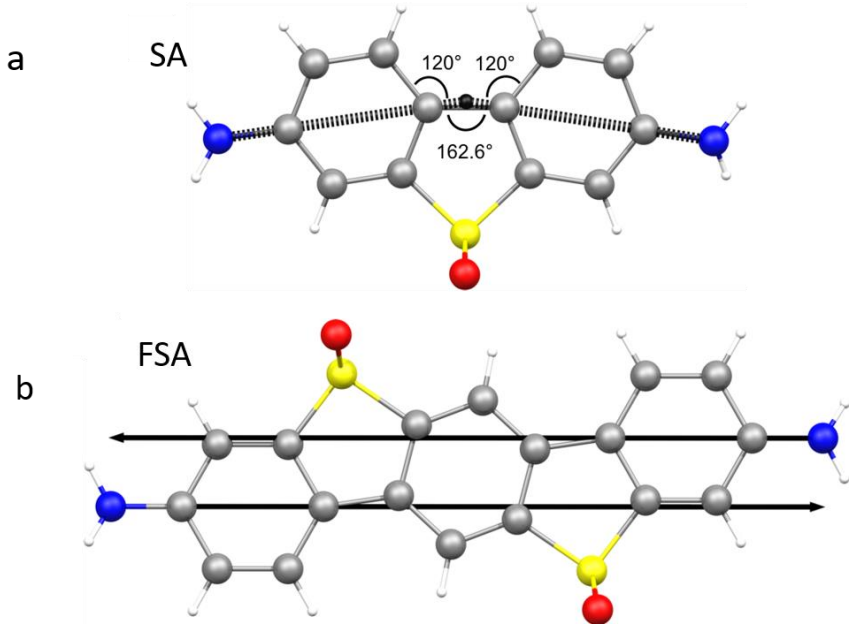

Figure 2-4. Geometry of aryl-NH_2 groups in the single crystal structure of (a) **SA** and (b) **FSA**.

FS-COF was synthetized by using **FSA** and **TFG** (Figure 2-5). As shown in Figure 2-6, **FS-COF** was more crystalline than **S-COF**. This might be because the using of parallel monomer (**FSA**) will make the regular hexagonal framework in **FS-COF** which was less sensitive than **S-COF** to the insertion of linkers in the 'wrong' geometry. Stacking between the fused and planar **FSA** linkers are more effective which can also be helpful to stabilize the frameworks.[5]

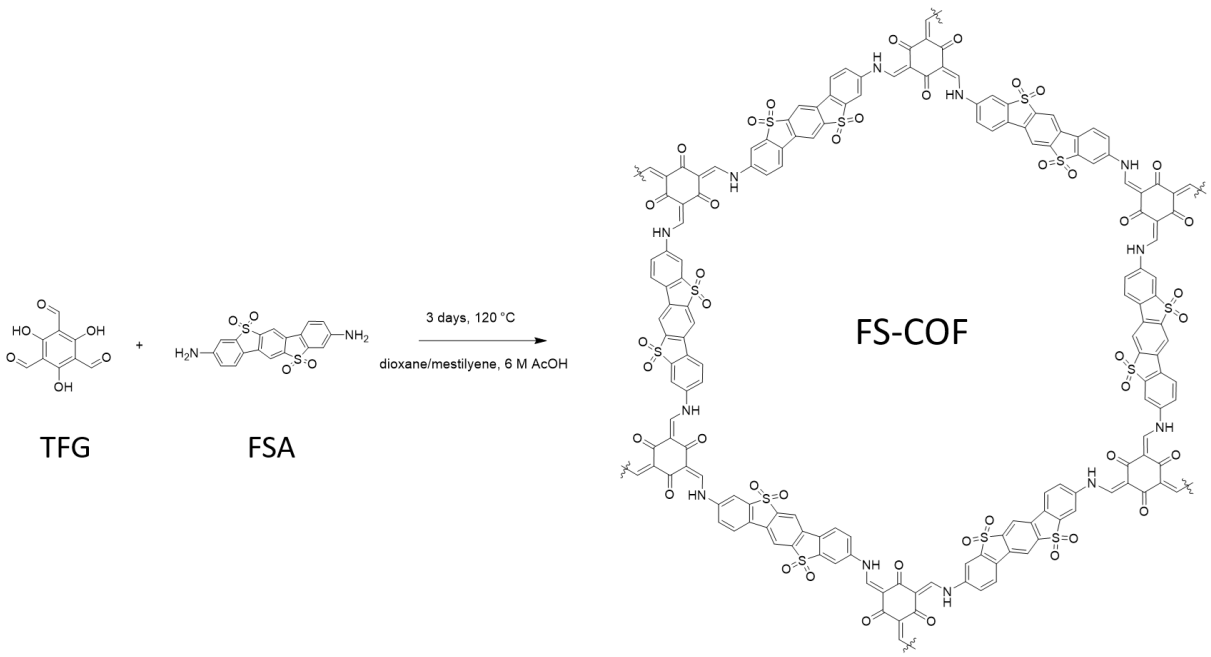

Figure 2-5. Scheme of the synthesis of **FS-COF**.

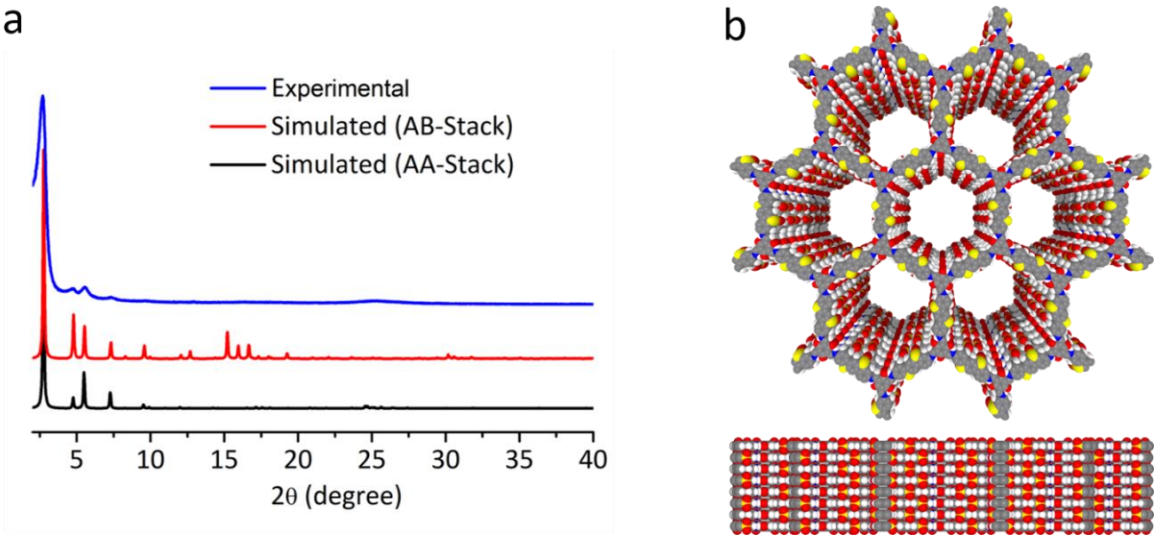

Figure 2-6. (a) Experimental powder X-ray diffraction pattern of **FS-COF** (blue) and simulated PXRD pattern (red and black). (b) Structural models for **FS-COF** with perfectly eclipsed AA stacking patterns, shown parallel to the pore channel along the crystallographic c axis (top) and parallel to the hexagonal layers (bottom). The pores of COF are lined with oxygen atoms. Grey, white, blue, red and yellow atoms represent carbon, hydrogen, nitrogen, oxygen and sulfur, respectively.

FS-COF shows diffraction peaks at 2.71, 4.73, 5.52 and 7.35° which were assigned to the (100), (110), (200) and (210) planes, respectively (Figure 2-6a). The broad peak at around 25.19° was corresponded to a layer spacing of 3.53 Å. Le Bail refinement for **FS-COF** agree well with the experimental values, which was consistent with a primitive hexagonal lattice with unit cell parameters (a = b = 36.205(6) Å, c = 7.285(5) Å) related to the AA stacking mode of **FS-COF**. However, there are a variety of possible AA stacking structures (Figure 2-7), such as idealised model in which layers are planar and the sulfone groups adopt opposing orientations in adjacent layers. We cannot distinguish between them from X-ray data (Figure 2-7a, b). These small structure changes will not greatly affect properties such as porosity, but have huge impact on the electronic structure of **FS-COF** which will be discussed later. Fused sulfonated polymer **FS-P** was made as an amorphous analogue for **FS-COF** to probe the influence of crystallinity.

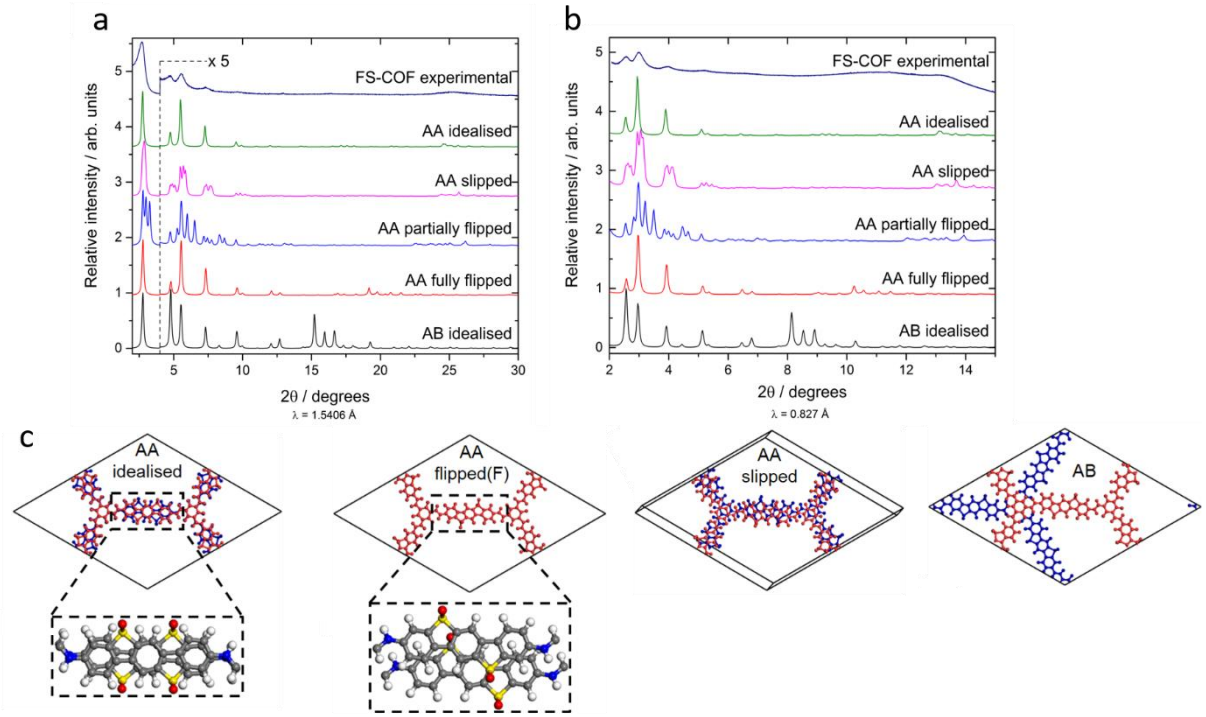

Figure 2-7. Comparison of experimental and simulated powder X-ray diffraction profiles calculated for several possible stacking models, based on the similarity with the (a) laboratory and (b) synchrotron diffraction patterns. (c) Different possible proposed models.

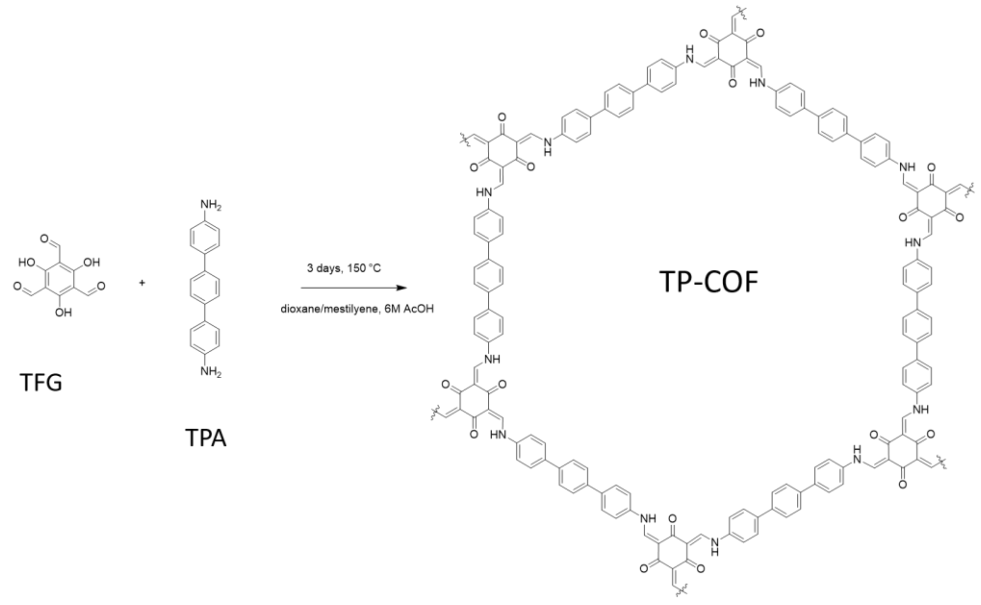

Figure 2-8. Scheme of the synthesis of **TP-COF**.

For comparison, an unfunctionalized analogue **TP-COF** was synthesized from 4, 4''-diamino-*p*-terphenyl (**TPA**) and **TFG**, which has been reported previously.[6] **TP-COF** is essentially **FS-COF** minus the sulfone moieties (Figure 2-8), and it has a 3.0 nm mesoporous structure. As

shown in Figure 2-9a, **TP-COF** is less crystalline than **FS-COF**, exhibiting a broad diffraction peak at 2.73°. Similar to **FS-COF** and **S-COF**, **TP-COF** also refer to AA stacking patterns (Figure 2-9b).

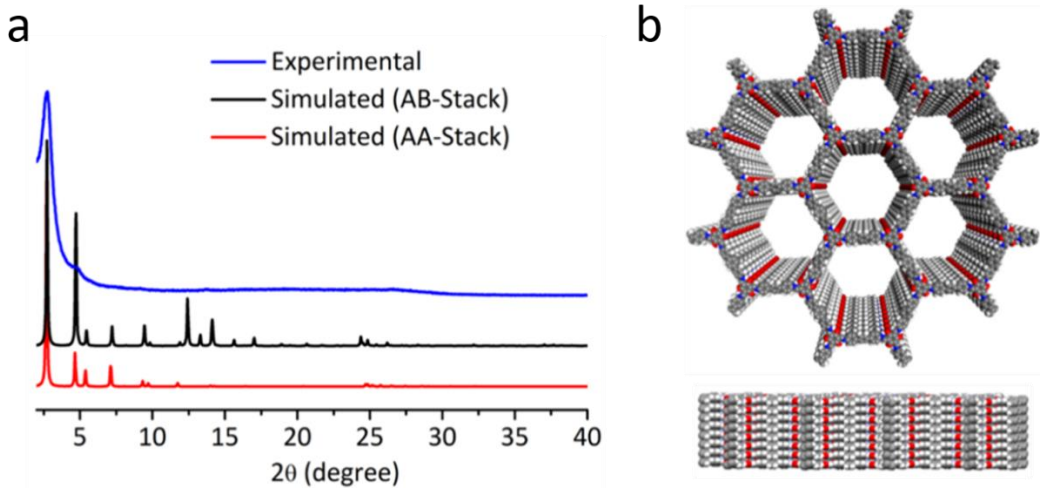

Figure 2-9. (a) Experimental powder X-ray diffraction pattern of **TP-COF** (blue) and simulated PXRD (red and black). (b) Structural models for **TP-COF** with perfectly eclipsed AA stacking patterns, shown parallel to the pore channel along the crystallographic c axis (top) and parallel to the hexagonal layers (bottom). The pores of COF are lined with oxygen atoms. Grey, white, blue and red atoms represent carbon, hydrogen, nitrogen and oxygen, respectively.

2.3.2 COF characterization

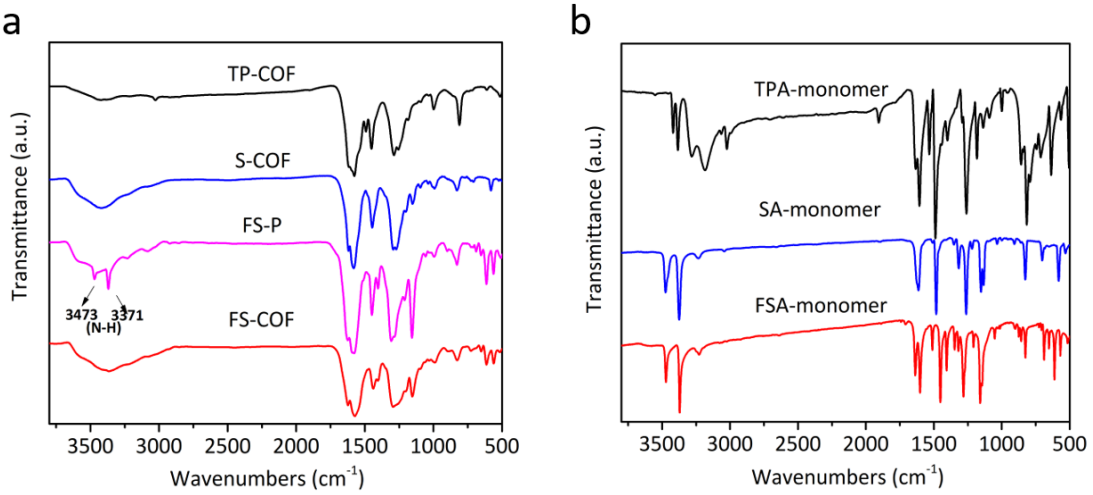

Figure 2-10. (a) FT-IR spectra of **FS-COF**, **FS-P**, **S-COF** and **TP-COF**. (b) FT-IR spectra of **FSA**, **SA** and **TPA** monomers.

All COF materials and analogous amorphous networks were insoluble in common organic solvents. Fourier transform infrared spectra (FT-IR) of **FS-COF** show the disappearance of the amine bands (3473 and 3371 cm^{-1} in **FSA**). Similar observations were made for **S-COF** and **TP-COF**. However, **FS-P** exhibts the remains of amine bands, which suggest that unreacted **FSA** was in polymer. Thermogravimetric analysis (TGA) showed that all materials are stable up to ~375 °C in air, indicating good thermal stability. All COFs exhibit near total decomposition with less than 1% incombustible residue at 600 °C (Figure 2-11).

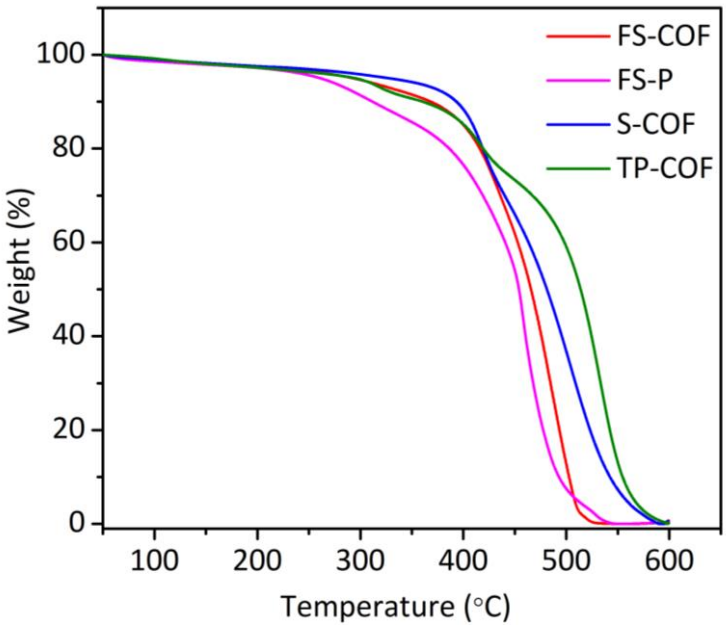

Figure 2-11. (a) TGA of **FS-COF**, **FS-P**, **S-COF** and **TP-COF** in air.

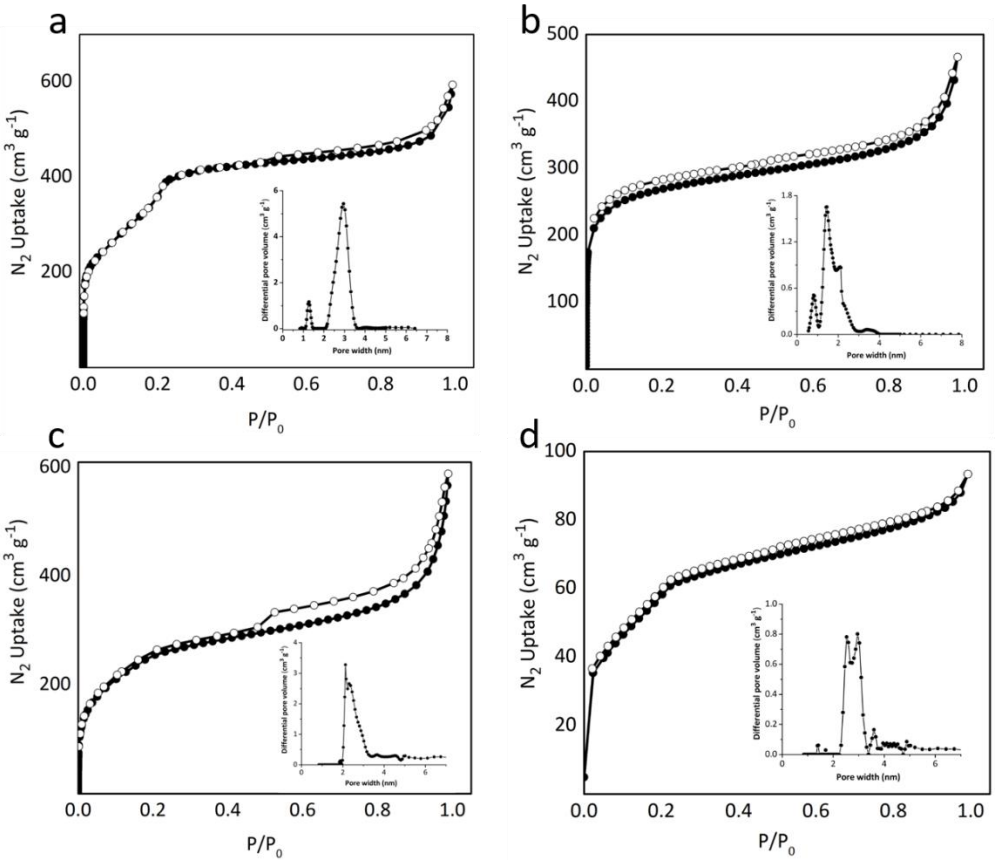

Figure 2-12. (a) Nitrogen adsorption/desorption isotherms for (a) **FS-COF**, (b) **S-COF** (c) **TP-COF** and (d) **FS-P** recorded at 77 K (filled symbols = adsorption; open symbols = desorption). Insets, pore size distribution profiles of **FS-COF** calculated by NL-DFT.

Nitrogen sorption measurements at 77.3 k were carried out to assess the porosity of these COFs. All COFs gave rise to nitrogen isotherms with shapes attributed to mesoporosity and multilayer pore filling (figure 2-12). The Brunauer–Emmett–Teller (BET) surface areas of **FS-COF**, **S-COF** and **TP-COF** were found to be 1288, 985 and 919 $m^2\ g^{-1}$, respectively. Amorphous analogue **FS-P** shows much lower BET surface (209 $m^2\ g^{-1}$) than **FS-COF**, which can be attributed to more defects in **FS-P**. The experimental surface area for **FS-COF** was 78% of the calculated nitrogen-accessible surface area for the idealized, eclipsed (AA stacking) structure shown in Figure 2-6b (1652 $m^2\ g^{-1}$). The experimental surface areas for **S-COF** and **TP-COF** were less than the idealized, calculated values (1690 and 2172 $m^2\ g^{-1}$ for **S-COF** and **TP-COF**). The pore diameters for **FS-COF**, **S-COF** and **TP-COF** were 27.6, 22.8 and 29.0 Å, respectively, which fitted by nonlocal density functional theory (DFT) models to the N_2 isotherms. The hysteresis was observed in **TP-COF** isotherm, this phenomenon can be

attributed to condensable gases in mesopores. However, hysteresis was not shown in **FS-COF** isotherm, which might because of heterogeneity of surface.

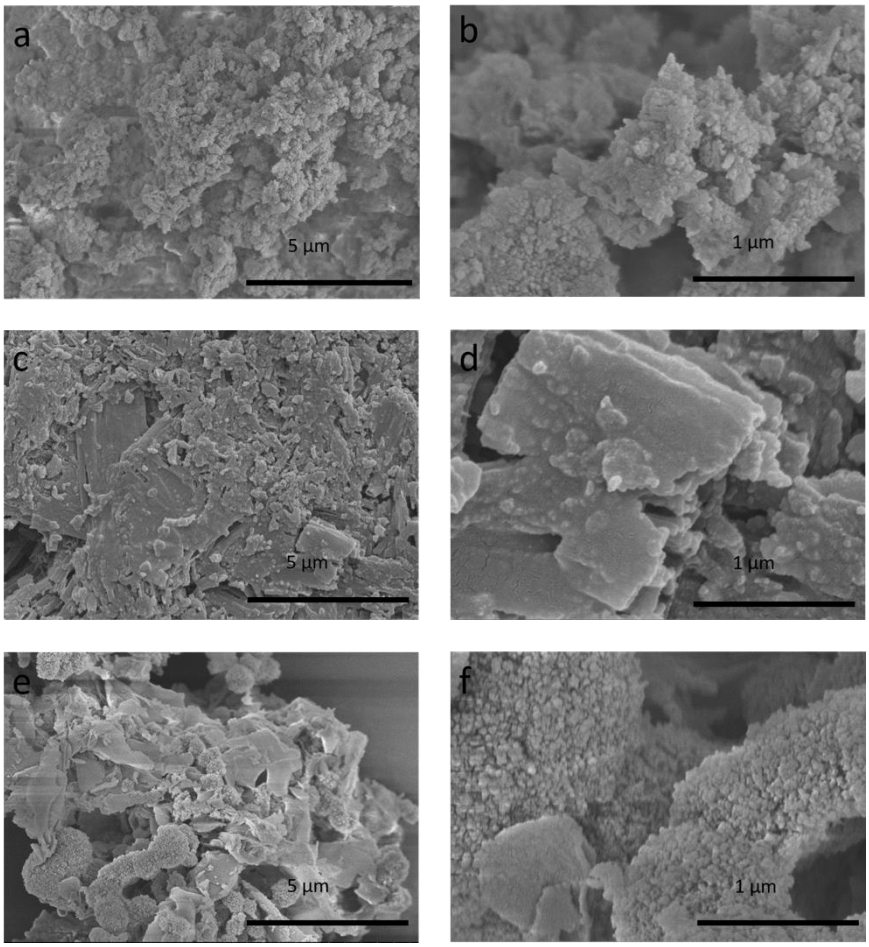

Figure 2-13. SEM images of (a, b) **FS-COF**, (c, d) **S-COF** and (e, f) **TP-COF**.

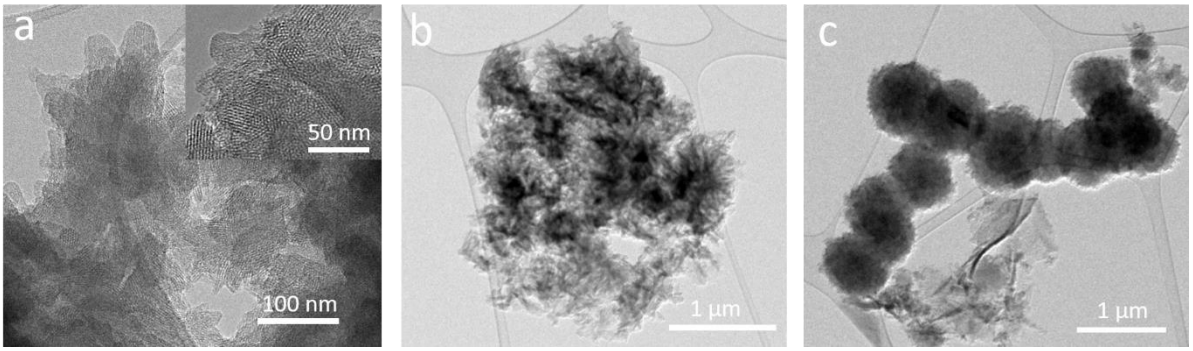

Figure 2-14. TEM images for (a) **FS-COF**, (b) **S-COF** and (c) **TP-COF**.

SEM images show a change in morphology from purely microball-like agglomerates in **FS-COF** to flake-like morphology in **S-COF** (Figure 2-13). SEM images for **TP-COF** shows hybrid compositions with both microball-like agglomerates and flake-like morphology. The

structure and morphology of all COFs was further investigated by transmission electron microscopy (TEM) analysis. TEM images of **FS-COF** (Figure 2-14a) exhibits an ordered, hexagonal pore structure with a periodicity of ~3.0 nm, which can be attributed to the in-plane pore channels of 3.2 nm in the proposed AA-stacked COF structure (Figure 2-6b). However, **S-COF** and **TP-COF** do not show such clear, ordered domains (Figure 2-14b, c).

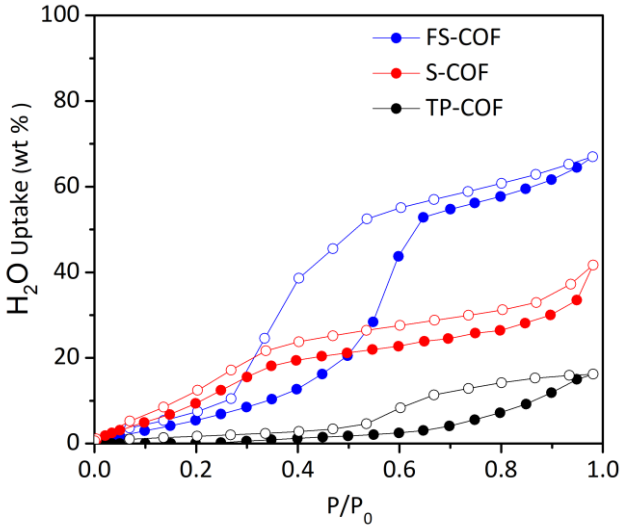

Figure 2-15. Water adsorption isotherms (filled symbols) and desorption isotherms (open symbols) for **FS-COF**, **S-COF** and **TP-COF**, measured at 293 K. P P_0^{-1}, vapour pressure over saturation pressure.

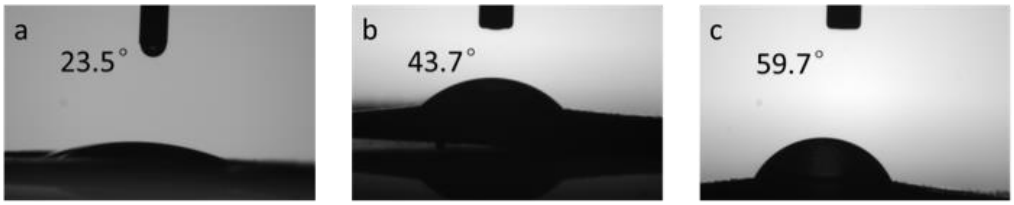

Figure 2-16. Water contact angles for pressed pellets of (a) **FS-COF**, (b) **S-COF** and (c) **TP-COF** at room temperature in air.

Water vapour isotherms for **FS-COF**, **S-COF** and **TP-COF** reveal different shapes and water capacities according to their porosity and pore wettability (Figure 2-15). Both **FS-COF** and **S-COF** shows water uptakes at low pressures ($P/P_0 < 0.4$) and the adsorption process is initially driven by interactions between water molecules and strong adsorption sites. **FS-COF** has a type IV isotherm with a large hysteresis loop due to water condensation within its mesopores.

For **TP-COF**, there is no noticeable uptake up to P/P_0 = 0.5, attributed to the relatively weak water–framework interaction in the absence of favourable adsorption sites. Functionalized **FS-COF** and **S-COF** adsorb 67 and 42 wt% water at 22.9 mbar and 293 K; however, **TP-COF** adsorbs only 16 wt% water under the same conditions. The contact angles measurements show that sulfonated **FS-COF** and **S-COF** has low contact angles with pure water, which were 23.6° and 43.7° respectively. These contact angles are lower than **TP-COF** (59.7°), most organic polymers (60–110°), and poly(vinyl alcohol) (~51°)[7]. Materials wettability is a critical factor for aqueous photocatalysis. This is because it will influence favourable interactions with water and the sacrificial donor and particle dispersibility, which will further influence the hydrogen production activity. The water isotherm and contact angle measurement for **FS-COF** shows that the internal pore and external surface of the material is accessible to water, thus potentially increasing the number of potential sites for photocatalytic water reduction.

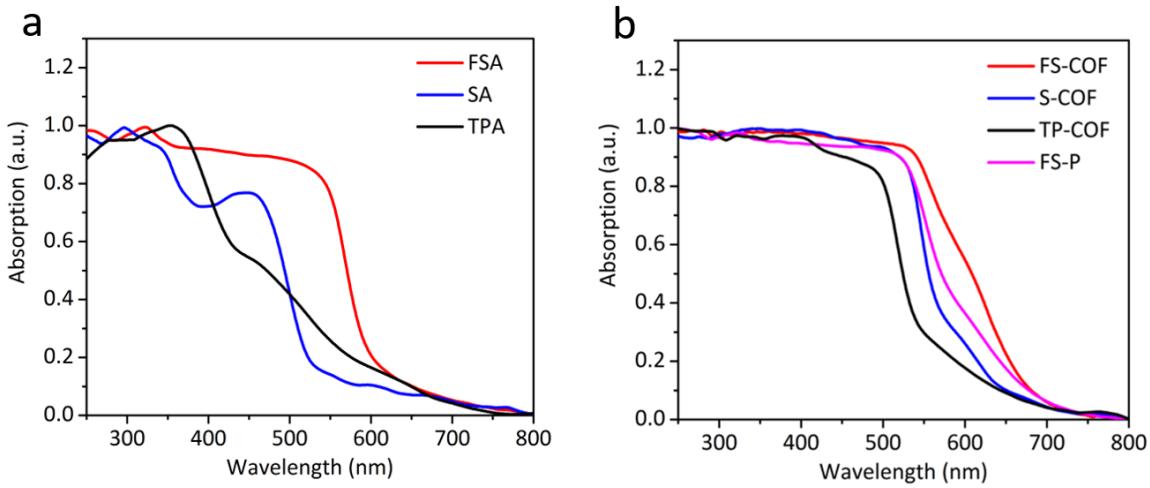

Figure 2-17. (a) UV–Vis absorption spectra of **FSA**, **SA** and **TPA** monomers measured in the solid state. (b) UV–Vis absorption spectra of **FS-COF**, **FS-P**, **S-COF** and **TP-COF** measured in the solid state.

UV–Vis reflectance spectra of the monomers and COFs were recorded in the solid state. The absorption onset for **FS-COF**, **S-COF** and **TP-COF** was measured to be 670, 590 and 540 nm respectively (Figure 2-17). Compared to COFs, the absorption onsets for **FSA**, **SA** and **TPA** are blueshifted by 70, 45 and 90 nm, respectively. **FS-P** shows a redshifted absorption onset compared to the diamine monomer but exhibits a blueshift compared with **FS-COF** (Figure 2-17b). The absorption onset for **FS-COF** also shows a significant redshift (by 210 and 184 nm) to linear dibenzo[*b*,*d*]thiophene sulfone-based polymers, **P7** and **P10**, respectively.[2]

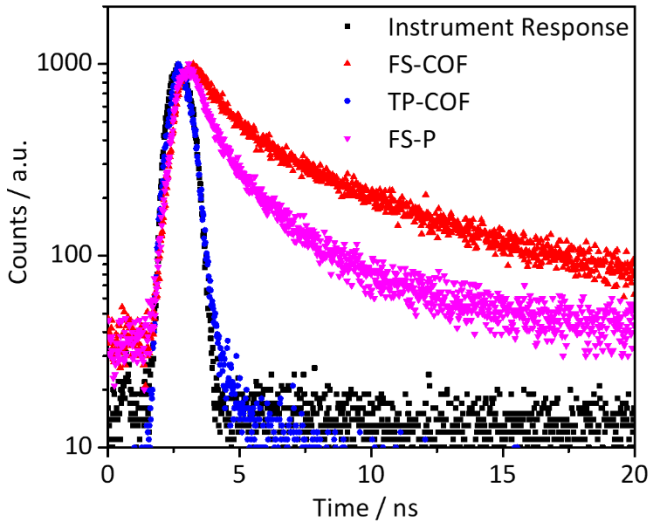

Figure 2-18. Time-correlated single-photon counting experiments for **TP-COF**, **FS-COF** and **FS-P** in water. Samples were excited with a λ_{exc} = 370.5 nm laser and emission was measured at λ_{em} = 550 nm.

Time-correlated single-photon counting (TCSPC) measurements were carried out to estimate the excited-state lifetimes for these materials in aqueous suspensions (Figure 2-18). The average weighted lifetime of **FS-COF**, **TP-COF** and **FS-P** was estimated to be τ_{avg} = 5.56, 0.25 and 2.21 ns, respectively. The significantly longer lifetime for **FS-COF** will potentially induce to better charge stabilization, which can increase the photocatalytic activity.

2.4 COFs for hydrogen evolution

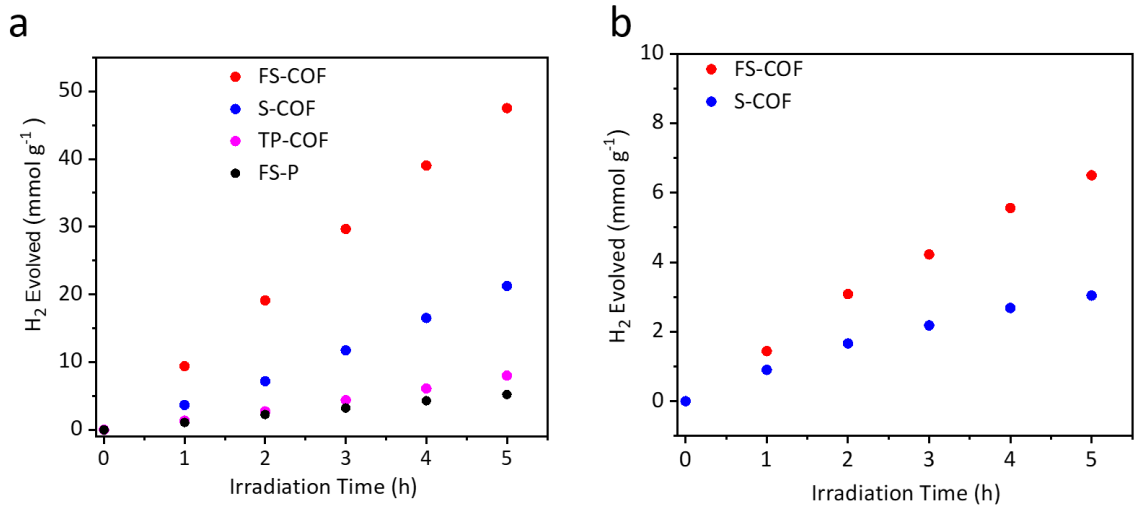

Figure 2-19. (a) Time course for photocatalytic H_2 production using visible light for **FS-COF**, **S-COF**, **TP-COF** and **FS-P** (5 mg catalyst in water, 5 μL (8 wt% H_2PtCl_6), 0.1 M ascorbic acid, λ > 420 nm). (b) Time course for photocatalytic H_2 production using visible light for (a) **FS-COF**, **S-COF** and **TP-COF** (5 mg catalyst in water, 0.1 M ascorbic acid, λ > 420 nm).

Photocatalytic water reduction for all COFs were measured using ascorbic acid as a sacrificial electron donor and Pt as a co-catalyst. All materials evolved hydrogen under visible light irradiation (λ > 420 nm, Figure 2-19a). The mass-normalized hydrogen evolution rate for **FS-COF**, **S-COF** and **TP-COF** were determined to be 10.1, 4.44 and 1.6 mmol g^{-1} h^{-1}, respectively. Amorphous **FS-P** shows a low hydrogen evolution rate of 1.12 mmol g^{-1} h^{-1}. **FS-COF** shows very high HER rate which is around 6 times higher than the optimized rate reported for **N_3-COF** by using triethanolamine as an electron donor[8], and 22 times higher than for **N_3-COF** (0.47 mmol g^{-1} h^{-1}), as measured by us under identical conditions (with ascorbic acid). However, without adding co-catalysts, the HER rate was smaller with rates of 0.6 and 1.32 mmol g^{-1} h^{-1} for **S-COF** and **FS-COF**, respectively. These results are consistent with previous reports for porous titania glasses[9], strontium titanate[10] and carbon nitride[11]. No hydrogen produced was observed after 5 hours irradiation for **TP-COF** without added Pt.

The better activity of **FS-COF** as compared to the isostructural framework **TP-COF** can be attributed to its wider range light absorption, allowing **FS-COF** to absorb more visible light. The higher surface area for **FS-COF** than **TP-COF** might be also important, because photogenerated charges may have more possibility to migrate to interface in porous materials

than non-porous materials, since exciton diffusion lengths for photogenerated charges are typically around 10 nm for conjugated polymers.[12–14] However, porosity of materials is not only the factor influence of activity. For example, **TP-COF** shows very similar hydrogen rate to **FS-P** (1.6 mmol g^{-1} h^{-1} versus 1.12 mmol g^{-1} h^{-1}), while **TP-COF** has much higher surface area than **FS-P** (919 m^2 g^{-1} versus 209 m^2 g^{-1}).

Compared to crystalline **FS-COF**, its amorphous analogue (**FS-P**) exhibits only 11% of the relative activity under similar conditions. Considering different surface areas of **FS-COF** and **FS-P**, the hydrogen rates were normalised as function of surface area, resulting higher hydrogen rate for **FS-COF** than **FS-P** (7.84 versus 5.36 mmol m^{-2} h^{-1}). Moreover, Semi-crystalline linear polymer **P7** and **P10** shows 8.3% and 11% of activity than **FS-COF** (Table 2-1). These results suggest that crystallinity of materials might be important to photocatalytic activity, which may be because crystalline materials exhibit more efficient charge transport.[15] It also should be noted that crystallinity was not the only property affected; for example, the surface area and conjugation length of the amorphous **FS-P** was much lower. Co-catalysts were added by using in situ photo-deposition. Figure 2-20 shows that Pt was uniform dispersed in the **FS-COF** with particles size of 3.0 ± 0.4 nm. Although the pore size of **FS-COF** is around 3 nm, from STEM image, it was still unclear that Pt was anchored in the pores or not. Pt nanoparticles tend to aggregate in the **FS-P**. This distribution difference might also influence materials activity.

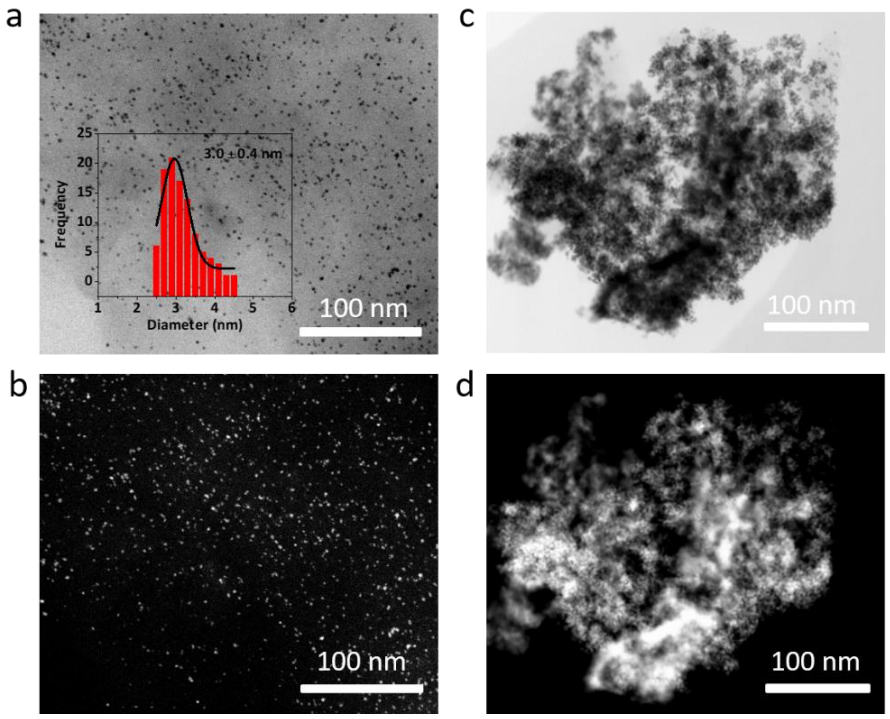

Figure 2-20. Bright field STEM (a, c) for Pt doped **FS-COF** and **FS-P**. HAADF-STEM images (b, d) for Pt doped **FS-COF** and **FS-P**. Inset image is size distributions of Pt nanoparticles.

Table 2-1. Photophysical properties and hydrogen evolution rates (HERs) for the COF photocatalysts.

Photocatalyst	**Degree of crystallinity**	**Optical gap[a] / eV**	**Hydrogen evolution rate[b] / mmol g^{-1} h^{-1}**	**Hydrogen evolution rate relative to FS-COF**
TP-COF	Crystalline	2.31	1.60 ± (0.08)	16%
S-COF	Crystalline	2.18	4.44 ± (0.14)	43%
FS-COF	Crystalline	1.59	10.1 ± (0.3)	–
FS-P	Amorphous	1.88	1.12 ± (0.16)	11%
N_3-COF	Crystalline	2.60	0.47 ± (0.06)	4.6%
P7	Semi-crystalline	2.70	0.84 ± (0.06)[c]	8.3%
P10	Semi-crystalline	2.55	1.48 ± (0.1)[c]	15%

[a] Calculated from tauc plot; [b] All rates measured using the same instruments, optical set-up and reaction conditions: 5 mg COF catalyst, 5 µL (8 wt% H_2PtCl_6), 25 mL ascorbic acid aqueous solution (0.1 M), 300 W Xe light source equipped with $\lambda > 420$ nm cut-off filter. Hydrogen evolution rates (HER) based on average over 5 hours irradiation and normalized to the COF mass; [c] As for [b], but with no additional platinum catalyst added; HER for **P10** in the presence of Pt was 1.92 mmol g^{-1} h^{-1}.

Table 2-2. Hydrogen evolution for **FS-COF** rates using other scavengers.

Scavenger	Ascorbic acid (10 g L^{-1})	Na_2S (10 g L^{-1})	Na_2SO_3 (10 g L^{-1})	TEOA (10 Vol %)	TEOA (1 Vol %)	TEA (1 Vol %)
HER / mmol g^{-1} h^{-1}	10.1	0	0	0	0.9	0

Reaction conditions: 5 mg of **FS-COF** was suspended in 25 mL of an aqueous solution of the sacrificial donors with different concentrations, irradiated by a 300 W Xe light source.

The difference electron donors were used for photocatalytic water reduction. As shown in Table 2-2, **FS-COF** can produce large amounts of hydrogen by using ascorbic acid, but no hydrogen production was observed using TEA, TEOA, Na_2SO_3 and Na_2S. These results indicate that activity of the catalyst for sacrificial water reduction is sensitive to electron donors, and a possible reason could be that **FS-COF** is not stable under basic conditions.

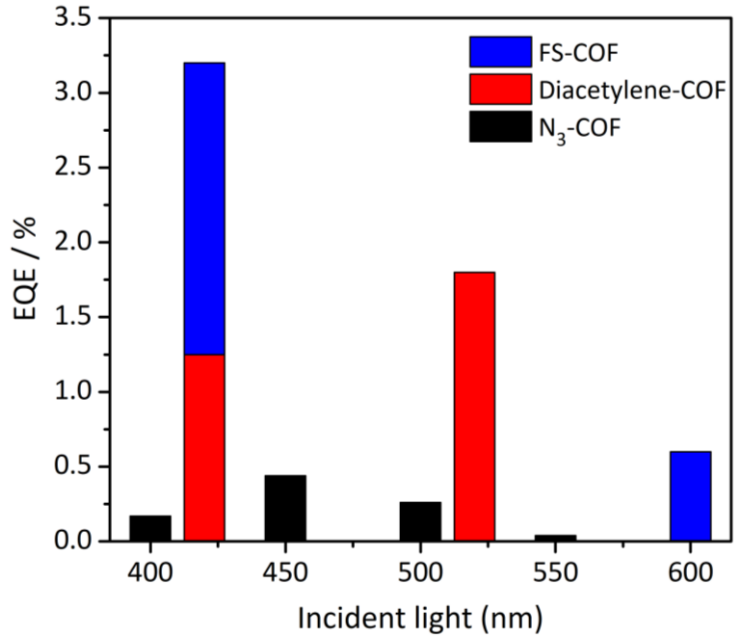

Figure 2-21. External quantum efficiencies (EQE) at given incident light wavelengths for **FS-COF** compared to reported values for **N_3-COF**[8] and **Diacetylene-COF**[16] photocatalysts.

External quantum efficiencies (EQE) for **FS-COF** were determined to be 3.2 and 0.6% at 420 and 600 nm respectively, using ascorbic acid as an electron donor, whereas 0.44% was reported

for **N_3-COF**[8] at 450 nm and 1.3% for **Diacetylene-COF**[16] at 420 nm, both using TEOA as an electron donor (Figure 2-21).

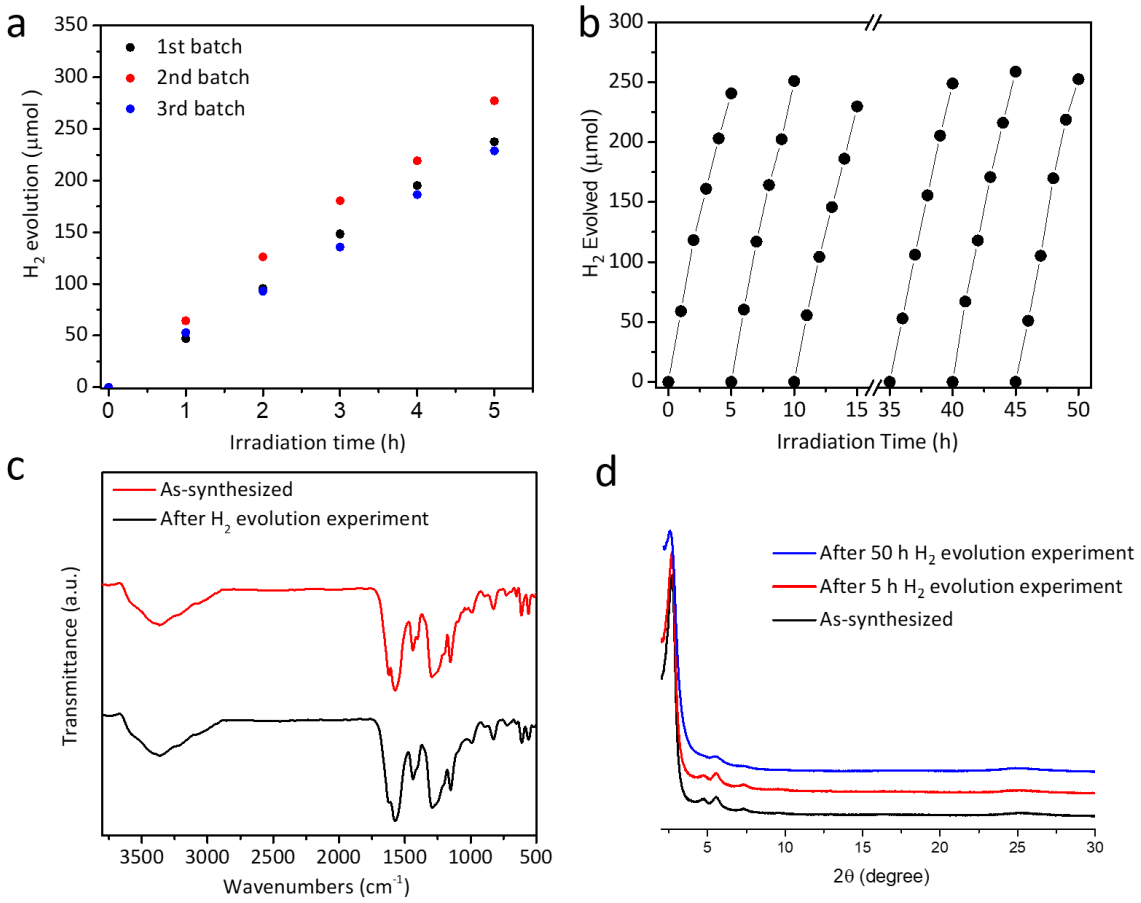

Figure 2-22. (a) Hydrogen evolution experiments for three different batches for **FS-COF** showing good batch-to-batch reproducibility of the measurement. For each experiment, 5 mg **FS-COF** with 8 wt% H_2PtCl_6 in a 0.1 M ascorbic acid water solution under $\lambda > 420$ nm irradiation. (b) H_2 production using visible light for **FS-COF** over 50 hours total photolysis (5 mg catalyst in water, 5 μL (8 wt% H_2PtCl_6), 0.1 M ascorbic acid, $\lambda > 420$ nm). The sample was degassed after 5 and 10 hours to prevent saturation of the detector, then left under continuous illumination for 20 hours and again degassed after 40 and 45 hours. After 35 hours, 1.25 mmol of ascorbic acid was added. (c) FTIR spectra of **FS-COF** before (red), after (black) 5 hours photocatalysis. (d) Experimental powder X-ray diffraction pattern of **FS-COF** before (black), after (red and blue) photocatalysis. The characterization was performed after 5 hours and 50 hours hydrogen evolution experiments under visible light ($\lambda > 420$ nm), respectively.

The reproducibility of the results obtained with **FS-COF** were measured by using **FS-COF** catalyst from 3 different batches. Figure 2-22a shows that hydrogen production rate from

different batches are consistent, indicating good batch-to-batch reproducibility for **FS-COF**. Cycling photolysis experiments for **FS-COF** shows no significant decrease in the catalytic performance over 50 hours of visible light irradiation ($\lambda > 420$ nm, Figure 2-22b), which indicating good stability for **FS-COF**. No obvious changes to the FTIR spectra and PXRD patterns were observed after 5 hours photolysis experiments for **FS-COF** (Figure 2-22c), which also suggest **FS-COF** was stable under photolysis conditions. After 50 hours, **FS-COF** still retained the long-ordered structure based on PXRD patterns (Figure 2-22d).

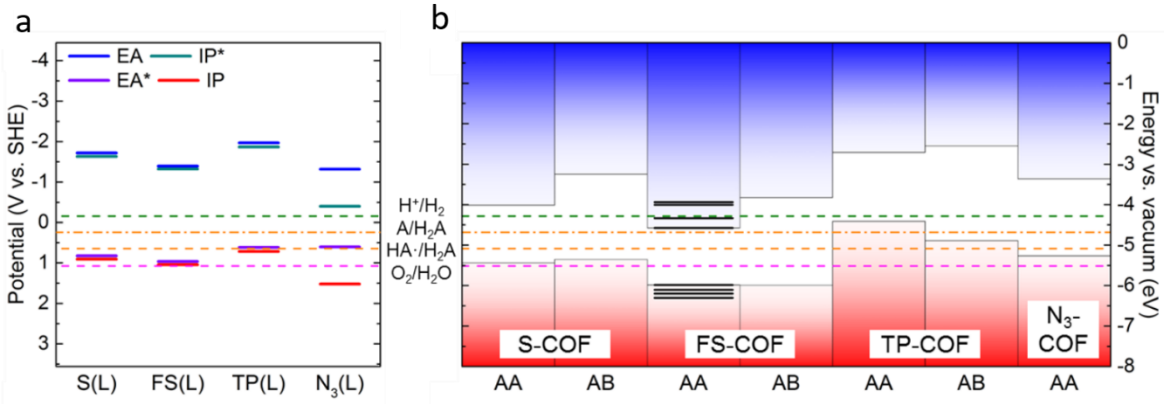

Figure 2-23. (a) Calculated potential of representative fragments of the different COFs in water; S(L), FS(L), TP(L) and N_3(L) are representative fragments of **S-COF**, **FS-COF**, **TP-COF** and **N_3-COF**, respectively. (b) Periodic DFT predicted VBM (red) and CBM (blue) of the COFs with respect to a common vacuum level. Both eclipsed (AA) and staggered (AB) stacking arrangements were considered. For **FS-COF**, multiple AA-stacked structures were generated, with the calculated VBM and CBM for each individual stacking shown as black horizontal lines in (b). Dashed coloured lines in figures indicate the potentials for different solution reactions: green, proton reduction; orange, two-hole (A/H_2A) and one-hole ($HA\cdot/H_2A$) oxidation of ascorbic acid; magenta, overall water oxidation. All solution potentials shown are for pH 2.6, the experimentally measured pH of a 0.1 M ascorbic acid solution.

For COFs hydrogen evolution photocatalysts, COFs must thermodynamically drive the reduction of protons and the oxidation of water/electron donor. Thus, electron affinity (EA) and ionization potential (IP) of and COFs should straddle the proton reduction and water/electron donor oxidation potentials.[17] Similarly, in exciton case, exciton ionization potential (IP*) and electron affinity (EA*) also should straddle the potential of both half-reactions. It should be noted that ascorbic acid was used as electron donor, which oxidation

potentials are more negative than the water oxidation potential, suggesting it is more easily oxidized. Cluster calculations and periodic calculations were used which calculated based on fragments and crystal structures of the COFs. These two approaches complement each other. For periodic calculations, influence of layer stacking was considered but they are hard to describe the effect of water. However, cluster calculations do not take the effect of stacking when in contact with water into account.

The cluster DFT calculations on fragments for **S-COF**, **FS-COF** and **TP-COF** shows that they all have thermodynamic driving force for proton reduction (Figure 2-23a). However, water oxidation was predicted to be endergonic, which means that an electron donor is necessary for hydrogen evolution. Cluster calculations for **N_3-COF** shows that the IP* of N_3(L) is more negative than the potential of proton reduction, and the EA* is more positive than the potential of the one-hole oxidation of ascorbic acid. Exciton binding energy for **N_3-COF** was predicted to be larger than other COFs. The relative low activity of **N_3-COF** can be attributed to small driving force and poor exciton dissociation at material-water interface.

For periodic calculations, both AA and AB stacking structure were considered for **S-COF**, **FS-COF** and **TP-COF**; the AA stacking structure of **N_3-COF** was also considered. All the COFs have driving force for protons reduction and ascorbic acid oxidization. The VBM and CBM for **FS-COF** were sensitive to small changes in AA stacking structure (black horizontal lines in Figure 2-23b). For example, the idealized AA-stacked **FS-COF** structure cannot thermodynamically drive the proton reduction, while the structure with offsets between neighbouring layers has the driving force. These results suggest that the electronic structure of **FS-COF** was sensitive to the small changes of AA stacking structure. However, we might not be able to distinguish each of them from either laboratory or synchrotron PXRD data (Figure 2-7). The calculation results demonstrate that all COFs have driving force for both redox half-reactions. As discussed above the other factors may also influence the activity, such as wettability, light absorption and surface areas.

2.5 Dye sensitization

2.5.1 Water soluble dyes

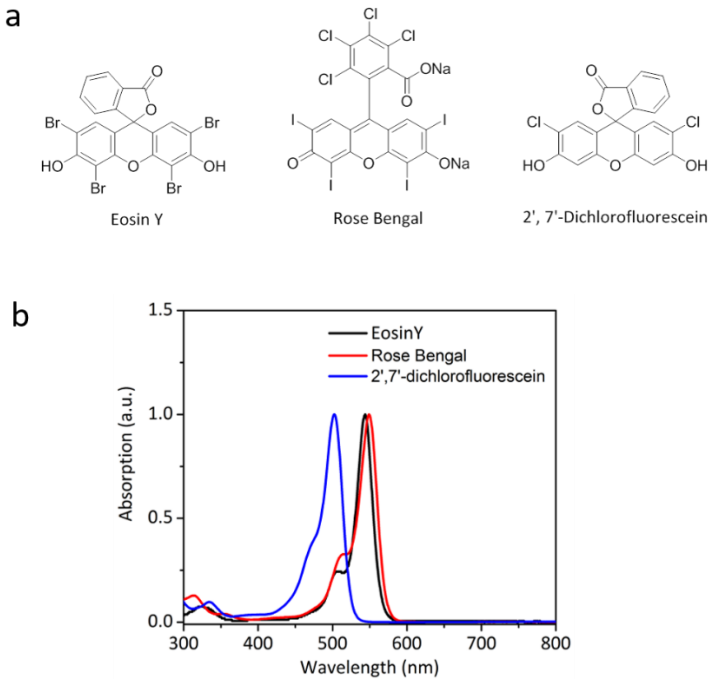

Figure 2-24. (a) Chemical structure of commercially available dyes (**Eosin Y**, **Rose Bengal** and **2′,7′-dichlorofluorescein**) used for sensitizing the COFs. (b) UV-Vis spectra of **Eosin Y**, **Rose Bengal** and **2′,7′-dichlorofluorescein** in aqueous solution.

Dye sensitization strategies have been widely used to improve the performance of solar cells and photocatalysts.[18–21] Here, to take advantage of large porosity for COFs, three commercially-available dyes (Figure 2-24a) were introduced into **FS-COF** to further increase the activity for **FS-COF**. As shown in Figure 2-24b, all 3 dyes can absorb the visible light, displaying peak absorption at 549 nm (**Eosin Y**), 553 nm (**Rose Bengal**), and 498 nm (**2′,7′-dichlorofluorescein**), respectively. After addition of 10 mg **Eosin Y** into reaction system, the hydrogen evolution rate was increased to 13 mmol g^{-1} h^{-1}, and it was further enhanced to 16.1 mmol g^{-1} h^{-1} after adding with 20 mg of **Eosin Y** (Figure 2-25b and Table 2-3). Similar enhancement was observed by adding **Rose Bengal** into the system, which was increased to 12.0 and 12.9 mmol g^{-1} h^{-1} after addition of 10 mg and 20 mg **Rose Bengal**. However, the hydrogen production rate was decreased after adding with **2′,7′-dichlorofluorescein**. **FS-P** was also attempted to be sensitized; however, an obvious decrease was observed after addition of 20 mg of **Eosin Y**, indicating that **FS-P** cannot be dye sensitised. To demonstrate dye

sensitization effect, the control experiment was conducted, which measured activity in absence of **FS-COF**. **Eosin Y** cannot produce hydrogen in the same condition without addition of **FS-COF**. These results suggest that **FS-COF** was successfully be dye sensitised.

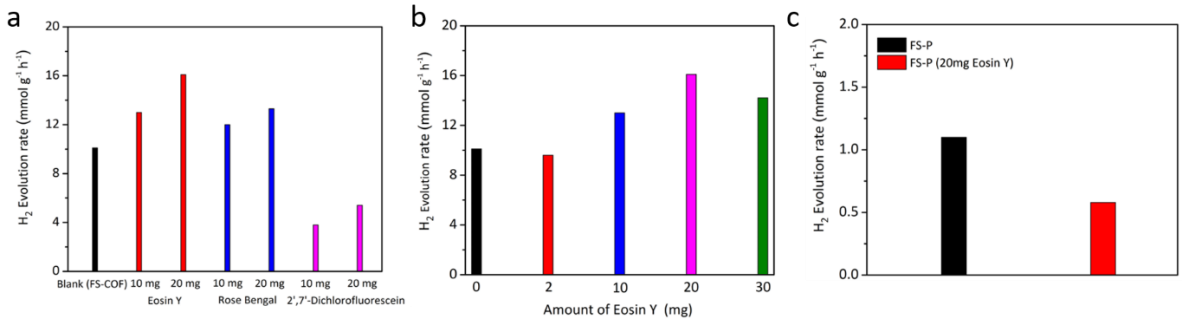

Figure 2-25. (a) Hydrogen evolution rates of different dye-sensitized COFs relative to the undoped **FS-COF** (black). (b) Hydrogen evolution rates for dye-sensitized **FS-COF** at different concentrations of **Eosin Y**. (c) Hydrogen evolution plot for **FS-P** after "sensitization" with **Eosin Y**. The hydrogen evolution rates were measured over 5 hours under visible light ($\lambda > 420$ nm).

Table 2-3. Hydrogen evolution rates (HERs) for the dye-sensitized photocatalysts and relative control experiments for dye photocatalysts.

Photocatalyst	**Hydrogen evolution rate / mmol g^{-1} h^{-1}**	**Hydrogen evolution rate relative to FS-COF**
FS-COF + **Eosin Y** (10 mg)	13.0 ± (0.24)	129%
FS-COF + **Eosin Y** (20 mg)	16.1 ± (0.34)	159%
FS-COF + **Rose Bengal** (10 mg)	12.0 ± (0.21)	119%
FS-COF + **Rose Bengal** (20 mg)	12.9 ± (0.45)	127%
FS-COF + **2′,7′-dichlorofluorescein** (10 mg)	3.84 ± (0.04)	38%
FS-COF + **2′,7′-dichlorofluorescein** (20 mg)	5.46 ± (0.06)	54%
FS-P + **Eosin Y**	0.58 ± (0.08)	5.8%
Eosin Y	trace	–

All rates were measured using the same instruments, optical set-up and reaction conditions: 5 mg catalyst, 5 µL (8 wt. % H_2PtCl_6), 25 mL ascorbic acid aqueous solution (0.1 M), 300 W Xe light source equipped with $\lambda > 420$ nm cut-off filter. The hydrogen evolution rates are based on average over 5 hours of irradiation.

2.5.2 Water insoluble dyes

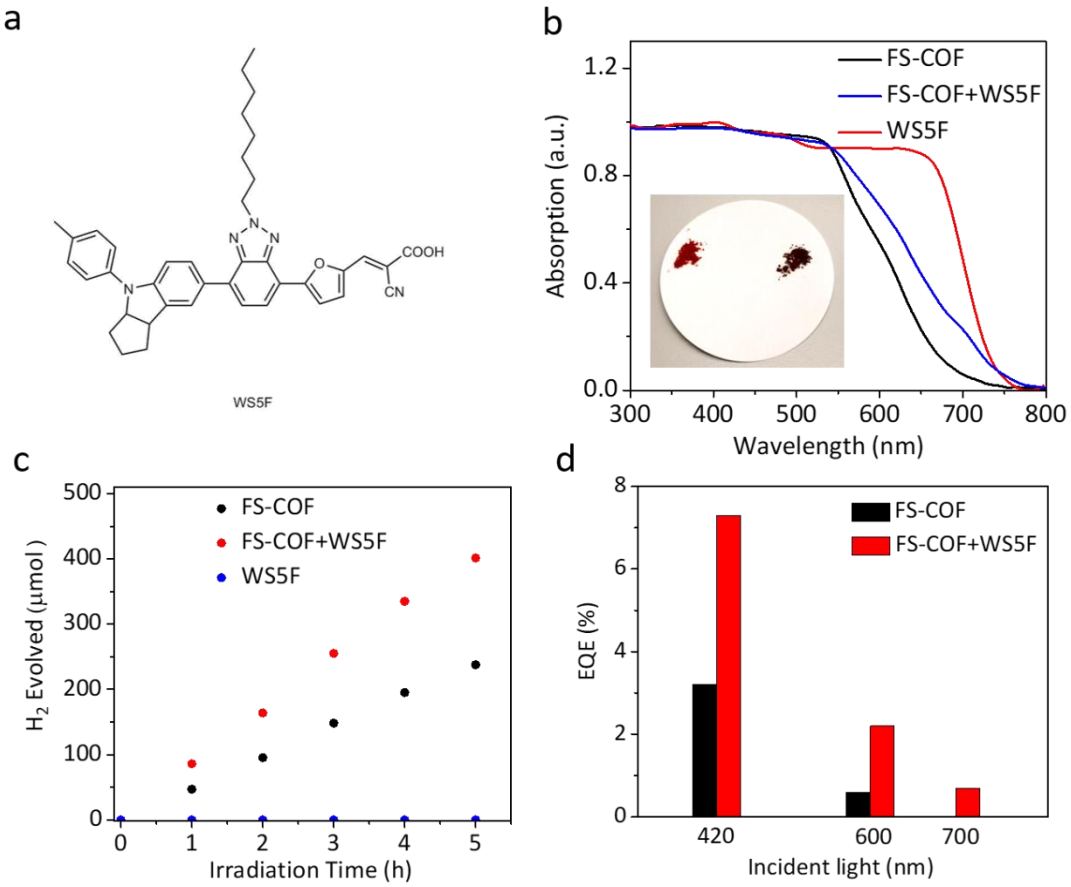

Figure 2-26. (a) Chemical structure of water-insoluble **WS5F** used for sensitizing the COFs. (b) Solid-state UV–Vis spectra for **FS-COF**, **WS5F** and **FS-COF**+**WS5F**. Inset image is as-synthesized **FS-COF** and the hydrides after addition of **WS5F**. (c) Time course for photocatalytic H_2 production using visible light for **FS-COF**, a neat, near-infrared dye (**WS5F**) and a dye-sensitized COF (**FS-COF**+**WS5F**); 5 mg material in water, 5 μL (8 wt% H_2PtCl_6), 0.1 M ascorbic acid, $\lambda > 420$ nm). (d) EQEs at three different incident light wavelengths for **FS-COF** and **FS-COF**+**WS5F** (5 mg catalyst in water, 5 μL (8 wt% H_2PtCl_6), 0.1 M ascorbic acid, $\lambda = 420 \pm 10$, $\lambda = 600 \pm 45$ and 700 ± 10 nm irradiation.

Since the absorption spectrum of **Eosin Y** shows overlaps with the absorption spectrum of **FS-COF**, thus the addition of dye may enhance the total absorption of the system. A near-infrared absorbing dye, **WS5F** (Figure 2-26a), was further used to sensitize **FS-COF**. **WS5F** is insoluble in the water, so the pre-loaded method was used to load **WS5F** into **FS-COF**. After immersion of **FS-COF** into **WS5F** acetone solution, sample colour of the hybrid (**FS-COF**+**WS5F**) became darker than as-synthesized **FS-COF** (Figure 2-26b). UV-Vis spectra of

hybrid show more wide range of light absorption than **FS-COF** precursor (Figure 2-26b), which absorption onset was redshifted from 670 nm to 735 nm.

The hydrogen production rate for **FS-COF**+**WS5F** was significantly enhanced to 16.3 mmol g^{-1} h^{-1} with same conditions for measuring **FS-COF**. The enhancement of activity may ascribe to the wider absorption of more photons at higher wavelengths by the **FS-COF**+**WS5F**. The EQE measurements also demonstrate this conclusion (Figure 2-26d). **FS-COF**+**WS5F** composite has an EQE of 7.3% at 420 nm. EQE for composite was measured to be of 2.2% at 600 nm, which is more 3 times higher than **FS-COF** (0.6%). At 700 nm, **FS-COF** is inactive, but the composite has an EQE of 0.7%.

Table 2-4. Photophysical properties and hydrogen evolution rates (HERs) for the COF photocatalysts.

Photocatalyst	**Hydrogen evolution rate / mmol g^{-1} h^{-1}**	**Hydrogen evolution rate relative to FS-COF**
FS-COF + **WS5F**	16.3 ± (0.29)	161%
FS-P + **WS5F**	0.23 ± (0.03)	2.3%
WS5F	trace	-

All rates measured using the same instruments, optical set-up and reaction conditions: 5 mg COF catalyst, 5 µL (8 wt. % H_2PtCl_6), 25 mL ascorbic acid aqueous solution (0.1 M), 300 W Xe light source equipped with $\lambda > 420$ nm cut-off filter. Hydrogen evolution rates (HER) based on average over 5 hours irradiation and normalized to the catalysts mass.

Similar to **FS-P**+**Eosin Y** composite, **FS-P**+**WS5F** exhibit decrease of activity than **FS-P** precursor (Table 2-4), which may because of low surface areas in **FS-P**. These results indicate that the hydrophilic and large mesopore channels in **FS-COF** play a critical role for dye sensitization. The control experiments for **WS5F**, showing negligible hydrogen produced under visible light in the absence of **FS-COF** (Figure 2-26). In order to investigate the effect of **FS-COF** in dye sensitization process, a photoinactive mesoporous silica (SBA-15) was pre-loaded with **WS5F**, Pt was also used to be a co-catalyst. However, the composite showed no hydrogen evolution under the same conditions, which indicated that **FS-COF** can transfer photoinduced charges with the dye.

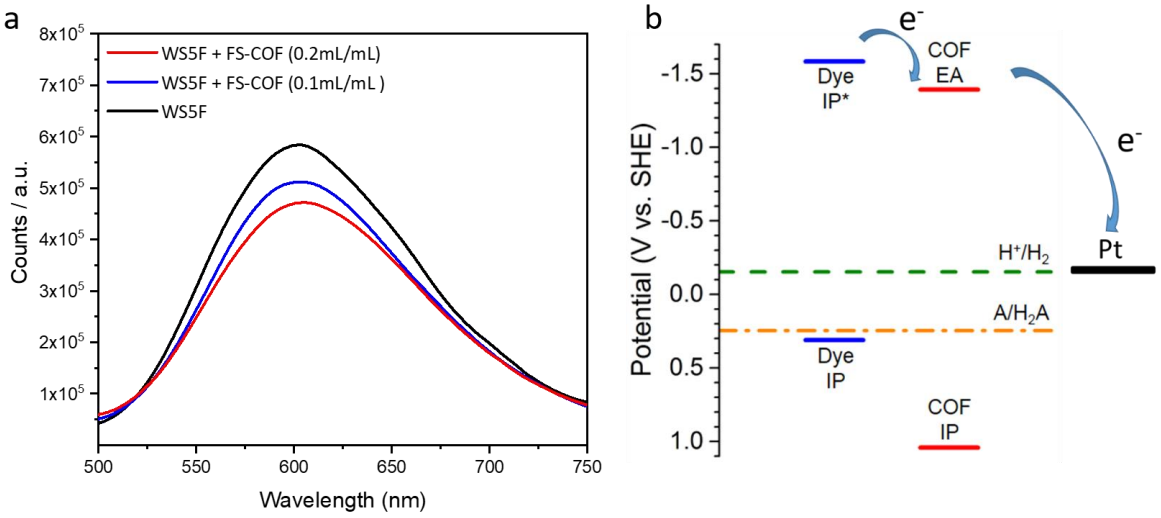

Figure 2-27. (a) Photoluminescence emission spectra of **WS5F** and **WS5F**+**FS-COF** hybrids in acetone (λ_{ex} = 410 nm). (b) Relative energy levels as calculated for ascorbic acid, **FS-COF**, Pt and a near-infrared dye, **WS5F**; dashed green and orange lines indicate potentials for proton reduction and the two-hole oxidation of ascorbic acid in solution, respectively.

The photoluminescence spectra were carried out to investigate the interaction between **FS-COF** and **WS5F**. As shown in Figure 2-27a, **WS5F** shows an emission maximum at 630 nm under 410 nm excitation. This emission can be quenched by continuously increasing the concentration of colloidal **FS-COF**. Since there is no obvious overlap between photoluminescence emission spectrum of **WS5F** and absorption spectrum of **FS-COF**, this fluorescence quenching in **WS5F**+**FS-COF** composite system may attribute to electron transfer from the excited dye to **FS-COF**. The calculations of energy levels for **FS-COF**, **WS5F** and ascorbic acid indicate a possible scheme, in which electrons transfer to **FS-COF** form the photoexcited dye and the dye is regenerated by ascorbic acid (Figure 2-27b).

2.6 COF films for hydrogen evolution

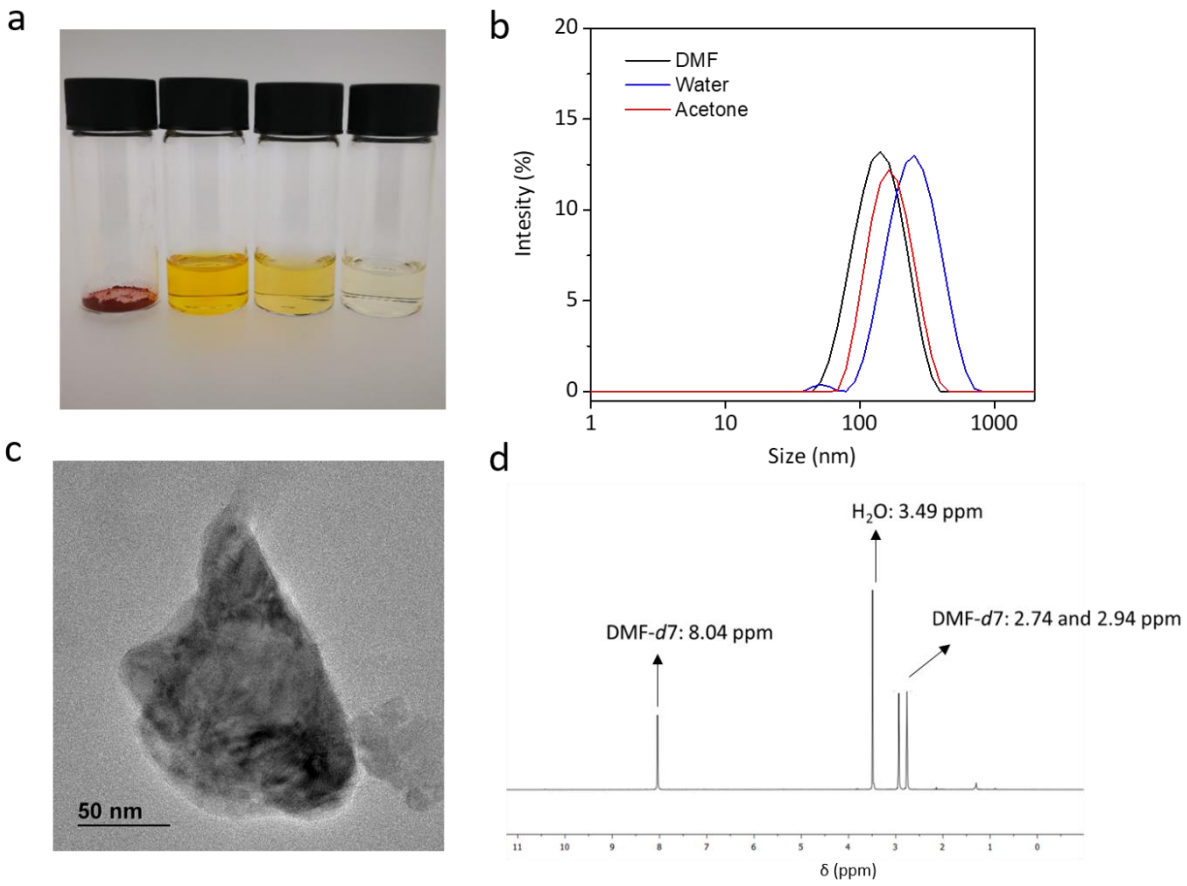

Figure 2-28. Photographs showing (left to right) (a) solid **FS-COF** and colloidal dispersions in DMF, water and acetone. (b) Average size of **FS-COF** colloidal dispersions derived from dynamic light scattering (DLS) of dispersions that were passed through a 0.45 μm filter. (c) TEM images of platinized **FS-COF** colloidal dispersion. (d) ^{1}H NMR spectrum of **FS-COF** colloid in DMF-d7 after soaking in DMF for 12 h. No signal for any decomposition species could be detected.

Processability is very important to make sophisticated architectures, such as Z schemes.[22,23] Here a solvent assistant exfoliation method was used to make COFs colloidal dispersions. As shown in Figure 2-28a, **FS-COF** solid can be dispersed as a colloidal solution in water acetone and DMF. Among these colloidal dispersions, DMF dispersions shows the highest concentration, which was confirmed by the darkest colour. The particles size in colloidal dispersions were measured by dynamic light scattering (DLS), showing the average DLS particle sizes of the **FS-COF** colloids (DMF, acetone and water) were 135, 268 and 139 nm

(Figure 2-28b). DLS results were consistent with TEM images analysis (Figure 2-28c), which particles size of DMF colloidal dispersions was around 100 nm. NMR measurements were carried out to demonstrate stability of colloidal dispersions. As shown in Figure 2-28d, only peaks belong to water and DMF can be observed in the spectrum of **FS-COF** colloid, suggesting no decomposition of **FS-COF** colloid.

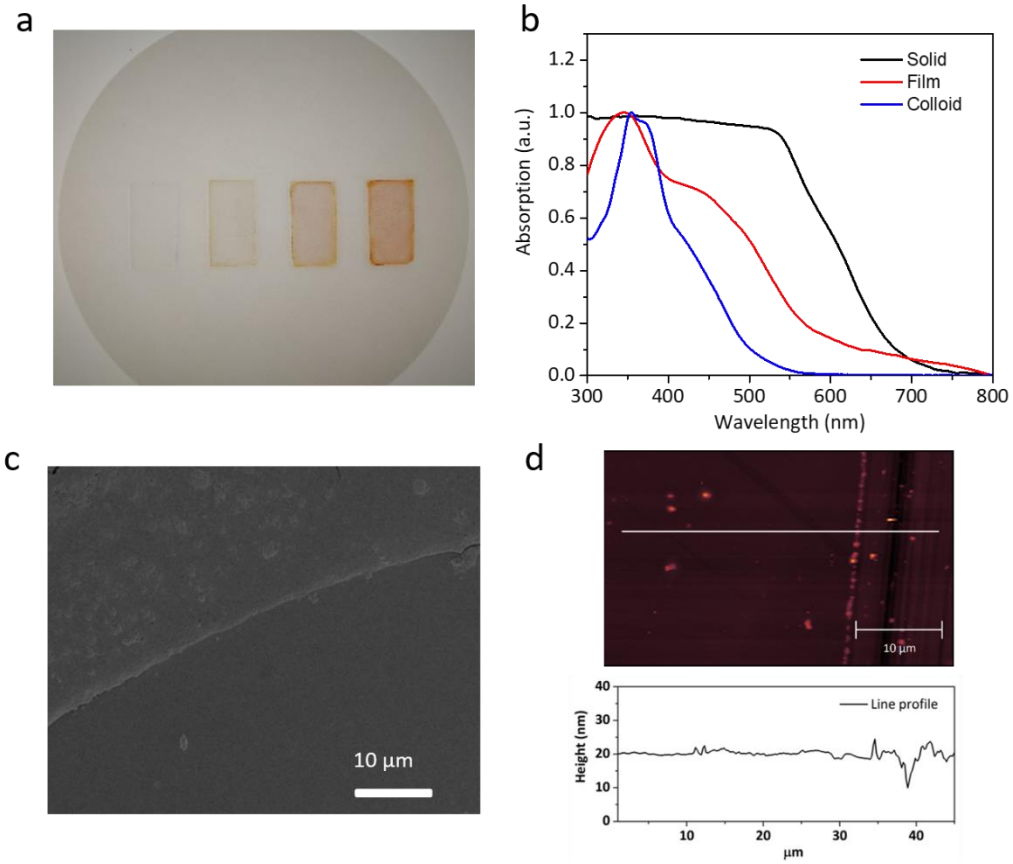

Figure 2-29. (a) Photographs of **FS-COF** on roughened glass after 0, 1, 5 and 10 deposition cycles. (b) UV–Vis spectra of **FS-COF** as a solid powder, cast as a film (5 cycles), and as a colloidal dispersion in DMF. (c) SEM image for a **FS-COF** film cast on a silicon wafer (one deposition). (d) AFM image for **FS-COF** film cast on the silicon wafer (top). The scratch was made to measure the sample thickness. Height profile alone the line in AFM image (bottom).

FS-COF films were made by drop-casting platinized **FS-COF** onto roughened glass supports. The more deposition cycles can give more deeply coloured samples (Figure 2-29a). UV-Vis spectra of **FS-COF** solid, colloidal dispersions and film shows visible light absorption. However, the absorption onset of **FS-COF** film was blue shifted compared to solid state, and the absorption onset of **FS-COF** colloidal dispersion shows more blue shifted than **FS-COF** film (Figure 2-29b), which may because exfoliation decrease the degree of π-π stacking.[24]

Scanning electron microscopy images (SEM) show that **FS-COF** film has a uniform and smooth surface on the microscale (Figure 2-29c). Atomic force microscopy (AFM) analysis (Figure 2-29d) was used to measure the thickness of the **FS-COF** film, which indicates that thickness of the film is ~10 nm after one dropcasting cycle.

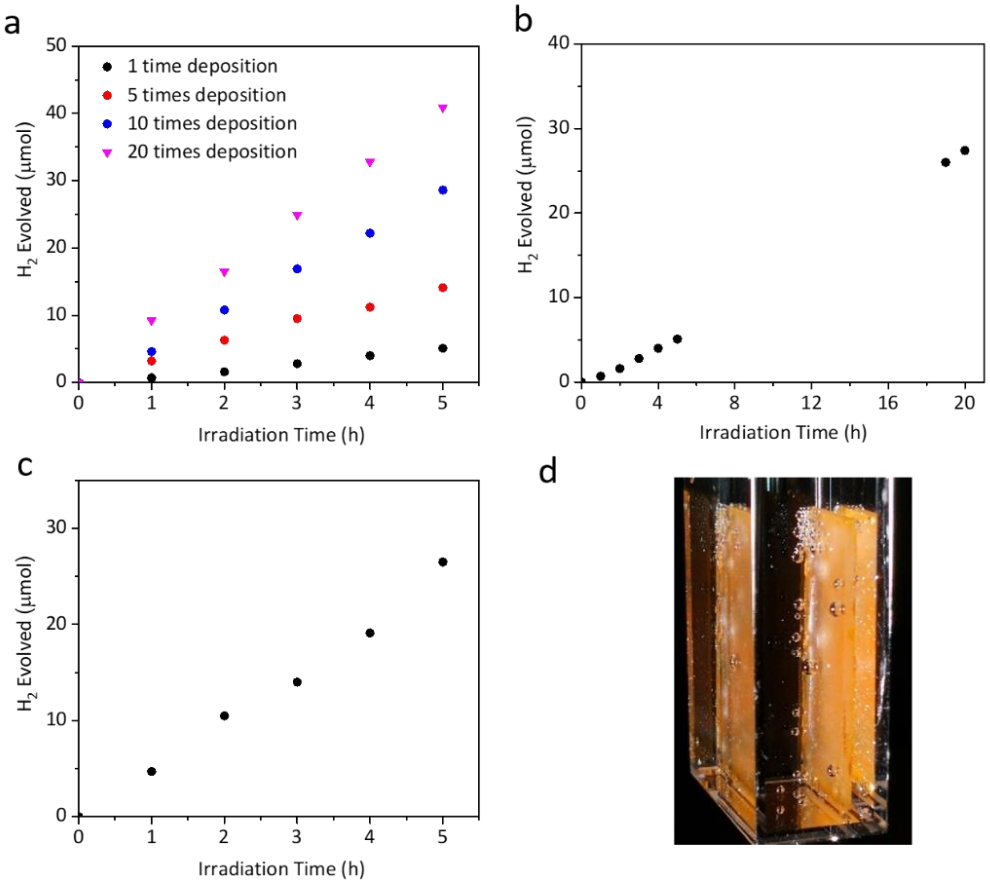

Figure 2-30. (a) Time-course for photocatalytic H_2 production (0.1 M ascorbic acid, $\lambda > 420$ nm) for **FS-COF** films on a glass support prepared using an increasing number of dropcasting cycles. (b) Photocatalytic H_2 production using **FS-COF** films: longer-term hydrogen evolution experiments for a COF film produced with a single dropcasting cycle. (c) Time-course for photocatalytic H_2 production (0.1 M ascorbic acid, AM 1.5g, class ABA) for 20 dropcasting cycles of **FS-COF** on a glass support. (d) Photographs for **FS-COF** film on glass producing hydrogen (20 dropcasting cycles, 0.1 M ascorbic acid, solar simulator AM1.5G, class ABA).

Photocatalytic hydrogen evolution experiments for **FS-COF** films show that hydrogen was produced linearly over 5 hours. The evolution rate was increased with the number of dropcasting cycles, which can be attributed to increased film thickness. **FS-COF** film with 20 times depositions of the colloidal solution shows highest hydrogen evolution rate, reaching of

24.9 mmol h^{-1} m^{-2} under visible light irradiation ($\lambda > 420$ nm) (Figure 2-30a). The stability for **FS-COF** film was tested by using a COF film produced with a single dropcasting cycle. This film shows a stable hydrogen evolution over 20 hours, suggesting the film was stable under reaction condition (Figure 2-30b). **FS-COF** film also measured by irradiated under solar simulator (AM1.5G, classification ABA), which shows hydrogen evolution rate of 15.8 mmol h^{-1} m^{-2} (Figure 2-30c, d). This result is comparable to carbon nitride films on a laboratory scale.[25]

2.7 Summary

Dibenzo[*b*,*d*]thiophene sulfone based amorphous polymers show decent photocatalytic activity which building blocks were successfully introduced into COFs to obtain much more active photocatalysts. A fused sulfone COF (**FS-COF**) linked by a planar building block, benzo[1,2-*b*:4,5-*b*′]bis[*b*]benzothiophene sulfone exhibits excellent activity, exceeding our best linear polymer **P10** as well as other reported COFs under the testing conditions.[26] **FS-COF** is stable for at least 50 hours under reaction conditions. A series of control experiments were carried out to find out factors which has impact on photocatalytic activity. Photocatalytic activity was found to be a composite property that depends on many factors, such as crystallinity, porosity, light absorption and wettability. For example, crystallinity has a huge influence on photocatalytic hydrogen evolution rate, which was demonstrated by crystalline COFs showing superior activity than its structurally related semi-crystalline or amorphous solids. The computational potential results for **FS-COF** indicates that the fine detail of the eclipsed stacking in COFs, which will hugely influence the prospects for thermodynamic proton reduction and water oxidation. In terms of improving our understanding of structure–property relationships, it is desirable to make highly crystalline COFs with long-range order.

Taking advantage of mesoporosity of **FS-COF**, dye- sensitization strategy was used to get even higher rates of up to 16.3 mmol g^{-1} h^{-1} with an EQE of 7.3 % at 420 nm. **FS-COF** thin-film can be formed by casting COF colloidal dispersions onto the glass supports, which can survive at least 20 hours under reaction conditions. These merits indicate that **FS-COF** is an attractive platform for developing hybrid photocatalyst. For example, the mesopores of COFs can be decorated with a second organic or inorganic photocatalysts with proper energy levels to produce a Z-scheme photocatalysts for overall water splitting.

2.8 Experimental methods

2.8.1 Materials and methods

All reagents were obtained from Sigma-Aldrich, TCI Europe or Carbosynth Ltd. Anhydrous solvents were purchased from Acros Organics or Fisher Scientific. All chemicals were used without further purification. The **N_3-COF** synthesis was based on a previous literature procedure.[8]

2.8.1.1 Solution nuclear magnetic resonance

^{1}H and $^{13}C\{^{1}H\}$ NMR spectra were recorded in solution at 400 MHz and 100 MHz, respectively, using a Bruker Avance 400 NMR spectrometer.

2.8.1.2 Powder X-ray diffraction

Laboratory powder X-ray diffraction (PXRD) data were collected in vertical transmission mode from loose powder samples held on Mylar film in aluminium well plates, using a Panalytical Empyrean diffractometer equipped with a high throughput screening XYZ stage, X-ray focusing mirror and PIXcel detector with Cu Kα radiation. Synchrotron data for **FS-COF** were collected at the I11 beamline at Diamond Light Source using the Mythen II position sensitive detector.

2.8.1.3 Thermogravimetric analysis

Thermogravimetric analysis was performed on an EXSTAR6000 by heating samples at 10 °C min^{-1} under air in open aluminium pans to 600 °C.

2.8.1.4 Gas sorption analysis

Apparent surface areas were measured by nitrogen sorption at 77.3 K using a Micromeritics ASAP 2420 volumetric adsorption analyzer. Powder Samples were degassed offline at 393 K for 12 h under dynamic vacuum (10^{-5} bar) before analysis, followed by degassing on the

analysis port under vacuum, also at 393 K. Pore size distributions of COFs from fitting the nonlocal density functional theory (NL-DFT) model to the adsorption data.

2.8.1.5 Fourier-transform infrared spectroscopy

IR spectra were recorded using a Bruker Tensor 27 FT-IR spectrometer. Samples were analyzed as KBr disks for 16 scans with a resolution of 4 cm^{-1}.

2.8.1.6 High resolution mass spectrometry

High resolution mass spectrometry (HR-MS) as performed on an Agilent Technologies 6530B accurate-mass QTOF mixed ESI/APCI mass spectrometer (capillary voltage 4000 V, fragmentor 225 V) in positive-ion detection mode.

2.8.1.7 UV-visible absorption spectra

UV-visible absorption spectra of the polymers were measured on a Shimadzu UV-2550 UV-Vis spectrometer by measuring the reflectance of powders in the solid state.

2.8.1.8 Contact angle measurements

Water contact angles were measured using a drop-shape analysis apparatus (Krüss DSA100). The samples were measured using pressed pellets. The contact angles were fitted by an ellipse fitting method.

2.8.1.9 Scanning electron microscopy

COF morphologies were imaged using a Hitachi S-4800 cold field emission scanning electron microscope (FE-SEM). Samples were prepared by depositing the dry powders on 15 mm Hitachi M4 aluminium stubs using an adhesive high-purity carbon tab before coating with a 2 nm layer of gold using an Emitech K550X automated sputter coater. Imaging was conducted at a working voltage of 3 kV and a working distance of 8 mm using a combination of upper and lower secondary electron detectors.

2.8.1.10 Transmission electron microscopy

TEM, bright field STEM and HAADF-STEM images were obtained on a JEOL 2100FCs microscopy at an accelerating voltage of 200 kV. The samples were prepared by drop-casting sonicated ethanol suspensions of the materials onto a copper grid.

2.8.1.11 Atomic force microscopy

The samples were mounted on Si wafer substrates and then these substrates were mounted on a magnetic puck. All AFM images were recorded in air on a Multimode 8 AFM (Bruker) using QNM tapping mode. The images were acquired using Scanasyst air probes (Bruker) with a nominal spring constant of 0.4 N m^{-1}. Images were processed using Gwyddion 2.38.

2.8.1.12 Time-correlated single photon counting (TCSPC) measurements

TCSPC experiments were performed on an Edinburgh Instruments LS980-D2S2-STM spectrometer equipped with picosecond pulsed LED excitation sources and a R928 detector, with a stop count rate below 3%. An EPL-375 diode (λ = 370.5 nm, instrument response 100 ps, fwhm) with a 450 nm high pass filter for emission detection was used. Suspensions were prepared by ultrasonicating the polymer in water. The instrument response was measured with colloidal silica (LUDOX® HS-40, Sigma-Aldrich) at the excitation wavelength without filter. Decay times were fitted in the FAST software using suggested lifetime estimates.

2.8.1.13 Water vapor isotherm measurements

Water vapor isotherms were determined at 293 K using an IGA gravimetric adsorption apparatus (Hiden Isochema, Warrington, UK) with anti-condensation system, which was carried out in an ultrahigh vacuum system equipped with a diaphragm and turbo pumps.

2.8.1.14 Hydrogen evolution experiments

A flask was charged with the COF powder (5 mg), 0.1 M ascorbic acid water solution (25 mL), and hexachloroplatinic acid (5 µl, 8 wt. % aqueous solution) as a platinum precursor. The resulting suspension was ultrasonicated for 20 minutes before degassing by N_2 bubbling for 30

minutes. The reaction mixture was illuminated with a 300 W Newport Xe light-source (Model: 6258, Ozone free) for the time specified using appropriate filters. The light source was cooled by water circulating through a metal jacket. Gas samples were taken with a gas-tight syringe and run on a Bruker 450-GC gas chromatograph. Hydrogen was detected with a thermal conductivity S3 detector referencing against standard gas with a known concentration of hydrogen. Hydrogen dissolved in the reaction mixture was not measured and the pressure increase generated by the evolved hydrogen was neglected in the calculations. The rates were determined from a linear regression fit. After the photocatalysis experiment, the **FS-COF** were recovered by washing with water and acetone then dried at 120 °C. After 5 hours of photocatalysis, no carbon monoxide associated with polymer or scavenger decomposition could be detected on GC system equipped with a pulsed discharge detector.

2.8.1.15 External quantum efficiency measurements

The external quantum efficiency for the photocatalytic H_2 evolution was measured using a λ = 420 nm LED (0.325 mW cm^{-2}), λ = 600 nm LED (0.263 mW cm^{-2}) and λ = 700 nm LED (0.194 mW cm^{-2}) controlled by an IsoTech IPS303DD power supply. For the experiments **FS-COF** (5 mg) was suspended in an aqueous solution containing ascorbic acid (0.1 M, 8 mL) and hexachloroplatinic acid (5 µl, 8 wt. % aqueous solution). An area of 8 cm^2 was illuminated and the light intensity was measured with a ThorLabs S120VC photodiode power sensor controlled by a ThorLabs PM100D Power and Energy Meter Console. The external quantum efficiencies were estimated using the equation below:

$$\eta EQE = \frac{moles\ of\ hydrogen\ evolved}{moles\ of\ the\ incidentphotons} \times 100\%$$

2.8.1.16 Dye sensitization COF hydrogen evolution experiments

Water insoluble dyes. Dye loaded **FS-COF** (**FS-COF**+**WS5F**) was prepared by impregnation using an organic solvent. To do this, 5 mg **WS5F** was dissolved in 10 mL acetone and then 5 mg **FS-COF** was added to the solution and stirred for 12 hours. The resulting mixture was filtered, and the filtrate was dried at 80 °C overnight. Amorphous **FS-P** was loaded with **WS5F** using the same method.

Water soluble dyes. For **Eosin Y** (2′,4′,5′,7′-tetrabromofluorescein), **2′,7′-dichlorofluorescein** and **Rose Bengal** (sodium salt of 4,5,6,7-tetrachloro-2′,4′,5′,7′-tetraiodofluorescein) sensitization experiments, a flask was charged with 5 mg COF powder, 25 mL aqueous 0.1 M ascorbic acid solution, and hexachloroplatinic acid (5 μL, 8 wt. % aqueous solution) and then the dye was added directly. The resulting mixture was ultrasonicated 20 minutes before degassing by N_2 bubbling for 30 minutes. Hydrogen evolution experiments for amorphous **FS-P** in the presence of **Eosin Y** were performed using the same loading conditions.

For photocatalytic testing, the reaction mixtures were illuminated with a 300 W Newport Xe light-source (Model: 6258, Ozone free) for the time specified using appropriate filters. The light source was cooled by water circulating through a metal jacket. Gas samples were taken with a gas-tight syringe and run on a Bruker 450-GC gas chromatograph. Hydrogen was detected with a thermal conductivity S3 detector referencing against standard gas with a known concentration of hydrogen. Hydrogen dissolved in the reaction mixture was not measured and the pressure increase generated by the evolved hydrogen was neglected in the calculations. The rates were determined from a linear regression fit.

Control experiments with neat dyes. Control experiments with aqueous solutions of **Eosin Y**, 0.1 M ascorbic acid solution, and hexachloroplatinic acid (5 μL, 8 wt. % aqueous solution) showed negligible hydrogen production over 5 hours. Likewise, the neat dye, **WS5F**, gave no hydrogen production under these conditions. To check that the photocatalytic activity of the **FS-COF**+**WS5F** composite was simply not a result of dispersing the dye in a mesoporous solid, we also carried out control experiments where **WS5F** was pre-loaded into a mesoporous zeolite, SBA15. No hydrogen evolution was observed, supporting the interpretation that **WS5F** acts as a sensitizer for **FS-COF**, rather than acting as a photocatalyst in its own right.

2.8.1.17 COF films

Typically, Pt-doped **FS-COF** (5 mg) powder (collected from powder suspension H_2 evolution measurements) was added into DMF (10 mL) and this mixture was sonicated for 2 h. After sonication, the mixture left for additional 6 h; this suspension was then filtered (Grade 1 Circles, 11 μm) to obtain a colloidal solution of the Pt-doped COF. **FS-COF** films were prepared by drop-casting these COF colloidal solutions onto roughened glass or silicon wafers. The resulting films were dried 60 °C yield the cast films. The film thickness could be increased by

carrying out multiple deposition cycles under the same conditions. Before catalytic measurements, films were washed with acetone and dried at 80 °C for 2 hours under vacuum. For the hydrogen evolution experiments using COF films, the COF-coated slides were immersed in a quartz cuvette charged with the 0.1 M ascorbic acid (8 ml) aqueous solution (*n.b.*, no platinum precursor was added because the COF has been pre-loaded with Pt before film formation). The slide was then illuminated with a 300 W Newport Xe light-source or solar simulator (AM 1.5G, class ABA) and the evolved hydrogen was detected, as for the powder suspension measurements. For AFM and SEM analyses, the colloid was produced from **FS-COF** powders without platinum pre-loading. The COF colloid was directly drop cast onto a silicon wafer to form a thin film.

2.8.2 Synthetic procedures

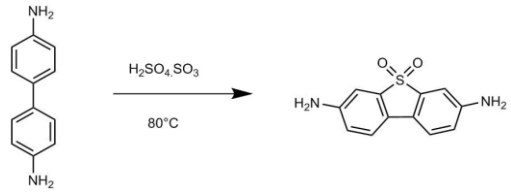

3,7-Diaminodibenzo[*b,d*]thiophene sulfone: [1,1'-Biphenyl]-4,4'-diamine (2.46 g, 10 mmol) was taken up in sulfuric acid (5 mL, 30% free SO_3) and the resulting brown solution was heated to 80 °C overnight with stirring to give a black mixture. After cooling to room temperature, the solution was poured into water and neutralized with saturated sodium bicarbonate solution. After drying at 80 °C, the product was obtained as a green powder (1.2 g, 48%). ^{1}H NMR (400 MHz, DMSO-d_6) δ [ppm]: 7.49 (s, 2H), 6.87 (d, *J* = 8.4 Hz, 2H), 6.80 – 6.77 (m, 2H) 5.73 (s, 4 H). ^{13}C{^{1}H} NMR (100 MHz, DMSO-d_6) δ [ppm]: 149.7, 137.9, 121.9, 119.9, 119.0, 105.9. HR-MS (CI, CH_4): m/z calcd for $C_{12}H_{10}N_2O_2S$: 247.0536 $(M)^+$; found: 247.0537. Anal. Calcd for $C_{12}H_{10}N_2O_2S$: C, 58.52; H, 4.09; N, 11.37; S, 13.02. Found: C, 57.79; H, 3.98; N, 11.22; S, 13.20.

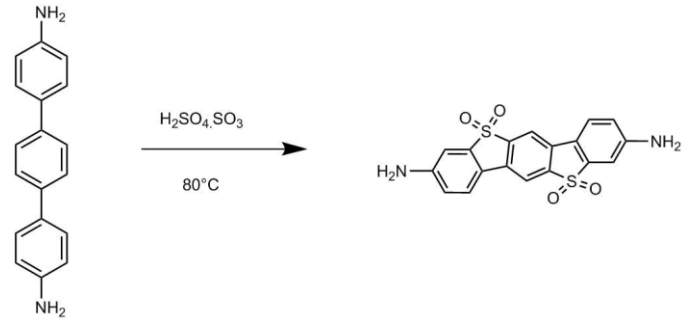

3,9-Diamino-benzo[1,2-*b*:4,5-*b*']bis[1]benzothiophene-5,5,11,11-tetraoxide (FSA): 4, 4''-Diamino-*p*-terphenyl (2.6 g, 10 mmol) was taken up in sulfuric acid (10 mL, 30% free SO_3) and the resulting purple solution was heated to 80 °C overnight with stirring to give a black mixture. After cooling to room temperature, the solution was poured into water, and the solids were filtered off and neutralized with saturated sodium bicarbonate solution. The crude product was purified by Soxhlet extraction with acetone. After drying at 80 °C, the product was obtained as an orange solid (1.5 g, 39%). ^{1}H NMR (400 MHz, DMSO-d_6) δ [ppm]: 8.46 (s, 2H), 7.93 (d, *J* = 8.4 Hz, 2H), 6.98 (d, *J* = 2.0 Hz, 2H), 6.90 – 6.87 (m, 2H), 6.26 (s, 4H).

$^{13}C\{^{1}H\}$ NMR (100 MHz, DMSO-d_6) δ [ppm]: 152.4, 141.5, 139.1, 132.6, 124.7, 118.9, 116.6, 114.8, 105.5. HR-MS (CI, CH_4): m/z calcd for $C_{18}H_{12}N_2O_4S_2$: 385.0311 (M)+; found, 385.0293. Anal. Calcd for $C_{18}H_{12}N_2O_4S_2$: C, 56.24; H, 3.15; N, 7.29; S, 16.68. Found: C, 50.04; H, 2.99; N, 6.06; S, 16.52.

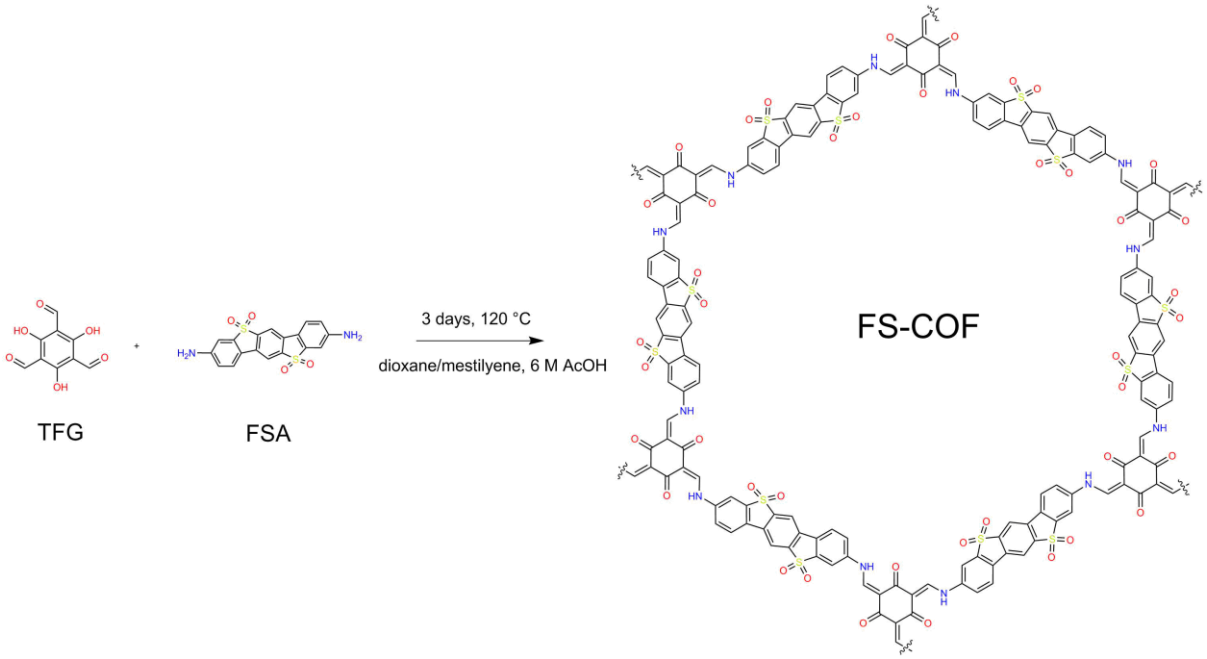

Figure 2-31. Synthesis of **FS-COF**.

Solvothermal synthesis of FS-COF: A Pyrex tube was charged with 2,4,6-triformylphloroglucinol (10.5 mg, 0.05 mmol), 3,9-diamino-benzo[1,2-*b*:4,5-*b*']bis[1]benzothiophene-5,5,11,11-tetraoxide (28.8 mg, 0.075 mmol), mesitylene (1.5 mL), 1,4-dioxane (1.5 mL), and aqueous acetic acid (0.3 mL, 6 M). This mixture was homogenized by sonication for 10 minutes and the tube was then flash frozen at 77 K (liquid N_2 bath) and degassed by three freeze-pump-thaw cycles and evacuated to an internal pressure of 100 mTorr. The tube was sealed off and then heated at 120 °C for 3 days. The brown precipitate was collected by centrifugation and washed with *N*,*N*-dimethylformamide (100 mL) and anhydrous acetone (200 mL). After drying at 120 °C, the product was obtained a deep red-coloured powder (21 mg, 58%). Anal. Calcd for $(C_{30}H_{22}N_2O_8S_2)_n$: C, 61.42; H, 3.78; N, 4.78; S, 10.93. Found: C, 44.80; H, 3.21; N, 3.95; S, 9.93.

Synthesis of FS-COF by reflux method: A flask was charged with 2,4,6-triformylphloroglucinol (31.5 mg, 0.15 mmol), 3,9-diamino-benzo[1,2-*b*:4,5-

b']bis[1]benzothiophene-5,5,11,11-tetraoxide (86.4 mg, 0.225 mmol), mesitylene (4.5 mL), 1,4-dioxane (4.5 mL) and aqueous acetic acid (0.9 mL, 6 M). This mixture was degassed by N_2 bubbling and heated at 120 °C for 3 days. The brown precipitate was collected by centrifugation and washed with *N*,*N*-dimethylformamide (300 mL) and anhydrous acetone (300 mL). After drying at 120 °C, the product was obtained a deep red-coloured powder (86 mg, 79%). Anal. Calcd for $(C_{30}H_{22}N_2O_8S_2)_n$: C, 61.42; H, 3.78; N, 4.78; S, 10.93. Found: C, 46.73; H, 3.32; N, 4.31; S, 8.73.

Synthesis of FS-P: A flask was charged with 2,4,6-triformylphloroglucinol (21 mg, 0.1 mmol), 3,9-diamino-benzo[1,2-*b*:4,5-*b*']bis[1]benzothiophene-5,5,11,11-tetraoxide (57.6 mg, 0.15 mmol), 1,2-dichlorobenzene (10 mL) and aqueous acetic acid (0.5 mL, 6 M). This mixture was degassed by N_2 bubbling and heated at 120 °C for 3 days. The brown precipitate was collected by centrifugation and washed with *N*,*N*-dimethylformamide (100 mL) and anhydrous acetone (200 mL). After drying at 120 °C, the product was obtained as a deep red-colored powder (32 mg, 43%). Anal. Calcd for $(C_{30}H_{22}N_2O_8S_2)_n$: C, 61.42; H, 3.78; N, 4.78; S, 10.93. Found: C, 45.88; H, 3.65; N, 4.76; S, 12.42.

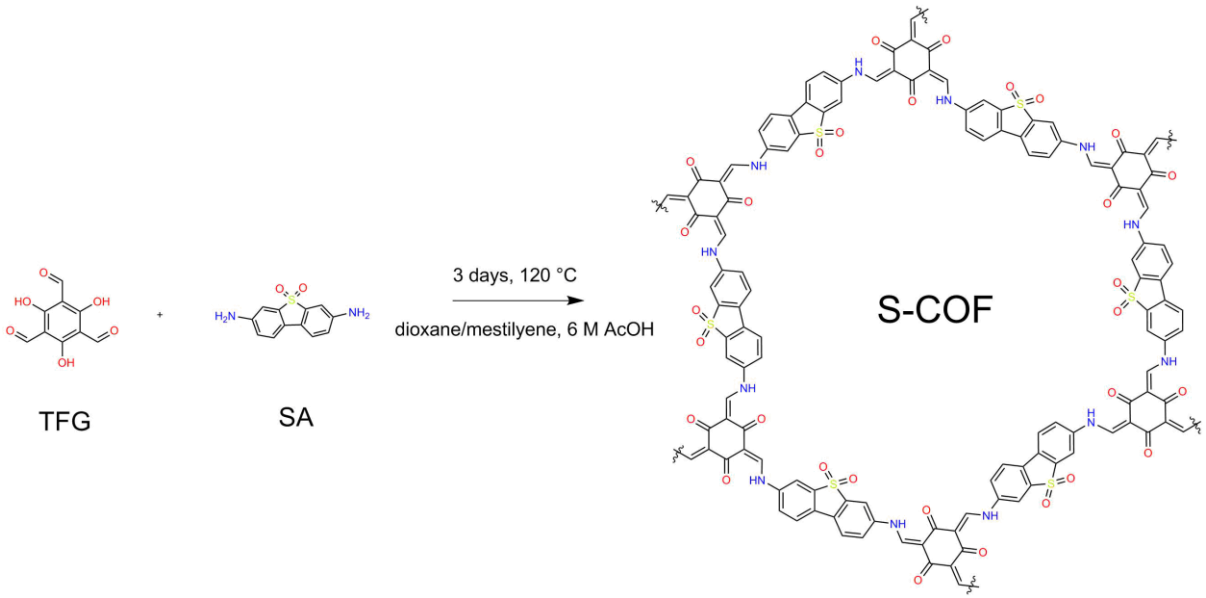

Figure 2-32. Synthesis of **S-COF**.

Synthesis of S-COF: A Pyrex tube was charged with 2,4,6-triformylphloroglucinol (14 mg, 0.66 mmol), 3,7-diaminodibenzo[*b*,*d*]thiophene sulfone (24.6 mg, 0.1 mmol), mesitylene (1.5 mL), 1,4-dioxane (1.5 mL), and aqueous acetic acid (0.3 mL, 6 M). This mixture was

homogenized by sonication for 10 minutes and the tube was then flash frozen at 77 K (liquid N_2 bath) and degassed by three freeze-pump-thaw cycles, and finally evacuated to an internal pressure of 100 mTorr. The tube was sealed off and then heated at 120 °C for 3 days. The orange precipitate was collected by centrifugation and washed with anhydrous acetone (200 mL). After drying at 120 °C, the product was obtained an orange powder (24 mg, 73%). Anal. Calcd for $(C_{24}H_{20}N_2O_5S)_n$: C, 64.27; H, 4.50; N, 6.25; S, 7.15. Found: C, 44.58; H, 4.69; N, 5.54; S, 6.74.

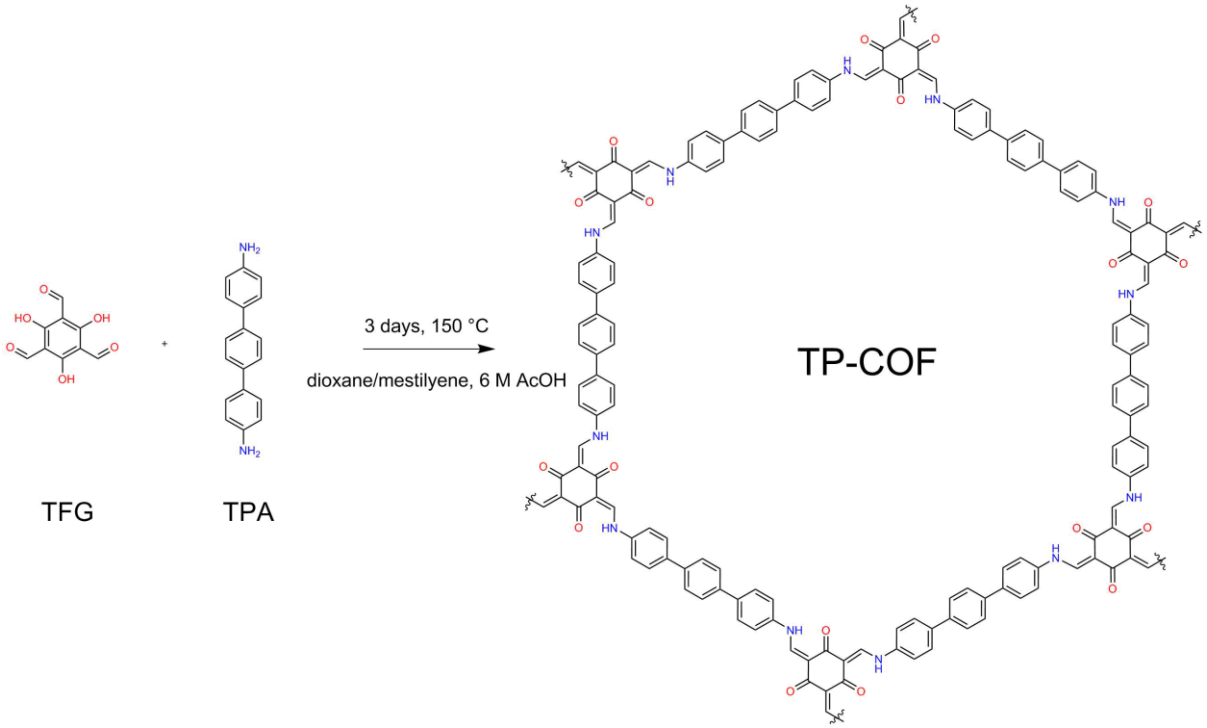

Figure 2-33. Synthesis of **TP-COF**.

Synthesis of TP-COF: A Pyrex tube was charged with 2,4,6-triformylphloroglucinol (21 mg, 0.1 mmol), 4,4" diamino-*p*-terphenyl (39 mg, 0.15 mmol), mesitylene (2 mL), 1,4-dioxane (4 mL), and aqueous acetic acid (0.2 mL, 6 M). This mixture was homogenized by sonication for 10 minutes and the tube was then flash frozen at 77 K (liquid N_2 bath) and degassed by three freeze-pump-thaw cycles, before evacuating to an internal pressure of 100 mTorr. The tube was then sealed off and heated at 150 °C for 3 days. The yellow precipitate was collected by centrifugation and washed with anhydrous acetone (200 mL). After drying at 120 °C, the product was obtained an orange powder (45 mg, 79%). Anal. Calcd for $(C_{30}H_{26}N_2O_3)_n$: C, 77.90; H, 5.67; N, 6.06. Found: C, 65.64; H, 4.40; N, 6.15.

2.8.3 NMR spectra

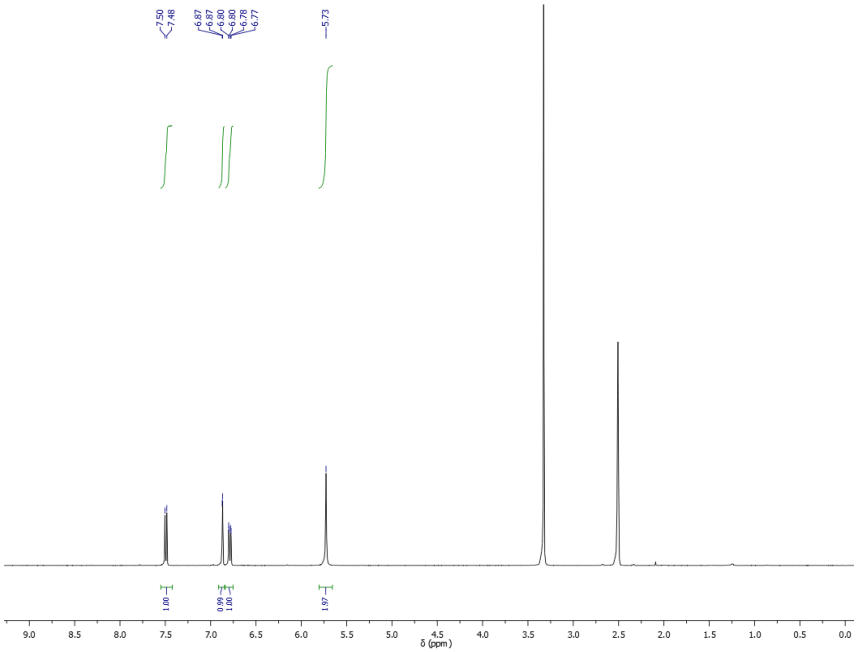

Figure 2-34. ^{1}H NMR spectrum of 3,7-diaminodibenzo[*b*,*d*]thiophene sulfone in DMSO-d_6.

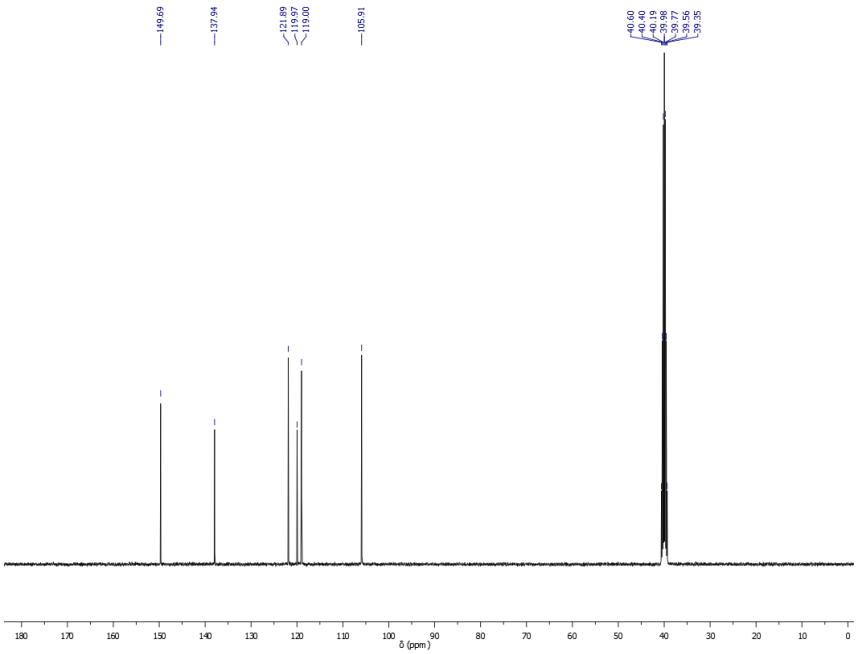

Figure 2-35. ^{13}C{^{1}H} NMR spectrum of 3,7-diaminodibenzo[*b*,*d*]thiophene sulfone in DMSO-d_6.

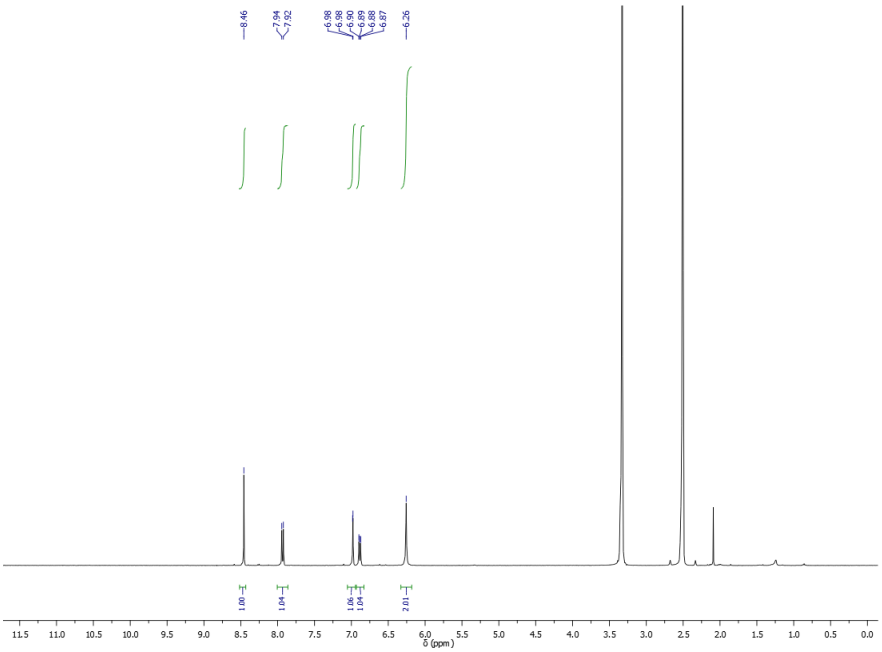

Figure 2-36. ^{1}H NMR spectrum of 3,9-diamino-benzo[1,2-*b*:4,5-*b*']bis[1]benzothiophene-5,5,11,11-tetraoxide in DMSO-d_6.

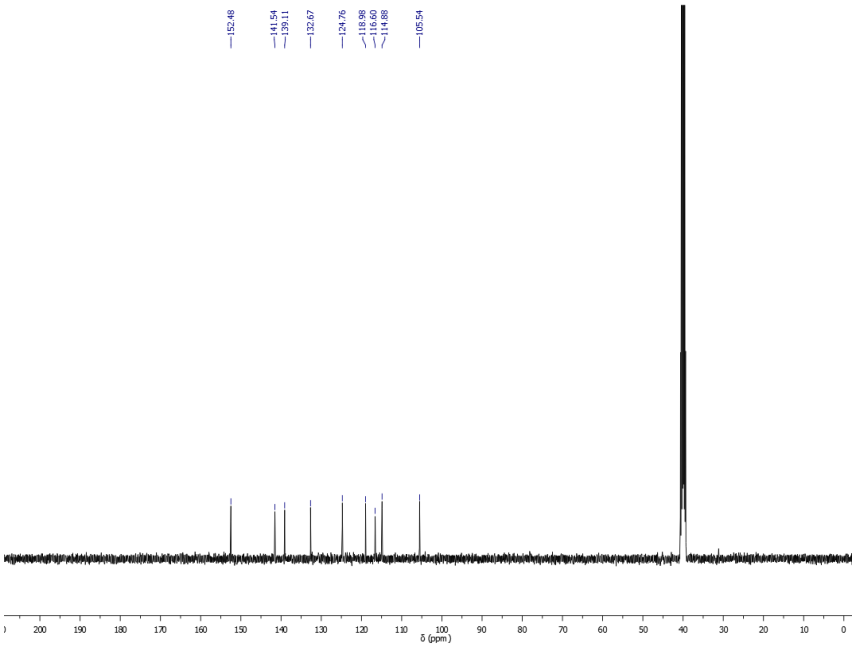

Figure 2-37. ^{13}C{^{1}H} NMR spectrum of 3,9-diamino-benzo[1,2-*b*:4,5-*b*']bis[1]benzothiophene-5,5,11,11-tetraoxide in DMSO-d_6.

2.8.4 Single crystal structures

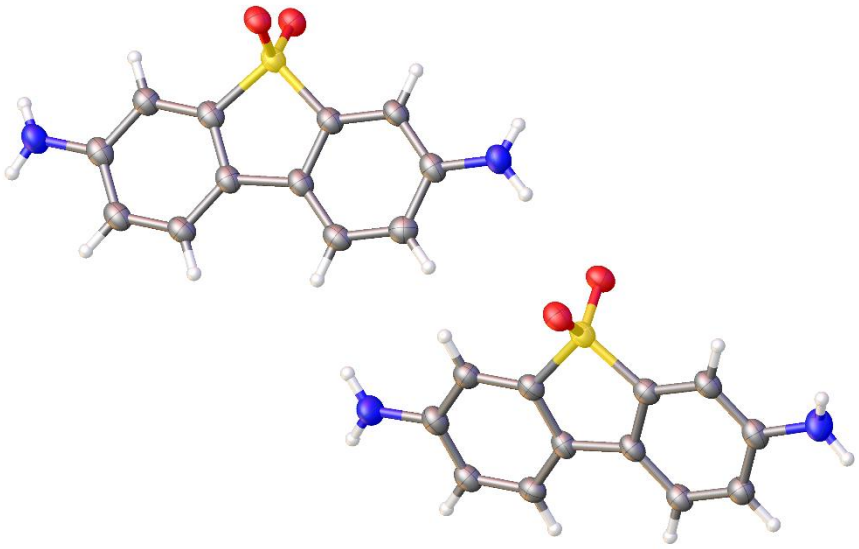

Figure 2-38. Displacement ellipsoid plot from of the asymmetric unit from the single crystal structure of 3,7-diaminodibenzo[*b*,*d*]thiophene sulfone; ellipsoids are displayed at 50% probability level (C = grey, N = blue, O = red, H = white, S = yellow).

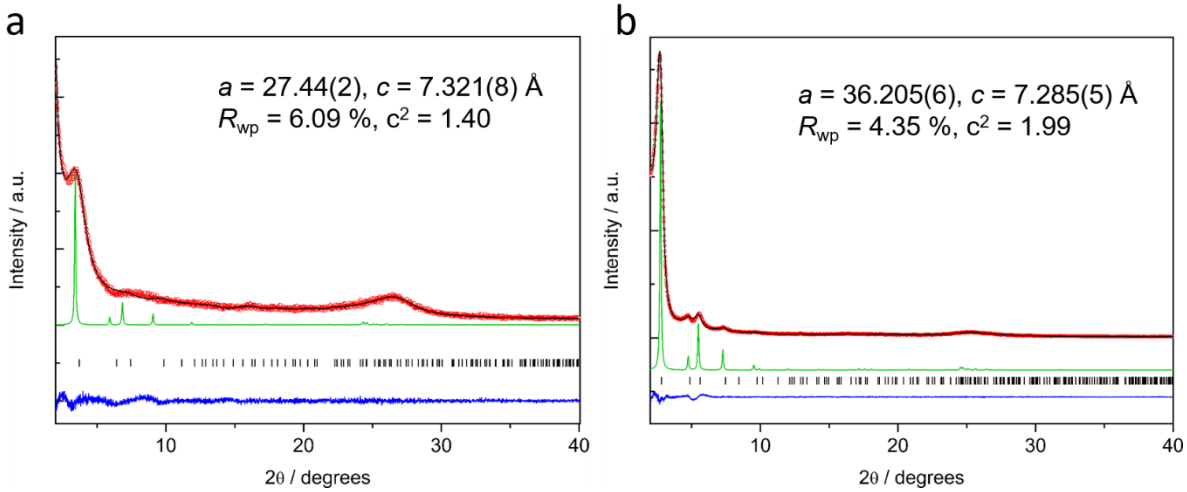

Figure 2-39. Experimental diffraction patterns (red), profiles calculated from Le Bail fitting (black) and residual (blue), and pattern simulated from the structural model (green) for (a) **S-COF** and (b) **FS-COF**. Reflection positions are shown by tick marks.

2.8.5 Time-correlated single photon counting

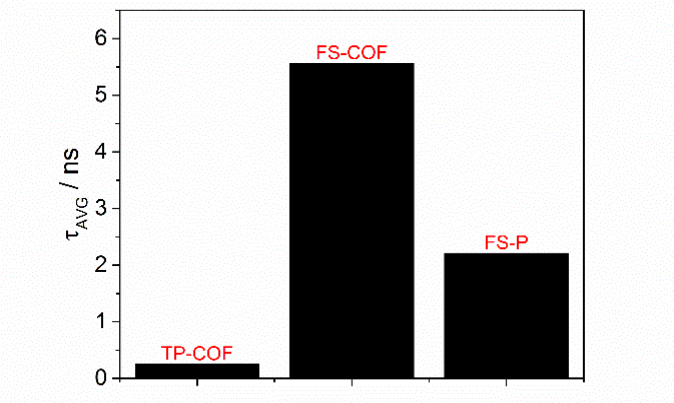

Figure 2-40. Fluorescence life-times in aqueous suspensions obtained by fitting time-correlated single photon counting decays to a sum of three exponentials, which yields τ_1, τ_2, and τ_3 according to $\sum_{i=1}^{n}(A + B_i \exp(-\frac{t}{\tau_i}))$. τ_{AVG} is the weighted average lifetime calculated as $\sum_{i=1}^{n} B_i \tau_i$.

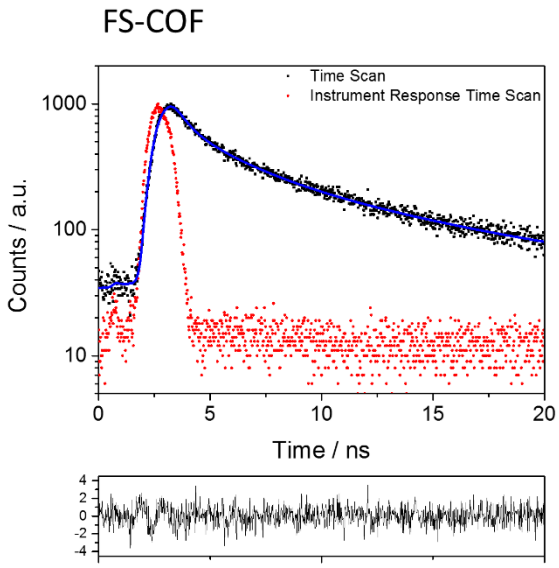

Figure 2-41. TCSPC experiment of **FS-COF** in water. The samples were excited with a λ_{exc} = 370.5 nm laser and emission was observed at λ_{em} = 550 nm. The blue line represents the fit and the black line are the weighted residuals of the fit.

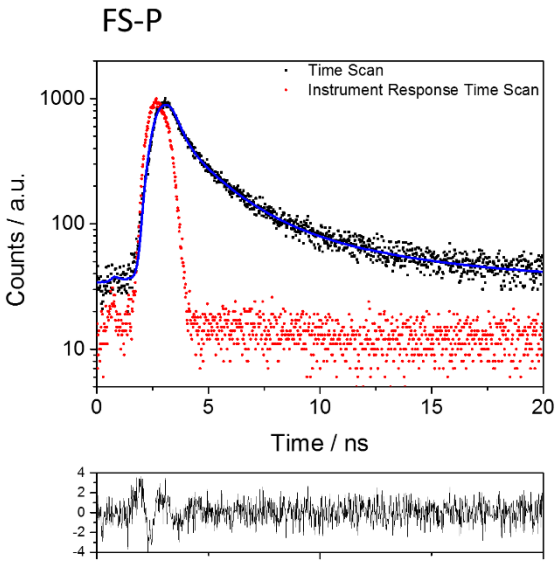

Figure 2-42. TCSPC experiment of **FS-P** in water. The samples were excited with a λ_{exc} = 370.5 nm laser and emission was observed at λ_{em} = 550 nm. The blue line represents the fit and the black line are the weighted residuals of the fit.

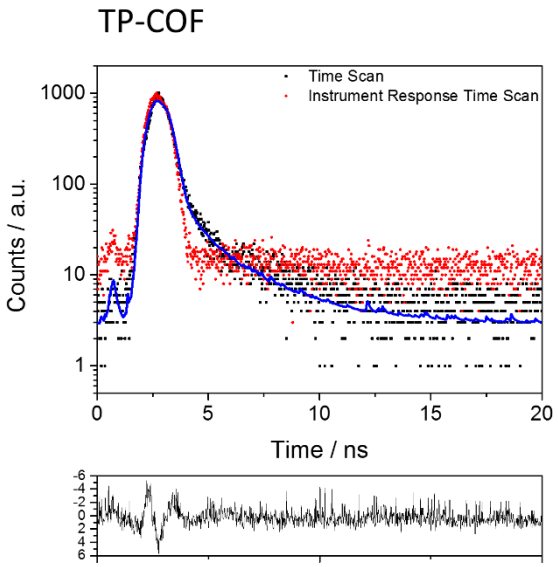

Figure 2-43. TCSPC experiment of **TP-COF** in water. The samples were excited with a λ_{exc} = 370.5 nm laser and emission was observed at λ_{em} = 550 nm. The blue line represents the fit and the black line are the weighted residuals of the fit.

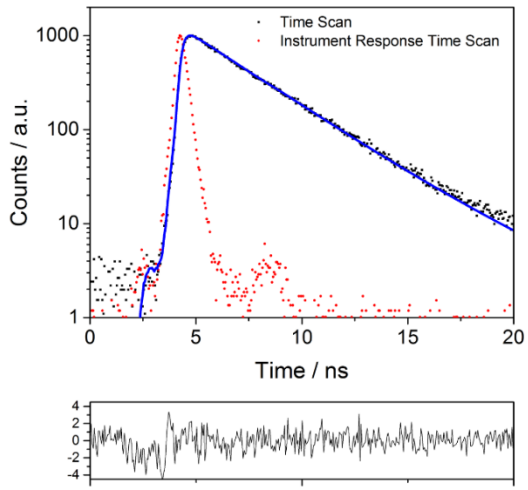

Figure 2-44. TCSPC experiment of **WS5F** in acetone. The samples were excited with a λ_{exc} = 370.5 nm laser and emission was observed at λ_{em} = 603 nm. The blue line represents the fit and the black line are the weighted residuals of the fit.

Table 2-5. Fluorescence life-time measurements.

Material	**λ_{exc} / nm**	**τ_1 / ns**	**B_1 / %**	**τ_2 / ns**	**B_2 / %**	**τ_3 / ns**	**B_3 / %**	**χ^2**
FS-P	550	0.28	25.82	1.45	34.30	4.11	39.89	1.28
FS-COF	550	0.27	8.85	1.75	23.96	7.62	67.19	1.28
TP-COF	550	0.12	92.32	1.82	7.68	-	-	1.90
WS5F	603	0.09	4.07	2.8	88.57	6.19	7.36	1.21

[a] Fluorescence life-times obtained upon excitation at λ_{exc} = 370.5 nm with a laser and observed at λ_{em} = 550, 603 nm. Note that the poor χ^2 value is due to the fast decay for this material close to the instrument response.

2.8.6 Characterization of N_3-COF

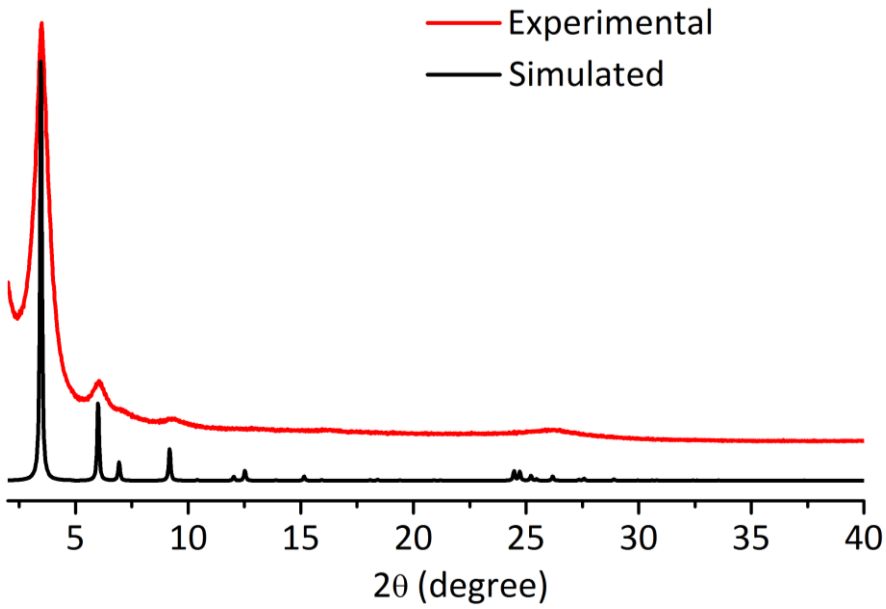

Figure 2-45. Experimental powder X-ray diffraction pattern for **N_3-COF** (red) and simulated PXRD pattern (black).

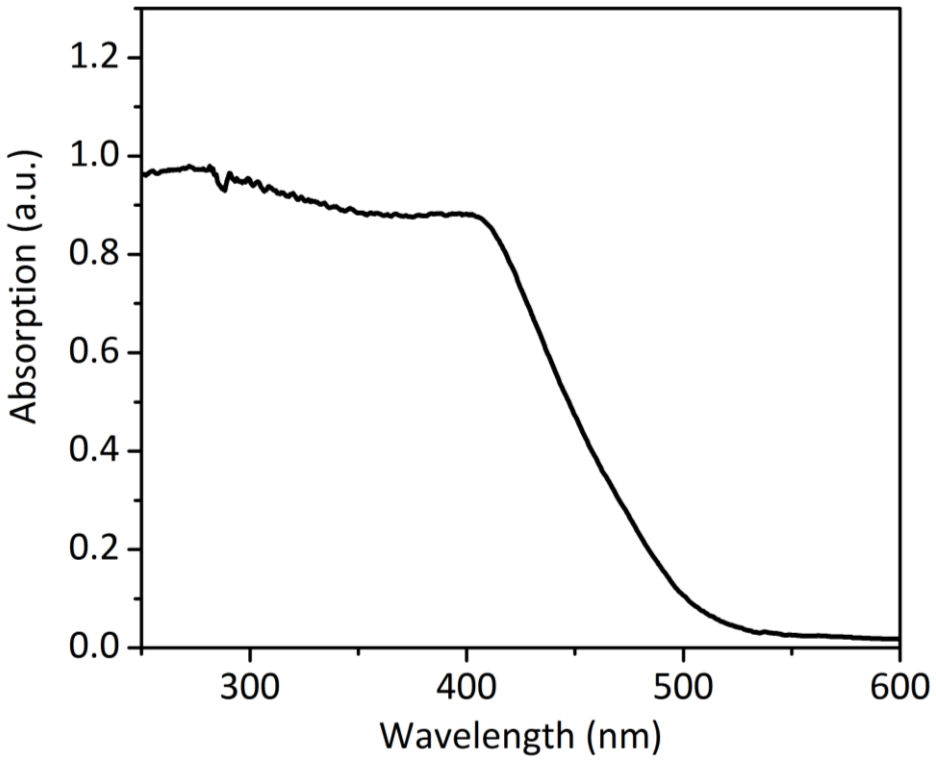

Figure 2-46. UV–Vis absorption spectrum of **N_3-COF** recorded in the solid state.

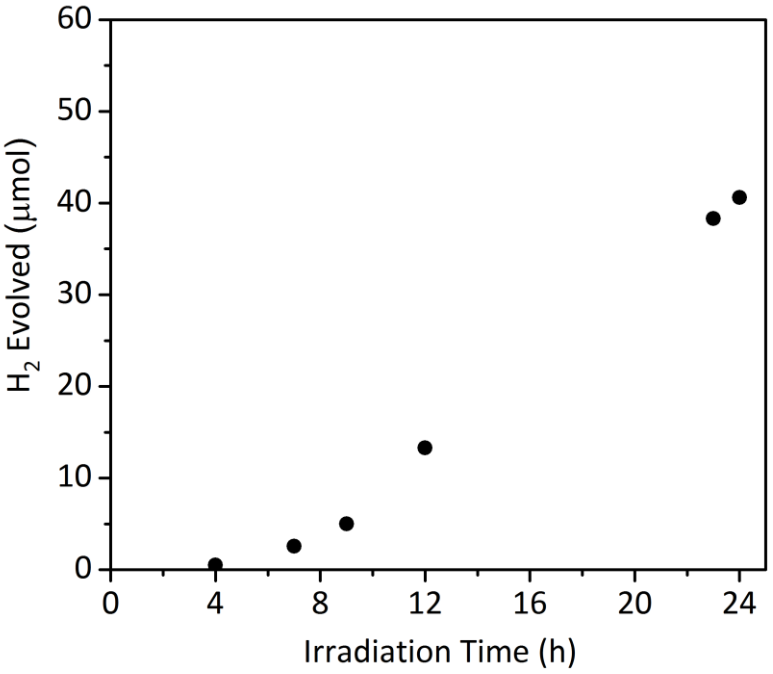

Figure 2-47. Hydrogen evolution plot for **N_3-COF** (5 mg) with 5 µL 8 wt. % hexachloroplatinic acid, dispersed in a 0.1 M ascorbic acid water solution under $\lambda > 420$ nm irradiation.

2.8.7 Characterization of dyes

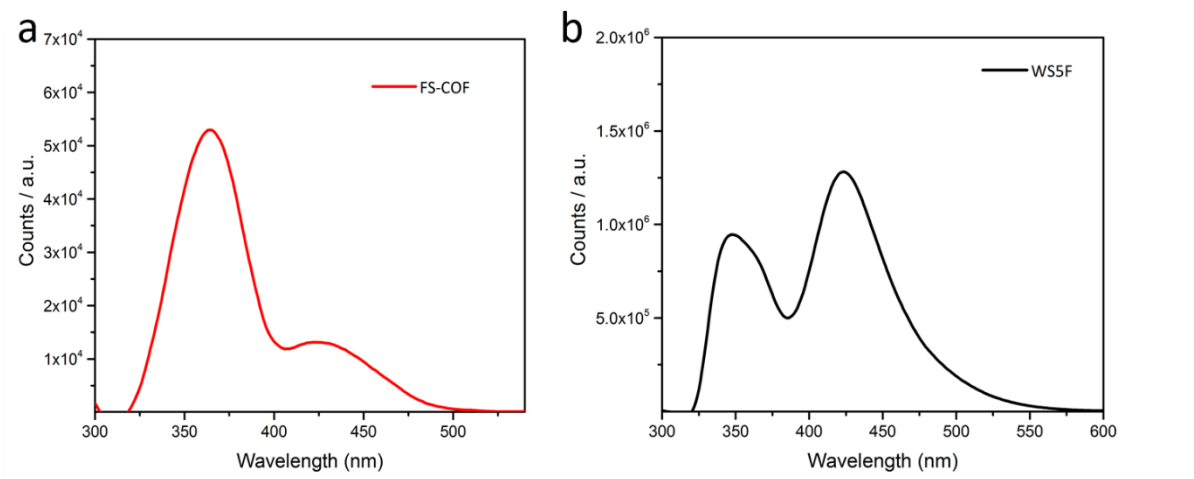

Figure 2-48. (a) Photoluminescence excitation spectra of **FS-COF** in acetone (λ_{em} = 550 nm). (b) Photoluminescence excitation spectra of **WS5F** in acetone (λ_{em} = 640 nm).

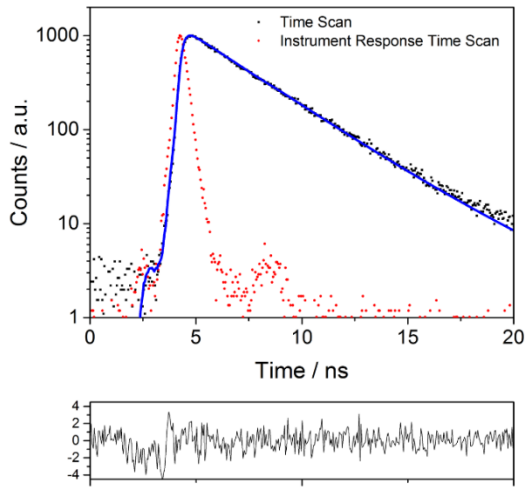

Figure 2-49. TCSPC experiment of **WS5F** in acetone. The samples were excited with a λ_{exc} = 370.5 nm laser and emission was observed at λ_{em} = 603 nm. The blue line represents the fit and the black line are the weighted residuals of the fit.

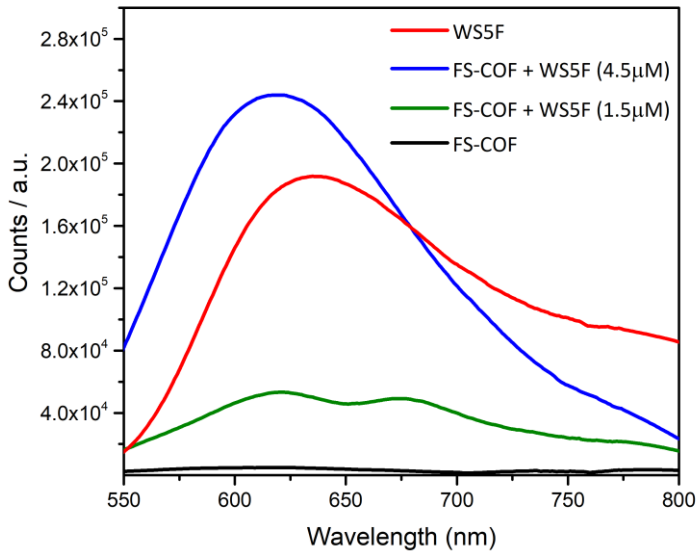

Figure 2-50. Photoluminescence emission spectra of **FS-COF**, **WS5F** and **FS-COF+WS5F** hybrids in acetone (λ_{ex} = 500 nm).

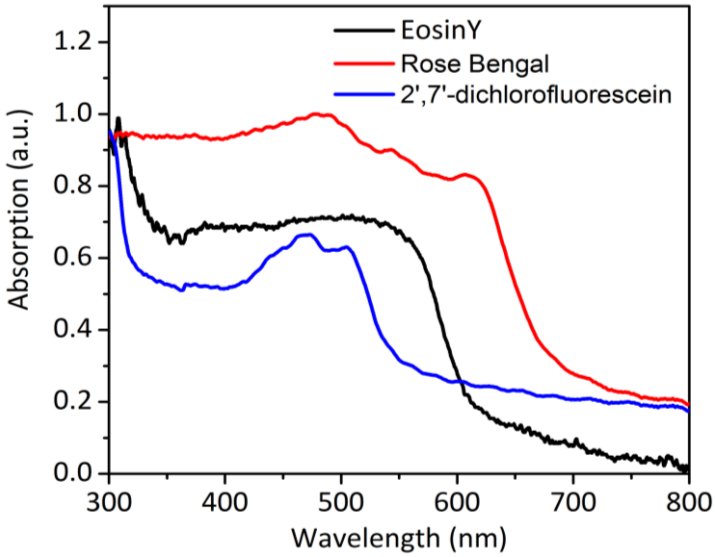

Figure 2-51. Solid-state UV-vis spectra of **Eosin Y**, **Rose Bengal** and **2′,7′-dichlorofluorescein**.

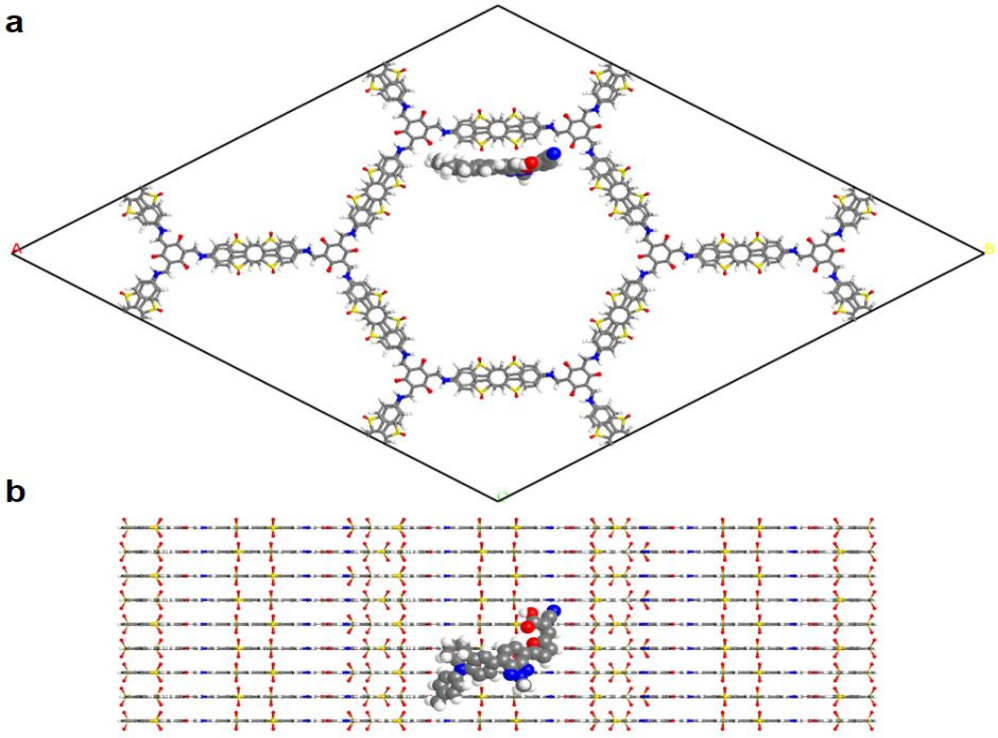

Figure 2-52. Figure showing simulated positioning of the **WS5F** dye in the **FS-COF** crystal structure, viewed parallel to the pore channel along the crystallographic c-axis (a) and perpendicular to the hexagonal layers (b). This model shows just one possible low-energy adsorption site in the COF pore channel, mostly to highlight the relative size of the dye molecule with respect to the mesopores (*i.e.*, the pore channel diameter is large enough to accommodate multiple dye molecules).

2.8.8 P10 polymer hydrogen evolution experiment

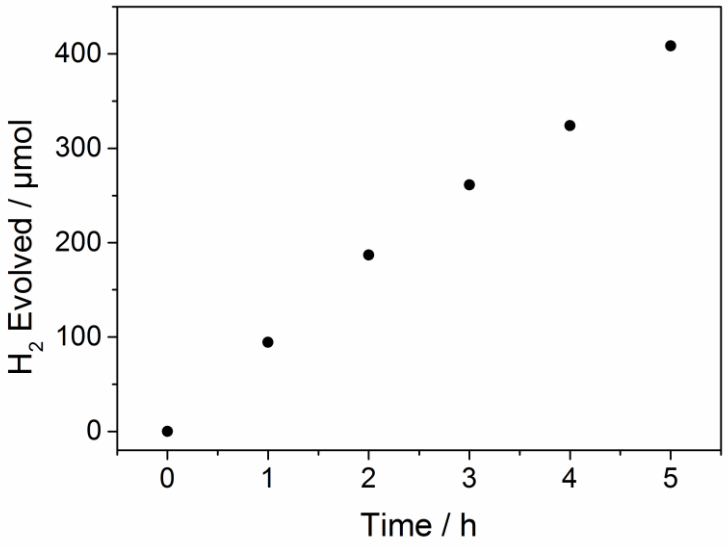

Figure 2-53. Hydrogen evolution plot under visible light illumination ($\lambda > 420$ nm) for **P10** (25 mg) dispersed in a 22.5 mL mixture consisting of equal volumes of H_2O, methanol, and triethylamine.

2.8.9 Tauc plot

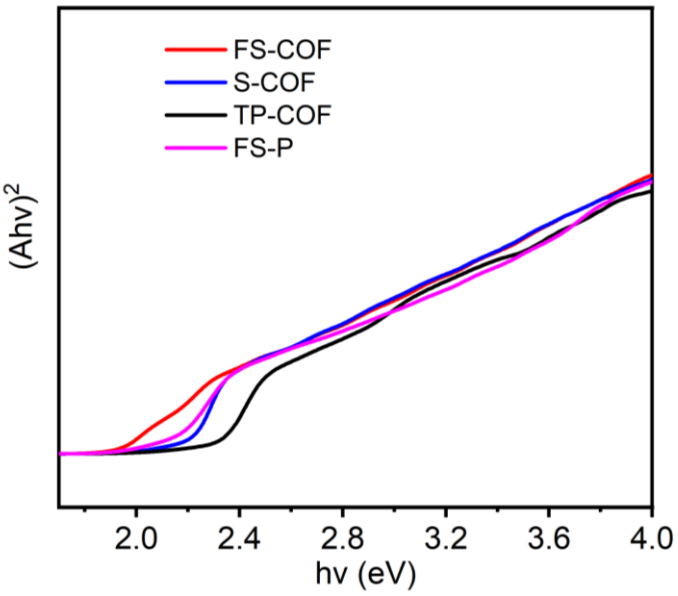

Figure 2-54. Tauc plot for **FS-COF**, **S-COF**, **TP-COF** and **FS-P**.

2.9 References

1. R. S. Sprick, B. Bonillo, R. Clowes, P. Guiglion, N. J. Brownbill, B. J. Slater, F. Blanc, M. A. Zwijnenburg, D. J. Adams and A. I. Cooper, *Angew. Chem. Int. Ed.*, 2016, **55**, 1792–1796.
2. M. Sachs, R. S. Sprick, D. Pearce, S. A. J. Hillman, A. Monti, A. A. Y. Guilbert, N. J. Brownbill, S. Dimitrov, X. Shi, F. Blanc, M. A. Zwijnenburg, J. Nelson, J. R. Durrant and A. I. Cooper, *Nat. Commun.*, 2018, **9**, 1–11.
3. S. Wan, F. Gándara, A. Asano, H. Furukawa, A. Saeki, S. K. Dey, L. Liao, M. W. Ambrogio, Y. Y. Botros, X. Duan, S. Seki, J. F. Stoddart and O. M. Yaghi, *Chem. Mater.*, 2011, **23**, 4094–4097.
4. S. Kandambeth, A. Mallick, B. Lukose, M. Mane, T. Heine, and R. Banerjee, *J. Am. Chem. Soc.*, 2012, **134**, 19524–19527.
5. N. Keller, D. Bessinger, S. Reuter, M. Calik, L. Ascherl, F. C. Hanusch, F. Auras and T. Bein, *J. Am. Chem. Soc.*, 2017, **139**, 8194-8199.
6. Y. Zhu and W. Zhang, *Chem. Sci.*, 2014, **5**, 4957–4961.
7. Y. Tezuka, A. Fukushima, S. Matsui and K. Imai, J. *Colloid Interface Sci.*, 1986, **114**, 16–25.
8. V. S. Vyas, F. Haase, L. Stegbauer, G. Savasci, F. Podjaski, C. Ochsenfeld and B. V Lotsch, *Nat. Commun.*, 2015, **6**, 8508.
9. L. Kruczynski, H. D. Gesser, C. W. Turner and E. A. Speers, *Nature*, 1981, **291**, 399–401.
10. F. T. Wagner and G. A. Somorjai, *Nature*, 1980, **285**, 559–560.
11. X. Wang, K. Maeda, A. Thomas, K. Takanabe, G. Xin, J. M. Carlsson, K. Domen and M. Antonietti, *Nat. Mater.*, 2009, **8**, 76–80.
12. A. Bruno, L. X. Reynolds, C. Dyer-Smith, J. Nelson and S. A. Haque, *J. Phys. Chem. C*, 2013, **117**, 19832–19838.
13. J. E. Kroeze, T. J. Savenije, M. J. W. Vermeulen and J. M. Warman, *J. Phys. Chem. B*, 2003, **107**, 7696–7705.
14. P. E. Shaw, A. Ruseckas and I. D. W. Samuel, *Adv. Mater.*, 2008, **20**, 3516–3520.
15. G. Zhang, G. Li, Z.-A. Lan, L. Lin, A. Savateev, T. Heil, S. Zafeiratos, X. Wang and M. Antonietti, *Angew. Chem. Int. Ed.* 2017, **56**, 13445–13449.
16. P. Pachfule, A. Acharjya, J. Roeser, T. Langenhahn, M. Schwarze, R. Schomaecker, A. Thomas and J. Schmidt, *J. Am. Chem. Soc.*, 2018, **140**, 1423-1427
17. P. Guiglion, A. Monti and M. A. Zwijnenburg, *J. Phys. Chem. C*, 2017, **121**, 1498–1506.
18. A. Hagfeldt, G. Boschloo, L. Sun, L. Kloo, H. Pettersson, *Chem. Rev.* 2010, **110**, 6595-6663
19. P. Wang, S. M. Zakeeruddin, J. E. Moser, M. K. Nazeeruddin, T. Sekiguchi and M. Grätzel, *Nat. Mater.*, 2003, **2**, 402–407.
20. J. He, J. Wang, Y. Chen, J. Zhang, D. Duan, Y. Wang and Z. Yan, *Chem. Commun.*, 2014, **50**, 7063–7066.
21. M. Grätzel, *J. Photochem. Photobiol. C Photochem. Rev.*, 2003, **4**, 145–153.
22. Q. Wang, T. Hisatomi, Y. Suzuki, Z. Pan, J. Seo, M. Katayama, T. Minegishi, H. Nishiyama, T. Takata, K. Seki, A. Kudo, T. Yamada and K. Domen, *J. Am. Chem. Soc.* 2017, **139**, 1675-1683
23. H. Tada, T. Mitsui, T. Kiyonaga, T. Akita and K. Tanaka, *Nat. Mater.*, 2006, **5**, 782–786.
24. J. Xu, L. Zhang, R. Shi and Y. Zhu, *J. Mater. Chem. A*, 2013, **1**, 14766–14772.
25. M. Schröder, K. Kailasam, J. Borgmeyer, M. Neumann, A. Thomas, R. Schomäcker and M. Schwarze, *Energy Technol.*, 2015, **3**, 1014–1017.

26. K. Geng, T. He, R. Liu, K. T. Tan, Z. Li, S. Tao, Y. Gong, Q. Jiang and D. Jiang, *Chem. Rev.*, doi.org/10.1021/acs.chemrev.9b00550.

Chapter 3

Fluorinated covalent organic frameworks for photocatalytic hydrogen evolution from water

3.1 Author contributions

All COFs were synthesized by the thesis author. Photocatalysis experiments were carried out by thesis author and Liang Luo. Zhiwei Fu carried out ICP measurements. Modelling calculations was performed by Dr Linjiang Chen and Xue Wang. Dr Samantha Y. Chong carried out PXRD analyses. Lunjie Liu carried out the SEM experiments. Yang Bai performed the light obscuration measurements. and particle size measurements. Dr Matthew Bilton captured the TEM images.

3.2 Introduction

As discussed in **Chapter 2**, several factors have been shown to have significant influence on photocatalytic activity such as light absorption, wettability and crystallinity. Beside these factors, particles size, thermodynamic driving force for redox reaction and porosity have also been found to influence on hydrogen evolution activity.[1–3] Among these factors, some of factors are independent, but most factors are be influenced by others. This makes it difficult to control one factor without changing others – for example, changing monomers can change the band gap, but is also likely to change wettability or the degree of crystallinity.

Fluorination is a strategy to make hydrophobic materials.[4-6] However, fluorinated poly(*p*-phenylene), PF-PPP-*n* shown higher hydrogen evolution activity than non-fluorinated counterpart, because of the better light absorption and higher solubility in methanol: note that dissolved PF-PPP-*n* can carry out homogenous catalysis in this reaction system.[7] Fluorination has also been developed a strategy to improve the hydrogen evolution activity of C_3N_4 material,[8] which show that the fluorinated C_3N_4 has better redox potential for hydrogen evolution reaction. In both cases, fluorination had changed many properties of materials compared to non-fluorinated counterpart. There are trade-off factors in fluorinated materials for hydrogen evolution, but nonetheless there was a net enhancement of activity after fluorination.

As discussed above, fluorination of COFs is expected to get a highly active hydrogen production catalyst. More importantly, the trade-off and interplay of the factors in photocatalytic hydrogen evolution can be further explored. In this chapter, a series fluorinated, isostructural COFs were made for photocatalytic hydrogen evolution. Fluorine atoms were systematically integrated onto frameworks to make isostructural COFs. Combing both experiments and calculations, more details of structure–property–activity relationships will be explored and discussed.

3.3 COFs synthesis

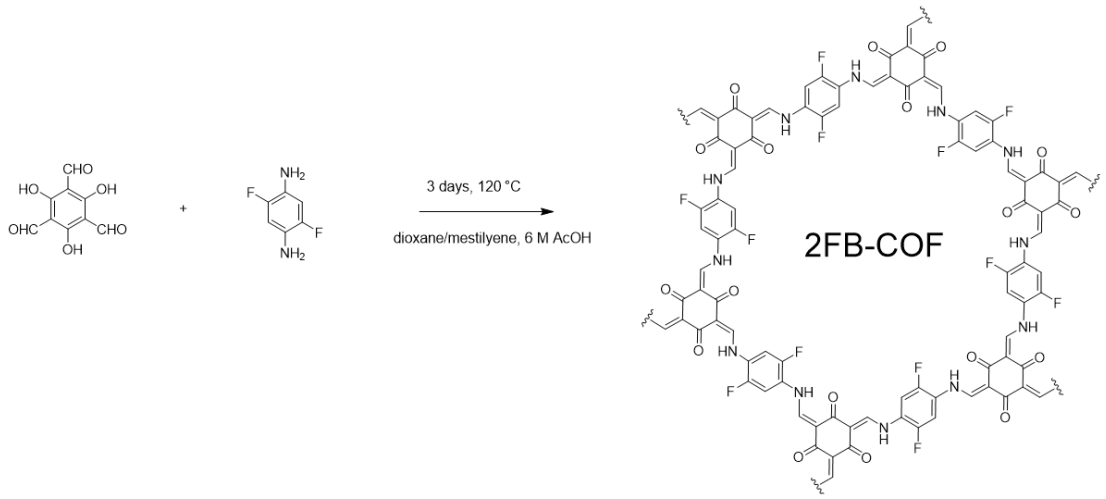

Scheme 3-1. Synthesis of **2FB-COF**

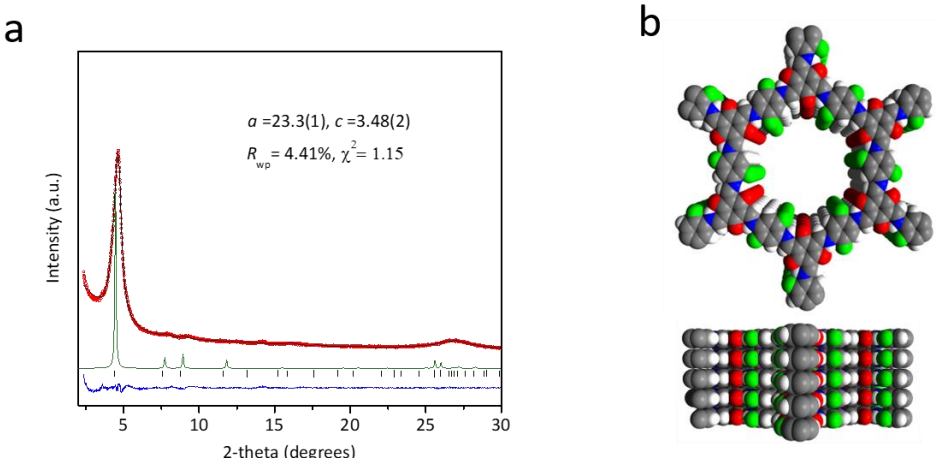

Figure 3-1. (a) Experimental diffraction pattern (red), profile calculated from Le Bail fitting (black) and residual (blue), and pattern simulated from the structural model (green) for **2FB-COF**. Reflection positions are shown by tick marks. (b) Structural models for **2FB-COF** with perfectly eclipsed AA stacking patterns, shown parallel to the pore channel along the crystallographic c axis (top) and parallel to the hexagonal layers (bottom). Grey, white, red, blue and green atoms represent carbon, hydrogen, oxygen, nitrogen and fluorine, respectively.

As discussed in **Chapter 2**, *β*-ketoenamine linked COFs shows decent stability for photocatalytic hydrogen evolution reaction. Thus, in this chapter, *β*-ketoenamine linkage was used to build fluorinated COFs. A series of fluorinated aromatic diamine monomers were used as precursors for COFs synthesis, which allow for obtaining fluorination COFs. As shown in Scheme 3-1, partially fluorinated COF (**2FB-COF**) was synthesized by condensation of 1,3,5-triformylphloroglucinol with a fluorinated diamine monomer (Diamino-2,5-difluorobenzene).

The resulting **2FB-COF** shows a dominant diffraction peak at around 4.64°, which is consistent with the hexagonal structure with an in-plane lattice parameter of 19.01 Å (Figure 3-1a). The broad peak at about 26.86° agree well with stacking parameters distance of 3.32 Å. Parameters extracted from Le Bail refinements for **2FB-COF** are consistent with the simulated AA stacking models.

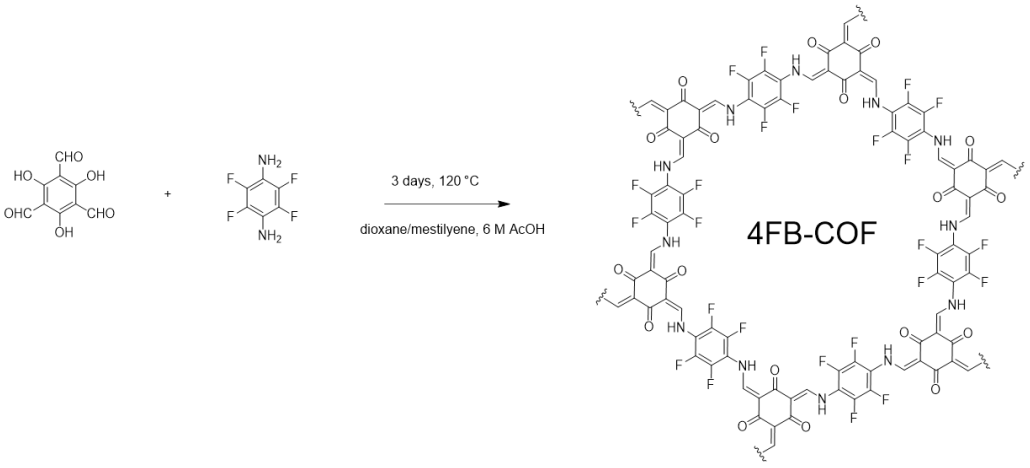

Scheme 3-2. Synthesis of **4FB-COF**

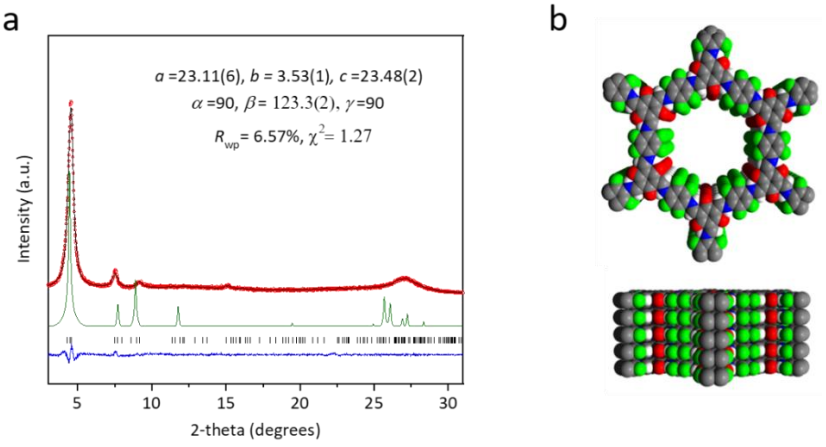

Figure 3-2. (a) Experimental diffraction pattern (red), profile calculated from Le Bail fitting (black) and residual (blue), and pattern simulated from the structural model (green) for **4FB-COF**. Reflection positions are shown by tick marks. (b) Structural models for **4FB-COF** with perfectly eclipsed AA stacking patterns, shown parallel to the pore channel along the crystallographic c axis (top) and parallel to the hexagonal layers (bottom). Grey, white, red, blue and green atoms represent carbon, hydrogen, oxygen, nitrogen and fluorine, respectively.

Fluorinated COF (**4FB-COF**) is a fully fluorinated counterpart for **2FB-COF**, which was synthesized by using 1,3,5-triformylphloroglucinol and 2,3,5,6-Tetrafluoro-1,4-phenylenediamine. Experimental powder X-ray diffraction (PXRD) patterns of **4FB-COF** show similar crystallinity than **2FB-COF**. The diffraction peaks at 4.45, 7.49, 9.10 and 27.05° can be assigned to the (001), (210), (002) and (111) planes, respectively (Figure 3-2a). Unit cell parameters extracted by Le Bail refinements are consistent with the parameters obtained by structure simulations (AA-stacking).

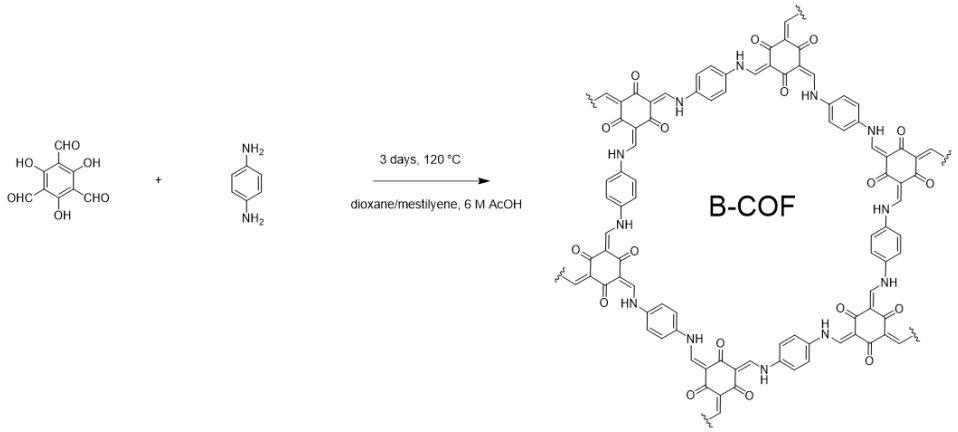

Scheme 3-3. Synthesis of **B-COF**.

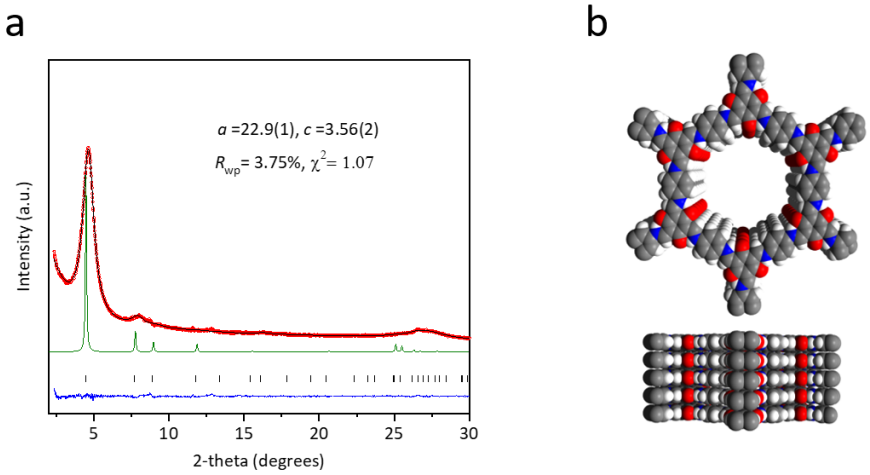

Figure 3-3. (a) Experimental diffraction pattern (red), profile calculated from Le Bail fitting (black) and residual (blue), and pattern simulated from the structural model (green) for **B-COF**. Reflection positions are shown by tick marks. (b) Structural models for **B-COF** with perfectly eclipsed AA stacking patterns, shown parallel to the pore channel along the crystallographic c axis (top) and parallel to the hexagonal layers (bottom). Grey, white, red and blue atoms represent carbon, hydrogen, oxygen and nitrogen, respectively.

For comparison, a non-fluorinated COF (**B-COF**) was synthesized by condensation of 1,3,5-triformylphloroglucinol and *p*-phenylenediamine. The resulting material exhibited a crystalline structure, showing diffraction peaks at 4.63 and 8.03 which can be assigned to the (010) and (110) planes, respectively (Figure 3-3a). The broad peak at around 26.58°, which is corresponded to the π-stacking distance of ~3.3 Å. Unit cell parameters extracted by Le Bail refinements agree well with the parameters from AA stacking mode.

3.4 COFs characterization

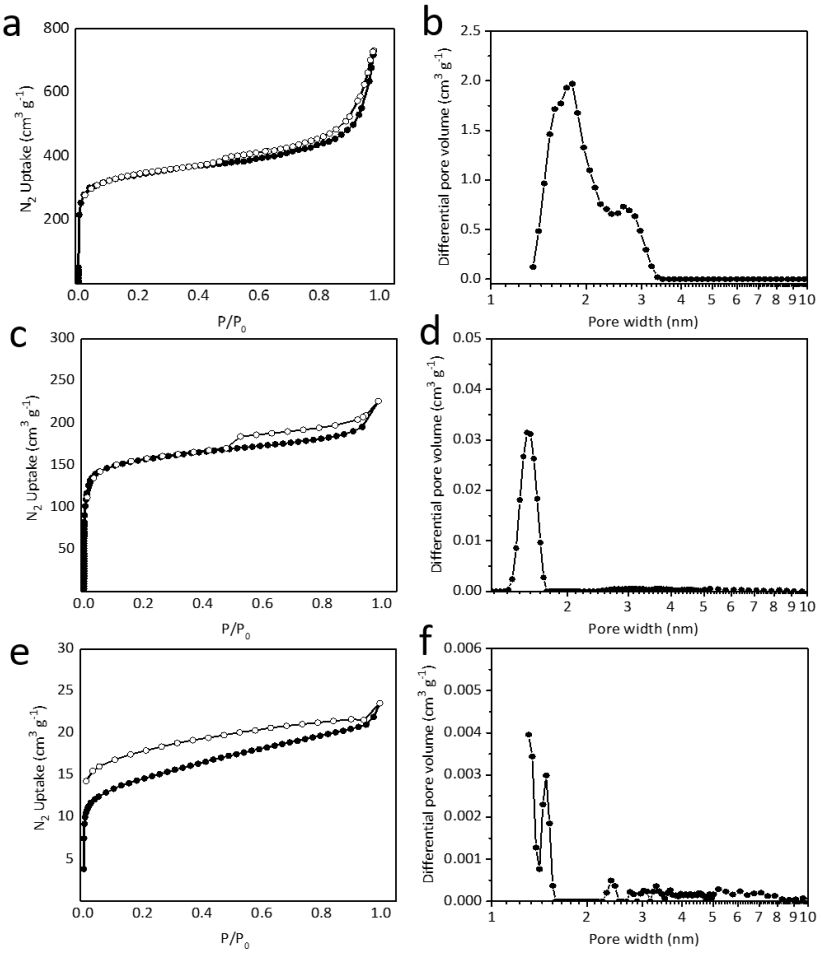

Figure 3-4. Nitrogen adsorption/desorption isotherms for **B-COF** (a), **2FB-COF** (c) and **4FB-COF** (e) recorded at 77 K. Pore size distribution profiles of **B-COF** (b), **2FB-COF** (d) and **4FB-COF** (f) calculated by NL-DFT.

Nitrogen sorption experiments were performed at 77 K to measure the porosity of COFs. From sorption results, the Brunauer−Emmett−Teller (BET) surface areas were calculated to be 611, 1087 and 54 m^2 g^{-1} for **B-COF**, **2FB-COF** and **4FB-COF**, respectively. The N_2 isotherms of

all COFs show rapidly increase at low pressure which can be attributed to microporosity. Pore diameters of COFs were calculated based on nonlocal density functional theory models. The pore diameters of **B-COF**, **2FB-COF** and **4FB-COF** were calculated to be 15.6, 18.1 and 14.9 Å respectively. The experimental surface areas for **B-COF**, **2FB-COF** and **4FB-COF** were less than the idealized, calculated values (1875 and 1577 and 1334 m^2 g^{-1} for **B-COF**, **2FB-COF** and **4FB-COF**). Although all COFs are crystalline, the surface area of **4FB-COF** is far more less than **B-COF** and **2FB-COF**, which might be attributed to blocking of pores by unreacted and insoluble materials. The hysteresis and disequilibrium from isotherm of **4FB-COF** was because of larger particle size of **4FB-COF** (Figure 3-7) than other two samples and remaining of unreacted materials in pores of **4FB-COF**.

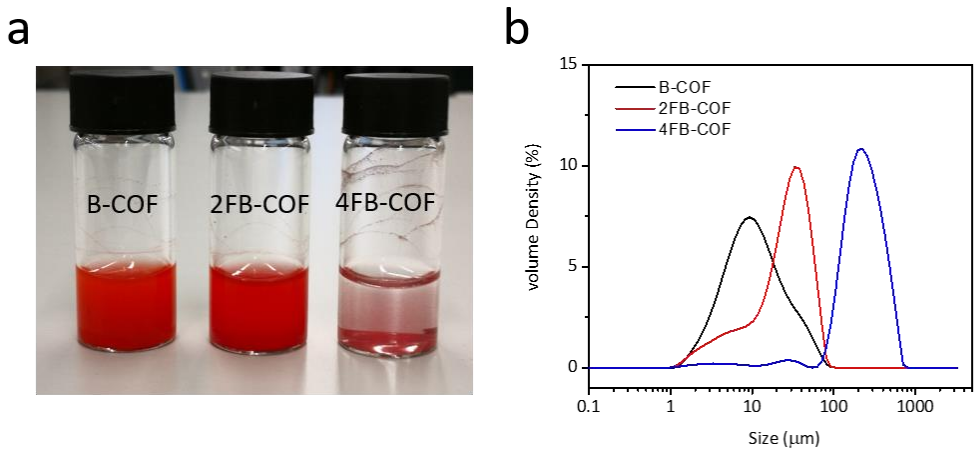

Figure 3-5. (a) Photograph of **B-COF, 2FB-COF** and **4FB-COF** in 0.1 M ascorbic acid aqueous solution. (b) Distribution of particle sizes for the **B-COF, 2FB-COF** and **4FB-COF** in 0.1 M ascorbic acid aqueous solution.

As shown in Figure 3-5a, **B-COF** and **2FB-COF** can uniformly disperse in ascorbic acid aqueous solution, while **4FB-COF** shows relatively poor dispersion under the same conditions, indicating poor wettability of **4FB-COF**. The hydrophobicity of all COFs was further assessed by light obscuration measurements which can measure the light transmittance of samples. The light transmittance was measured directly after dispersing the COFs sample in ascorbic acid solution. The values of transmittance range from 100% to 0%, which indicate the total transmittance and total scattering and/or absorption of the light. The light transmittance of **B-COF** and **2FB-COF** in ascorbic acid aqueous solution was found to be 0.19% and 3.76%, suggesting good wettability of **B-COF** and **2FB-COF**. However, **4FB-COF** based aqueous mixture show a high transmittance of 56.19%. These results indicate that COFs materials

become more hydrophobic after fluorination. More importantly, these wettability differences will have influence on the catalytic activity, which will be discussed later.

Particle sizes is a critical parameter for photocatalysis, for example, the increase in particle size can enhance photocatalytic activity which might cause by improved charge-transport properties or/and light absorption and light scattering.[9,10] However, large particles will also reduce the activity in some cases, because of loss of active surface area of the catalysts and sedimentation.[11] Particle sizes of COFs were measured by static light scattering under catalytic conditions. Sauter mean diameter is an average of particle size, which define as the diameter of sphere that has same surface area or volume.[12] As shown in Figure 3-5b, the particle size distribution of **B-COF** and **2FB-COF** range from 1–100 μm while **4FB-COF** has larger particle size ranging from 55–800 μm. Although **B-COF** and **2FB-COF** shows similar range of particle size distribution, the Sauter mean diameter of **B-COF** was smaller than **2FB-COF** (7.6 μm *vs* 13 μm). **4FB-COF** had the largest diameter of 81.7 μm, which indicates that **4FB-COF** was aggregated in ascorbic acid aqueous solution.

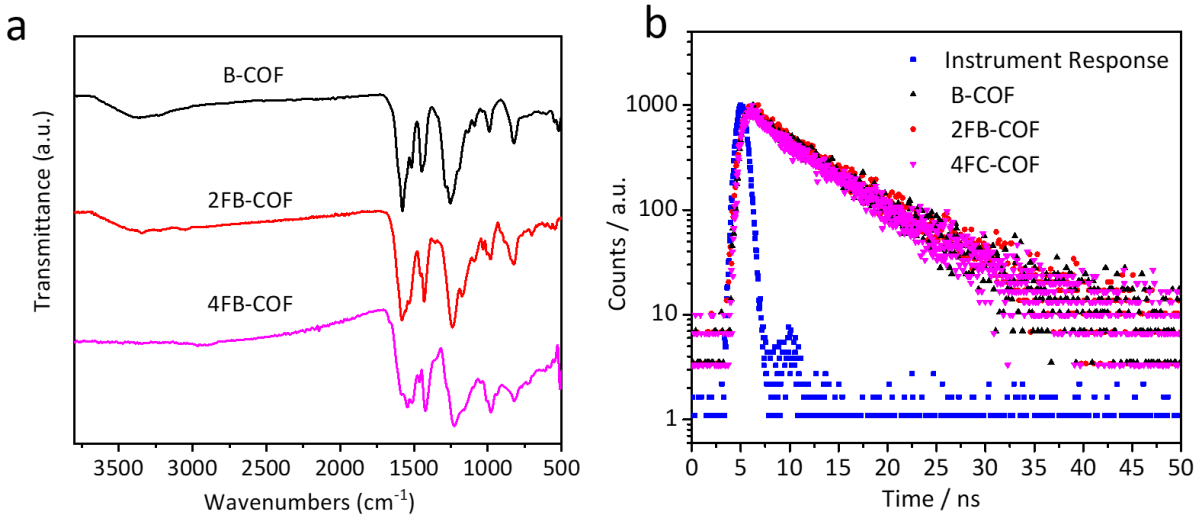

Figure 3-6. (a) FT-IR spectra of **B-COF**, **2FB-COF** and **4FB-COF**. (b) TCSPC experiment of **B-COF**, **2FB-COF** and **4FB-COF** in water. The samples were excited with a λ_{exc} = 310 nm laser and emission was observed at λ_{em} = 410 nm.

All COFs were insoluble in common organic solvents. As shown in Figure 3-6a, Fourier transform infrared spectra (FT-IR) of all COFs show the disappearance of the amine bands (~ 3300 cm^{-1}), suggesting negligible amounts of amine monomers remain in all COFs. Time-correlated single-photon counting (TCSPC) measurements were performed to estimate the

excited-state lifetimes for COFs in aqueous suspensions (Figure 3-6b). The average weighted lifetime of **B-COF**, **2FB-COF** and **4FB-COF** was estimated to be τ_{avg} = 6.83, 6.84 and 7.37 ns, respectively. The results of lifetime measurements indicate that this series COFs have similar lifetimes.

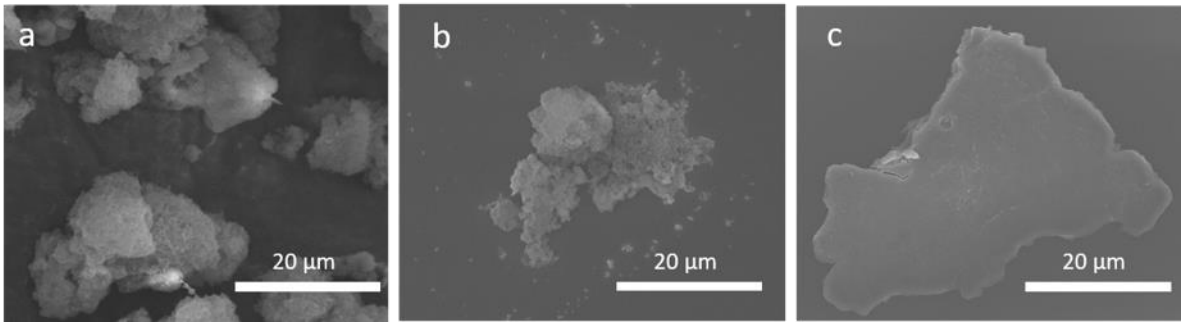

Figure 3-7. SEM images of **B-COF** (a), **2FB-COF** (b) and **4BF-COF** (c).

SEM imaging was used to determine the morphology for COFs. The SEM images of **B-COF** and **2FB-COF** show that they have similar morphology of microplate like structure with agglomeration. However, 4FB-COF show a brick-like morphology with diameter around of 40 µm.

3.5 COFs for hydrogen evolution

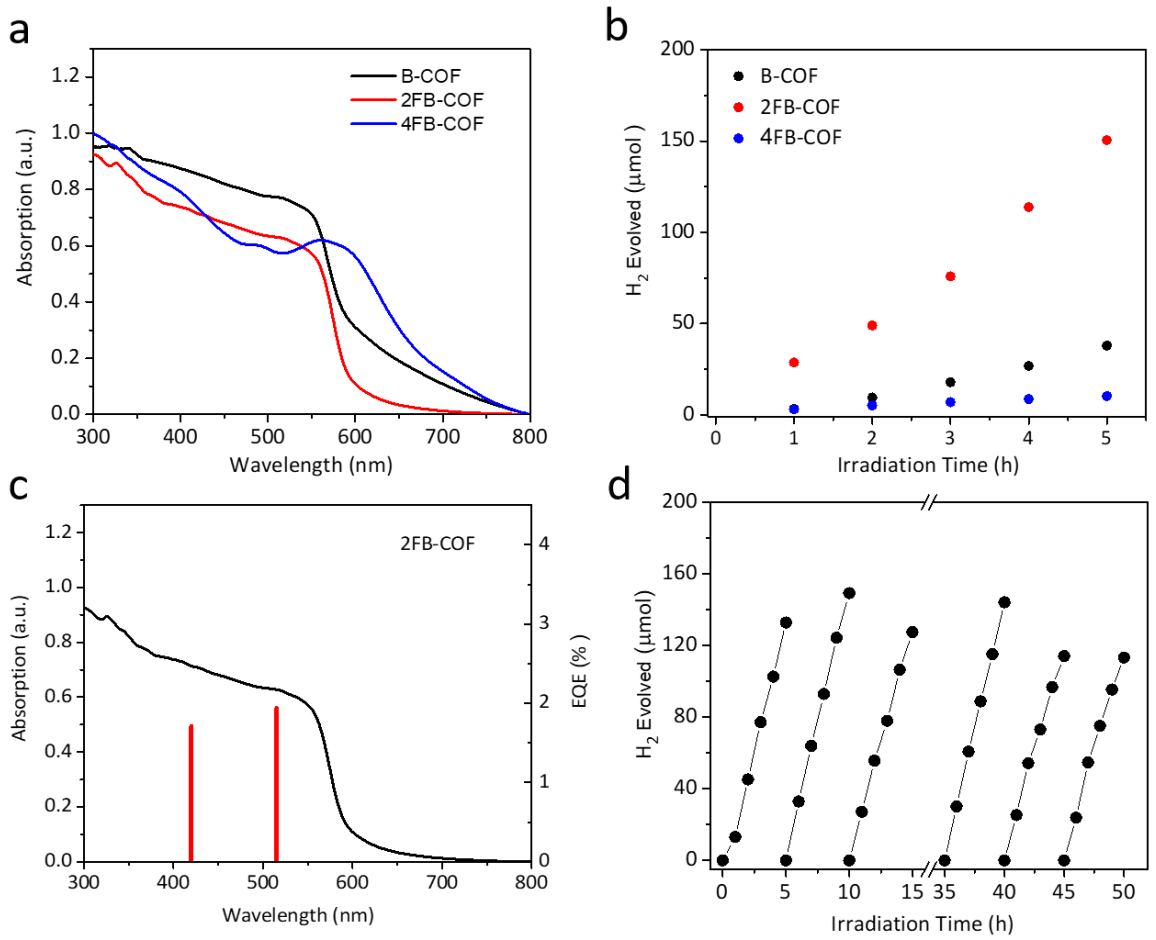

Figure 3-8. (a) Solid state UV–Vis absorption spectra for **B-COF**, **2FB-COF** and **4FB-COF**. (b) Time course for photocatalytic H_2 production using visible light for **B-COF**, **2FB-COF** and **4FB-COF** (5 mg catalyst in water, 5 μL (8 wt% H_2PtCl_6), 0.1 M ascorbic acid, $\lambda > 420$ nm). (c) External quantum efficiency (EQE) of **2FB-COF** (5 mg) in a 0.1 M ascorbic acid water solution under $\lambda = 420$ and 515 nm irradiation, plotted alongside UV-Vis absorption spectra of solid **2FB-COF**. (d) Hydrogen evolution using visible light for **2FB-COF** over 50 hours total photolysis (5 mg catalyst in water, 5 μl (8 wt% H_2PtCl_6), 0.1 M ascorbic acid, $\lambda >$ 420 nm). The sample was degassed after 5 and 10 hours to prevent saturation of the detector, then left under continuous illumination for 20 hours and again degassed after 40 and 45 hours. After 35 hours, 1.25 mmol of ascorbic acid was added.

As shown in UV–Vis absorption spectra, the absorption onset for **B-COF, 2FB-COF** and **4FB-COF** was measured to be 592, 595, 672 nm respectively (Figure 3-8a). Compared to **B-COF** and **2FB-COF**, the absorption onsets for **4FB-COF** was redshifted by ~80 nm. Hydrogen evolution for all COFs were measured using Pt as a co-catalyst and ascorbic acid as an electron

donor. All COFs can produce hydrogen under visible light irradiation. The hydrogen evolution rates were normalized by mass of catalysts, which were found to be 1728, 6169 and 375 μmol g^{-1} h^{-1} for **B-COF, 2FB-COF** and **4FB-COF** respectively. Partially fluorinated **2FB-COF** shows a decent hydrogen production rate which is comparable to state of art catalyst hydrogen evolution catalysts.[13–15] However, it is still lower than **FS-COF**, which we have discussed in **chapter 2**. The hydrogen evolution rate of **2FB-COF** was much higher activity than its isostructural **B-COF** and **4FB-COF**, which reasons will be discussed later.

As shown in Figure 3-8c, external quantum efficiency (EQE) of **2FB-COF** were determined to be 1.71 and 1.94 % at 420 and 515 nm respectively, which is higher than **Diacetylene-COF** (1.3 %)[14] at 420 nm and **N_3-COF** (0.44%)[13] at 450 nm, using TEOA as electron donor. Photocatalysis cycling tests for **2FB-COF** have been performed to measure the stability of **2FB-COF**. Figure 3-8d shows that **2FB-COF** retained the activity after 50 hours visible light irradiation.

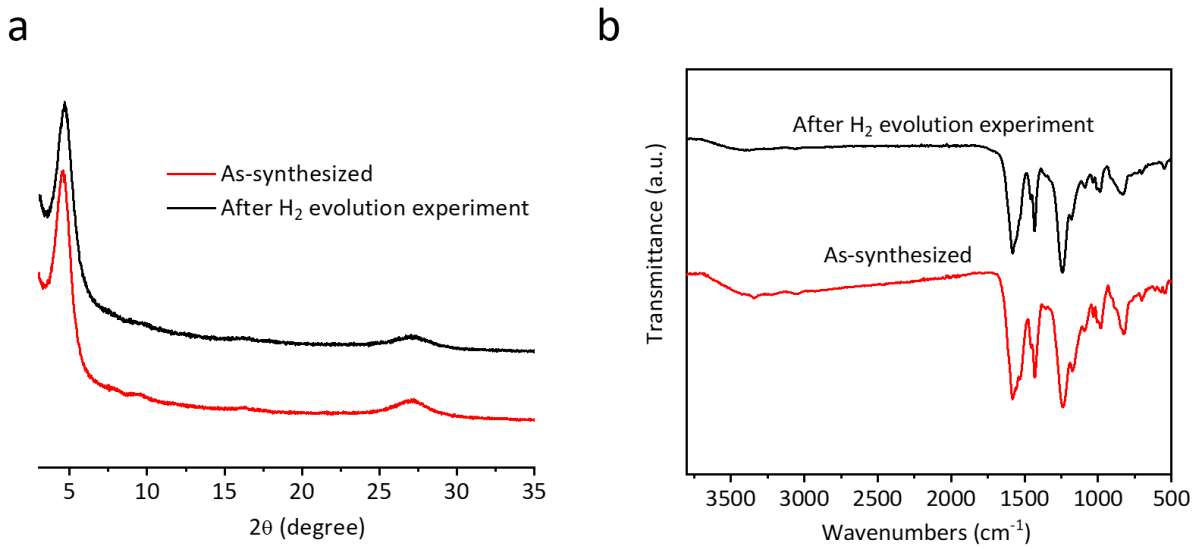

Figure 3-9. (a) Experimental powder X-ray diffraction pattern of **2FB-COF** before (red), after (black) photocatalysis. The characterization was performed after 5 hours hydrogen evolution experiment under visible light (λ > 420 nm). (b) FTIR spectra of **2FB-COF** before (red) and after (black) photocatalysis. The characterization was performed after 5 hours hydrogen evolution experiment under visible light (λ > 420 nm).

In order to measure the stability of **2FB-COF**, FTIR spectra and PXRD patterns were carried out after photocatalysis experiments. As shown in Figure 3-9, no obvious changes can be

observed from FTIR spectra and PXRD patterns after 5 hours photolysis experiments for **2FB-COF**, suggesting good stability of **2FB-COF** under photolysis conditions.

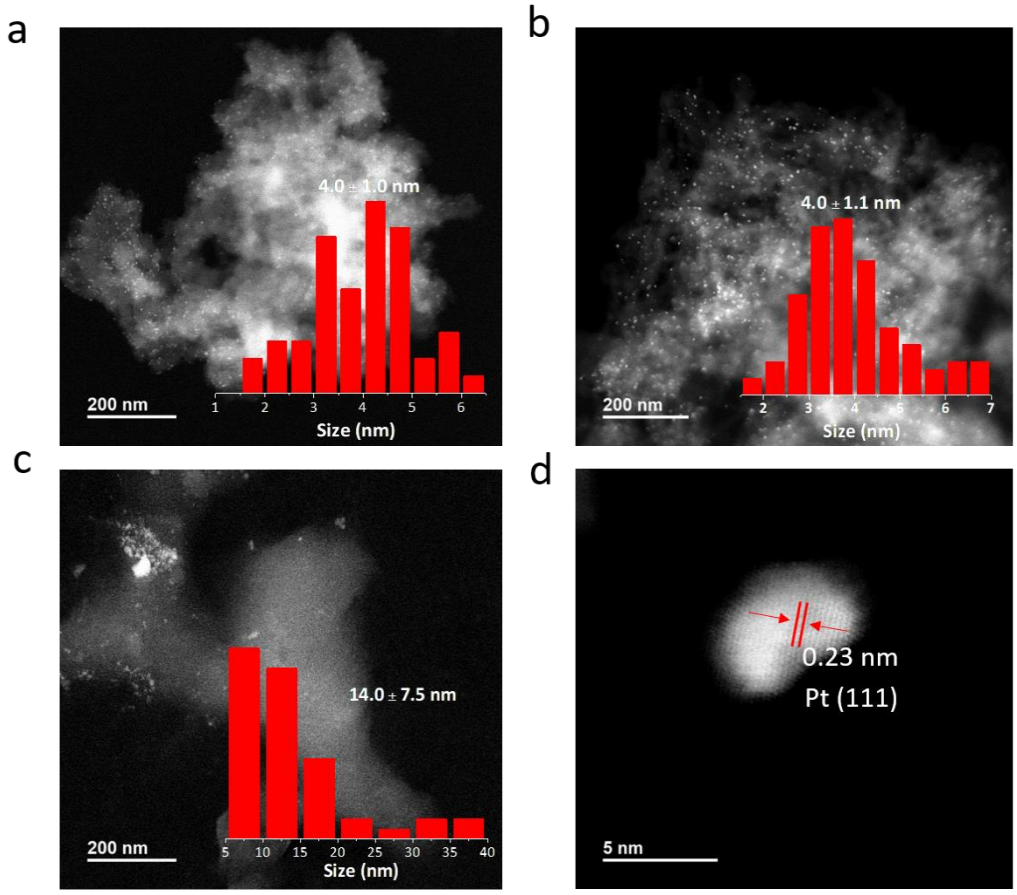

Figure 3-10. HAADF-STEM images of Pt doped (a) **B-COF** (b) **2FB-COF** and (c) **4FB-COF**. Inset image is size distributions of Pt nanoparticles. (d) HAADF-STEM image of Pt nanoparticle for platinized **2FB-COF**.

HAADF-STEM were performed to measure the Pt particle size. As shown in Figure 3-10a, b, **B-COF** and **2FB-COF** shows uniform Pt distribution, which has particles size of 4.0 ± 1.0 and 4.0 ± 1.1 nm, respectively. However, Pt nanoparticles were aggregated in **4FB-COF** with particles size of 14.0 ± 7.5 nm (Figure 3-10c). Figure 3-10d shows the lattice spacing of ca. 0.23 nm corresponds to the (111) planes of Pt. The amount of Pt was determined by inductively coupled plasma-optical emission spectrometry. The weight percent of Pt on COFs were found to be 1.0, 0.67 and 0.19 wt% to **B-COF**, **2FB-COF** and **4FB-COF** respectively. The particle size and concentration of Pt in these COFs are different, which can be attributed to different surface wettability of COFs. These results suggest that wettability of COFs can influence the deposition of co-catalysts, which will in turn influence hydrogen production activity.

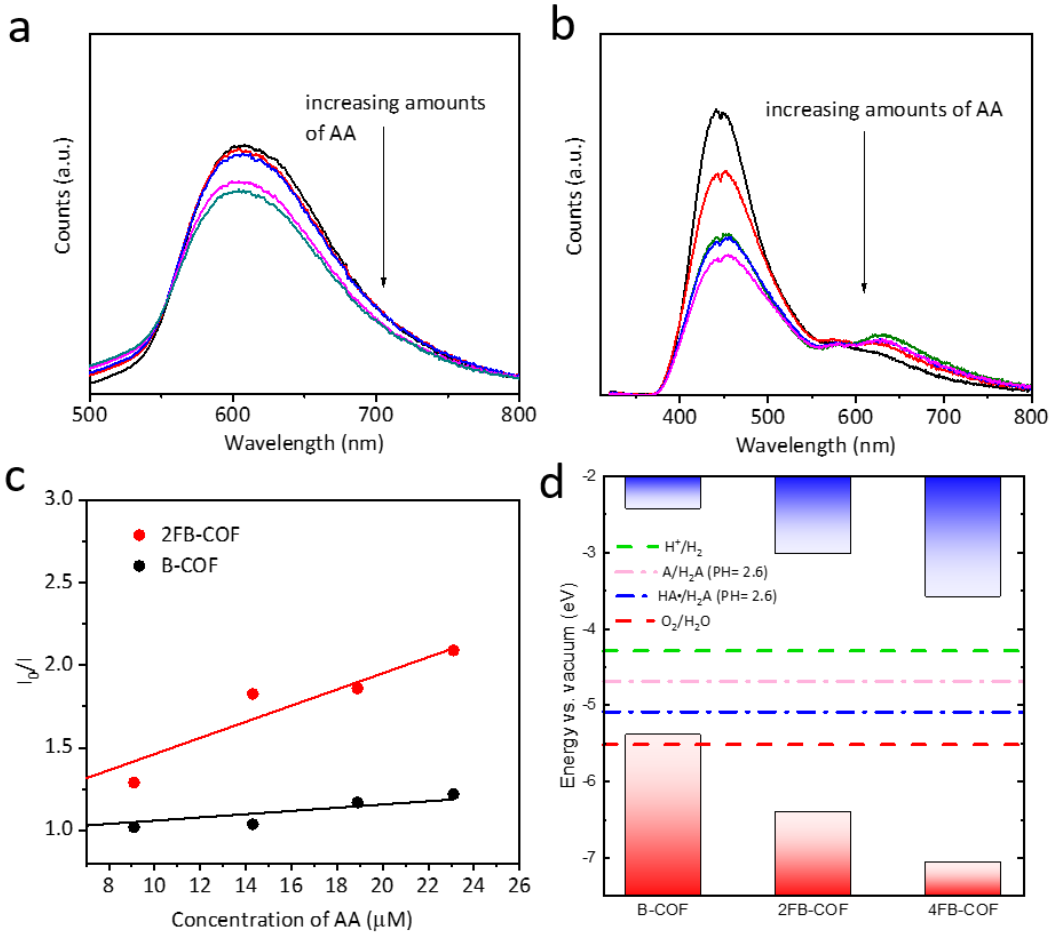

Figure 3-11. (a) Steady-state PL spectra of (a) **B-COF** and (b) **2FB-COF** in water upon the addition of increasing amounts of ascorbic acid (0, 9.1, 14.3, 18.9 and 23.1 μM). The samples are excited at λ_{ex} = 375 and 310 nm, respectively. (c) The Stern–Volmer equation of $(I_0/I) = K_{sv}[C] + 1$ was used to calculate the quenching efficiencies, where I_0 is the initial fluorescence intensity without ascorbic acid, I is the fluorescence intensity after adding ascorbic acid of concentration [C], and K_{sv} is the Stern–Volmer constant. (d) Periodic DFT predicted VBM (red) and CBM (blue) of the COFs with respect to a common vacuum level. Eclipsed (AA) stacking arrangements was considered. For Dashed colored lines indicate the potentials for different solution reactions. All solution potentials shown are for pH 2.6, the experimentally measured pH of a 0.1 M ascorbic acid solution.

In order to measure the capability of COFs for ascorbic acid oxidation, steady-state PL spectra quenching experiments were performed. As shown in Figure 3-11a, **B-COF** aqueous solution excited at 375 nm shows a broad PL peak at around 600 nm. **2FB-COF** aqueous solution excited at 310 nm exhibits two PL peaks at around 450 nm and 630 nm. PL emission peak of

B-COF was quenched by adding ascorbic acid, while PL emission peak of **2FB-COF** was significantly quenched by adding same amount of ascorbic acid. Stern–Volmer constant (K_{SV}) was calculated to quantify these quenching behaviors, which found that K_{SV} of ascorbic acid with **B-COF** and **2FB-COF** was 9.8 and 48.9 mM^{-1}. These results indicate that a higher rate of photoinduced electrons transfer from **2FB-COF** to ascorbic acid than **B-COF**. Figure 3-11d, shows the predicted VBM of the **B-COF** and **2FB-COF** was -5.39 and -6.39 eV. Although both **B-COF** and **2FB-COF** have the thermodynamic driving force for oxidation of ascorbic acid, the values of driving force are different. The driving force of **B-COF** and **2FB-COF** was -0.7 and -1.7 eV for two-hole (A/H_2A) oxidation of ascorbic acid. For one-hole ($HA\cdot/H_2A$) oxidation of ascorbic acid, the oxidation potential of **B-COF** and **2FB-COF** was -0.3 and -1.3 eV. **2FB-COF** has larger oxidation potential than **B-COF** in both case, which suggest that **2FB-COF** can oxidize ascorbic acid more efficiently.

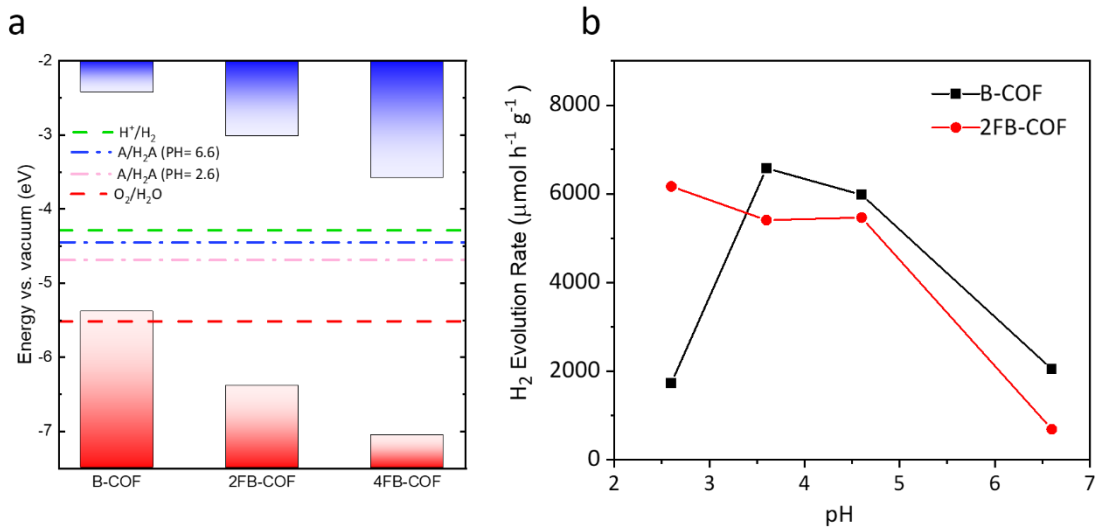

Figure 3-12. (a) Periodic DFT predicted VBM (red) and CBM (blue) of the COFs with respect to a common vacuum level. Eclipsed (AA) stacking arrangements was considered. For dashed colored lines indicate the potentials for different solution reactions. All solution potentials shown are for pH 2.6, the experimentally measured pH of a 0.1 M ascorbic acid solution. (b) Plot of hydrogen evolution rate against reaction system PH for **B-COF** and **2FB-COF**.

As shown in Figure 3-12a, increasing pH of ascorbic acid aqueous solution will give a more positive oxidation potential for ascorbic acid. For example, the oxidation potential for two-hole (A/H_2A) oxidation of ascorbic acid is -4.63 eV under condition of pH=2.6, while it increase to -4.57 eV under condition of pH=6.6. This increase provides more driving force for **B-COF** to

oxidize ascorbic acid. The pH-depend hydrogen evolution experiments were performed to demonstrate this prediction. Figure 3-12b shows that hydrogen evolution rate of **B-COF** was significantly increased when pH was 3.6 and 4.6, reaching of 6579 and 5980 μmol g^{-1} h^{-1}, respectively. Hydrogen production rate of **B-COF** was decreased to 2046 μmol g^{-1} h^{-1} under condition of PH=6.6. However, for **2FB-COF**, the hydrogen production rate was decreased with increasing of pH, which because the more positive oxidation potential will promote ascorbic acid oxidation back reaction. These results indicate that it is important to have a proper driving force to oxidize electron donors for sacrificial hydrogen evolution reaction. The better activity of **2FB-COF** than its isostructural **B-COF** can be attributed to its larger driving force to oxidize ascorbic acid. **2FB-COF** also has a much higher hydrogen evolution rate than **4FB-COF**, which because **2FB-COF** shows better wettability and higher surface areas.

3.6 Summary

Although fluorination makes materials more hydrophobic, it is nevertheless a viable strategy to enhance the activity of organic materials for photocatalytic water splitting, such as conjugated polymers and C_3N_4, because fluorinated materials show broader light absorption and better reduction potentials. In this chapter, a series fluorinated *β*-ketoenamine COFs was synthesized to investigate how the introduction of fluorine into COFs will influence their activity for photocatalytic hydrogen evolution, and to understand how these photoactivity relevant factors interplay.

Partially fluorinated *β*-ketoenamine COF (**2FB-COF**) shows better performance than its isostructural non-fluorinated COF (**B-COF**) and fully fluorinated COF (**4FB-COF**), reaching a hydrogen production rate of 6169 μmol g^{-1} h^{-1} with an EQE of 1.94 % at 515 nm. These results suggest that introducing fluorine into COFs can be a strategy to improve photocatalytic hydrogen production performance. **2FB-COF** shows better predicted driving force of electron donor (ascorbic acid) oxidation while worse wettability than non-fluorinated counterpart (**B-COF)**. However, fully fluorinated **4FB-COF** is less active than **2FB-COF** and **B-COF**, which is because **4FB-COF** is much more hydrophobic and less porous than **2FB-COF** and **B-COF**. Furthermore, the wettability will influence the dispersion of the co-catalysts (Pt), which Pt nanoparticles tend to aggregate on the surface of **4FB-COF**. The trade-off in activity between wettability and driving force indicates that it is challenging to optimize only one factor for improving photocatalytic activity. More comprehensive factors should be considered when we design these materials.[16,17] Finally, for sacrificial hydrogen evolution, not only reduction potential should be considered, but also oxidation potential for scavengers.

3.7 Experimental methods

3.7.1 Materials and methods

All reagents were obtained from Sigma-Aldrich, TCI Europe or Carbosynth Ltd. Anhydrous solvents were purchased from Acros Organics or Fisher Scientific. All chemicals were used without further purification.

3.7.1.1 Powder X-ray diffraction

Powder X-ray diffraction (PXRD) data were collected in vertical transmission mode from loose powder samples held on Mylar film in aluminium well plates, using a Panalytical Empyrean diffractometer equipped with a high throughput screening XYZ stage, X-ray focusing mirror and PIXcel detector with Cu K radiation

3.7.1.2 Gas sorption analysis

Apparent surface areas were measured by nitrogen sorption at 77.3 K using a Micromeritics ASAP 2420 volumetric adsorption analyzer. Powder samples were degassed offline at 393 K for 12 h under dynamic vacuum (10^{-5} bar) before analysis, followed by degassing on the analysis port under vacuum, also at 393 K. Pore size distributions of COFs from fitting the nonlocal density functional theory (NLDFT) model to the adsorption data.

3.7.1.3 Fourier-transform infrared spectroscopy

IR Spectra were recorded using a Bruker Tensor 27 FT-IR spectrometer. Samples were analyzed as KBr disks for 16 scans with a resolution of 4 cm^{-1}.

3.7.1.4 UV-Vis absorption spectra

UV-Vis absorption spectra of the polymers were measured on Agilent Cary 5000 UV-Vis-NIR Spectrometer. UV-Vis spectrometer by measuring the reflectance of powders in the solid state.

3.7.1.5 Static light scattering measurements

Static light scattering measurements were performed on a Malvern Mastersizer 3000 Particle Sizer. COFs were dispersed in ascorbic acid aqueous solution (0.1 M) by 10 minutes of ultrasonication and the resultant suspensions were injected into a stirred Hydro SV quartz cell, containing more of ascorbic acid aqueous solution (0.1 M). Particle sizes were fitted according to Mie theory, using the Malvern 'General Purpose' analysis model, for non-spherical particles with fine powder mode turned on.

3.7.1.6 Scanning electron microscopy

COF morphologies were imaged using a Hitachi S-4800 cold field emission scanning electron microscope (FE-SEM). Samples were prepared by depositing the dry powders on 15 mm Hitachi M4 aluminium stubs using an adhesive high-purity carbon tab before coating with a 2 nm layer of gold using an Emitech K550X automated sputter coater. Imaging was conducted at a working voltage of 3 kV and a working distance of 8 mm using a mix of upper and lower secondary electron detectors.

3.7.1.7 Transmission electron microscopy

HAADF-STEM Images were obtained on a JEOL 2100FCs microscopy at an accelerating voltage of 200 kV. The samples were prepared by drop-casting sonicated acetone suspensions of the materials onto a copper grid.

3.7.1.8 Time-correlated single photon counting (TCSPC) measurements

TCSPC Experiments were performed on an Edinburgh Instruments LS980-D2S2-STM spectrometer equipped with picosecond pulsed LED excitation sources and a R928 detector, with a stop count rate below 5%. Suspensions were prepared by ultrasonicating the polymer in water. The instrument response was measured with colloidal silica (LUDOX® HS-40, Sigma-Aldrich) at the excitation wavelength without filter. Decay times were fitted in the FAST software using suggested lifetime estimates.

3.7.1.9 Hydrogen evolution experiments

A flask was charged with the COF powder (5 mg), 0.1 M ascorbic acid water solution (25 mL), and hexachloroplatinic acid (5 µl, 8 wt. % aqueous solution) as a platinum precursor. The resulting suspension was ultrasonicated 20 minutes before degassing by N_2 bubbling for 30 minutes. The reaction mixture was illuminated with a 300 W Newport Xe light-source (Model: 6258, Ozone free) for the time specified using appropriate filters. The lamp was cooled by water circulating through a metal jacket. Gas samples were taken with a gas-tight syringe, and run on a Bruker 450-GC gas chromatograph. Hydrogen was detected with a thermal conductivity S3 detector referencing against standard gas with a known concentration of hydrogen. Hydrogen dissolved in the reaction mixture was not measured and the pressure increase generated by the evolved hydrogen was neglected in the calculations. The rates were determined from a linear regression fit. After the photocatalysis experiment, COFs were recovered by washing with water and acetone then dried at 120 °C.

3.7.1.10 External quantum efficiency measurements

The external quantum efficiency for the photocatalytic H_2 evolution was measured using a λ = 420 nm LED and λ = 515 nm LED controlled by an IsoTech IPS303DD power supply. For the experiments **2FB-COF** (5 mg) was suspended in an aqueous solution containing ascorbic acid (0.1 M, 8 mL) and hexachloroplatinic acid (5 µl, 8 wt. % aqueous solution). An area of 8 cm^2 was illuminated and the light intensity was measured with a ThorLabs S120VC photodiode power sensor controlled by a ThorLabs PM100D Power and Energy Meter Console. The external quantum efficiencies were estimated using the equation below:

$$\eta EQE = \frac{moles\ of\ hydrogen\ evolved}{moles\ of\ the\ incidentphotons} \times 100\%$$

3.7.2 Synthetic procedures

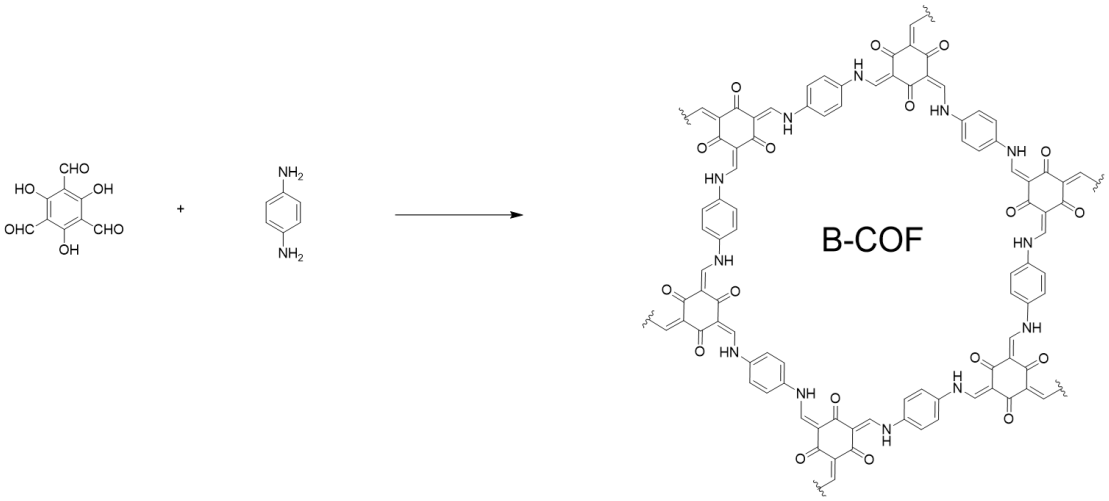

Scheme 3-4. Synthesis of **B-COF**.

B-COF: A Schlenk tube was charged with 2,4,6-triformylphloroglucinol (63 mg, 0.3 mmol), *p*-phenylenediamine (48.7 mg, 0.45 mmol), mesitylene (1.5 mL), 1,4-dioxane (1.5 mL) and aqueous acetic acid (0.5 mL, 6 M). This mixture was homogenized by sonication for 10 minutes and the tube was then flash frozen at 77 K (liquid N_2 bath) and degassed by three freeze-pump-thaw cycles. The tube was sealed off and then heated at 120 °C for 3 days. The precipitate was collected by centrifugation and washed with anhydrous acetone (300 mL). After drying at 120 °C, the product was obtained a deep red-colored powder (86 mg, 79%). Anal. Calcd for $(C_{42}H_{40}N_4O_6)_n$: C, 72.40; H, 5.79; N, 8.04; O, 13.78. Found: C, 57.02; H, 3.79; N, 10.90.

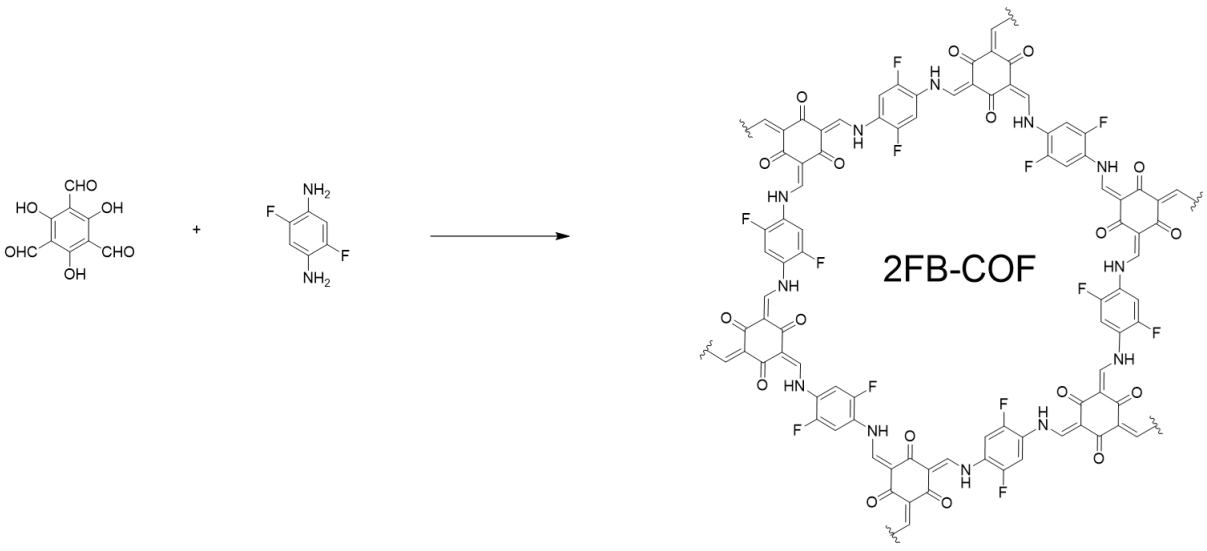

Scheme 3-5. Synthesis of **2FB-COF**.

2FB-COF: A Schlenk tube was charged with 2,4,6-triformylphloroglucinol (63 mg, 0.3 mmol), Diamino-2,5-difluorobenzene (64.9 mg, 0.45 mmol), mesitylene (1.5 mL), 1,4-dioxane (1.5 mL) and aqueous acetic acid (0.5 mL, 6 M). This mixture was homogenized by sonication for 10 minutes and the tube was then flash frozen at 77 K (liquid N_2 bath) and degassed by three freeze-pump-thaw cycles. The tube was sealed off and then heated at 120 °C for 3 days. The precipitate was collected by centrifugation and washed with anhydrous acetone (300 mL). After drying at 120 °C, the product was obtained a deep red-colored powder (86 mg, 79%). Anal. Calcd for $(C_{42}H_{34}F_6N_4O_6)_n$: C, 62.69; H, 4.26; F, 14.16; N, 6.96; O, 11.93 . Found: C, 49.44; H, 2.52; N, 9.68.

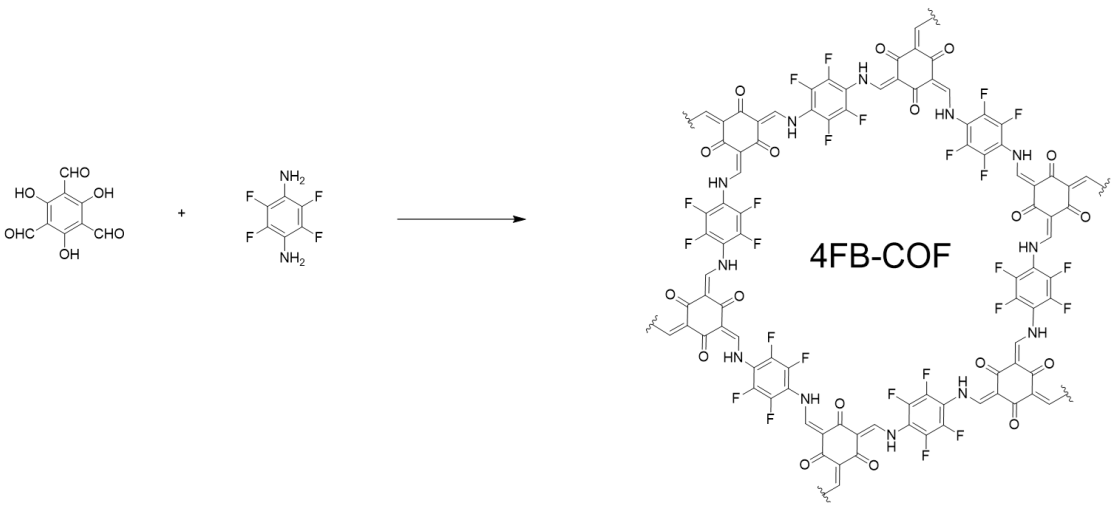

Scheme 3-6. Synthesis of **4FB-COF**.

4FB-COF: A Schlenk tube was charged with 2,4,6-triformylphloroglucinol (63 mg, 0.3 mmol), 2,3,5,6-Tetrafluoro-1,4-phenylenediamine (81 mg, 0.45 mmol), mesitylene (1.5 mL), 1,4-dioxane (1.5 mL) and aqueous acetic acid (0.5 mL, 6 M). This mixture was homogenized by sonication for 10 minutes and the tube was then flash frozen at 77 K (liquid N_2 bath) and degassed by three freeze-pump-thaw cycles. The tube was sealed off and then heated at 120 °C for 3 days. The precipitate was collected by centrifugation and washed with anhydrous acetone (300 mL). After drying at 120 °C, the product was obtained a deep red-colored powder (86 mg, 79%). Anal. Calcd for $(C_{42}H_{28}F_{12}N_4O_6)_n$: C, 55.27; H, 3.09; F, 24.98; N, 6.14; O, 10.52. Found: C, 49.07; H, 1.60; N, 10.14.

3.7.3 Powder X-ray diffraction

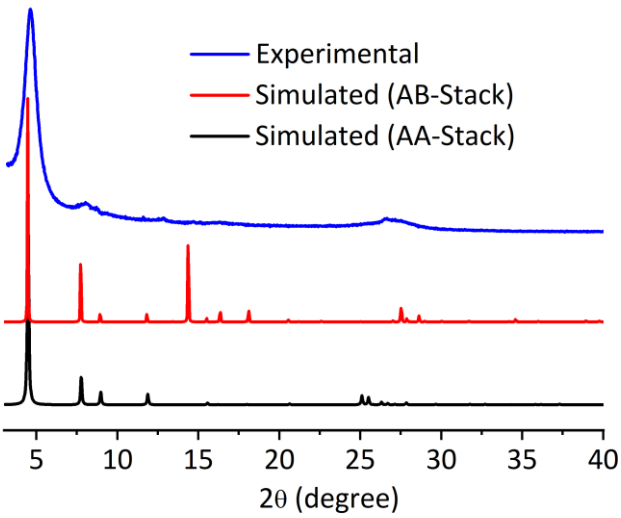

Figure 3-13. Experimental powder X-ray diffraction pattern of **B-COF** (blue) and simulated PXRD pattern (red and black).

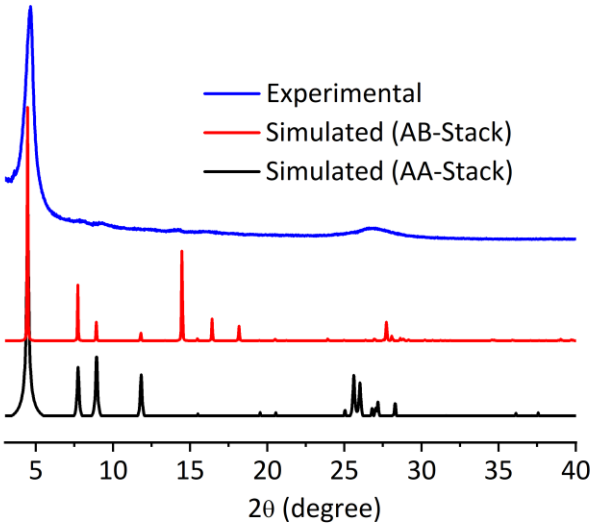

Figure 3-14. Experimental powder X-ray diffraction pattern of **2FB-COF** (blue) and simulated PXRD pattern (red and black).

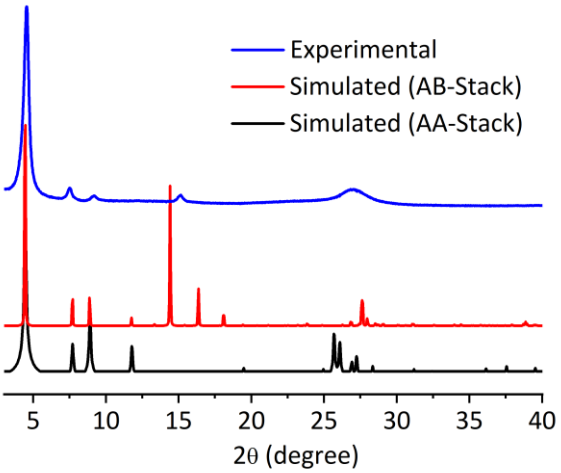

Figure 3-15. Experimental powder X-ray diffraction pattern of **4FB-COF** (blue) and simulated PXRD (red and black).

3.7.4 Hydrogen evolution experiments

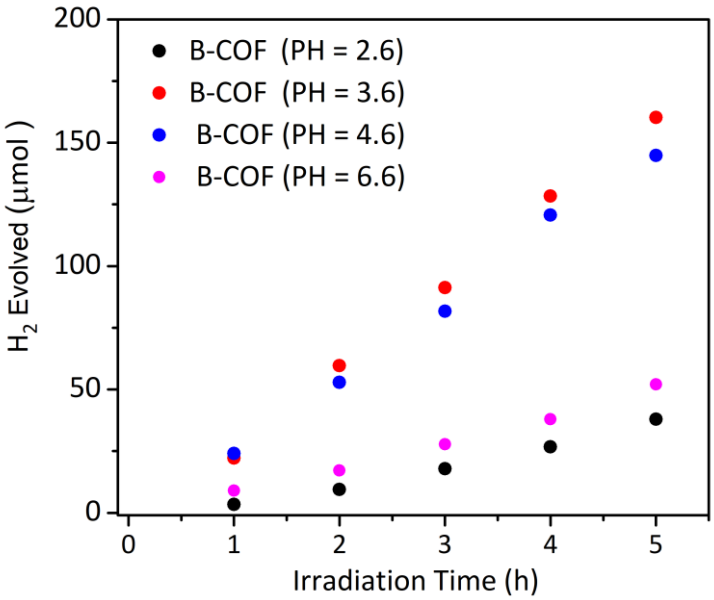

Figure 3-16. Hydrogen evolution rate for **B-COF** at different pH values under λ > 420 nm irradiation using ascorbic acid (0.1 M) as scavenger.

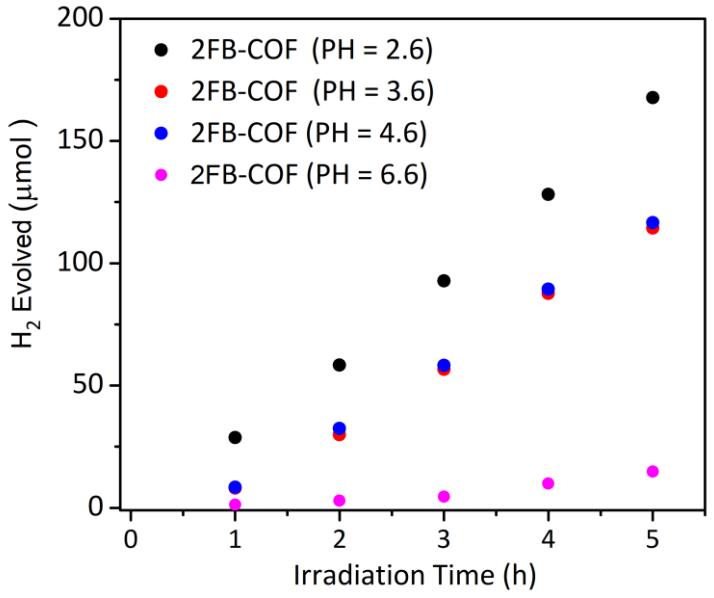

Figure 3-17. Hydrogen evolution rate for **2FB-COF** at different pH values under λ > 420 nm irradiation using ascorbic acid (0.1 M) as scavenger.

3.7.5 Time-correlated single photon counting

Table 3-1. Fluorescence life-time measurements in water suspension.

Material	λ_{exc} / nm	τ_1 / ns	B_1 / %	τ_2 / ns	B_2 / %	τ_3 / ns	B_3 / %	χ^2	τ_{avg}[b] / ns
B-COF	310	0.247	4.386	3.87	28.47	8.52	67.14	1.062	6.83
2FB-COF	310	0.626	4.645	4.41	29.71	8.32	65.60	1.28	6.84
4FB-COF	310	1.034	7.3	6.62	85.07	21.81	7.63	1.03	7.37

[a] Fluorescence life-times in water suspension obtained upon excitation at λ_{exc} = 310 nm with a laser and observed at λ_{em} = 410 nm. Note that the poor χ^2 value is due to the fast decay for this material close to the instrument response. [B] Fluorescence life-times in water suspension obtained from fitting time-correlated single photon counting decays to a sum of three exponentials, which yield τ_1, τ_2, and τ_3 according to $\sum_{i=1}^{n}(A + B_i \exp(-t/\tau_i))$. τ_{AVG} is the weighted average lifetime calculated as $\sum_{i=1}^{n} B_i \tau_i$.

3.8 References

1. R. S. Sprick, Y. Bai, A. A. Y. Guilbert, M. Zbiri, C. M. Aitchison, L. Wilbraham, Y. Yan, D. J. Woods, M. A. Zwijnenburg and A. I. Cooper, *Chem. Mater.*, 2019, **31**, 305–313.
2. R. S. Sprick, L. Wilbraham, Y. Bai, P. Guiglion, A. Monti, R. Clowes, A. I. Cooper and M. A. Zwijnenburg, *Chem. Mater.*, 2018, **30**, 5733–5742.
3. C. M. Aitchison, R. S. Sprick and A. I. Cooper, *J. Mater. Chem. A*, 2019, **7**, 2490–2496.
4. Q. Sun, B. Aguila, G. Verma, X. Liu, Z. Dai, F. Deng, X. Meng, F. Xiao, S. Ma, *Chem*, 2016, **1**, 628-639.
5. I. Woodward, W. C. E. Schofield, V. Roucoules and J. P. S. Badyal, *Langmuir*, 2003, **19**, 3432-3438.
6. D. O. H. Teare, C. G. Spanos, P. Ridley, E. J. Kinmond, V. Roucoules, J. P. S. Badyal, S. A. Brewer, S. Coulson and C. Willis, *Chem. Mater.* 2002, **14**, 4566-4571.
7. K. Maruo, K. Yamada, Y. Wada and S. Yanagida, *Bull. Chem. Soc. Jpn.*, 1993, **66**, 1053-1064.
8. Y. Wang, Y. Di, M. Antonietti, H. Li, X. Chen, and X. Wang, *Chem. Mater.*, 2010, **22**, 5119–5121.
9. R. Noriega, J. Rivnay, K. Vandewal, F. P. V. Koch, N. Stingelin, P. Smith, M. F. Toney and A. Salleo, *Nat. Mater.*, 2013, **12**, 1038–1044.
10. C. M. Aitchison, R. S. Sprick and A. I. Cooper, *J. Mater. Chem. A*, 2019, **7**, 2490–2496
11. L. Wang, R. Fern´andez-Ter´an, L. Zhang, D. L. A. Fernandes,L. Tian, H. Chen and H. Tian, *Angew. Chem., Int. Ed.*, 2016, **55**, 12306–1231

12. H. Ghassemi, *Macromolecules*, 1994, **27**, 3116–3118.
13. V. S. Vyas, F. Haase, L. Stegbauer, G. Savasci, F. Podjaski, C. Ochsenfeld and B. V Lotsch, *Nat. Commun.*, 2015, **6**, 8508.
14. P. Pachfule, A. Acharjya, J. Roeser, T. Langenhahn, M. Schwarze, R. Schomaecker, A. Thomas and J. Schmidt, *J. Am. Chem. Soc.*, 2018, **140**, 1423-1427
15. E. Jin, Z. Lan, Q. Jiang, K. Geng, G. Li, X. Wang and D. Jiang, *Chem*, 2019, **5**, 1632–1647.
16. Y. Bai, L. Wilbraham, B. J. Slater, M. A. Zwijnenburg, R. S. Sprick, and A. I. Cooper, *J. Am. Chem. Soc.*, 2019, **141**, 9063-9071.
17. R. S. Sprick, Y. Bai, A. A. Y. Guilbert, M. Zbiri, C. M. Aitchison, L. Wilbraham, Y. Yan, D. J. Woods, M. A. Zwijnenburg, and A. I. Cooper, *Chem. Mater.*, 2019, **31**, 305-313.

Chapter 4

Covalent organic framework nanosheets embedding single cobalt sites for efficient photoreduction of carbon dioxide

4.1 Author contributions

All new COFs and their nanosheets materials were synthesized by the thesis author. **BP-COF** was prepared by Zhiwei Fu. Prof. Lirong Zheng performed the XAS characterization and analyses. Modelling calculations were performed by Dr Linjiang Chen, Xue Wang and Chenxi Zhao. Dr Samantha Y. Chong carried out PXRD analyses. Lunjie Liu captured the SEM images. Dr Fiona McBride performed the AFM and XPS measurements. Dr Matthew Bilton captured the TEM images.

This chapter is based on the following publication: X. Wang, Z. Fu, L. Zheng, C. Zhao, X. Wang, S. Y. Chong, F. McBride, R. Raval, M. Bilton, L. Liu, X. Wu, L. Chen, R. S. Sprick, and A. I. Cooper, Covalent organic framework nanosheets embedding single cobalt sites for photocatalytic reduction of carbon dioxide. *Chem. Mater., Accepted*.

4.2 Introduction

The conversion of CO_2 into chemical fuels is considered as a promising avenue for research to address rising levels of climate gases that have resulted in the global climate crisis and also in potentially addressing the rising energy demand of the growing population on the planet.[1–3] Photocatalytic reduction of CO_2 has been extensively studied using homogeneous catalysts. For example, Co, Fe, Ni and Re complex are developed for photocatalytic CO_2 reduction.[4–6] Although these molecular catalysts have high initial photocatalytic activity and selectivity for the desired products but are often not stable over extended time periods. Heterogeneous catalysts are one of solutions for these issues, but often show poor activity. Single-atom catalysts embedded in semiconductors potentially fill this gap in between heterogeneous and homogeneous catalysis as they usually exhibit very high activity, reusability and high stability.[7–9] To make these single-atom catalysts, the interaction between the catalyst and the semiconductor has to be strong. Coordination bound has been used to fix metals atom onto semiconductors, for example, bipyridine based MOFs and COFs are good candidates for single-atom catalysts.[10,11] Iminopyridine moiety is a versatile metal coordination site for different transition metals.[12,13] However, it has not yet been explored in the context of COF catalysts. In this chapter, iminopyridine moieties were introduced into COFs to explore the ligation with metal catalysts.

Two-dimensional (2D) COFs have been reported as highly active photocatalysts for hydrogen production[10,14–16] and CO_2 reduction,[11,17,18] and have the potential to be ideal supports for anchoring atomically distributed metal centers. Although these 2D COF materials show decent activity, utilization of the catalytic metal sites has often been shown to be poor, resulting low turnover numbers (TONs).[19] Exfoliation of 2D COFs into 2D nanosheets is one way to expose more catalytic metal sites, potentially resulting in higher overall activity. Furthermore, for CO_2 reduction, the affinity of the materials for CO_2 is also important. Introduction of functional groups with affinity to CO_2, such as cyano or fluorine,[20–22] can improve the adsorption of CO_2 on the material, which is a promising strategy to create a local environment with high CO_2 content close to photoreduction sites.

4.3 Materials synthesis and characterization

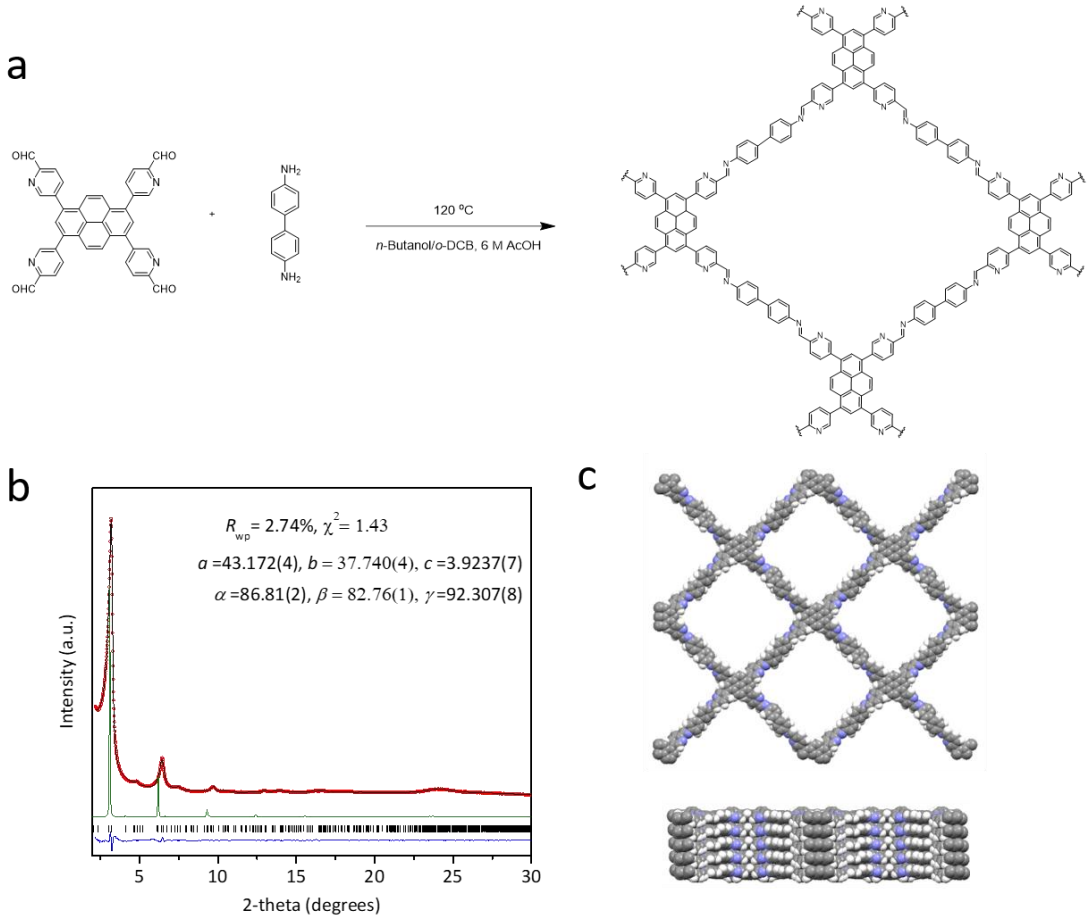

Figure 4-1. Scheme of the synthesis of **Py-COF**. (b) Experimental diffraction pattern (red), profile calculated from Le Bail fitting (black) and residual (blue), and pattern simulated from the structural model (green) for **Py-COF**. Reflection positions are shown by tick marks. (c) Structural models for **Py-COF** with eclipsed AA stacking patterns. Grey, white and blue atoms represent carbon, hydrogen and nitrogen, respectively.

To introduce iminopyridine moiety to frameworks, a pyridine based 5,5',5",5"'-(pyrene-1,3,6,8-tetrayl)tetrapicolinaldehyde was synthesized. **Py-COF** was synthesized *via* a Schiff base condensation of 5,5',5",5"'-(pyrene-1,3,6,8-tetrayl)tetrapicolinaldehyde with benzidine (Figure 4-1a). Experimental powder X-ray diffraction (PXRD) patterns of **Py-COF** show diffraction peaks at 3.27, 4.77, 6.55, 7.56, and 9.83°, which can be assigned to the (110), (210), (220), (130) and (330) planes, respectively (Figure 4-1b). The broad reflections positioned at 2θ = ~23.9° were calculated to be distance of ~3.7 Å which attributed to the interlayer stacking distances. Unit cell parameters extracted by Le Bail refinements are similar to the parameters

obtained by structure simulations. Experimental PXRD data of **Py-COF** was consistent with the simulated diffraction profile for the AA stacking model (Figure 4-1b).

The isostructural **FPy-COF** was synthesized *via* a Schiff base condensation of 5,5',5",5"'-(pyrene-1,3,6,8-tetrayl)tetrapicolinaldehyde with 4,4'-diamino-2,2'-difluorobiphenyl (Figure 4-2a). **FPy-COF** shows similar crystalline structure and the diffraction peaks at 3.20, 6.50, 7.30, and 9.62° were assigned to the (110), (220), (130) and (330) planes, respectively (Figure 4-2b). Similar to **Py-COF**, experimental PXRD data for **FPy-COF** is consistent with simulated diffraction data from AA stacking model.

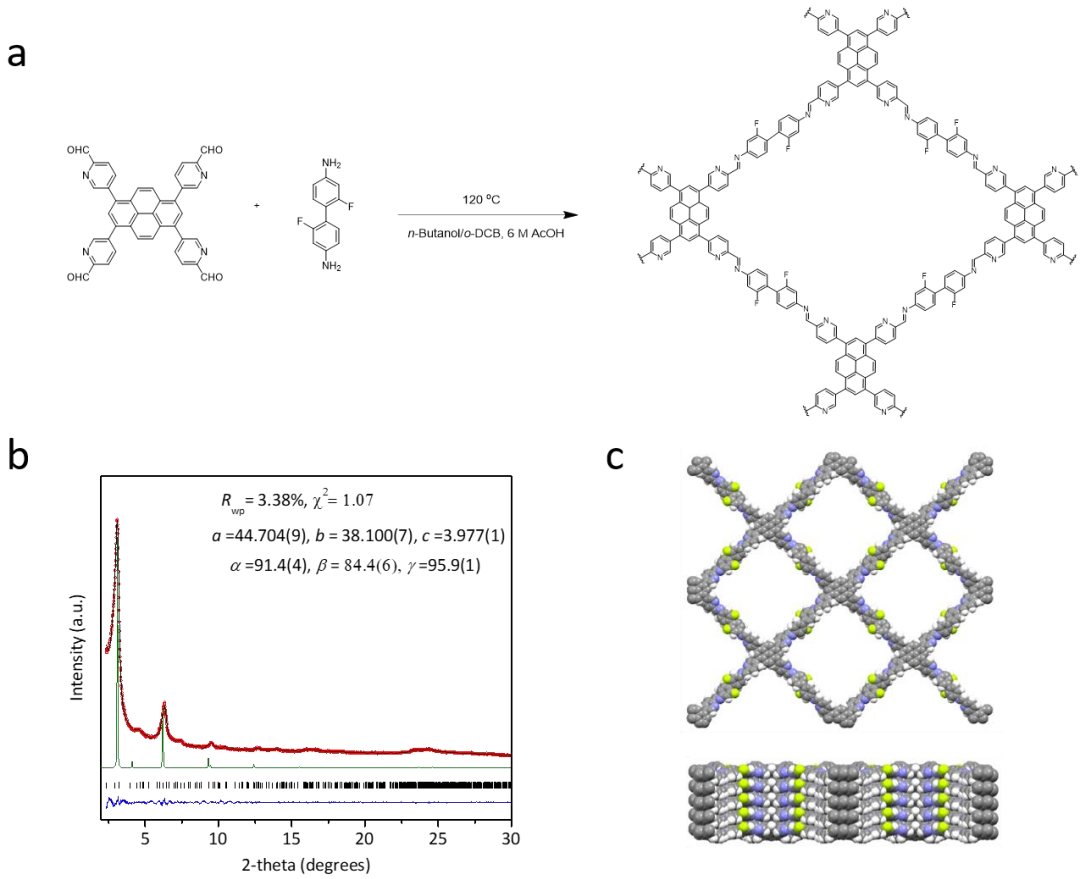

Figure 4-2. Scheme of the synthesis of **FPy-COF**. (b) Experimental diffraction pattern (red), profile calculated from Le Bail fitting (black) and residual (blue), and pattern simulated from the structural model (green) for **FPy-COF**. Reflection positions are shown by tick marks. (c) Structural models for **FPy-COF** with eclipsed AA stacking patterns. Grey, white, blue and green atoms represent carbon, hydrogen, nitrogen and fluorine, respectively.

4.3 CONs synthesis and characterization

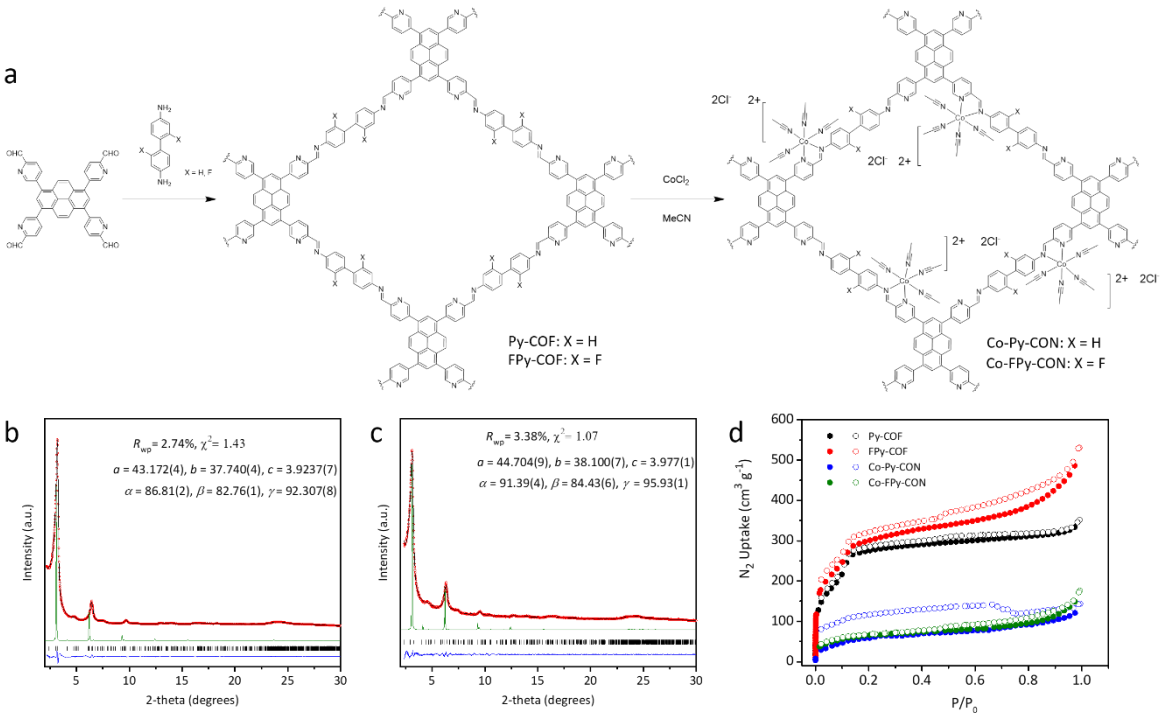

Figure 4-3. (a) Synthesis scheme of **Co-Py-CON** and **Co-FPy-CON**. (b) Experimental diffraction patterns for **Py-COF** and **Co-Py-CON**. (c) Experimental diffraction patterns for **FPy-COF** and **Co-FPy-CON**. (d) Nitrogen adsorption isotherm (filled symbols) and desorption isotherm (open symbols) for **Py-COF**, **FPy-COF**, **Co-Py-CON** and **Co-FPy-CON** recorded at 77.3 K.

Exfoliation of bulk COFs were carried out by ultrasonicating bulk COFs in acetonitrile solution with metal precursors. The coordination environment of CONs will be discussed later. As shown in Figure 4-3b, c, the resulting cobalt doped nanosheets **Co-Py-CON** and **Co-FPy-CON** show the decrease of diffraction peaks intensity, indicating CON are less crystalline than bulk COF counterparts. This can be attributed to exfoliation and metal loading.[23,24] Nitrogen sorption experiments were carried out at 77 K, and the Brunauer−Emmett−Teller (BET) surface areas of **Py-COF** and **FPy-COF** were calculated to be 924 and 1136 m^2 g^{-1}. The N_2 isotherms of **Py-COF** and **FPy-COF** indicates their mesoporosity and multilayer pore filling. The pore diameters of **Py-COF** and **FPy-COF** were found to be 24.5 and 23.8 Å, respectively, which fitted by nonlocal density functional theory models. The BET surface areas of **Co-Py-CON** and **Co-FPy-CON** were determined to be 207 and 238 m^2 g^{-1}, respectively. This decrease can be attributed to the loss of long-range order in bulk COFs.[24] After exfoliation, both **Co-Py-**

CON and **Co-FPy-CON** show more larger pores and nonuniform pore size distribution than **Py-COF** and **FPy-COF** (Figure 4-20), because changing of morphology and loss of long-range order for CONs.

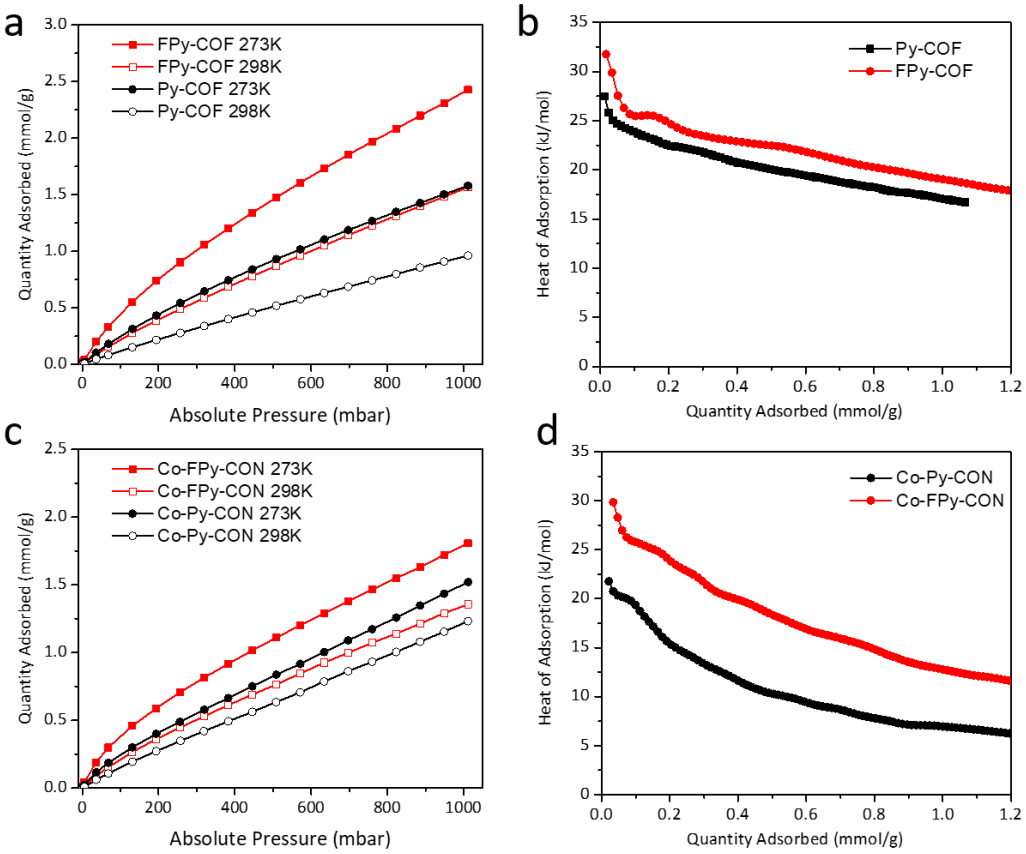

Figure 4-4. (a) CO_2 adsorption isotherms for **Py-COF** and **FPy-COF** collected at 273 K and 298 K. (b) Isosteric heats of adsorption for CO_2 calculated from the adsorption isotherms collected at 273 K and 298 K. (c) CO_2 adsorption isotherms for **Co-Py-CON** and **Co-Fpy-CON** collected at 273 K and 298 K. (d) Isosteric heats of adsorption for CO_2 calculated from the adsorption isotherms collected at 273 K and 298 K.

The CO_2 uptake of COFs and CONs were measured up to 1 bar at 273 and 298 K, respectively (Figure 4-4a, c). **FPy-COF** shows much higher CO_2 uptake capacity, reaching of 2.42 mmol g^{-1} at 273 K than **Py-COF** with a similar surface area (1136 m^2 g^{-1} *vs* 924 m^2 g^{-1}). To gain further insight into the CO_2 affinity of materials, the isosteric heat of adsorption (*Q*st) were calculated. As shown in Figure 4-4b, **FPy-COF** exhibits higher isosteric heats than **Py-COF**, indicative of a stronger interaction between **FPy-COF** with CO_2 than **Py-COF**. Similar results were found for CONs adsorption measurements, **Co-FPy-CON** shows better CO_2 uptake

capacity and larger isosteric heats than its non-fluorinated counterpart **Co-Py-CON**, which confirmed that introducing fluorine atom into framework can improve interaction to CO_2 molecules.[25]

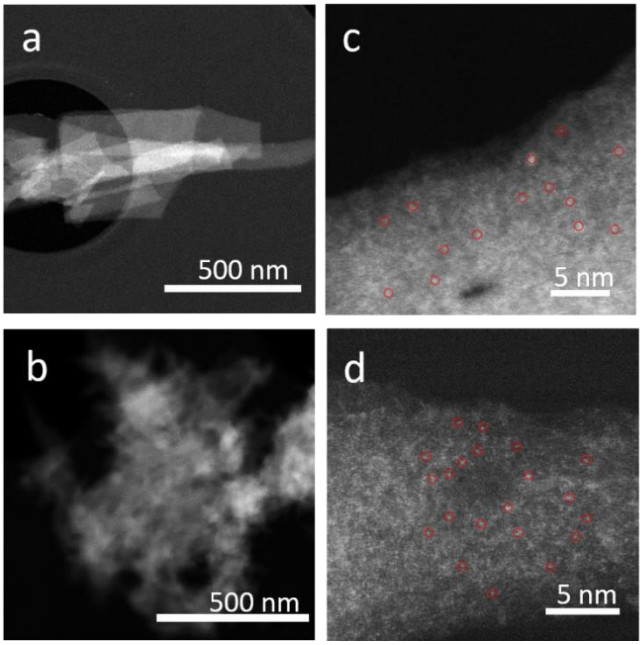

Figure 4-5. HAADF-STEM image for (a) **Co-Py-CON** and (b) **Co-FPy-CON**. High resolution HAADF-STEM image of (c) **Co-Py-CON** and (d) **Co-FPy-CON**.

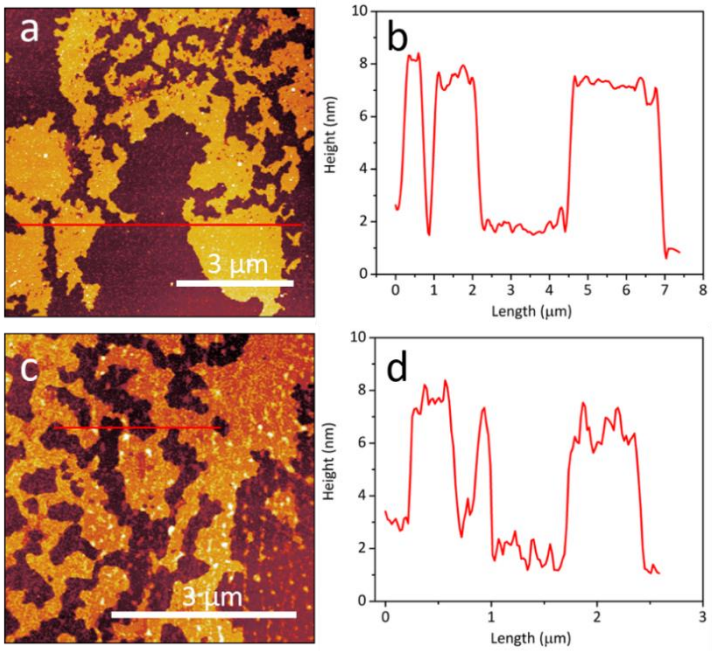

Figure 4-6. AFM image and measured thickness of **Co-Py-CON** (a, b) and **Co-FPy-CON** (c, d).

To further determined morphology of CONs, high-angle annular dark-field scanning transmission electron microscopy (HAADF-STEM) was performed. As shown in Figure 4-5a, **Co-Py-CON** shows nanosheets morphology with hundreds of nanometres scale. **Co-FPy-CON** exhibits smaller nanosheets aggregates morphology. Co nanoparticles and clusters were not observed in these pictures, indicating that the Co species were too small to identify in this magnification. Thus, aberration-corrected HAADF-STEM was used to characterize the **Co-FPy-CON**. Figure 4-5c, d show that isolated Co atoms were uniformed distributed on the CON matrix, shown as bright dots which highlight by red cycles. The thickness of these CONs was measured by atomic force microscopy (AFM). AFM images of **Co-Py-CON** (Figure 4-6a, b) and **Co-FPy-CON** (Figure 4-6c, d) show both micro-metres width nanosheets with average thickness of ~1.0-5.3 nm and ~1.9-4.4 nm, respectively. The thickness for one-layer COF is 0.4 nm, thus these thicknesses are corresponding to few layers, which are common to exfoliated COFs.[23,26,27]

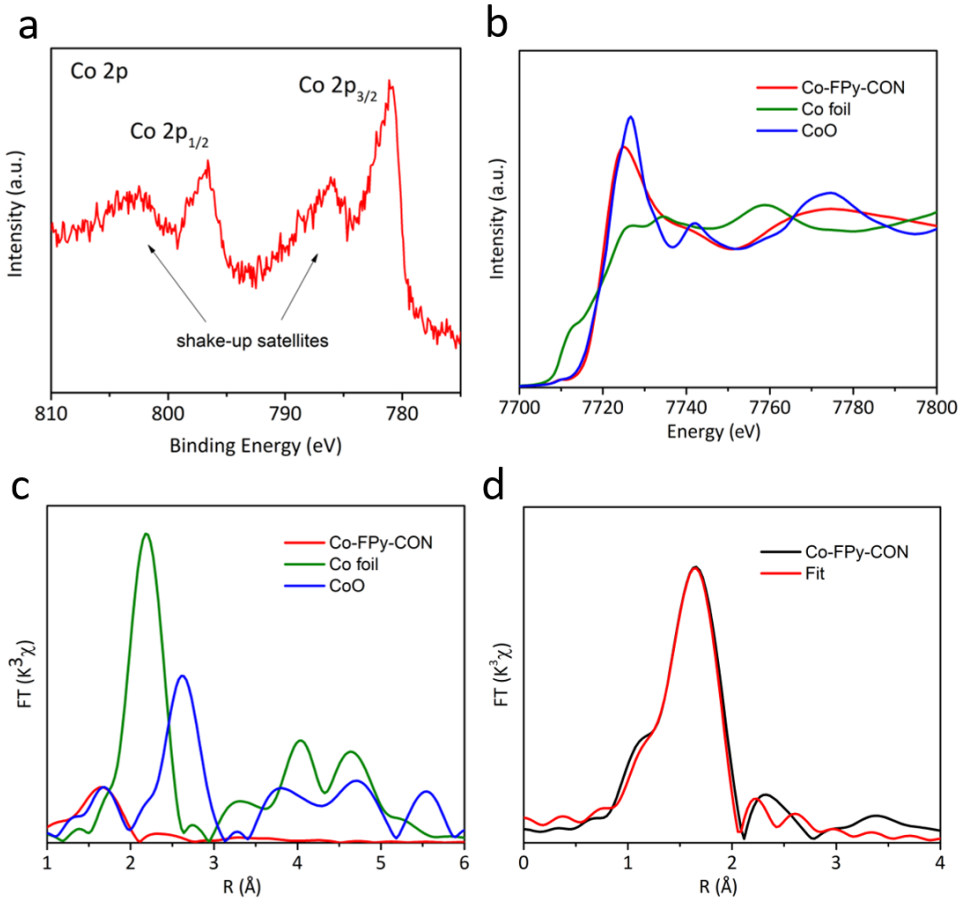

Figure 4-7. (a) XPS spectra of **Co-FPy-CON**. (b) XANES spectra at the Co K-edge and (c) k^3-weighted Fourier-transformed Co K-edge EXAFS spectra of **Co-FPy-CON**, CoO and Co foil. (d) The EXAFS fitting curve of **Co-FPy-CON**.

Table 4-1. EXAFS fitting parameters at the Co K-edge for various samples

Sample	Shell	N[a]	R (Å)[b]	σ^2 (Å$^2\cdot10^{-3}$)[c]	ΔE_0 (eV)[d]	R factor (%)
Co-FPy-CON	Co-N	6.0	2.13	8.6	1.4	0.7

[a] *N*: coordination number; [b] *R*: bond distance; [c] σ^2: Debye-Waller factor; [d] ΔE_0: the inner potential correction. *R* factor: goodness of the fit. S_0^2 for Co–N was set to 0.88, which was obtained from the experimental EXAFS fit of CoPc reference by fixing CN as the known crystallographic value and was fixed to all the samples.

X-Ray photoelectron spectroscopy (XPS) of **Co-FPy-CON** shows peaks at 780.8 eV and the shake-up satellites, suggesting that Cobalt in **Co-FPy-CON** are mostly present in +2 valence state.[9,28] The local coordination of cobalt species in **Co-FPy-CON** were measured using synchrotron-based X-ray absorption near-edge structure spectroscopy (XANES) and extended X-ray fine structure (EXAFS). Co foil and cobalt (II) oxide (CoO) were used as reference in the measurements. The XANES spectrum of **Co-FPy-CON** (Figure 4-7a) exhibits that the Co K-edge absorption edge position is similar to CoO, suggesting that the oxidation state of Co atoms in **Co-FPy-CON** are +2. These results are agreed with XPS data. X-Ray absorption fine structure spectroscopy (EXAFS) was performed to further investigate the coordination environment of cobalt in **Co-FPy-CON**. As shown in Figure 4-7c, a sharp peak at 2.2 Å was observed in Fourier transformed R-space spectrum of Co foil, which can assign to Co–Co bond. The R-space spectrum of CoO shows a peak at 2.6 Å, corresponding to the shortest Co···Co distance in CoO. Compared to Co and CoO, these two peaks are absent in the spectrum of **Co-FPy-CON**. The R-space spectrum of **Co-FPy-CON** exhibits distinct peak around 1.6 Å that corresponds to the Co–N bonds.[29] This peak in line with the first peak (1.6 Å) of CoO spectrum which can be assigned to the Co–O bond. From best EXAFS curve fitting results (Figure 4-7d and Table 4-1), the coordination number of Co atoms in **Co-FPy-CON** was 6.0, which bond length is 2.13 Å. This shows that Co atom were successfully ligated onto iminopyridine moiety, and acetonitrile molecules also participate the coordination with Co (as shown in Figure 4-3a). There are three different types of Co–N bonds in the Co-FPy-CON, while only one peak was observed in the EXAFS spectrum can be assigned to the Co–N pair. Because the differences in

the Co–N bond lengths are small, approximately 0.1 Å,[30,31] which are not distinguishable in EXAFS spectra. These results show that short Co···Co distances were not observe in Co-FPy-CON, suggesting Co centers were atomically distributed within the COF.

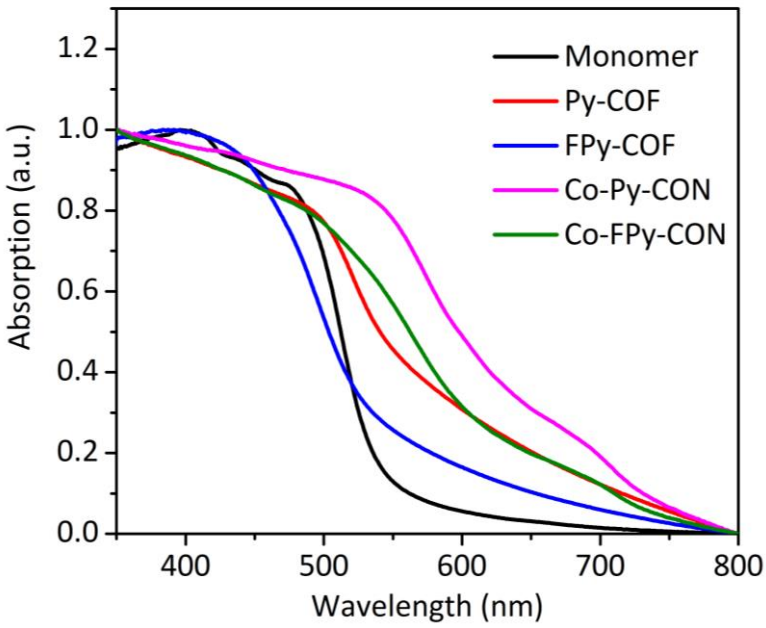

Figure 4-8. UV–Vis absorption spectra of monomer (**PTA**), **Py-COF**, **Co-Py-CON**, **FPy-COF** and **Co-FPy-CON** measured in the solid-state.

UV–Vis reflectance spectra of the monomers and COFs were measured in the solid state. The absorption onset for **Py-COF**, **Co-Py-CON**, **FPy-COF** and **Co-FPy-CON** was measured to be 560, 650, 545 and 610 nm respectively (Figure 4-8). Both COFs show a redshifted absorption onset compared to the **PTA** monomer. After loaded with Co, **Co-Py-CON** and **Co-FPy-CON** show a redshifted absorption onset compared to their COF precursors, which are consistent with previous literatures.[11]

Time-correlated single-photon counting (TCSPC) measurements were measured to estimate the excited-state lifetimes for these materials in aqueous suspensions (Figure 4-9). The average weighted lifetime of **Py-COF**, **Co-Py-CON**, **FPy-COF** and **Co-FPy-CON** was estimated to be τ_{avg} = 3.2, 3.1, 2.64 and 2.02 ns, respectively. The similar lifetimes for these materials indicate similar capability for charge stabilization.

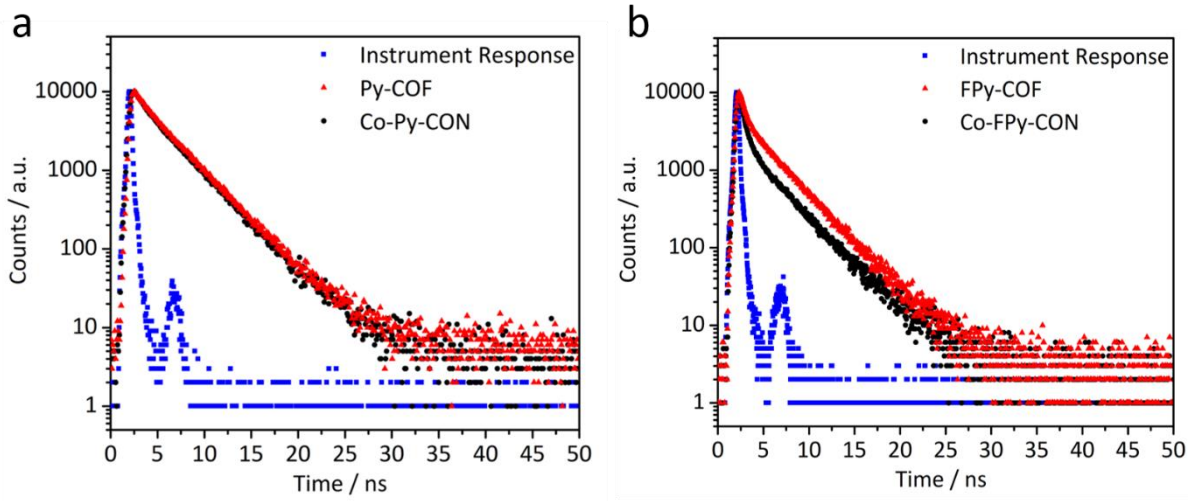

Figure 4-9. Time-correlated single-photon counting experiments for (a) **Py-COF**, **Co-Py-CON** and (b) **FPy-COF**, **Co-FPy-CON** in acetonitrile. Samples were excited with a λ_{exc} = 390.5 nm laser and emission was measured at λ_{em} = 505 nm in acetonitrile.

4.4 Photocatalytic CO_2 reduction

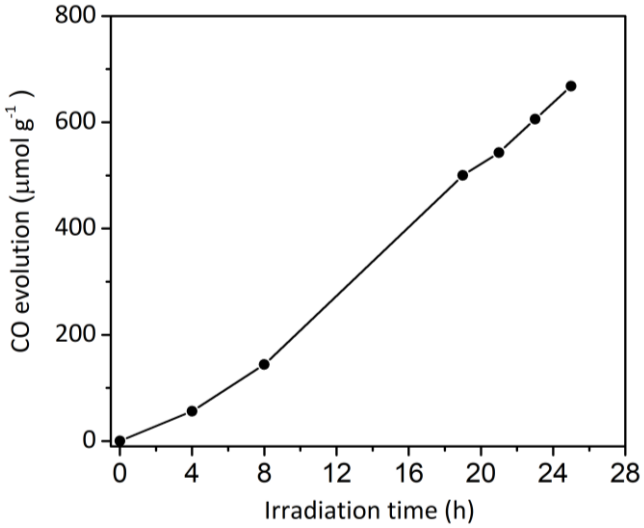

Figure 4-10. CO_2 reduction experiments of **Co-FPy-CON** over 25 hours total photolysis (1 mg catalyst in MeCN, water and TEOA (5 mL, 3/1/1) under visible light irradiation (λ > 420 nm, 300 W Xe light source).

Photocatalytic CO_2 reduction activity of **Co-FPy-CON** was tested in water, acetonitrile, and TEOA (1:3:1 vol. mixtures) under visible light irradiation (λ > 420 nm). 2,2'-bipyridine was added to form catalytic Co centers.[18] As shown in Figure 4-10, **Co-FPy-CON** can produce only trace amounts of carbon monoxide under these conditions. The inter-fragment energy transfer

in **Co-FPy-CON** might be responsible for the low activity of **Co-FPy-CON**, which will be discussed in simulation section.

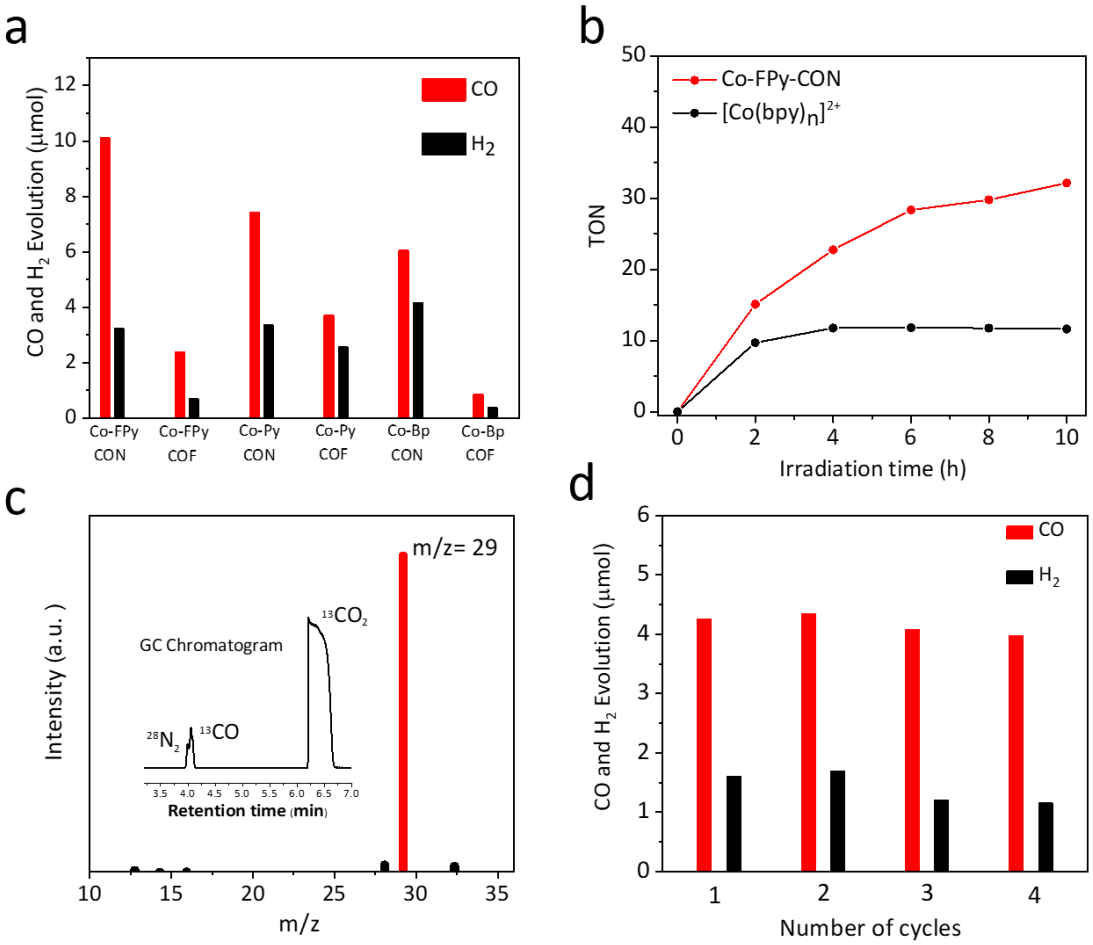

Figure 4-11. (a) CO and H_2 production by the nanosheet (denoted CON) and bulk (denoted COF) of **Co-FPy-COF**, **Co-Py-COF** and **Co-Bp-COF**, over 6 hours under visible-light irradiation (λ > 420 nm, 300 W Xe light source) with $(Ir[dF(CF_3)ppy]_2(dtbpy))PF_6$ as photosensitizer. (b) TONs of CO production by **Co-FPy-CON** and $[Co(Bpy)_n]^{2+}$ under visible-light irradiation (λ > 420 nm, 300 W Xe light source) with $(Ir[dF(CF_3)ppy]_2(dtbpy))PF_6$ as photosensitizer. (c) Mass spectrum of ^{13}CO produced using **Co-FPy-CON** as the catalyst in the photocatalytic reduction of $^{13}CO_2$; inset: the corresponding gas chromatogram. (d) CO and H_2 production by **Co-FPy-CON** over multiple 2-hour cycling runs. The sample was degassed and 1 μmol of $(Ir[dF(CF_3)ppy]_2(dtbpy))PF_6$ was added after each cycle.

Based on these observations, $(Ir[dF(CF_3)ppy]_2(dtbpy))PF_6$ was used as a photosensitizer in system. As shown in Figure 4-11a, **Co-FPy-CON** produced 10.01 μmol of CO over 6 hours with selectivity of 76% over competing H_2 generation (Figure 4-11a and Table 4-2). The

turnover number (TON) was determined to be 28.1. Isotope labelling experiments with $^{13}CO_2$ show that ^{13}CO was produced from $^{13}CO_2$, which indicates that there was no obvious degradation of the photocatalyst, photosensitizer or scavenger occurs. External quantum efficiency (EQE) of **Co-FPy-CON** was measured to be 6.6% at 420 nm. This EQE value was higher than previously reported of Ni-TpBpy-COF and Co-ZIF-9, both with $[Ru(bpy)_3]Cl_2$ as photosensitizer and TEOA as scavenger at 420 nm.[3,18] Bulk **Co-FPy-COF** produced 2.36 μmol CO over 6 hours with a TON of 15.5, which was 4.3 times lower than that of **Co-FPy-CON**. This can be partially attributed to the lower Co loading in **Co-FPy-COF**, which has Co content of 0.9 wt% and 2.1 wt% for COF and CON, respectively. Non-fluorinated **Co-Py-CON** exhibits lower CO production than **Co-FPy-CON**, producing 7.4 μmol of CO over 6 hours (TON=10.9), which probably because **Co-FPy-CON** has a stronger binding affinity to CO_2 and dye, however **Co-FPy-CON** has a lower Co loading (2.1 wt. %) than **Co-Py-CON** (4.0 wt. %). The bulk sample of **Co-Py-COF** also showed a lower CO production than **Co-Py-CON**.

For comparison, isostructural bipyridine-COF (**BP-COF**) and its CON were also synthesised, which use bipyridine to ligate metals instead of the iminopyridine sites as in **Py-COF**. **Co-Bp-CON** has a lower CO production than **Co-Py-CON** over 6 hours period with a lower CO/H_2 selectivity. These results indicate that incorporating iminopyridine moieties into porous materials can provide metal coordination site, which are promising and general strategy to introduce catalytically active metal centers for photocatalysis. **Zn-FPy-CON** was made by using **FPy-COF**, which showed measurable CO_2 reduction activities under the same conditions (Table 4-2). Kinetic CO production measurements were carried out to measure the stability of materials (Figure 4-11b). Homogeneous catalyst $[Co(bpy)_n]^{2+}$ has a TON of 11.6 over 10 hours, 2.8 times lower than heterogeneous counterpart **Co-FPy-CON**. This difference can be partially attributed to the fact that the homogeneous catalyst $[Co(bpy)_n]^{2+}$ is less stable than **Co-FPy-CON** which was deactivated after 3 hours, an observation that is consistent with previous literatures.[6,32,33] Cycling experiments were carried out to measure the stability of the **Co-FPy-CON**. As shown in Figure 4-11d, these experiments show that **Co-FPy-CON** retained its photocatalytic activity over four runs.

Table 4-2. CO and H_2 production under different experimental conditions over 6 hours.

Entry	Photocatalyst	Co content (wt%)	CO (μmol)	H_2 (μmol)	CO selectivity (%)
1[a]	**Co-FPy-CON** + photosensitizer	2.1	10.01 (TON_{6h} =28.1)	3.21	76
2[a]	**Co-Py-CON** + photosensitizer	4.0	7.4 (TON_{6h} =10.9)	3.34	69
3[a]	**Co-Bp-CON** + photosensitizer	4.1	6.03 (TON_{6h} =8.87)	4.14	59
4[a]	Zn-FPy-CON + photosensitizer	4.9	0.15 (TON_{6h} =0.21)	0.11	59
5[a]	Bulk **Co-FPy-COF** + photosensitizer	0.9	2.36 (TON_{6h} =15.5)	0.68	78
6[a]	Bulk **Co-Py-COF** + photosensitizer	1.9	3.69 (TON_{6h}=11.7)	2.54	59
7[a]	Bulk **Co-Bp-COF** + photosensitizer	4.0	0.83 (TON_{6h} =1.2)	0.36	69
8[b]	$[Co(bpy)_n]^{2+}$ + photosensitizer		TON_{6h} = 11.8	TON_{6h} = 6.3	65
9[c]	$[Co(bpy)_n]^{2+}$		n.d.	n.d.	

[a]Reaction conditions: COFs (1 mg), 2,2'-Bipyridine (1.5 mg), solvent (5 mL, acetonitrile/TEOA/water = 3 : 1 : 1), CO_2 (1 atm.), 300 W Xe light source equipped with $\lambda >$ 420 nm cut-off filter, 6 hours; [b]Photocatalyst (0.356 μmol $CoCl_2$ and 1.5 mg 2,2'-Bipyridine), Solvent (5 mL, acetonitrile/TEOA/water = 3 : 1 : 1), CO_2 (1 atm.), 300 W Xe light source equipped with $\lambda >$ 420 nm cutoff filter, 6 hours; [c]Reaction conditions was same as [b] but photocatalysis time was 25 hours; Photosensitizer: $(Ir[dF(CF_3)ppy]_2(dtbpy))PF_6$; n.d.: not detected.

Table 4-3. Performance comparison of our samples with state-of-the-art COFs and MOFs catalysts for the photocatalytic CO_2.

Photocatalyst	**Main products and highest yield ($\mu mol\ h^{-1}\ g^{-1}$)**	**TON**	**Selectivity**	**EQE (%)**	**Irradiation condition**	**Reference**
Co-FPy-CON ($Ir[dF(CF_3)ppy]_2(dtbpy))PF_6$	1681 (CO)	28.1 (6 h)	76% (CO)	6.6 (420 nm)	$\lambda > 420$ nm (300 W Xe light source)	This work
DQTP-COF-Co $[Ru(bpy)_3]Cl_2$	1020 (CO)	2.18 (4 h)	59.4% (CO)	-	$\lambda \geq 420$ nm (300 W Xe light source)	[34]
CdS/UiO-bpy/Co	235 (CO)	-	85% (CO)	0.65 (420 nm)	$\lambda \geq 420$ nm (300 W Xe light source)	[29]
Co-ZIF-9 $[Ru(bpy)_3]Cl_2$	-	52.3 (0.5 h)	58.3% (CO)	1.48 (420 nm)	$\lambda \geq 420$ nm (300 W Xe light source	[3]
MOF-525-Co	200.6 (CO) 36.67 (CH_4)	-	-	-	$\lambda \geq 400$ nm (300 W Xe light source	[35]
CoN_4-SiO_2 g-C_3N_4	19.9 (CO)	4.5 (20 h)	33% (CO)	0.17 (450 nm)	LED lamp ($\lambda max = 450$ nm	[36]
Ni-TpBpy-COF $[Ru(bpy)_3]Cl_2$	966 (CO)	13.6	96% (CO)	0.3 (420 nm)	$\lambda \geq 420$ nm (300 W Xe light source)	[18]
N_3-COF	0.57 (CH_3OH)	-	-		800 nm $\geq \lambda \geq$ 420 nm (500 W Xe light source)	[37]

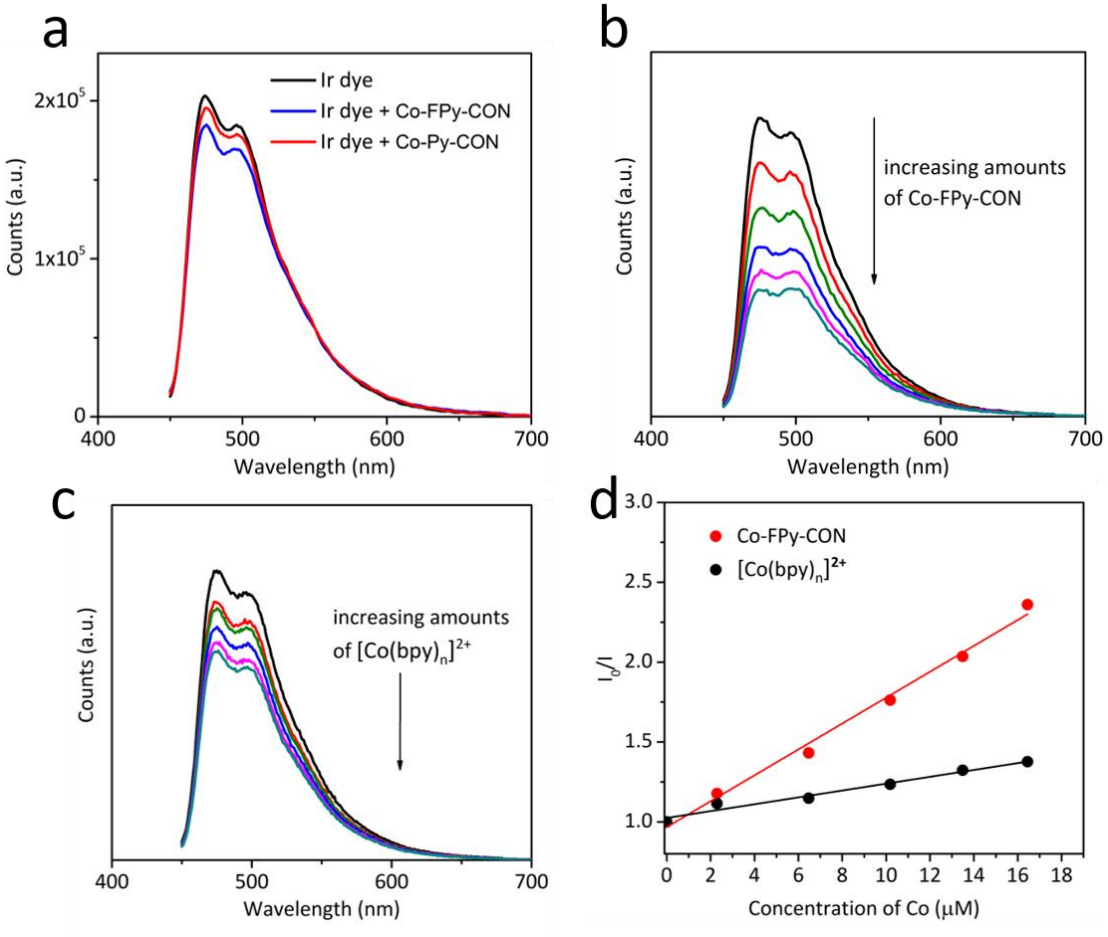

Figure 4-12. (a) Steady-state PL spectra of 0.2 mM dye $(Ir[dF(CF_3)ppy]_2(dtbpy))PF_6$ acetonitrile solution upon the addition 1 mg of **Co-FPy-CON** and **Co-Py-CON**. The samples were excited at λ_{ex} = 440 nm. Steady-state PL spectra of $(Ir[dF(CF_3)ppy]_2(dtbpy))PF_6$ acetonitrile solution upon addition of increasing amounts of **Co-FPy-CON** (b) and $[Co(bpy)_n]^{2+}$ (c) (0, 2.3, 6.48, 10.19, 13.49, and 16.45 μM). The samples are excited at λ_{ex} = 440 nm. The concentrations of **Co-FPy-CON** are given according to the contents of Co atoms. (d) The Stern–Volmer equation of $(I_0/I) = K_{sv}[C] + 1$ was used to calculate the quenching efficiencies, where I_0 is the initial fluorescence intensity without Co catalyst, I is the fluorescence intensity after adding Co catalyst of concentration [C], and K_{sv} is the Stern–Volmer constant.

Dye adsorption capability for **Co-FPy-CON** and **Co-Py-CON** was measured by impregnation of these materials in $(Ir[dF(CF_3)ppy]_2(dtbpy))PF_6$ solution. The CONs were then separated by centrifugation and the concentration of the dye in the liquid supernatant was determined using a PL spectrophotometer. As shown in Figure 4-12a, the filtered dye solution from **Co-FPy-CON** mixture shows lower PL intensity than **Co-Py-CON** counterpart, indicating better dye

adsorption capability for **Co-FPy-CON**. To further understand the photogenerated electrons transfer from $(Ir[dF(CF_3)ppy]_2(dtbpy))PF_6$, to the catalysts, photoluminescence (PL) quenching experiments were carried out. The PL intensity of $(Ir[dF(CF_3)ppy]_2(dtbpy))PF_6$ can be quenched with addition of catalysts indicating electrons transfer from dye to catalysts. As shown in Figure 4-12b, $(Ir[dF(CF_3)ppy]_2(dtbpy))PF_6$ acetonitrile solution excited at 440 nm shows two broad emission peak around 475 and 500 nm. With addition of **Co-FPy-CON**, the PL peak of excited $(Ir[dF(CF_3)ppy]_2(dtbpy))PF_6$ was quenched. Comparing to **Co-FPy-CON**, the PL intensity of $(Ir[dF(CF_3)ppy]_2(dtbpy))PF_6$ can be quenched less efficiently with addition of $[Co(bpy)_n]^{2+}$. Stern–Volmer constant (K_{SV}) was calculated to quantify these quenching behaviors. Figure 4-12d shows the K_{SV} of $(Ir[dF(CF_3)ppy]_2(dtbpy))PF_6$ with **Co-FPy-CON** and $[Co(bpy)_n]^{2+}$ was 81.0 and 21.5 mM^{-1}, suggesting a higher photoinduced electrons transfer rate from $(Ir[dF(CF_3)ppy]_2(dtbpy))PF_6$ to **Co-FPy-CON** than to $[Co(bpy)_n]^{2+}$.

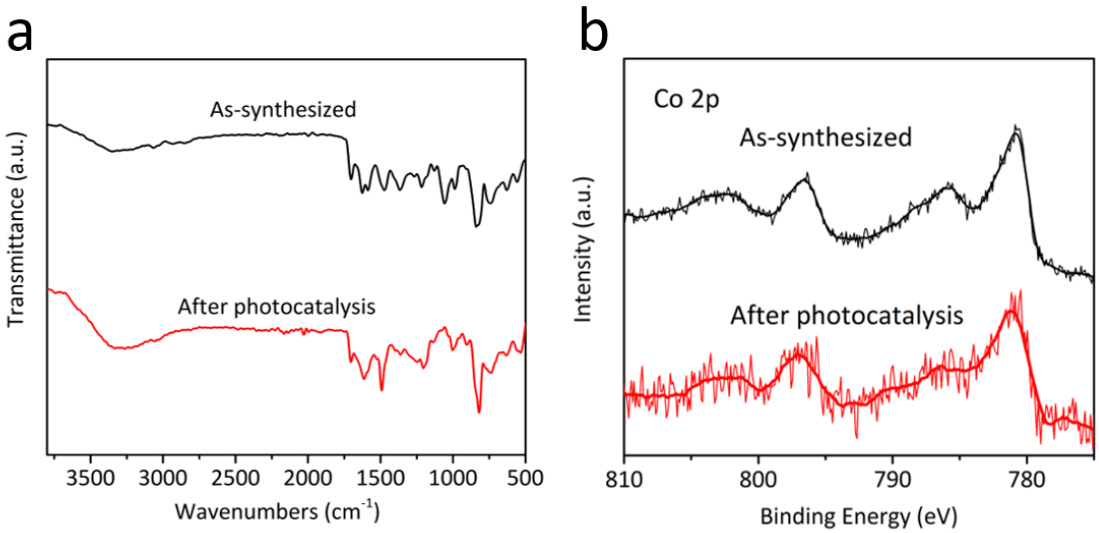

Figure 4-13. (a) FTIR spectra of **Co-FPy-CON** before (black) and after (red) 8 hours photocatalysis. (b) XPS spectra of **Co-FPy-CON** before (blacks) and after (red) 8 hours photocatalysis.

As discussed above, **Co-FPy-CON** catalyst is stable after several cycles' experiments. FTIR and XPS were used to further determine the stability of **Co-FPy-CON**. FT-IR spectra (Figure 4-13a) of **Co-FPy-CON** shows negligible change after cycling experiments. XPS measurements (Figure 4-13b) of **Co-FPy-CON** also indicate that the oxidation state of Co retained +2 after the photocatalysis experiments. The concentration of cobalt in filtered solution

after photocatalysis were measured by inductively coupled plasma-optical emission spectrometry, which found that only trace of cobalt (6.6 ppm) remained in solution. These results indicate **Co-FPy-CON** is stable in photocatalysis environment.

4.5 Calculations

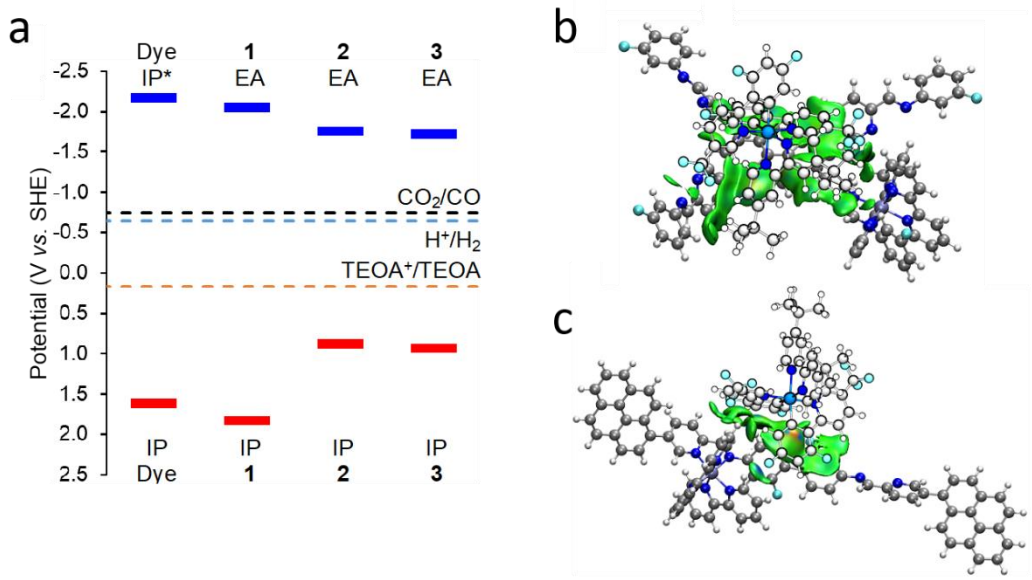

Figure 4-14. (a) (TD-)DFT predicted potentials of the free charge carriers (IP and EA) and excitons (IP*) of the dye, the molecular catalyst $[Co(Bpy)_3]^{2+}$ (**1**), and representative fragments $[Co\text{-}Py(L)]^{2+}$ (**2**) and $[Co\text{-}FPy(L)]^{2+}$ (**3**) of **Co-Py-COF** and **Co-FPy-COF**, respectively. Dashed colored lines indicate the potentials for CO_2 reduction to CO, proton reduction, and TEOA oxidation, respectively. DFT-optimized adsorption configuration of the dye on the pyrene moiety (b) or the difluorobiphenyl moiety (c) of **Co-FPy-COF**. Colored isosurfaces are intermolecular interactions identified and quantified by non-covalent interaction analyses. COF fragments are shown in full atomic, ball-and-stick representation, with the dye shown as a lighter sketch.

Calculations were performed on representative molecular models $[Co\text{-}Py(L)]^{2+}$ and $[Co\text{-}FPy(L)]^{2+}$ of **Co-Py-COF** and **Co-FPy-COF**, respectively. The electron affinity (EA) and the ionization potential (IP) of both COFs and molecular catalyst $[Co(Bpy)_3]^{2+}$ straddle the reduction potential of CO_2 to CO, the oxidation potential of TEOA and the proton reduction potential (Figure 4-14a), which suggest these COFs and $[Co(Bpy)_3]^{2+}$ can thermodynamically drive CO_2 reduction using TEOA as a scavenger. However, excited-state and inter-fragment

charge transfer analyses of **Co-FPy-COF** and **Co-Py-COF** show that there are negligible amounts of electrons transferred between the pyrene fragment and the Co-loaded iminopyridine fragment (Table 4-4), for the first three low-energy, excited electronic states with an appreciable oscillator strength. These results can explain the low activity of **Co-FPy-COF** without dye. Combining of computational and experimental results indicate that a dye is required to facilitate CO_2 reduction, and COFs provide metal coordination sites for the cobalt to form catalytic centers.

The comparison of energy level between dye and molecular COF (or $[Co(Bpy)_3]^{2+}$) models indicate that photoelectrons from dye can thermodynamically transfer to COF and $[Co(Bpy)_3]^{2+}$, which is consistent with experimental data. The simulation of dye adsorption on a single **Co-FPy-COF** layer shows that dye was strongly bound on both pyrene moiety (Figure 4-14b) and the difluorobiphenyl moiety (Figure 4-14c) of **Co-FPy-COF**. The interaction between dye and single **Co-FPy-COF** layer is inter-molecular interactions: Van der Waals and electrostatic interactions. These binding sites are in the immediate vicinity of the photocatalytic Co site, which can benefit electrons transfer from the dye to the COF.

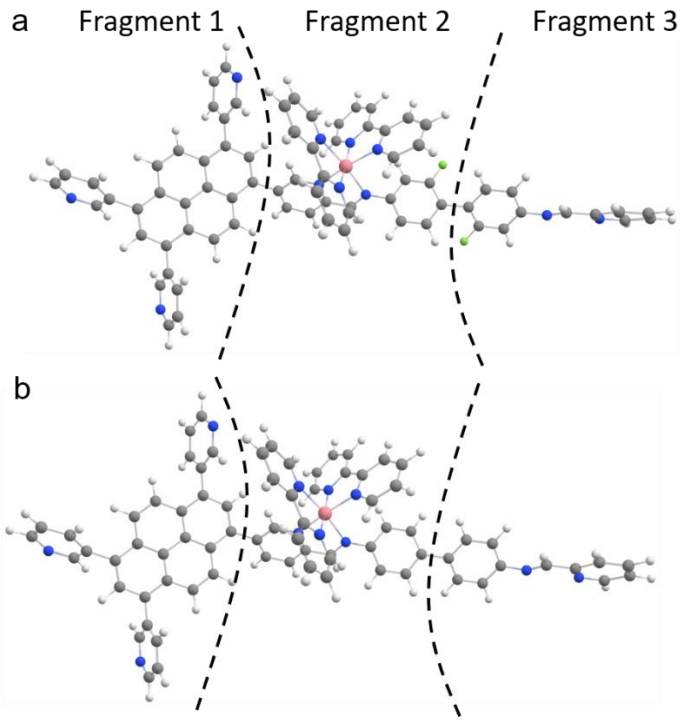

Figure 4-15. Representative molecular models (a) $[Co\text{-}FPy(L)]^{2+}$ and (b) $[Co\text{-}Py(L)]^{2+}$ of Co-FPy-COF and Co-Py-COF, respectively, together with fragment definition for inter-fragment charge transfer calculations.

Table 4-4. Calculated inter-fragment charge transfer (in number of electrons) in excited states (TD-wB97XD), with fragment definitions shown in Figure 4-15. Arrows indicate the electron transfer direction between the fragments; a negative value for the net transfer means that the electrons are transferred in the opposite direction to the one indicated by the arrow. The three lowest-energy transitions (E), with an oscillator strength (f) > 0.001, are shown here. Almost no electrons transferred from the pyrene fragment to Co-loaded iminopyridine fragment in both $[Co\text{-}FPy(L)]^{2+}$ and $[Co\text{-}Py(L)]^{2+}$ for the three lowest-energy, excited electronic states.

$[Co\text{-}FPy(L)]^{2+}$					
9^{th} excited state (E = 2.50 eV / 495 nm, f = 0.0014)					
1 → 2:	0.000	1 ← 2:	0.000	Net 1 → 2:	0.000
1 → 3:	0.000	1 ← 3:	0.000	Net 1 → 3:	0.000
2 → 3:	0.000	2 ← 3:	0.000	Net 2 → 3:	0.000
10^{th} excited state (E = 2.55 eV / 487 nm, f = 0.0023)					
1 → 2:	0.000	1 ← 2:	0.007	Net 1 → 2:	-0.007
1 → 3:	0.000	1 ← 3:	0.000	Net 1 → 3:	0.000
2 → 3:	0.001	2 ← 3:	0.003	Net 2 → 3:	-0.002
11^{th} excited state (E = 2.60 eV / 477 nm, f = 0.0036)					
1 → 2:	0.000	1 ← 2:	0.007	Net 1 → 2:	-0.007
1 → 3:	0.000	1 ← 3:	0.000	Net 1 → 3:	0.000
2 → 3:	0.003	2 ← 3:	0.006	Net 2 → 3:	-0.003
$[Co\text{-}Py(L)]^{2+}$					
9^{th} excited state (E = 2.51 eV / 494 nm, f = 0.0046)					
1 → 2:	0.000	1 ← 2:	0.005	Net 1 → 2:	-0.005
1 → 3:	0.000	1 ← 3:	0.000	Net 1 → 3:	0.000
2 → 3:	0.008	2 ← 3:	0.013	Net 2 → 3:	-0.005
10^{th} excited state (E = 2.54 eV / 489 nm, f = 0.0035)					
1 → 2:	0.000	1 ← 2:	0.009	Net 1 → 2:	-0.009
1 → 3:	0.000	1 ← 3:	0.000	Net 1 → 3:	0.000
2 → 3:	0.016	2 ← 3:	0.020	Net 2 → 3:	-0.004
11^{th} excited state (E = 2.58 eV / 481 nm, f = 0.0022)					
1 → 2:	0.000	1 ← 2:	0.001	Net 1 → 2:	-0.001
1 → 3:	0.000	1 ← 3:	0.000	Net 1 → 3:	0.000
2 → 3:	0.016	2 ← 3:	0.013	Net 2 → 3:	0.003

4.6 Summary

Homogeneous CO_2 reduction catalysts, such as organometallic complexes, are synthetically versatile but suffer from poor long-term stability. Heterogeneous catalysts are easier to recover but often show low activity. To overcome these issues, a series of COF nanosheets (CONs) single atom catalysts was synthesised from two-dimensional COFs incorporating iminopyridine moieties for metal coordination, which show great potential for photocatalytic CO_2 reduction. A partially-fluorinated, cobalt-loaded CON achieved a high CO production of 10.01 μmol (TON = 28.1) and a CO/H_2 selectivity of 76% over 6 hours irradiation under visible light, as well as a high external quantum efficiency of 6.6% under 420 nm irradiation. This performance is comparable with the state-of-the-art heterogeneous catalysts published in the literature under comparable conditions. The ultra-thin CONs outperformed their bulk counterparts in all cases, indicating that exfoliation is a potential strategy to enhance the photocatalytic activities of 2D COF materials. High resolution HAADF-STEM, X-ray absorption near-edge structure spectroscopy (XANES) and extended X-ray absorption fine structure spectroscopy (EXAFS) were used to probe the spatial distribution of the catalytic metal centers ligated onto the iminopyridine moieties, confirming that single cobalt species were incorporated into the CON materials. This work also highlights the potential of the iminopyridine moiety being an alternative to bipyridine as metal coordination site for ligation of catalytic metal centers into the backbone of porous networks, such as COFs, CMPs or MOFs, which has not yet been widely explored in the literature.

4.7 Experimental methods

4.7.1 Materials and methods

All reagents were obtained from Sigma-Aldrich, TCI Europe and ABCR. Anhydrous solvents were purchased from Acros Organics or Fisher Scientific. All chemicals were used without further purification.

4.7.1.1 Solution nuclear magnetic resonance

^{1}H NMR spectra were recorded in solution at 400 MHz, using a Bruker Avance 400 NMR spectrometer.

4.7.1.2 Powder X-ray diffraction

Powder X-ray diffraction (PXRD) data were collected in vertical transmission mode from loose powder samples held on Mylar film in aluminium well plates, using a Panalytical Empyrean diffractometer equipped with a high throughput screening XYZ stage, X-ray focusing mirror and PIXcel detector with Cu K radiation.

4.7.1.3 Thermogravimetric analysis

Thermogravimetric analysis was performed on an EXSTAR6000 by heating samples at 10 °C min^{-1} under air in open aluminium pans to 800 °C.

4.7.1.4 Gas sorption analysis

Apparent surface areas were measured by nitrogen sorption at 77.3 K using a Micromeritics ASAP 2420 volumetric adsorption analyzer. Powder samples were degassed offline at 393 K for 12 h under dynamic vacuum (10^{-5} bar) before analysis, followed by degassing on the analysis port under vacuum, also at 393 K. Pore size distributions of COFs from fitting the nonlocal density functional theory (NL-DFT) model to the adsorption data. Carbon dioxide isotherms were collected up to a pressure of 1 bar on a Micromeritics ASAP2020 at 273 and 298 K.

4.7.1.5 Fourier-transform infrared spectroscopy

IR spectra were recorded using a Bruker Tensor 27 FT-IR spectrometer. Samples were analyzed as KBr disks for 16 scans with a resolution of 4 cm^{-1}.

4.7.1.6 UV-Vis absorption spectra

UV-Vis absorption spectra of the polymers were measured on a Cary 5000 UV-Vis-NIR spectrometer by measuring the reflectance of powders in the solid state.

4.7.1.7 Scanning electron microscopy

Imaging was performed using a Hitachi S-4800 cold field emission scanning electron microscope (FE-SEM). Samples were prepared by depositing the dry powders on 15 mm Hitachi M4 aluminium stubs using an adhesive high-purity carbon tab before coating with a 2 nm layer of gold using an Emitech K550X automated sputter coater. Imaging was conducted at a working voltage of 3 kV and a working distance of 8 mm using a combination of upper and lower secondary electron detectors.

4.7.1.8 Transmission electron microscopy

HAADF-STEM images were obtained on a JEOL 2100FCs microscope at an accelerating voltage of 200 kV. The samples were prepared by drop-casting sonicated acetonitrile suspensions of the materials onto a copper grid.

4.7.1.9 Atomic force microscopy

The samples were mounted on Si wafer substrates and then these substrates were mounted on a magnetic puck. All AFM images were recorded in air on a Multimode 8 AFM (Bruker) using QNM tapping mode. The images were acquired using Scanasyst air probes (Bruker) with a nominal spring constant of 0.4 N m^{-1}. Images were processed using Gwyddion 2.38.

4.7.1.10 X-Ray photoelectron spectroscopy measurements

X-Ray photoelectron spectra were measured on an Axis-Supra instrument from Kratos Analytical using monochromatic Al Kα radiation (225 W) and a low-energy electron flood source for charge compensation. Survey scan spectra were acquired using a pass energy of 160 eV and a 1 eV step size. Narrow region scans were acquired using a pass energy of 20 eV and a 0.1 eV step size. The hybrid lens mode was used in both cases. The sample powder was mounted on adhesive carbon tape mounted on a piece of silicon wafer, electrically isolated from the sample bar. The data were calibrated to a binding energy of 285.0 eV for the hydrocarbon C 1s peak post-acquisition. The data were converted into VAMAS file format (vms) and imported into the CasaXPS software package for analysis (CasaXPS version 2.3.20rev1.2H).

4.7.1.11 Time-correlated single photon counting (TCSPC) measurements

Time-correlated single photon counting experiments were performed on an Edinburgh Instruments LS980-D2S2-STM spectrometer equipped with picosecond pulsed LED excitation sources and a R928 detector, with a stop count rate below 3%. Suspensions were prepared by ultrasonicating the polymer in acetonitrile. The instrument response was measured with colloidal silica (LUDOX® HS-40, Sigma-Aldrich) at the excitation wavelength without filter. Decay times were fitted in the FAST software using suggested lifetime estimates.

4.7.1.12 X-Ray absorption fine structure spectra measurements and analysis

X-Ray absorption fine structure spectra (Co K-edge) were collected at 1W1B station in Beijing Synchrotron Radiation Facility (BSRF). The storage rings of BSRF was operated at 2.5 GeV with a maximum current of 250 mA. Using Si(111) double-crystal monochromator, the data collection were carried out in transmission mode using ionization chamber. All spectra were collected under ambient conditions. The acquired extended X-ray absorption fine structure spectroscopy (EXAFS) data were processed according to the standard procedures using the ATHENA module in the IFEFFIT software packages. The k^3-weighted EXAFS spectra were obtained by subtracting the post-edge background from the overall absorption and then normalizing with respect to the edge-jump step. Subsequently, k^3-weighted $\chi(k)$ data of Co K-edge was Fourier transformed to real (R) space using a Hanning window (dk=1.0 $Å^{-1}$) to

separate the EXAFS contributions from different coordination shells. To obtain the quantitative structural parameters around central atoms, least-squares curve parameter fitting was performed using the ARTEMIS module of IFEFFIT software packages.

4.7.1.13 Carbon dioxide reduction experiments

A quartz flask was charged with the COF nanosheets powder (1 mg), 2,2'-bipyridyl (1.5 mg), acetonitrile, water and triethanolamine (3:1:1 vol. mixture, 5 mL) and sealed with a septum. The resulting suspension was ultrasonicated for 5 minutes and then purged with CO_2 for 5 minutes. The reaction mixture was illuminated with a 300 W Newport Xe light source (model: 6258, Ozone free) equipped with a $\lambda > 420$ nm cut-off filter. Gaseous products were taken with a gas-tight syringe and run on a Shimadzu GC-2014 gas chromatograph equipped with a ShinCarbon ST micropacked column (Restek 80-100 mesh, 2 m length, 0.53 mm inner diameter) and a thermal conductivity detector calibrated against standard gas mixtures of known concentration.

4.7.1.14 Isotope–labelling experiment

Isotope–labelling experiment for CO_2 reduction was performed using COF nanosheets powder (1 mg), 2,2'-bipyridyl (1.5 mg), acetonitrile, water and triethanolamine (3:1:1 vol. mixture, 5 mL) and sealed with a septum. The resulting suspension was ultrasonicated for 5 minutes and then purged with $^{13}CO_2$ for 5 minutes. The reaction mixture was illuminated with a 300 W Newport Xe light source (model: 6258, Ozone free) equipped with a $\lambda > 420$ nm cut-off filter. The gas phase was analyzed by using a gas chromatography (Agilent GC-MS 7890B) with a mass-spectrometer (Agilent GC-MS 5977B) equipped with a GC-CARBONPLOT column (60 m length, 0.32 mm inner diameter).

4.7.1.15 External quantum efficiency measurements

The external quantum efficiency for the photocatalytic CO evolution was measured using a $\lambda = 420$ nm LED (0.325 mW cm^{-2}), controlled by an IsoTech IPS303DD power supply. For the experiments Co-FPy-CON (1 mg), 2,2'-bipyridyl (1.5 mg), acetonitrile (MeCN), water and triethanolamine (TEOA) (3:1:1 vol. mixture, 5 mL) and sealed with a septum. The resulting suspension was ultrasonicated for 5 minutes and then purged with CO_2 for 5 minutes. An area

of 5 cm^2 was illuminated and the light intensity was measured with a ThorLabs S120VC photodiode power sensor controlled by a ThorLabs PM100D Power and Energy Meter Console. The external quantum efficiencies were estimated using the equation below: The external quantum efficiencies were estimated using the equation below:

$$\eta EQE\ (\%) = \frac{2 \times n_{CO} \times N_A \times h \times c}{t \times I \times \lambda \times A} \times 100\%$$

where, n_{CO} is number of moles of CO produced, N_A is Avogadro's number, h is Planck constant, c is speed of light, t is reaction time, I is intensity of light, λ is the wavelength of incident light, and A is cross-sectional area of irradiation.

4.7.2 Synthetic procedures

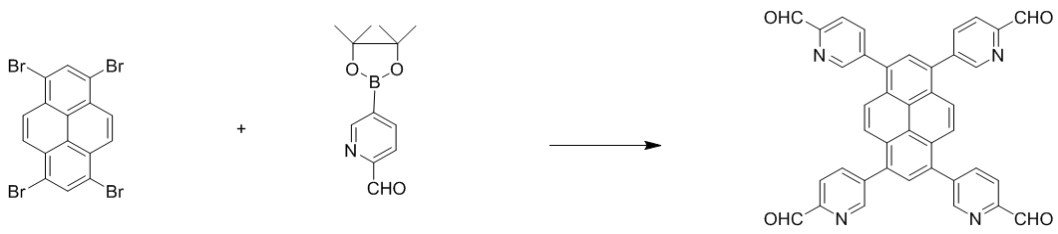

5,5',5'',5'''-(Pyrene-1,3,6,8-tetrayl)tetrapicolinaldehyde (PTA): A flask was charged with 1,3,6,8-tetrabromopyrene (517 mg, 1.0 mmol), 6-formylpyridine-3-boronic acid pinacol ester (932 mg, 4 mmol), [Pd(PPh_3)$_4$] (40 mg, 0.032 mmol), 1,4-dioxane (20 mL) and K_2CO_3 (1 g, 7.24 mmol). The mixture was degassed by bubbling with N_2 for 30 minutes and heated to 105 °C for 48 hours. The mixture was cooled to room temperature and poured into ice water. The precipitate was collected by filtration and washed with H_2O (3 × 100 mL), methanol (2 × 100 mL) and THF (2 × 100 mL). After drying at 80 °C, the product was obtained a yellow powder (384 mg, 62%). ^{1}H NMR (400 MHz, 1,1,2,2-tetrachloroethane-d_2) δ [ppm]: 10.29 (s, 4H), 9.16 (s, 4H), 8.61 (d, *J* = 8.5 Hz, 4H), 8.23 (m, 8H), 8.11 (s, 2 H). HR-MS (APCI): m/z calcd for $C_{40}H_{22}N_4O_4$: 622.1641 $[M+H]^+$; found: 623.1720. Anal. Calcd for $C_{40}H_{22}N_4O_4$: C, 77.16; H, 3.56; N, 9.00. Found: C, 67.80; H, 3.47; N, 8.01.

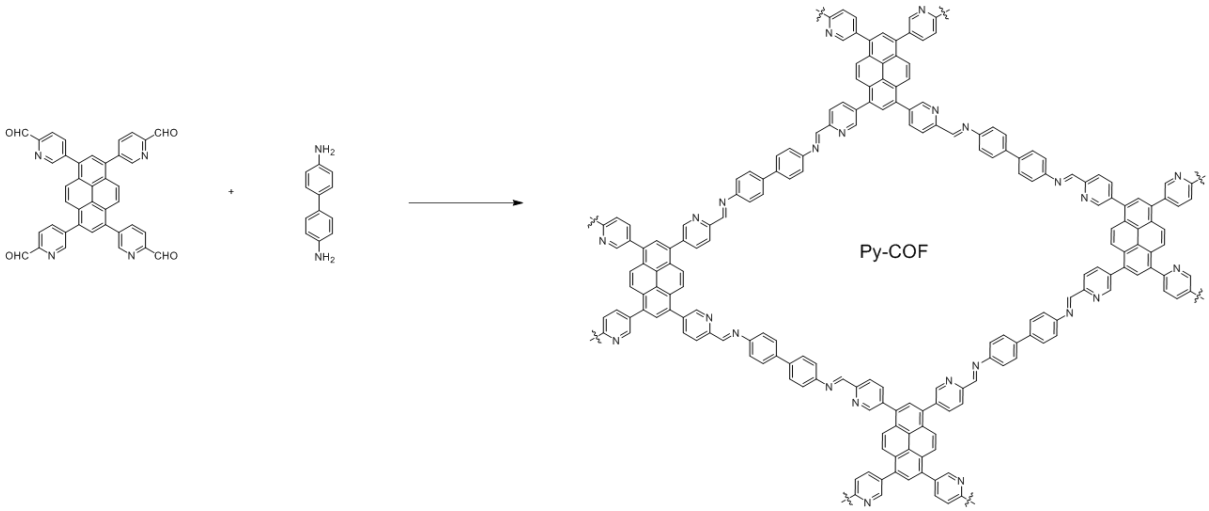

Scheme 4-1. Synthesis of **Py-COF**.

Synthesis of Py-COF: A Schlenk tube was charged 5,5',5'',5'''-(pyrene-1,3,6,8-tetrayl)tetrapicolinaldehyde (49.8 mg, 0.08 mmol), 1,1'-biphenyl-4,4'-diamine (19.6 mg, 0.16

mmol), 1,2-dichlorobenzene (2 mL), *n*-butanol (2 mL), and aqueous acetic acid (0.4 mL, 6 M). This mixture was homogenized by ultrasonication for 10 minutes and the tube was then flash-frozen at 77 K (liquid N_2 bath) and degassed by three freeze-pump-thaw cycles. The tube was then sealed off and then heated at 120 °C for 5 days. The yellow precipitate was collected by centrifugation (3000/min) and washed with *N*,*N*-dimethylformamide (100 mL), THF (100 mL) and anhydrous acetone (200 mL). After drying at 120 °C, the product was obtained a yellow powder (59 mg, 92%). Anal. Calcd for $(C_{68}H_{54}N_8)_n$: C, 83.07; H, 5.54; N, 11.40. Found: C, 69.78; H, 3.55; N, 8.69.

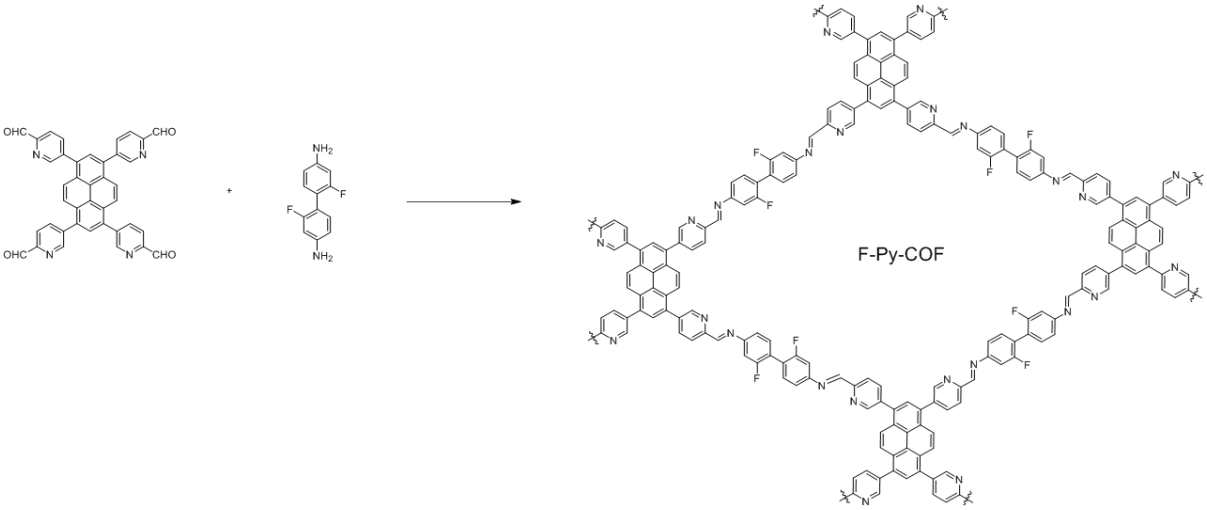

Scheme 4-2. Synthesis of **F-Py-COF**.

Solvothermal synthesis FPy-COF: A Schlenk tube was charged 5,5',5'',5'''-(pyrene-1,3,6,8-tetrayl)tetrapicolinaldehyde (24.9 mg, 0.04 mmol), 4,4'-diamino-2,2'-difluorobiphenyl (17.6 mg, 0.08 mmol), 1,2-dichlorobenzene (0.5 mL), *n*-butanol (0.5 mL), and aqueous acetic acid (0.1 mL, 6 M). This mixture was homogenized by ultrasonication for 10 minutes and the tube was then flash-frozen at 77 K (liquid N_2 bath) and degassed by three freeze-pump-thaw cycles. The tube was then sealed off and then heated at 120 °C for 7 days. The yellow precipitate was collected by centrifugation (3000/min) and washed with *N*,*N*-dimethylformamide (100 mL), THF (100 mL) and anhydrous acetone (200 mL). After drying at 120 °C, the product was obtained a yellow powder (35 mg, 88%). Anal. Calcd for $(C_{68}H_{50}F_4N_8)_n$: C, 77.40; H, 4.78; F, 7.2; N, 10.62. Found: C, 70.68; H, 3.48; N, 9.06.

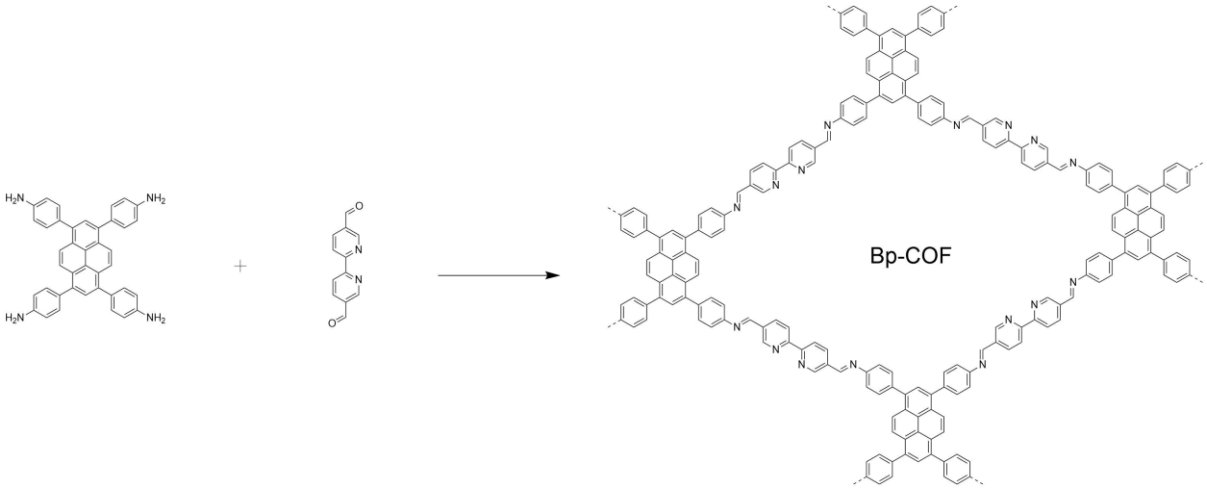

Scheme 4-3. Synthesis of Bp-COF.

Synthesis of Bp-COF[38]**:** A Schlenk tube was charged with 4,4',4'',4'''-(pyrene-1,3,6,8-tetrayl) tetraaniline (85 mg, 0.15 mmol) and 2,2'-bipyridine-5,5'-dicarbaldehyde (64.0 mg, 0.30 mmol), mesitylene (1.5 mL), 1,4-dioxane (1.5 mL) and aqueous acetic acid solution (0.5 mL, 3 M). This mixture was homogenized by ultrasonication for 10 minutes and the tube was then flash-frozen at 77 K (liquid N_2 bath) and degassed by three freeze-pump-thaw cycles. The tube was then sealed off and then heated at 120 °C for 3 days. The yellow precipitate was collected by centrifugation (3000/min) and washed with THF (100 mL) and anhydrous acetone (200 mL). After drying at 120 °C, the product was obtained a yellow powder (130 mg, 89%). Anal. Calcd for $(C_{64}H_{38}N_8)_n$: C, 83.64; H, 4.17; N, 12.19. Found: C, 80.16; H, 4.14; N, 11.45.

Cobalt loading onto Py-CON: **Py-COF** (20 mg) was mixed with $CoCl_2 \cdot 6H_2O$ (9 mg, 0.0378 mmol) in acetonitrile (20 mL) and the resulting suspension was ultrasonicated for 6 hours at room temperature. After this the solid was filtered off and washed with of acetonitrile (200 mL). The resulting solid was dried in vacuum at 60 °C overnight to give **Co-Py-CON**. The cobalt content of **Co-Py-CON** was determined by inductively coupled plasma-optical emission spectrometry to be approximately 4 wt%.

Cobalt loading onto bulk Py-COF using impregnation: Bulk **Py-COF** (20 mg) was mixed with $CoCl_2 \cdot 6H_2O$ (9 mg, 0.0378 mmol) in acetonitrile (20 mL) and the suspension was left standing for 6 hours at room temperature. The solid was filtered and washed with acetonitrile (200 mL) and methanol (200 mL) before drying under vacuum at 60 °C overnight to give bulk

Co-Py-COF. The cobalt content of bulk **Co-Py-COF** was determined by inductively coupled plasma-optical emission spectrometry to be approximately 1.9 wt%.

Cobalt loading onto FPy-CON: **FPy-COF** (20 mg) was mixed with $CoCl_2 \cdot 6H_2O$ (9 mg, 0.0378 mmol) in acetonitrile (20 mL) and the resulting suspension was ultrasonicated for 6 hours at room temperature. After this the solid was filtered off and washed with of acetonitrile (200 mL). The resulting solid was dried under vacuum at 60 °C overnight to give **Co-FPy-CON**. The cobalt content of **Co-FPy-CON** was determined by inductively coupled plasma-optical emission spectrometry to be approximately 2.1 wt%.

Cobalt loading onto bulk FPy-COF using impregnation: Bulk **FPy-COF** (20 mg) was mixed with $CoCl_2 \cdot 6H_2O$ (9 mg, 0.0378 mmol) in acetonitrile (20 mL) and the suspension was left standing for 6 hours at room temperature. The solid was filtered and washed with acetonitrile (200 mL) and methanol (200 mL) before drying under vacuum at 60 °C overnight to give bulk **Co-FPy-COF**. The cobalt content of bulk **Co-FPy-COF** was determined by inductively coupled plasma-optical emission spectrometry to be approximately 0.9 wt%.

Cobalt loading onto Bp-CON: **Bp-COF** (20 mg) was mixed with $CoCl_2 \cdot 6H_2O$ (9 mg, 0.0378 mmol) in acetonitrile (20 mL) and the resulting suspension was ultrasonicated for 6 hours at room temperature. After this the solid was filtered off and washed with of acetonitrile (200 mL). The resulting solid was dried under vacuum at 60 °C overnight to give **Co-Bp-CON**. The cobalt content of **Co-Bp-CON** was determined by inductively coupled plasma-optical emission spectrometry to be approximately 4.1 wt%.

Cobalt loading onto bulk Bp-COF using impregnation: Bulk **Bp-COF** (20 mg) was mixed with $CoCl_2 \cdot 6H_2O$ (9 mg, 0.0378 mmol) in acetonitrile (20 mL) and the suspension was left standing for 6 hours at room temperature. The solid was filtered and washed with acetonitrile (200 mL) and methanol (200 mL) before drying under vacuum at 60 °C overnight to give bulk **Co-Bp-COF**. The cobalt content of bulk **Co-Bp-COF** was determined by inductively coupled plasma-optical emission spectrometry to be approximately 4.0 wt%.

Zinc loading onto FPy-CON: Bulk **FPy-COF** (20 mg) was mixed with $Zn(OAc)_2$ (9 mg, 0.049 mmol) in acetonitrile (20 mL) and the resulting suspension was ultrasonicated for 6 hours at room temperature. After this the solid was filtered off and washed with of acetonitrile (200

mL). The resulting solid was dried under vacuum at 60 °C overnight to give **Zn-Py-CON**. The zinc content of **Zn-Py-CON** was determined by inductively coupled plasma-optical emission spectrometry to be approximately 4.9 wt%.

4.7.3 NMR spectra

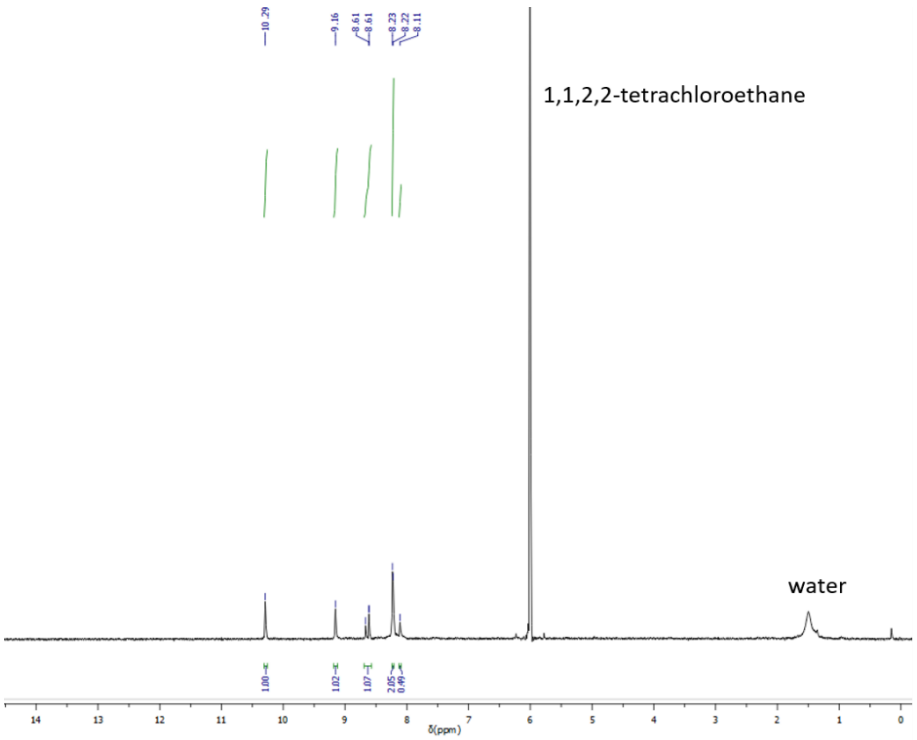

Figure 4-16. ^{1}H NMR spectrum of 5,5',5",5"'-(pyrene-1,3,6,8-tetrayl)tetrapicolinaldehyde (PTA) measured in 1,1,2,2-tetrachloroethane-d_2 at 80 °C.

4.7.4 Fourier-transform infrared spectroscopy

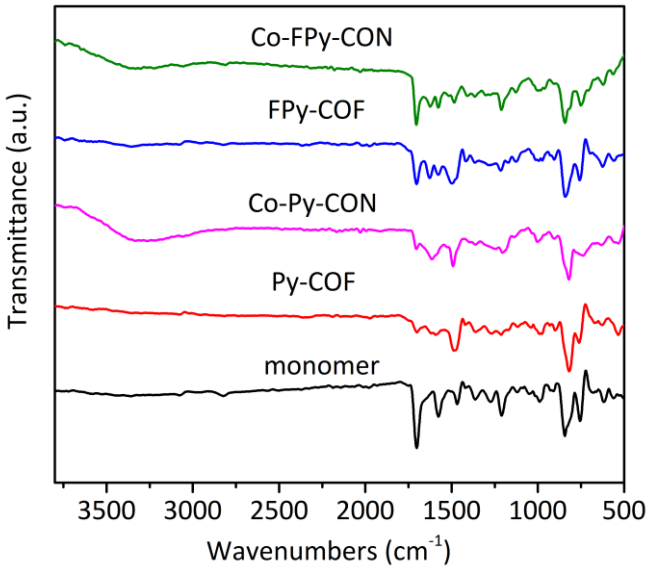

Figure 4-17. FT-IR spectra of monomer (**PTA**), **Py-COF**, **Co-Py-CON**, **FPy-COF** and **Co-FPy-CON**.

4.7.5 Thermogravimetric analysis

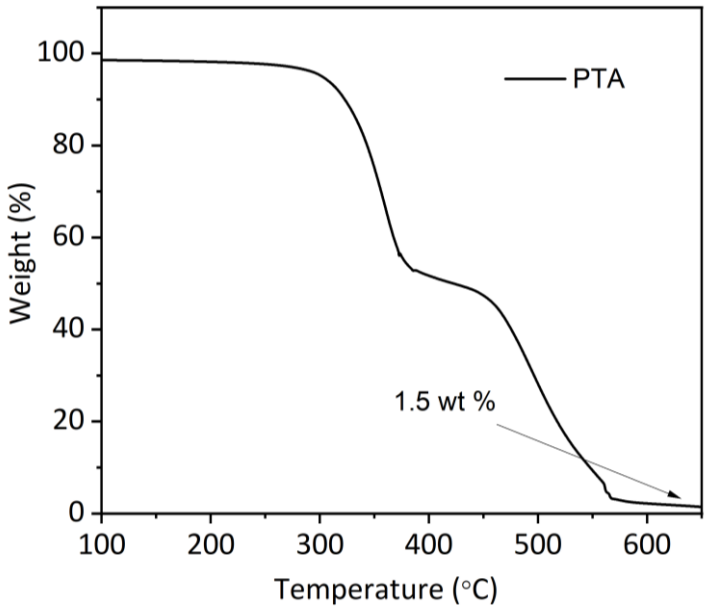

Figure 4-18. TGA trace of 5,5',5",5"'-(pyrene-1,3,6,8-tetrayl)tetrapicolinaldehyde (**PTA**) heated in air. The residue at 650°C presumably originates from inorganic residues from the synthesis.

4.7.6 Gas sorption isotherms

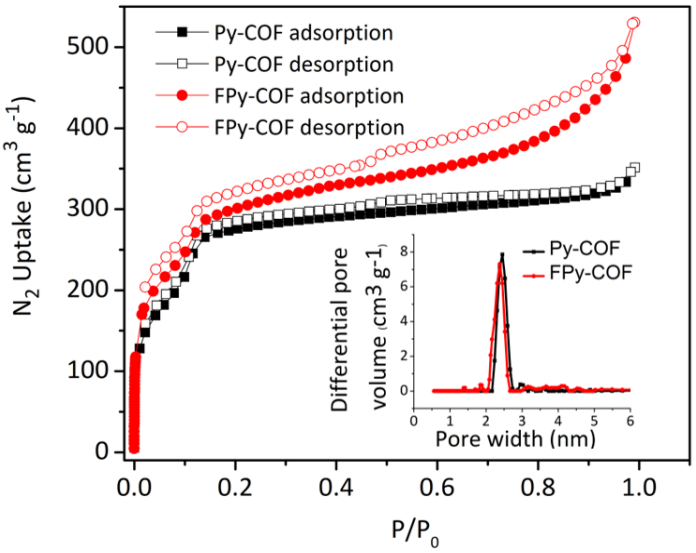

Figure 4-19. Nitrogen adsorption/desorption isotherms for COFs recorded at 77 K. Insets, pore size distribution profiles of COFs calculated by NL-DFT.

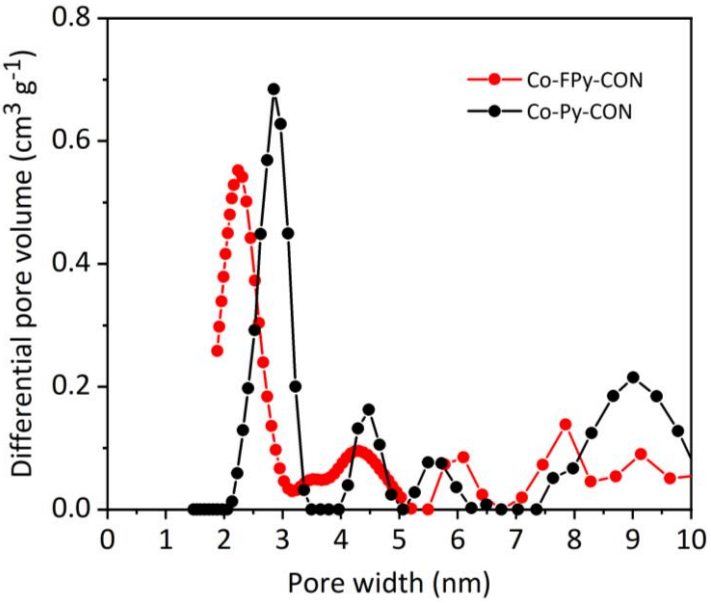

Figure 4-20. Pore size distribution profiles of CONs calculated by NL-DFT.

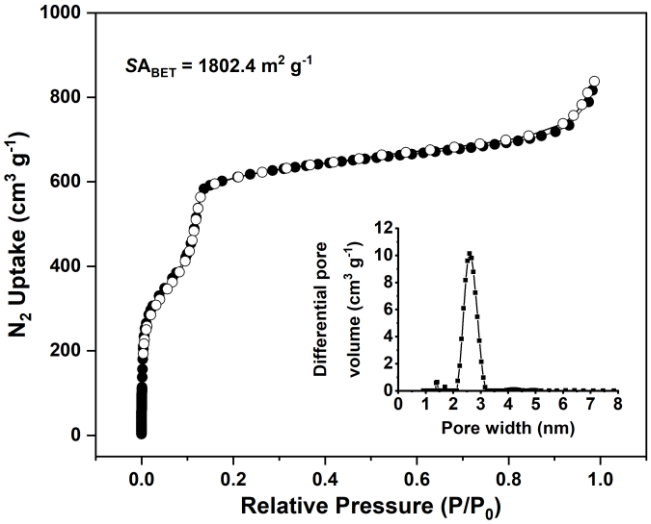

Figure 4-21. Nitrogen adsorption/desorption isotherms for **Bp-COF** recorded at 77 K. Insets, pore size distribution profiles of COFs calculated by NL-DFT.

Table 4-5. Unit cell parameters of **Py-COF**.

Unit cell parameters of Py-COF	
Simulated	Refined
Space group: P1	Space group: P1
a/Å = 43.11	a/Å = 43.172(4)
b/Å = 38.03	b/Å = 37.740(4)
c/Å =3.783	c/Å = 3.9237(7)
α/° = 90.09	α/° = 86.81(2)
β/° = 86.5	β/° = 82.76(1)
γ/° = 90.05	γ/° = 92.307(8)
Volume/ $Å^3$ = 6202.13	Volume/ $Å^3$ = 6325(1)

Table 4-6. Unit cell parameters of **FPy-COF**.

Unit cell parameters of FPy-COF	
Simulated	Refined
Space group: P1	Space group: P1
a/Å = 43.11	a/Å = 44.704(9)
b/Å = 38.03	b/Å = 38.100(7)
c/Å =3.78	c/Å = 3.977(1)
α/° = 90.1	α/° = 91.39(4)
β/° = 86.5	β/° = 84.43(6)
γ/° = 90.05	γ/° = 95.93(1)
Volume/ $Å^3$ = 6197.21	Volume/ $Å^3$ = 6705(3)

4.7.7 STEM and element mapping

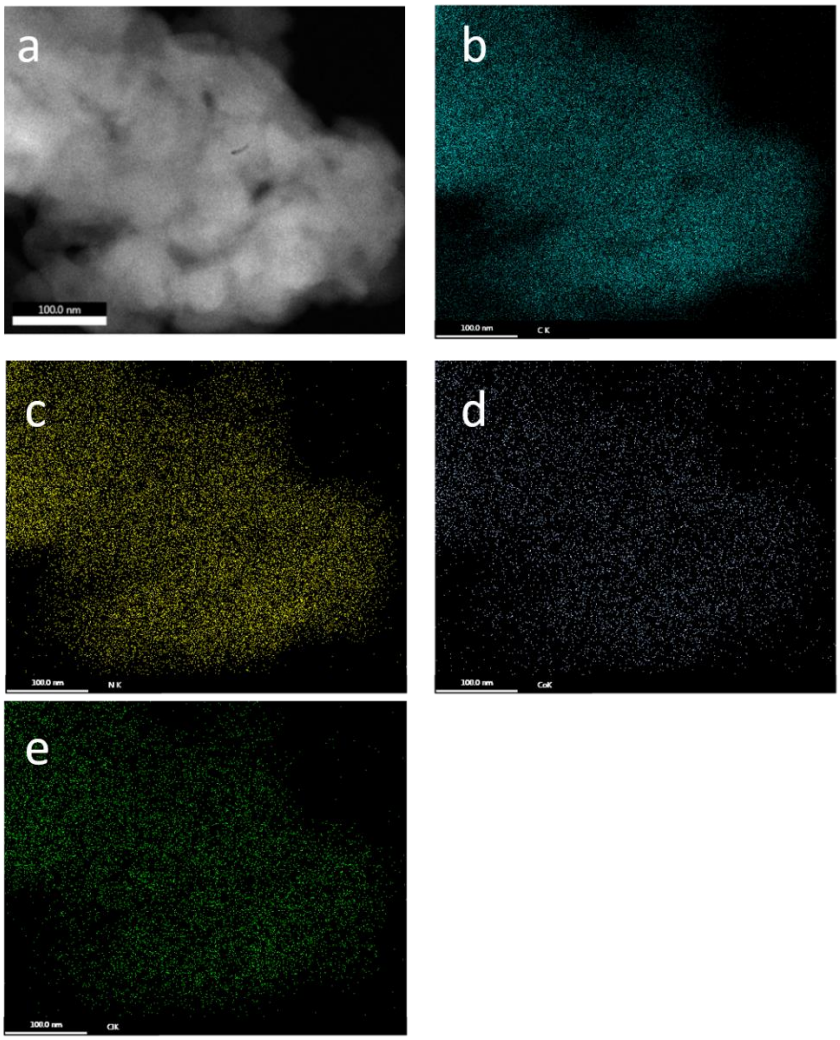

Figure 4-22. HAADF-STEM images of the **Co-Py-CON** (a) and the corresponding element mapping of (b) C, (c) N, (d) Co and (e) Cl.

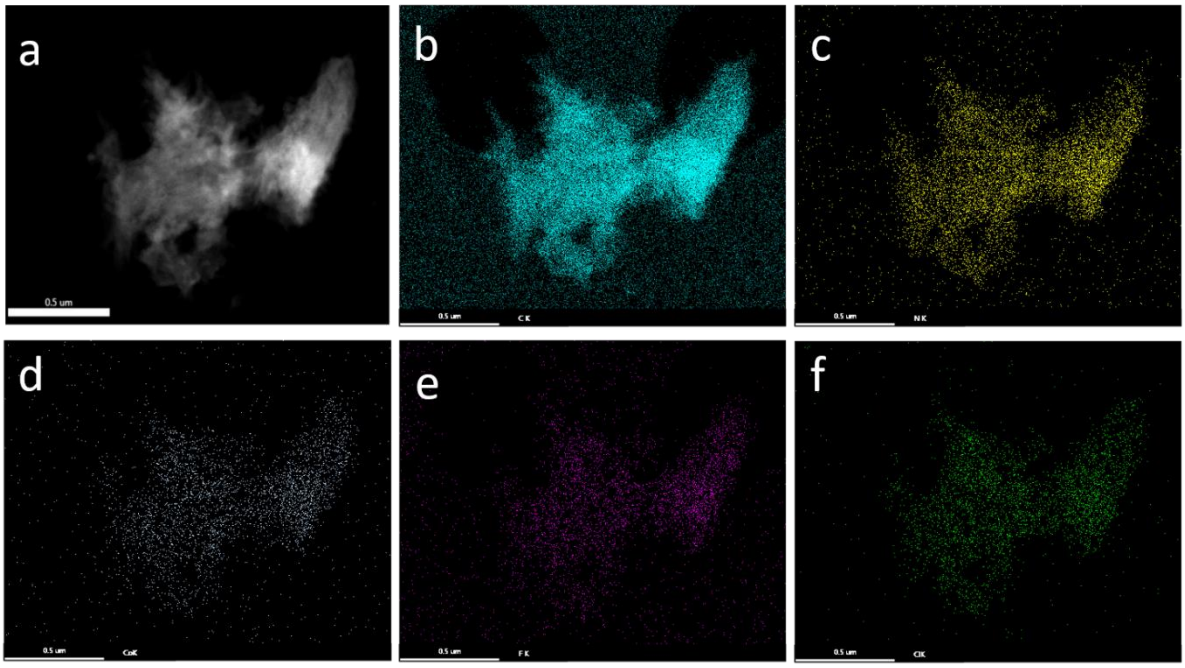

Figure 4-23. HAADF-STEM images of the **Co-FPy-CON** (a) and the corresponding element mapping of (b) C, (c) N, (d) Co, (e) F and (f) Cl.

4.7.8 Scanning electron microscopy

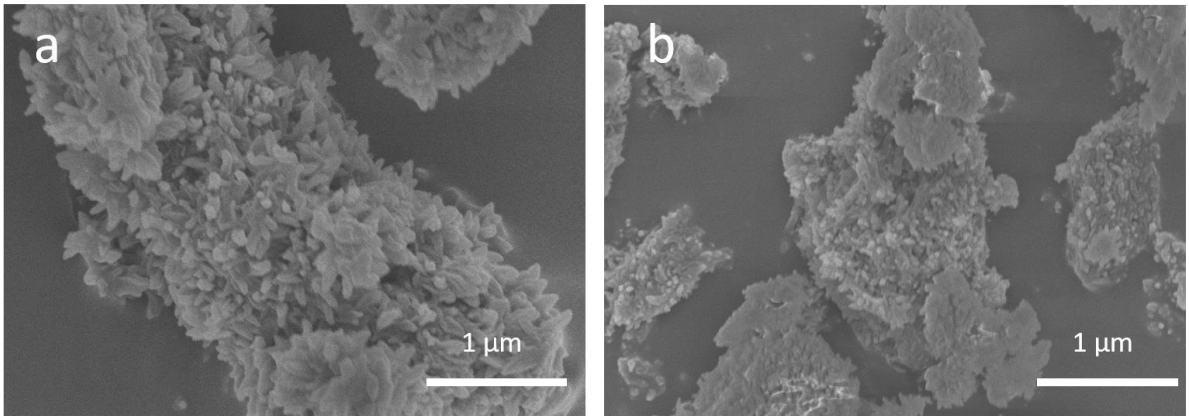

Figure 4-24. SEM images of **Co-Py-CON**(a) and **Co-FPy-CON**(b).

4.7.9 Photoluminescence spectra

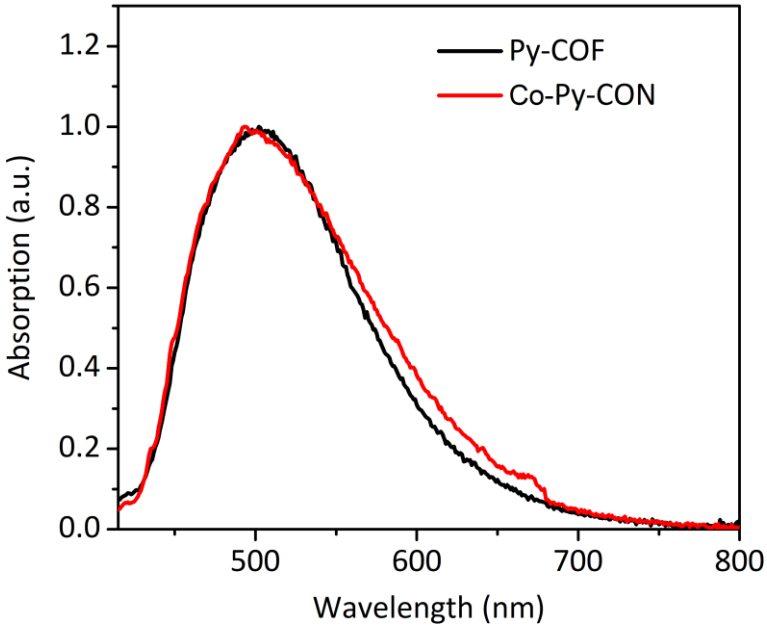

Figure 4-25. Photoluminescence spectra of **Py-COF** and **Co-Py-CON** suspended in acetonitrile (λ_{exc} = 395 nm).

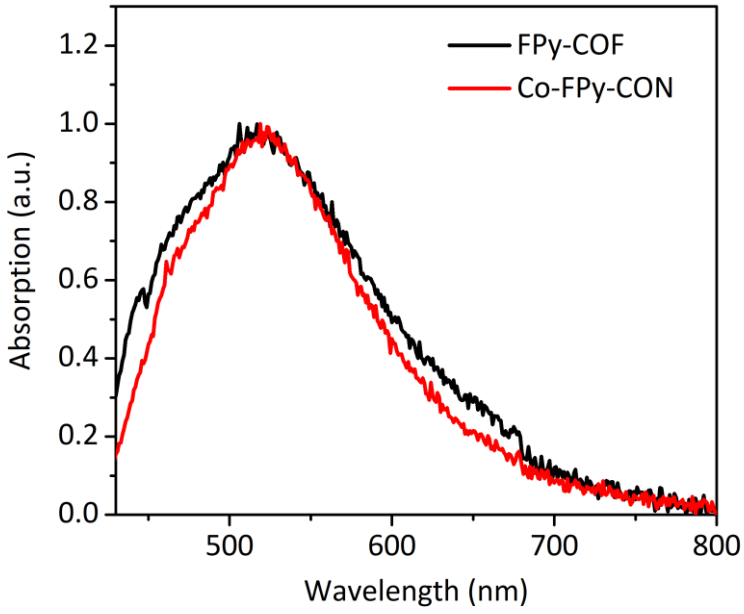

Figure 4-26. Photoluminescence spectra of **FPy-COF** and **Co-FPy-CON** in acetonitrile suspension (λ_{exc} = 405 nm).

4.7.10 Time-correlated single-photon counting

Table 4-7. Fluorescence life-time measurements.

Material	**λ_{exc} /nm**	**τ_1 /ns**	**B_1 /%**	**τ_2 /ns**	**B_2 /%**	**τ_3 /ns**	**B_3 /%**	**χ^2**	**τ_{avg}[a] /ns**
Py-COF	405	0.22	2.19	1.26	10.37	3.50	87.43	1.16	3.20
Co-Py-CON	405	0.60	6.07	1.54	10.76	3.48	83.16	1.32	3.10
FPy-COF	405	0.44	23.18	1.92	13.68	3.60	63.14	1.31	2.64
Co-FPy-CON	405	0.357	37.72	1.32	18.06	3.72	44.22	1.19	2.02

Fluorescence life-times obtained upon excitation at λ_{exc} = 405 nm with a laser and observed at λ_{em} = 500, 520 nm. Note that the poor χ^2 value is due to the fast decay for this material close to the instrument response. [a] Fluorescence life-times in water suspension obtained from fitting time-correlated single photon counting decays to a sum of three exponentials, which yield τ_1, τ_2, and τ_3 according to $\sum_{i=1}^{n}(A + B_i \exp(-t/\tau_i))$. τ_{AVG} is the weighted average lifetime calculated as $\sum_{i=1}^{n} B_i \tau_i$.

4.8 References

1. T. Inoue, A. Fujishima, S. Konishi and K. Honda, *Nature*, 1979, **277**, 637–638.
2. J. L. White, M. F. Baruch, J. E. Pander, Y. Hu, I. C. Fortmeyer, J. E. Park, T. Zhang, K. Liao, J. Gu, Y. Yan, T. W. Shaw, E. Abelev and A. B. Bocarsly, *Chem. Rev.*, 2015, **115**, 12888–12935.
3. S. Wang, W. Yao, J. Lin, Z. Ding and X. Wang, *Angew. Chem. Int. Ed.*, 2014, **53**, 1034–1038.
4. T. W. Schneider, M. Z. Ertem, J. T. Muckerman and A. M. Angeles-Boza, *ACS Catal.*, 2016, **6**, 5473–5481.
5. V. S. Thoi, N. Kornienko, C. G. Margarit, P. Yang and C. J. Chang, *J. Am. Chem. Soc.*, 2013, **135**, 14413–14424.
6. Z. Guo, S. Cheng, C. Cometto, E. Anxolabéhère-Mallart, S. M. Ng, C. C. Ko, G. Liu, L. Chen, M. Robert and T. C. Lau, *J. Am. Chem. Soc.*, 2016, **138**, 9413–9416.
7. B. Qiao, A. Wang, X. Yang, L. F. Allard, Z. Jiang, Y. Cui, J. Liu, J. Li and T. Zhang, *Nat. Chem.*, 2011, **3**, 634–641.
8. L. Jiao and H. L. Jiang, *Chem*, 2019, **5**, 786–804.
9. C. Gao, S. Chen, Y. Wang, J. Wang, X. Zheng, J. Zhu, L. Song, W. Zhang and Y. Xiong, *Adv. Mater.*, 2018, **30**, 1704624.
10. S. Yang, B. Pattengale, S. Lee, J. Huang, *ACS Energy Lett.* 2018, **3**, 532-539.
11. S. Yang, W. Hu, X. Zhang, P. He, B. Pattengale, C. Liu, M. Cendejas, I. Hermans, X. Zhang, J. Zhang and J. Huang, *J. Am. Chem. Soc.*, 2018, **140**, 14614–14618.
12. T. J. Ozumerzifon, R. F. Higgins, J. P. Joyce, J. L. Kolanowski, A. K. Rappé and M. P. Shores, *Inorg. Chem.*, 2019, **58**, 7785–7793.
13. D. Zhang, T. K. Ronson and J. R. Nitschke, *Acc. Chem. Res.*, 2018, **51**, 2423–2436.
14. X. Wang, L. Chen, S. Y. Chong, M. A. Little, Y. Wu, W. H. Zhu, R. Clowes, Y. Yan, M. A. Zwijnenburg, R. S. Sprick and A. I. Cooper, *Nat. Chem.*, 2018, **10**, 1180–1189.
15. T. Banerjee, K. Gottschling, G. Savasci, C. Ochsenfeld and B. V. Lotsch, *ACS Energy Lett.*, 2018, **3**, 400-409
16. P. Pachfule, A. Acharjya, J. Roeser, T. Langenhahn, M. Schwarze, R. Schomaecker, A. Thomas and J. Schmidt, *J. Am. Chem. Soc.*, 2018, **140**, 1423-1427
17. M. Lu, J. Liu, Q. Li, M. Zhang, M. Liu, J.-L. Wang, D.-Q. Yuan and Y.-Q. Lan, *Angew. Chem. Int. Ed.*, 2019, **58**, 12392–12397.
18. W. Zhong, R. Sa, L. Li, Y. He, L. Li, J. Bi, Z. Zhuang, Y. Yu and Z. Zou, *J. Am. Chem. Soc.*, 2019, **141**, 7615–7621.
19. M. Lu, Q. Li, J. Liu, F. M. Zhang, L. Zhang, J. L. Wang, Z. H. Kang and Y. Q. Lan, *Appl. Catal. B Environ.*, 2019, **254**, 624–633.
20. A. H. Alahmed, M. E. Briggs, A. I. Cooper and D. J. Adams, *J. Mater. Chem. A*, 2019, **7**, 549–557.
21. J. Lü, C. Perez-Krap, M. Suyetin, N. H. Alsmail, Y. Yan, S. Yang, W. Lewis, E. Bichoutskaia, C. C. Tang, A. J. Blake, R. Cao and M. Schröder, *J. Am. Chem. Soc.*, 2014, **136**, 12828–12831.
22. Z. Fu, X. Wang, A. M. Gardner, X. Wang, S. Y. Chong, G. Neri, A. J. Cowan, L. Liu, X. Li, A. Vogel, R. Clowes, M. Bilton, L. Chen, R. S. Sprick and A. I. Cooper, *Chem. Sci.*, 2020, **11**, 543–550.
23. D. N. Bunck and W. R. Dichtel, *J. Am. Chem. Soc.*, 2013, **135**, 14952–14955.
24. T. Sick, J. M. Rotter, S. Reuter, S. Kandambeth, N. N. Bach, M. Döblinger, J. Merz, T. Clark, T. B. Marder, T. Bein and D. D. Medina, *J. Am. Chem. Soc.*, 2019, **141**, 12570–12581.

25. G. Li, B. Zhang and Z. Wang, *Macromolecules*, 2016, **49**, 2575–2581.
26. S. Wang, Q. Wang, P. Shao, Y. Han, X. Gao, L. Ma, S. Yuan, X. Ma, J. Zhou, X. Feng, and B. Wang, *J. Am. Chem. Soc.* 2017, **139**, 4258–4261.
27. C. Zhang, S. Zhang, Y. Yan, F. Xia, A. Huang, and Y. Xian *ACS Appl. Mater. Interfaces* 2017, **9**, 13415−13421.
28. S. Xiong, J. S. Chen, X. W. Lou and H. C. Zeng, *Adv. Funct. Mater.*, 2012, **22**, 861–871.
29. C. Chen, T. Wu, H. Wu, H. Liu, Q. Qian, Z. Liu, G. Yang and B. Han, *Chem. Sci.*, 2018, **9**, 8890–8894.
30. C. C. Hojilla Atienza, A. C. Bowman, E. Lobkovsky, P. J. Chirik, *J. Am. Chem. Soc.* 2010, **132**, 16343–16345.
31. A. C. Bowman, C. Milsmann, C. C. H. Atienza, E. Lobkovsky, K. Wieghardt, P. J. Chirik, *J. Am. Chem. Soc.* 2010, **132**, 1676–168.
32. C. Liu, K. D. Dubois, M. E. Louis, A. S. Vorushilov and G. Li, *ACS Catal.*, 2013, **3**, 655–662.
33. D. Il Won, J. S. Lee, J. M. Ji, W. J. Jung, H. J. Son, C. Pac and S. O. Kang, *J. Am. Chem. Soc.*, 2015, **137**, 13679–13690.
34. M. Lu, Q. Li, J. Liu, F. M. Zhang, L. Zhang, J. L. Wang, Z. H. Kang and Y. Q. Lan, *Appl. Catal. B Environ.*, 2019, **254**, 624–633.
35. H. Zhang, J. Wei, J. Dong, G. Liu, L. Shi, P. An, G. Zhao, J. Kong, X. Wang, X. Meng, J. Zhang and J. Ye, *Angew. Chem. Int. Ed.*, 2016, **55**, 14310–14314.
36. J. C. Hu, M. X. Gui, W. Xia, J. Wu, Y. N. Zhou, N. Feng, J. Xiao, H. Liu, C. H. Tung, L. Z. Wu and F. Wang, *J. Mater. Chem. A*, 2019, **7**, 10475–10482.
37. Y. Fu, X. Zhu, L. Huang, X. Zhang, F. Zhang and W. Zhu, *Appl. Catal. B Environ.*, 2018, **239**, 46–51.
38. W. Leng, Y. Peng, J. Zhang, H. Lu, X. Feng, R. Ge, B. Dong, B. Wang, X. Hu and Y. Gao, *Chem. Eur. J.*, 2016, **22**, 9087–9091.

Chapter 5

Summary and Outlook

In this thesis, photoactive COFs were synthesized by integrating functional building blocks into COFs that allowed us to fine-tune photocatalysts for hydrogen evolution and for CO_2 reduction. The properties of COFs, such as light absorption, porosity, hydrophobicity, charge transport and photoluminescent lifetime, were systematically tuned. Structure-function relationships were then investigated, showing that the photocatalytic activities of COFs are the net result of a complex set of interdependent factors.

In **Chapter 2**, dibenzo[*b,d*]thiophene sulfone building blocks were successfully introduce into crystalline COFs. A fused sulfone COF (**FS-COF**) shows a highly ordered structure built from a planar and linear moiety (benzo[1,2-*b*:4,5-*b′*]bis[*b*]benzothiophene). This was demonstrated by the PXRD of COFs, which **FS-COF** shows more peaks and shaper peaks than **S-COF**, indicating **FS-COF** is more crystalline than **S-COF**. This is because the non-linear linker can stack in more than one geometry, which makes it more likely to introduce defects in the resulting framework. **FS-COF** also exhibits excellent photocatalytic hydrogen evolution activity, exceeding its isostructural unfunctionalized **TP-COF**, the best linear polymer **P10** and other reported COFs under comparable conditions. **FS-COF** also can survive at least 50 hours under visible light irradiation (> 420 nm). Based on the above results, photocatalytic hydrogen evolution activity was found to be a composite property that was influenced by a number of factors such as crystallinity, porosity and light absorption.

Dye sensitized strategy has been used to improve photocatalytic activity for inorganic photocatalysts. Here, both water soluble and oil soluble dyes were introduced to sensitize **FS-COF**. Hydrogen evolution rates were increased to 16.1 and 16.3 mmol g^{-1} h^{-1} with addition of **Eosin Y** and **WS5F**. The control experiments were performed using amorphous counterpart **FS-P**, showing that **FS-P** cannot be 'dye sensitized' which may be because of much smaller surface areas for **FS-P**. **FS-COF** can also dispersed into different solvents to form colloidal dispersions, and a thin-film was made by drop casting **FS-COF** dispersions onto the glass supports. This **FS-COF** based thin-film can retain its photoactivity under visible light irradiation (> 420 nm) at least 20 hours.

In **Chapter 3**, fluorine was introduced into *β*-ketoenamine COFs to explore the influence of fluorination for photocatalytic hydrogen production. Partially fluorinated COF (**2FB-COF**) shows the highest hydrogen evolution rate in this series COFs, reaching of 6169 μmol g^{-1} h^{-1}

with an EQE of 1.94 % at 515 nm. This can be attributed to that **2FB-COF** was wettable and had proper driving force for ascorbic acid oxidation.

From light obscuration measurements results, non-fluorinated **B-COF** and **2FB-COF** are hydrophilic, while fully fluorinated **4FB-COF** was more hydrophobic than **B-COF** and **2FB-COF**. Because of different wettability for COFs, the particle size of **B-COF** and **2FB-COF** are smaller than **4FB-COF** in aqueous solution. Furthermore, the *in situ* deposed Pt nanoparticles were homogeneously dispersed on the **B-COF** and **2FB-COF**, but Pt nanoparticles were aggregated on **4FB-COF**. These results explain the higher activity of **B-COF** and **2FB-COF** than **4FB-COF**. Moreover, **2FB-COF** has a greater driving force for oxidation of ascorbic acid than **B-COF**, which can explain its better performance for photocatalytic hydrogen production. In this work, the trade-off between wettability and driving force indicate that it is challenging to optimize only one factor to improve sacrificial hydrogen evolution performance. More importantly, for sacrificial hydrogen production, the driving force of oxidation potential for electron donors should be also considered which will make the system too complicated to optimise, thus overall water splitting without scavengers is highly desirable.

Photocatalytic CO_2 reduction into chemical fuels has attracted great research attention because of global climate crisis and rising energy demand. In this **Chapter 4**, a series of two-dimensional COFs were functionalized with iminopyridine moieties for metal coordination. Then, COF nanosheet (CON) catalysts prepared from iminopyridine based CONs by embedding with single Co atoms onto nanosheets matrix. A cobalt-loaded, partially-fluorinated CON shows a high CO production of 10.01 μmol with CO/H_2 selectivity of 76% over 6 hours visible light irradiation. This performance is comparable with state-of-the-art CO_2 reduction catalysts in the literature under comparable conditions. The spatial distribution of the cobalt metal centers was measured by X-ray absorption near-edge structure spectroscopy (XANES), extended X-ray absorption fine structure spectroscopy (EXAFS) and high resolution HAADF-STEM, which found that Co sites were successfully ligated onto the CONs. This work shows great potential of using iminopyridine moiety as a metal coordination sites for incorporation of catalytic metal centers onto porous materials such as COFs, CMPs and MOFs. Furthermore, the exfoliated CONs show better photocatalytic performance than their bulk counterparts, which indicate the potential of strategy to enhance the activity for two dimensional COFs.

Sacrificial hydrogen evolution is only the first step towards overall water splitting. However, until now, most materials developed for overall water splitting are inorganic semiconductors. These inorganic materials commonly contain rare elements, which will make it challenging for large-scale and sustainable development. Organic semiconductors are earth-abundant, environmentally friendly and structure tunable, which are promising for overall water splitting. In this thesis, we already demonstrate that COFs were used for hydrogen evolution reaction synthesized by using photoactive building blocks. The properties such as light absorption, porosity and hydrophobicity were fine-tuned in COFs by using different moieties. More importantly, the processability of COFs allows to make devices for water splitting application. Z-scheme is a promising strategy to achieve overall water splitting, which has two separate and coupled semiconductors and each semiconductor performed one of the half reactions in overall water splitting. COFs can be the platform materials to build Z-scheme composites, because COFs have large porosity and ordered structure. For example, the pores of COFs can be decorated with a second semiconductor nanoparticles to a make the Z-scheme catalyst. Overall water splitting is challenging because of the water formation (reverse reaction) was found to be accompanied with overall water splitting reaction. This water formation reaction is a thermodynamically downhill reaction which can occur spontaneously and decease the water splitting performance. Hence, further research will be also focus on property–activity relationships between catalysts and activity which will aid to create more efficient system.

For photocatalytic CO_2 reduction, homogenous molecular catalyst systems for CO_2 reduction are quite widely developed. However, these systems are typically not stable for long duration experiments. Recently, the strategy of using porous materials (CMPs, COFs and MOFs) as platforms to stabilize molecular catalysts has gathered momentum. These porous materials can also play a light-harvesting and electron-transfer role, rather than being simple inert supports. Thus, an assembly of porous materials with molecular catalysts allows for making highly active and stable CO_2 reduction catalyst. This area is in its infancy, and the complex synergistic and interactions between different porous materials and molecular catalysts needs deeper consideration. For example, hydrogen production is a competing reaction for CO_2 reduction, which may decrease efficiency of CO_2 reduction. One of strategies to increase selectivity is to introduce moieties with strong affinity to CO_2 molecules, which can create a CO_2 abundant microenvironment around metal catalysts, resulting CO_2 reduction prior to H_2 production. This is challenging, however, since many moieties that will attract CO_2 may also attract water – often more effectively.

Co-catalysts also are one of important factors need to be further investigated. The development of highly active, selective and stable co-catalysts is essential for CO_2 reduction, because co-catalyst play pivotal roles such as activating CO_2 molecules, enhancing selectivity and suppressing the back reactions. In addition to current inorganic co-catalysts such as Pt, Re, Ru, Co nanoparticles and/or their complexes, novel biological cocatalysts (enzymes and bacteria) might also be incorporated into organic porous materials, and this is a promising new area for the future.